RUHR-UNIVERSITÄT BOCHUM
Bauingenieurwesen

RUB

Felix Clauß

Thermo-Mechanical Investigations of Reinforced Concrete Structures Using Coda Wave Interferometry

Concrete Damage
Assessment by
CODA Waves

Schriftenreihe des Instituts für
Konstruktiven Ingenieurbau, Heft 2022-02

Thermo-Mechanical Investigations of Reinforced Concrete Structures Using Coda Wave Interferometry

by

Felix Clauß, M. Sc.

Ph.D. Thesis

for the degree of

Doctor of Engineering (Dr.-Ing.)

Faculty of Civil and Environmental Engineering
Ruhr University Bochum

Bochum, February 2022

Schriftenreihe des Instituts für Konstruktiven Ingenieurbau

Herausgeber:
Geschäftsführender Direktor des
Instituts für Konstruktiven Ingenieurbau
Ruhr-Universität Bochum

Heft 2022-2

Felix Clauß

Thermo-Mechanical Investigations of Reinforced Concrete Structures Using Coda Wave Interferometry

Shaker Verlag
Düren 2022

Bibliografische Information der Deutschen Nationalbibliothek
Die Deutsche Nationalbibliothek verzeichnet diese Publikation in der Deutschen Nationalbibliografie; detaillierte bibliografische Daten sind im Internet über http://dnb.d-nb.de abrufbar.

Zugl.: Bochum, Univ., Diss., 2022

Printed in Germany.

ISBN 978-3-8440-8698-0
ISSN 1614-4384

Shaker Verlag GmbH • Am Langen Graben 15a • 52353 Düren
Telefon: 02421 / 99 0 11 - 0 • Telefax: 02421 / 99 0 11 - 9
Internet: www.shaker.de • E-Mail: info@shaker.de

You can't stop the waves, but you can learn to surf.

— JON KABAT-ZINN

Abstract

Civil engineering structures are aging. Ultrasonic coda waves offer an auspicious opportunity to monitor this deterioration. Coda waves detect changes both sensitively and integrally over wide regions, rendering them suitable for monitoring entire structures. Current approaches with coda wave–based monitoring of concrete (structures) focus on specimens that are only a few centimeters small or on detecting cracks in reinforced concrete. The empirical model introduced in this thesis enables evaluating the load-bearing capacity of reinforced concrete structures subjected to bending using coda waves. The model involves the complex material behavior of reinforced concrete, from the linear-elastic range to the range of cracking and completed cracking.

The underlying methodology is based on mechanical, thermal and thermo-mechanical experiments on reinforced concrete beams. Ultrasonic measurements are evaluated using coda wave interferometry. This method yields the relative velocity change. The strain of the component is used as a reference. Investigations into the application, assembly and accuracy of strain measurement techniques reveal fiber optics as a suitable technique. Mutual influences of strain and temperature effects in fiber optic measurements were quantified. In this manner, strains are recorded quality-assured quasi-continuously along the fiber and provide detailed information on initial and later also progressive cracking.

The relative velocity change is correlated with the measured strain. The idea is based on the volume-like collection of influences by coda waves. Following this, the strain of the reinforcement is likewise averaged across a region. The correlation of the two respective quantities (relative velocity change and average steel strain) exhibits a linear relationship. This gives a first-order approach. Using this approach, the strain of the beam can be accurately calculated via the relative velocity change. Statistically, the model is of high quality ($R^2 = 0.99$) and low error (RMSE $\approx 0.09\,‰$).

Consequently, it becomes feasible to monitor reinforced concrete structures by means of ultrasonic measurements and to accurately indicate the load-bearing capacity even under progressive cracking.

Kurzfassung

Infrastrukturbauwerke altern. Um ihre Deterioration im Blick zu behalten, bieten sich Ultraschall Codawellen an. Sie erfassen sensitiv und zugleich integral Zustandsänderungen in großen Bereichen und eignen sich dadurch hervorragend zur Überwachung ganzer Strukturen. Aktuelle Ansätze zur codawellenbasierten Zustandsüberwachung fokussieren sich auf Probekörper in der Größe weniger Zentimeter oder die Erkennung von Rissen in Stahlbetontragwerken. Der in dieser kumulativen Dissertation vorgestellte empirische Ansatz ermöglicht es die Tragfähigkeit von biegebeanspruchten Stahlbetonstrukturen mit Ultraschall Codawellen zu bewerten. Der Ansatz berücksichtigt das komplexe Materialverhalten von Stahlbeton vom linear-elastischen Bereich über die beginnende Rissbildung bis hin zum abgeschlossenen Rissbild.

Die zugrunde liegende Methodik basiert auf mechanischen, thermischen und thermo-mechanischen Versuchen an Stahlbetonbalken. Die Ultraschallmessungen werden mit der Codawelleninterferometrie ausgewertet. Aus Zustandsänderungen resultiert die relative Geschwindigkeitsänderung. Als Referenz dient die Dehnung des Bauteils. In Untersuchungen zur Anwendung, Montage und Genauigkeit von Dehnungsmesstechniken wird die Faseroptik als geeignet nachgewiesen. Gegenseitige Beeinflussungen von Dehnungs- und Temperatureinflüssen in faseroptischen Messungen wurden quantifiziert. Dehnungen werden auf diese Weise qualitätsgesichert, quasi-kontinuierlich entlang einer Faser aufgenommen und liefern genaue Informationen über die beginnenden und später auch fortschreitende Rissbildung.

Die relative Geschwindigkeitsänderung wird mit der gemessenen Dehnung in Korrelation gesetzt. Die Idee basiert auf der volumenartigen Akkumulation von Einflüssen durch Codawellen. Inspiriert davon, wird die Dehnung des Bewehrungsstahls bereichsweise zusammengefasst. Die Korrelation der beiden Größen (relative Geschwindigkeitsänderung und mittlere Bauteildehnung) zeigt einen linearen Zusammenhang. Daraus folgt ein Ansatz erster Ordnung, mit dessen Hilfe die Dehnung des Bauteils über die relative Geschwindigkeitsänderung treffend vorausgesagt werden kann. Statistisch weist das Modell eine hohe Güte ($R^2 = 0.99$) und einen geringen Fehler (RMSE $\approx 0.09\,‰$) auf. Praktisch ist es so möglich, Stahlbetonstrukturen mithilfe von Ultraschallmessungen zu überwachen und auch unter fortschreitender Rissbildung die Tragfähigkeit stets genau anzugeben.

Preamble

This thesis was written between 2019 and 2022 during my work as a research assistant at the Institute of Concrete Structures at Ruhr University Bochum. It was accepted as a Ph.D. thesis by the Department of Civil and Environmental Engineering of Ruhr University Bochum.

First of all, I would like to express my gratitude to Prof. Dr.-Ing. habil. Peter Mark for giving me the opportunity to work at his institute and for his ongoing guidance, encouragement, and support. Thank you to Prof. Dr.-Ing. Christoph Gehlen and PD Dr. rer. nat. Ernst Niederleithinger for the invariably enriching cooperation within the research unit CoDA and for taking over the second and third opinions, respectively. Moreover, I would like to thank Prof. Dr. sc. techn. habil. Markus Knobloch for chairing the examination commission.

Special thanks go to Dr.-Ing. Mark Alexander Ahrens for the valuable exchange and the careful review of the manuscript. I would like to thank all colleagues at the Institute of Concrete Structures and at the Structural Testing Laboratory KIBKON for the pleasant time.

Lastly, I would like to express my deepest gratitude to my family and friends—my parents and my brother for their constant encouragement, Lukas for your interdisciplinary support, and especially you, Anna, for always having my back and promoting me in every situation in life.

Bochum, June 2022 Felix Clauß

Date of submission:	February 24, 2022
Date of oral examination:	June 15, 2022
1st referee:	Prof. Dr.-Ing. habil. Peter Mark, Ruhr University Bochum, Germany
2nd referee:	Prof. Dr.-Ing. Christoph Gehlen, Technical University of Munich, Germany
3rd referee:	PD Dr. rer. nat. Ernst Niederleithinger, Federal Institute for Materials Research and Testing, Germany
4th referee:	Prof. Dr. sc. techn. habil. Markus Knobloch, Ruhr University Bochum, Germany

Contents

List of Publications

Chapter 2	CLAUß, F.; AHRENS, M. A. and MARK, P. *A Comparative Evaluation of Strain Measurement Techniques in Reinforced Concrete Structures—A Discussion of Assembly, Application, and Accuracy*. Structural Concrete, 2021. 22(5): pp. 2992–3007. doi: 10.1002/suco.202000706.
Chapter 3	CLAUß, F.; LÖSCHMANN, J.; AHRENS, M. A. and MARK, P. *Temperaturinduktion in Betontragwerke – Experimentelle Untersuchungen zur Methode*. Beton- und Stahlbetonbau, 2021. 116(7): pp. 539–550. doi: 10.1002/best.202100010.
Chapter 4	CLAUß, F.; AHRENS, M. A. and MARK, P. *Thermo-Mechanical Experiments on Reinforced Concrete Beams—Assessing Thermal, Mechanical and Mixed Impacts on Fiber Optic Measurements*. Submitted to Structural Concrete in December, 2021.
Chapter 5	CLAUß, F.; EPPLE, N.; AHRENS, M. A.; NIEDERLEITHINGER, E. and MARK, P. *Comparison of Experimentally Determined Two-Dimensional Strain Fields and Mapped Ultrasonic Data Processed by Coda Wave Interferometry*. Sensors, 2020. 20(14): 4023. doi: 10.3390/s20144023.
Chapter 6	CLAUß, F.; EPPLE, N.; AHRENS, M. A.; NIEDERLEITHINGER, E. and MARK, P. *Correlation of Load-Bearing Behavior of Reinforced Concrete Members and Velocity Change of Coda Waves*. Materials, 2022. 15(3): 738. doi: 10.3390/ma15030738.
Chapter 7	KONERTZ, D.; LÖSCHMANN, J.; CLAUß, F. and MARK, P. *Faseroptische Messung von Dehnungs- und Temperaturfeldern*. Bauingenieur, 2019. 94(7/8): pp. 292–300. doi: 10.37544/0005-6650-2019-07-08-70.
Chapter 8	LÖSCHMANN, J.; CLAUß, F. and MARK, P. *Verstärken von Stahlbetontragwerken mit Temperaturinduktion*. Beton- und Stahlbetonbau, 2020. 115(10): pp. 746–757. doi: 10.1002/best.202000038.
Chapter 9	GRABKE, S.; CLAUß, F.; BLETZINGER, K.-U.; AHRENS, M. A.; MARK, P. and WÜCHNER, R. *Damage Detection at a Reinforced Concrete Specimen with Coda Wave Interferometry*. Materials, 2021. 14(17): 5013. doi: 10.3390/ma14175013.

Chapter 1

Introduction

1.1 Motivation

More than 52,000 bridges form part of Germany's network of trunk roads (retrieved 2020) [21]. If bridges in municipal ownership are considered, this figure is significantly higher. Bridges made using reinforced concrete (RC) and prestressed concrete account for the largest share of these structures, making up about 87 % of the total bridge area [21]. As Figure 1.1 reveals, the majority of these bridges was built between 1960 and 1990. This period, as well as subsequent years, were accompanied by

- rapid changes in design codes (*Standards*, cf. Figure 1.1),
- increasing traffic volume and design loads adapted thereto (*Loads*) and
- the occurrence of prominent material deficiencies (*Material*).

Pertinent changes in standards include the introduction of minimum reinforcement for prestressed concrete bridges (ZB DIN 4227:1966 [20]), the immediate decree for adapting the design rules for coupling joints (immediate decree 02.77 [32]), the reduction of shear force resistance by switching to truss analogy (DIN 4227:1979 [34]) and the launch of minimum reinforcement requirements to announce tendon failure (DIN 4227-1/A1 [37]). Concomitantly, the share of heavy traffic and load allowed on the bridges increased [52, 54, 136]. This increase was considered by the launch of new traffic load models (BK 60 [33], BK 60/30 [36], LM 1 [40] and LMM [42]).
These rapid changes resulted in bridges being built, quickly ceasing to comply with the current state of the art. This issue requires a watchful eye. A possible consequence of this is damage to the structures (cf. Figure 1.1, due to concurrent arising issues: *Standards*—no minimum reinforcement to announce tendon failure ⇔ *Material*—stress corrosion cracking). More common damage to bridges (Figure 1.2a), but also drastic incidents such as the collapse of the POLCEVERA viaduct (Figure 1.2b), show its immediate effects on people. These effects can range from time loss due to bridge closures and traffic congestion to potentially life-threatening situations in the worst case.

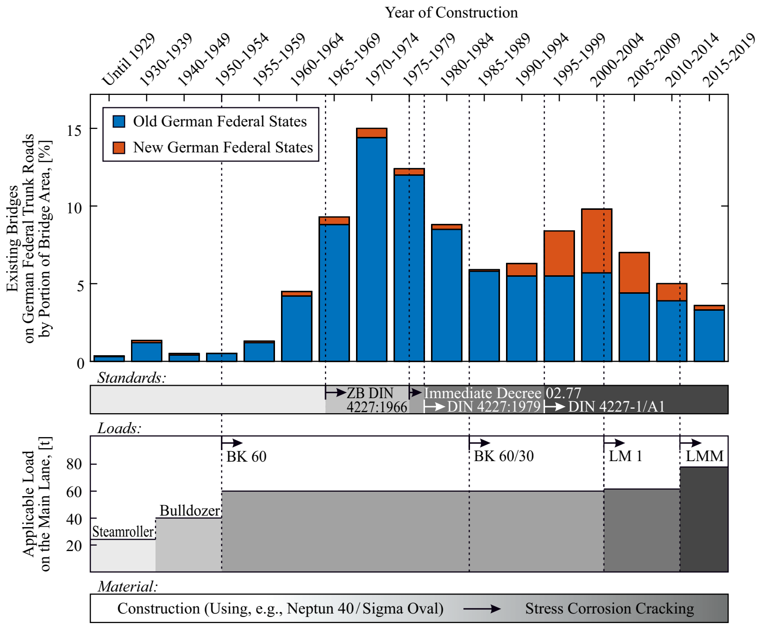

Figure 1.1: Top: Age of existing bridges on German federal trunk roads by portion of bridge area [21]. Bottom: Relevant regulatory and material changes for bridges [52, 127, 136, 173].

All damage has one characteristic in common: it starts small and grows larger over time. Measure to detect damage and keep a watchful eye is structural inspection. To find potential damage, in Germany, simple inspections take place annually and more thorough structural inspections take place every six years [38]. Visual inspections of buildings aim to identify damage that has occurred, which must then be responded to as fast as possible. However, what happens in the time between the structural inspections, with damage in places that are difficult to inspect or if the damage is (still) too small to discern for the eye?

One paradigm which addresses this issue is the monitoring of structures. The methods associated with this term are manifold. They can be distinguished by the principle of operation (electric, optic, fiber-optic, acoustic) or the information content to be obtained (punctual, linear, areal, voluminous). Classical methods of monitoring are strain gauges or displacement transducers (electrical). They provide punctual information. Even if adjacent points are interdependent in the structure-mechanical sense, the informative significance is limited locally.

Advances in camera and computer technology have made optical methods such as digital image correlation (DIC; point-wise up to area-wise information content) available, at least in theory. These methods are rarely used for long-term monitoring due to their lack of robustness against the harsh environmental conditions in real-world scenarios.

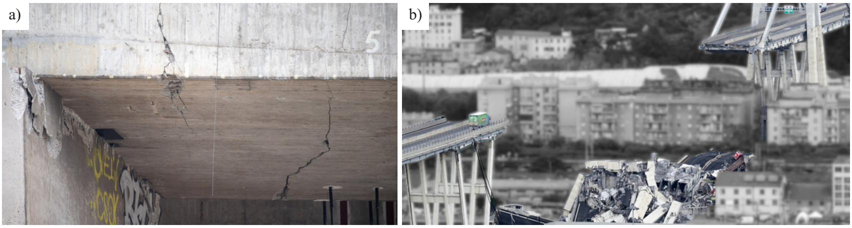

Figure 1.2: Example of a) common [186] and b) catastrophic [187] damage of bridge structures

Fiber optics (line-like information content) has attracted a great deal of attention in recent years. In addition to being established in research (e.g., [25, 56, 100, 195]; cf. the following chapters), it is increasingly being used in practice for civil engineering structures [5, 6, 130]. The sensitivity of unprotected glass fibers or, in the case of more stable fiber optic cables, the smoothing of the measurement results pose challenges to its application [25, 56, 100].

Acoustic methods, which comprise ultrasonic (US) methods, are advantageous because ultrasound propagates through the medium and large areas can be covered. In acoustic emission, the system permanently checks for an event. Damage, e.g., tendon fracture, triggers such an event. The damage location can be narrowed down using ultrasound propagation time differences in a network of transducers. Drawbacks of this method are its limited reproducibility, sensitivity to disturbing noise and mandatory permanent monitoring [69].

In addition to this passive method, US methods exist; here, a signal is actively emitted. These include US transmission [171], reflection or impulse-echo [103, 196, 206] as well as impact [22, 170] methods. They primarily analyze the direct wave between US transmitter and receiver. Typical applications include the detection of flaws such as ungrouted tendon ducts, voids, delaminations or component thickness measurements. These examples demonstrate that the use of these methods is limited by the size of the objects or defects to be detected.

As well as the direct wave, a later segment of the US signal can likewise offer valuable information. This part is called coda. The corresponding coda waves are scattered several times and consequently spend more time in the concrete. On their way, coda waves interact with strains [72, 107, 114, 138, 151, 183, 216], temperatures [49, 141, 217], moisture [110] (see also [67, 94]) and other structural changes such as cracks [66, 108, 126, 137, 174]. The US signal can reveal the alterations of these effects, for example, by coda wave interferometry (CWI). This method is able to detect even minute changes such as compressive strains of 0.001 ‰ [107].

The characteristics of US coda waves are that they

- are sensitive to small changes,
- can scan large volumes and
- can detect externally invisible structural changes.

These characteristics have spurred a variety of investigations. To begin, research has focused on small-scale specimen (size in the range of a few centimeters) and only examined pure concrete. At this scale, research has compared results calculated using coda (from now on commonly referred to as coda quantities) and strains. Compressive strains [72, 107, 151, 183, 215] have been more extensively examined than tensile strains [216]. This might be reasoned, on the one hand, by the more pronounced linear-elastic range of concrete in compression. On the other hand, it may be because, in tension, micro-cracking starts early, superimposing effects from pure elastic (tensile) strain [175, 197]. Once the concrete's tensile strength is exceeded in tests on plain concrete (on this scale, usually uni-axial tensile test), the specimen fails brittle. Suddenly, the experiment ends and the process of cracking that is essential for RC cannot be investigated.

In real structures, however, concrete is used with reinforcement to take over tensile stresses. On large-scale specimen (size in the range of meters), the focus has so far been laid on the localization of cracks. Mostly RC [66, 108, 126, 174, 199] and, at rare times, prestressed structures have been investigated [137].

However, cracks are of central importance in RC structures. The reinforcement is only exposed to load and begins to exert its effect after the concrete has cracked. For this reason, cracks are considered to be damage only when exceeding a defined width. In prestressed concrete components, by contrast, cracks must be avoided in their entirety. Strain is the intrinsic quantity that drives planned (RC) but also avoidable (prestressed concrete) cracks. The comparison of strain and coda quantities on structural (i.e., large) scale has hardly received any attention so far. One cause may live in the counteracting effects of cracks on coda waves and on concrete strain. Immense changes can be detected when cracks emerge using coda waves. The concrete strain, by contrast, decreases sharply, even to zero in the crack.

The correlation of strain and coda quantities manifests itself in the vision of a transparent bridge (Figure 1.3):

- Detect deficiencies already when forming, *far before* they reach a *visible* and eventually critical level.

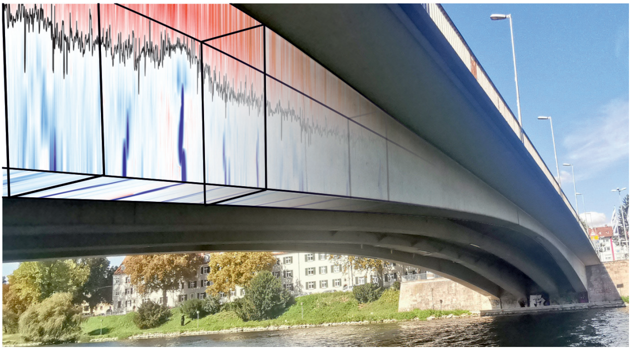

Figure 1.3: The vision of the transparent bridge exemplified on the GÄNSTORBRÜCKE in Ulm, Germany

- Visualize *internal* strain states, and *locate* highly stressed regions and damage.
- Monitor entire structures with a *few sensors*.

1.2 Research Unit

Monitoring the health of reinforced and prestressed concrete structures with coda waves is the focus of Research Unit 2825 "Concrete Damage Assessment by Coda Waves." The German Research Foundation–funded research unit started in 2019 with its work in the first funding period (three years and three additional years in the second period). Due to the diversity of the coda technique, it is approached simultaneously using (geo-)physics, automation technology, numerical and experimental structural mechanics as well as materials technology. The research unit consists of six individual teams and projects at four universities or research institutions (BAM: Federal Institute for Materials Research and Testing, TUM: Technical University of Munich, RUB: Ruhr University Bochum, BU: Bochum University of Applied Sciences). The projects, including the heads and project workers, are listed in Table 1.1.

Table 1.1: Overview research unit 2825 "Concrete Damage Assessment by Coda Waves"

Acronym	Project title	Heads and project workers
BAM	Coda wave based ultrasonic methods for concrete	PD Dr. rer. nat. Ernst Niederleithinger Dr. rer. nat. Herbert Wiggenhauser Niklas Epple, M. Sc. Daniel Fontoura Barroso, Engineer
TUM1	Environmentally / mechanically caused changes in microstructure and their effect on coda signals	Prof. Dr.-Ing. Christoph Gehlen Prof. Dipl.-Ing. Charlotte Thiel Fabian Diewald, M. Sc.
TUM2	Large scale hybrid models for structure identification, simulation and prognosis	Prof. Dr.-Ing. Kai-Uwe Bletzinger Prof. Dr.-Ing. habil. Roland Wüchner Stefan Grabke, M. Sc.
RUB1	Scale-bridging modeling of microstructural changes in concrete and damage analysis of concrete structures for the identification of coda signals	Prof. Dr. techn. Günther Meschke Dr.-Ing. Jithender Jaswant Timothy Thi Truc Giao Vu, M. Sc.
RUB2	Thermo-mechanical experiments of RC structures correlated to distributed coda signals	Prof. Dr.-Ing. habil. Peter Mark Dr.-Ing. Mark Alexander Ahrens Felix Clauß, M. Sc.
BU	High-performance simulations of wave propagation for structure analysis of concrete	Prof. Dr. rer. nat. Erik H. Saenger Martin Balcewicz, M. Sc. Leslie Anne Saydak, M. Sc.

The hallmark of a research unit is the collaboration of different disciplines towards a common objective. The scope of the individual projects can be divided into small-scale versus large-scale and experiments versus simulations, as Figure 1.4 depicts.

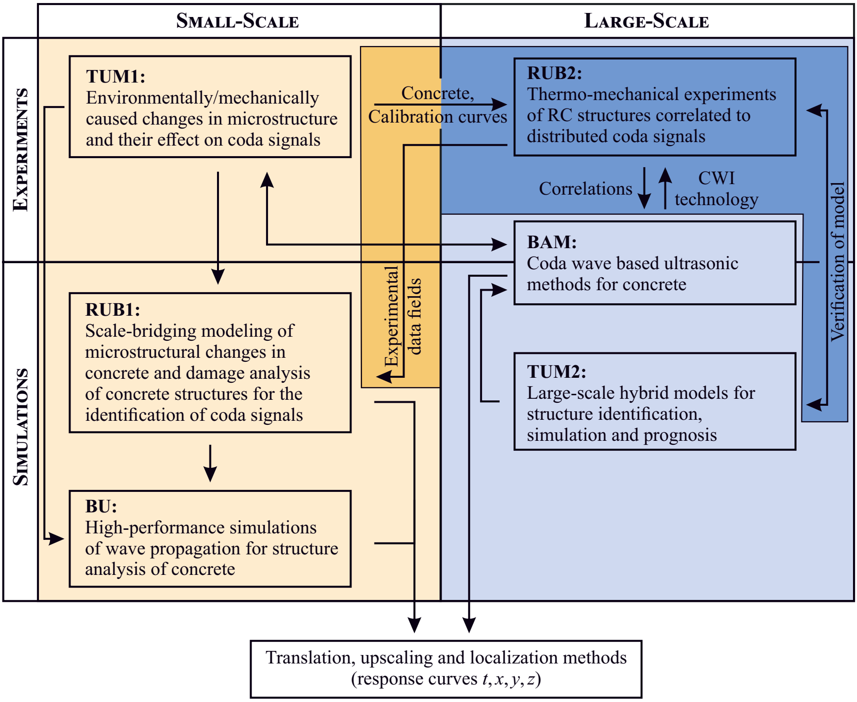

Figure 1.4: Structure of the research unit with highlighted subproject RUB2 and interactions in the first funding period

This thesis considers research within the subproject RUB2 "Thermo-mechanical experiments of RC structures correlated to distributed coda signals." The main interactions with the other subprojects exist in the field of the concrete design, calibration curves, CWI technology, providing quality-assured experimental data fields, model verification, and the correlation of coda and structural quantities.

1.3 Objectives

This thesis contributes to the health monitoring of RC structures by coda waves. This goal is pursued bilaterally. On the one hand, the thesis deals with recording the influence strain in a quality-assured manner. On the other hand, it investigates the response of the coda to this influence. It works out similarities and correlations to each other. In detail, the key aspects are

- Identification of reference measurement techniques for recording strain in terms of the accuracy, repeatability, assembly and application in RC structures.

- Development and assessment of heating and cooling methods for temperature induction, with particular focus on arising component deformations in thermo-mechanical experiments.
- Investigation of the metrological coupling of influences in thermo-mechanical experiments.
- Correlation of coda and structure-mechanical quantities.
- Formulation of a model to evaluate the load-bearing capacity of RC structures subjected to bending by coda waves.

1.4 Outline

This thesis is a compilation of eight publications. Each publication forms a separate chapter. Seven publications (Chapters 2, 3, 5–9) are published in WEB OF SCIENCE–listed journals. One has been submitted for publication to the journal "Structural Concrete" (Online ISSN: 1751-7648, likewise WEB OF SCIENCE–listed, Chapter 4) and is available herein as a preprint (as of 02/24/2022).
Preceded by abstracts in English, Chapters 3, 7 and 8 are offered in German, while the remaining Chapters are drafted in English.

Following the motivation and objectives of the thesis laid out in **Chapter 1**, the synopsis (Section 1.5) discusses the thematic classification and content-related linking of the publications. The synopsis discusses the first five publications (Chapters 2–6, see also Figure 1.5). These publications are first authorships of this thesis' author. They form the framework of this thesis. The other three publications are co-authorships and result from cooperation within the research unit (cf. Section 1.2) or at the Institute of Concrete Structures of Ruhr University Bochum. Nevertheless, they thematically intersect with certain aspects of this thesis. Therefore, the associated chapters are denoted with the addition "*Supplement*" and referenced at appropriate places within the synopsis.
The individual publications follow the synopsis in **Chapters 2–9**. The content is taken verbatim from the publication listed at the beginning of each chapter. Text and figures have been adapted to the format and layout of this thesis. However, the scientific content remains identical.
The thesis concludes in **Chapter 10** with a synthesis of the main conclusions and provides an outlook on further research.

1.5 Synopsis

1.5.1 Framework of Investigations

The overall objective of the investigations is the health monitoring of entire (concrete) structures with coda waves. For this purpose, US transducers are installed into the concrete. When a transmitter emits a US signal, it propagates through the concrete before parts of the signal arrive at the receiver, where they are recorded (for more details, see Sections 5.2.2, 6.3.2, 9.3). Unlike the direct wave between transmitter and receiver, coda waves are scattered multiply and hence spend more time in the concrete. On their way, they interact with influences such as strain, temperature, moisture and cracks.

In the volume that the US waves pass through, all these influences alter the signal. However, the magnitude of the change differs according to the type of influence. The changes are quantified using CWI in the form of the coda quantities correlation coefficient *CC* and relative velocity change dv/v. Accordingly, the correlation coefficient and the relative velocity change react to these influences (*active* ⇔ *reactive*). Henceforth, only the relative velocity change is used.
Figure 1.5 outlines the structure of both synopsis and thesis. First, the thesis considers the influences (*active*) and subsequently the reactions of the coda waves (*reactive*).
As it is in the design of components, strain (in engineering terms closely related to internal force) is the key parameter of the investigations. This work aims to predict the strain of a component using coda waves. It requires a correlation between strain, which serves as a reference, and the relative velocity change. Previous work [107, 138, 183] has shown that coda waves are sensitive to even small strain. Therefore, it is essential to ensure an always precise recording of strain. Chapter 2 addresses this by studying the assembly, application and offers an evaluation of the accuracy of different strain measurement techniques (strain gauges, fiber optic sensors [FOS], DIC). Chapter 3 investigates temperature induction into RC structures. Based on this, the prerequisites for the thermo-mechanical experiment are set. Chapter 4 investigates the coupling of strain and temperature in fiber optic measurements by means of a thermo-mechanical experiment.
Ensuingly, one can proceed thematically to the changes of the coda waves with respect to strain. For this purpose, Chapter 5 sets up and compares strain fields and two-dimensional representations of relative velocity changes. At the same time, it establishes the resemblance of coda waves' relative

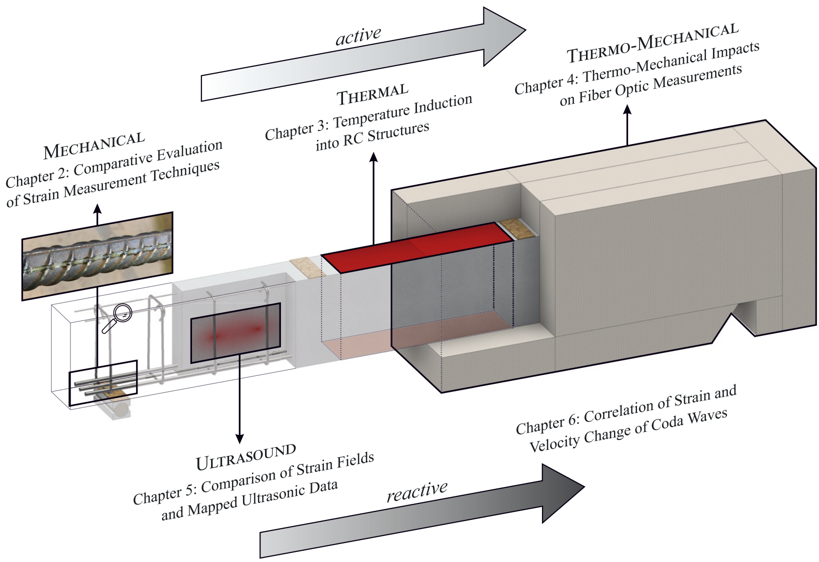

Figure 1.5: Structure of the thesis

velocity changes to moment-curvature relations. Chapter 6 further investigates and exploits this similarity. It derives a model that allows for the inference of component strain via coda waves and thus the evaluation of the load-bearing capacity of RC structures.

1.5.2 Comparative Evaluation of Strain Measurement Techniques

The high sensitivity of coda waves makes it mandatory to record strain changes with high accuracy. **Chapter 2** investigates strain measurement techniques such as strain gauges, FOS and DIC. Besides their accuracy, assembly and application of these techniques influence the quality of measured data. For this reason, the investigations to determine the most suitable reference measurement technique focus on assembly, application and accuracy.

Assembly and Application

Strain gauges only provide punctual information. Therefore, they are not considered a reference for the US measurements that integrate information over volumes. Nevertheless, for later accuracy assessments, they serve as a reference for the remaining strain measurement techniques.

More promising techniques are FOS and DIC. Especially, the FOS require detailed consideration in terms of its assembly and application. The sensors are tailor-made from supply fiber, sensor fiber and termination (see also Chapter 7). The sensor fiber consists (from the inside to the outside) of core, cladding and coating. Light entering the core is reflected at the interface with the cladding and thus travels along the sensor fiber. The coating (usually polyimide or acrylate) protects the sensor fiber and makes it more robust. However, the coating is also a layer to be overcome for strain transfer from the outside into the core. Hence, there is a balance to be stuck in this trade-off. The same applies to the adhesive used to attach the sensor fiber to the component: It represents another layer to be overcome.

In the case of a soft layer, strain is transferred to the core more gradually, over a larger range. This results in a smoothing of the measured strain curve. As a result, high local strain peaks are no longer adequately represented. However, cracked RC exhibits high strain gradients in the immediate vicinity of cracks (strong increase in strain in the reinforcement or decrease in the concrete). Such strain curves are more accurately captured using stiffer layers. However, the maximum stiffness of the surrounding layers does not lead to the most adequate results. After all, the stiffness aimed for is limited by the measurement technology. Suppose the strain jump between two measuring points exceeds approx. $0.15\,‰$, these points are dropped completely. The choice of coating and adhesive must therefore be well balanced. The stiffer coating polyimide and the adhesive Polytec PT AC2411 have proven to be suitable.

The assembly and application of DIC are comparatively simple under laboratory conditions. The camera position, light and speckle pattern can be adjusted well before the experiment and corrected if necessary.

Accuracy

The investigations reveal that the accuracy of FOS and DIC can be deemed equivalent. More decisive is repeatability. In the case of DIC, repeatability depends on the facet size (image pixels are combined

into larger sets, called facets). The facet size corresponds to the resolution of the strain results and can be chosen freely. Small facets imply a higher level of detail but simultaneously a lower repeatability. On average, this starts at a standard deviation $\sigma = 0.3\,‰$ for a $19 \times 19\,\text{pixel}^2$ facet and ends at $\sigma = 0.025\,‰$ for a $100 \times 100\,\text{pixel}^2$ facet. The low repeatability across relevant facet sizes entails that the DIC is only viable at higher strain levels.
The high repeatability of the fiber optics of $\sigma = 0.007\,‰$ allows the examination of RC elements far before initial cracking (for comparison, first cracks occur at about $0.1\,‰$).

Contextualization

If field-like information (as in Chapter 5) is requested, the conclusions drawn turn out more differentiated. Strain maps result straightforwardly from DIC. FOS must be regularly placed on or in a structure to obtain field-like information via interpolation. Consequently, the level of detail in non-fiber directions depends on the distance of the fibers to one another. According to the respective requirements,

- Accuracy (FOS $>$ DIC)
- Magnitude of expected strain (FOS $<$ DIC)
- Material: concrete (FOS and DIC) or reinforcement strain (FOS)
- Required dimension of information (1D, 2D)

either FOS, DIC or a combination of both is to be selected.

1.5.3 Temperature Induction into RC Structures

To examine the measurement of strain and temperature, also in a coupled fashion, it is necessary to investigate the induction of temperature into RC structures. **Chapter 3** analyzes and evaluates both the heating and cooling of RC components using different methods.

Methods for Temperature Induction

In the temperature range of building practice (about $-20\,°\text{C}$ to $+60\,°\text{C}$), heating is easier than cooling. This is because of the simplicity of heat conversion processes such as Joule heating. Therefore, it is not surprising that the range of methods for heating components exceeds the one for cooling. The development of the Peltier cooling for application with concrete structures in this work (see Table 1.2) is a first step to adjust this imbalance.

Table 1.2: Methods for temperature induction

Heating	Cooling
Heated water	Cooled water
Heating mats	Peltier cooling
Infrared heaters	

For the optimal temperature control of the component, the following factors are crucial:

- Maximum power
- Heat transfer into the component
- Interaction with the component
- Heat loss

Power

In the temperature range considered, the performance of the heating methods does not differ significantly. The main difference concern the cooling methods. The cooled water method reaches a minimum temperature of $+5\,°\mathrm{C}$, Peltier cooling $-10\,°\mathrm{C}$.

Heat Transfer

For heat transfer, it is essential to couple the systems for temperature induction to the component. High contact pressure leads to improved heat transfer. Heated, cooled water and Peltier cooling methods employ steel pressure vessels through which tempered water flows. If the systems are placed on top of the component, the high self-weight guarantees the contact pressure. If temperature is induced from below, the steel vessels can be attached to the component. In this case, the contact pressure can be regulated using an appropriate construction with threaded rods (cf. Chapter 8). The heating mats must be encumbered or suspended. Infrared heaters do not require direct contact with the component at all.

Interaction with the Component

The thermo-mechanical experiments discussed later require temperature induction under simultaneous loading (and thus associated deformation). However, the systems for temperature induction (all except from infrared heaters) necessitate full contact with the component. In case of rigid systems (heated, cooled water and Peltier cooling), the component's deformations can be compensated by thermal pads (thickness $\approx 10\,\mathrm{mm}$). In principle, heating mats exhibit the required flexibility. As pointed to earlier, there is no contact between the infrared heater and component.

Loss

Heat loss inevitably occurs at the transition between components (e.g., Peltier cooling – thermal pad – component) and likewise to the environment. The former can be minimized using a high contact pressure, and the latter by appropriate insulation.

Contextualization

For the purpose of this thesis, the heating mat is the method of choice. It is characterized by its high power, low weight and inherent flexibility. A high weight would imply additional strain in the thermo-mechanical experiment. Possible losses due to low contact pressure are compensated by exaggerating (artificially increasing) the temperature. Peltier cooling is likewise used as the cooling method. Its performance exceeds that of water cooling by far. The weight and rigidity of both cooling systems are in a similar range. Thermal pads are used to compensate for component deformation.

1.5.4 Thermo-Mechanical Impacts on Fiber Optic Measurements

Chapter 4 merges the influences examined beforehand. Mechanical, thermal, and thermo-mechanical experiments on RC beams are performed. Strains are measured using FOS and DIC. Temperatures inside the concrete are recorded using embedded thermocouples and FOS.
Strain measurements have already been covered in Section 1.5.2. For this reason, this section does not discuss isolated strain measurement. Nevertheless, an (alleged) isolated temperature measurement is needed to evaluate the coupling of strain and temperature in fiber optic measurements.

Temperature Measurement

Regardless of the type of measurement (strain or temperature), the fundamental quantity of fiber optic measurements is the frequency shift of the backscatter of the light emitted into the fiber. This frequency shift can be transformed into a change in strain or temperature through various factors. Mathematically, this can be captured by a first-order polynomial approach. [121, 122] have found that the accuracy of fiber optic temperature measurement can be increased via a fourth-order polynomial approach. This polynomial is obtained by applying linear regression.
To do so, the actual temperature of the fiber is needed. The temperature read from thermocouples is used as actual temperature. Therefore, a thermocouple is mounted on each FOS. The fourth-order polynomial is then approximated by matching the actual temperature and the frequency shift in linear regression. Using this approach, the error of the measurement decreases from an initial RMSE $= 2.15\,°\text{C}$ (first-order approach) to $0.12\,°\text{C}$ (fourth-order approach). The coefficient of determination after fitting is close to one ($R^2 > 0.99$).

Coupled Influences

On the part of the fiber optics, particularities exist with regard to strain and temperature measurements. Frequency shift is simultaneously varied by strain and temperature changes. If strain and temperature alter contemporaneously, the share of the individual effects cannot be inferred clearly from only one FOS. By adding a second fiber isolated against strain influences (decoupled laying of the FOS in a capillary), it is possible to make a distinction. Disruptive influences, such as unplanned strain changes in temperature measurements and vice versa, irretrievably distort the results. These cross-influences need to be quantified.
Unplanned strain influences on temperature measurements may arise due to friction between the glass fiber and the surrounding capillary. For the type of glass fiber used ($Ø = 0.125\,\text{mm}$, polyimide-coated), a force of $0.05\,\text{N}$ (corresponding to a weight force of $5\,\text{g}$) initiates already a temperature deviation of $6\,°\text{C}$.
Conversely, an unplanned temperature change of $10\,°\text{C}$ leads to strain deviations of $0.1\,‰$. Such unplanned changes do not occur in laboratory tests, but they do occur in real-world scenarios caused by diurnal temperature fluctuations.

Contextualization

For the fiber optic strain measurements, this implies that even changes in ambient temperature of 1 °C – 2 °C can be expected to have negligible effects on pure strain measurements. Furthermore, embedded FOS are hardly affected by changes of ambient temperature due to the inertia of concrete towards heat conduction.
By contrast, temperature measurements are significantly more vulnerable to perturbations caused by strain. Friction between the FOS and the capillary occurs easily and distorts the results. Even if the skewed readings are difficult to clean up in retrospective, it is easy to pinpoint a distortion. After all, temperature profiles are characterized by smooth curves. By contrast, strain influences from friction that superimpose on the temperature reading are locally pronounced in an abrupt manner.

1.5.5 Comparison of Strain Fields and Mapped US Data

So far, the influences of strain have been investigated in detail. After evaluating the assembly, application and accuracy of the measurement techniques as well as the metrological cross-influences, strains can be recorded in a quality-assured manner. The following chapters are devoted to the *reactive* part—the response of coda waves to strain influences. **Chapter 5** contrasts and likens the measured strain to US results evaluated via CWI.

Experimental Concept

An RC beam is subject to four-point bending. The specimen is loaded in a step-wise manner. Strain and US measurements are carried out on each constant load. Of particular interest is the shear-free region between the concentrated loads, since the acting moment is constant there. The metrological equipment (strain and ultrasound) concentrates exclusively on this region. Strain is measured using FOS and DIC. The FOS are bonded to the lateral surface in a staggered fashion over the depth. They are aligned in the longitudinal direction of the beam and measure the principal horizontal strains. The DIC measures the strain field on the opposite lateral surface.
The US transducers are arranged in a network within the component (in the shear-free region). On each load level, the US measurements are successively performed between all neighboring transducers, and the signals are evaluated with CWI. The resulting relative velocity change dv/v is compared with the load and concrete strain.

Comparison of Fields

A relative velocity change is obtained for each transmitter-receiver combination and load level as a result of the US measurements evaluated using CWI. The results are locally assigned to the center between the respective transmitters and receivers. This creates a net-like structure of dv/v-results. A field-like representation can then be calculated by interpolating said values. Chapter 9 presents more sophisticated methods to obtain field-like representations of the relative velocity change.
Field-like representations can also be derived from the staggered FOS. As with the FOS, the strain results are localized horizontally, in the longitudinal direction of the beam, in several planes. A strain field is determined via interpolation based on their position. The DIC natively provides strain fields. The most accurate method for recording them has proven to be the application of the said

measurement techniques in accordance with the load. Therefore, fiber optic results are used for the load range before exceeding the concrete's tensile strength, and after exceeding the strength, DIC ones are used. A comparison can then be made between the strain and US fields.
As expected, the relative velocity changes increase over the entire load history. It is striking that they are exclusively negative. A negative sign indicates deceleration of the coda waves. An obvious expectation was acceleration (positive) in the compression zone and deceleration (negative) in the tension zone. The fact that the relative velocity change increases continuously but is negative throughout leads to equivocations in the assignment to the negative compressive and positive tensile strains. This prevents a direct correlation to the strain fields.
A qualitative comparison indicates that the relative velocity changes in the compression zone are closer to zero than in the tension zone. As the distance to the most compressed fiber increases, the velocity changes become more negative. Accordingly, more serious changes are observed in the tension zone. The reason for the strong increase is crack formation. Cracks have a greater impact on the US signal than altered strains.
Furthermore, the US measurements in the compression zone collect the amplified influence of cracks. The influence of the cracks masks the positive velocity changes resulting from the elastic compressive strains. This is why relative velocity changes evolve to be negative in the compression zone. Hence, tension and compression zones can only be qualitatively assigned.

Coda Waves Imply Load-Bearing Behavior of RC

Relative velocity changes are likewise juxtaposed with the applied force. In the linear-elastic range (state I, force $F < F_{\mathrm{cr}}$), the velocity change also rises linearly. As the cracking force F_{cr} is exceeded, changes occur in the progression. The velocity change develops disproportionately. With further increase of force by approx. 30 %, the velocity change stabilizes and continues to increase linear again.
Therefore, characteristic points are F_{cr} and $1.3\,F_{\mathrm{cr}}$. These points are strongly reminiscent of load ranges from the moment-curvature relation [31, 222]: linear elastic range (state I) $< F_{\mathrm{cr}}$, range of cracking at $F_{\mathrm{cr}} - 1.3\,F_{\mathrm{cr}}$ and completed cracking at $1.3\,F_{\mathrm{cr}} - F_{\mathrm{y}}$.

Contextualization

Coda waves collect influences integratively in the passed volume. The larger the influences (for example, increasing tensile strain), the stronger is the change in relative velocity. In case of additional influences (e.g., cracks in addition to the strain), the relative velocity change increases disproportionately. A similar trend exists in moment-curvature relationships. Approaches exist that extend beyond the elastic range and consider cracks. Comparable to ultrasound, not every single crack is accounted for, but rather an integral average value is. Thus, these approaches allow to calculate the average strain state in the reinforcement, considering concrete cracking. Overall, the combination of these findings underpins the observed similarities between the relative velocity change and the average steel strain.

1.5.6 Correlation of Strain and Velocity Change of Coda Waves

Chapter 6 investigates the assumed similarity in more depth. It also addresses the correlation between the average steel strain and the relative velocity change. Both quantities are obtained experimentally.

Experimental Concept

The experimental concept follows the same procedure as Section 1.5.5. An RC beam is subjected to four-point bending. The main focus lies on the central, shear-free region (between the two concentrated loads). A constant bending moment acts in this region. The load-bearing behavior is essentially determined by the tension zone or the contribution of the reinforcement. For this reason, emphasis is given to the tension zone. US transducers are attached to the bending reinforcement of the beam, and FOS are bonded to it.

Sequential US measurements are performed during loading. The US signals are processed using CWI. The relative velocity changes are used for the following evaluations.

For comparison, strains are measured using FOS. In the non-cracked state, the strain of the flexural reinforcement corresponds to the acting bending moment. Both the strain and the bending moment are constant in the region between the concentrated loads. Entering the cracked state, the reinforcement takes over the tensile portion of the concrete released by cracking. As a result, the strain profile locally rises and lowers according to the crack pattern. The mean value of the strain measured with the fiber optics in the central region is calculated following the procedure of the stress average-strain relation of the reinforcing steel σ_s - ε_{sm} (an approach of the moment-curvature relation, cf. [31, 222]). Corresponding to the external load, this results in

- relative velocity changes dv/v from the US measurements and
- average steel strains ε_{sm} from the fiber optic measurements.

Correlation

These two quantities are compared for equal load levels. A linear dependence is observed. This starts in the linear-elastic range, continues through the range of cracking and extends to the range of completed cracking just before the reinforcement yields. When the yielding of the reinforcement starts, about 90 % of the ultimate load is reached.

Once yielding sets in during the experiments, an increase in strain occurs despite the load being held constant. As a constant state is no longer achieved, the sequential US measurements cannot be assigned to a certain strain without doubt.

Derived Model

The observed correlation is described by the following model:

$$\begin{aligned} \varepsilon_{sm} &= c \cdot dv/v \\ \text{with} \quad c &= \text{const.} \left[\frac{\mu\text{strain}}{\%}\right] \end{aligned} \tag{1.1}$$

The parameter $c = -280\,\mu\text{strain}/\%$ is determined by employing a linear regression. With a high coefficient of determination of 0.99, the model explains 99 % of the strain increase through the increase in relative velocity change. The corresponding error RMSE $= 88\,\mu$strain is low.

Contextualization

In a practical sense, after calculating the relative velocity change using CWI, this model obtains the average steel strain. The load-bearing capacity of the structural element can then be evaluated using the strain.
It is emphasized that the constant c is explicitly determined for this specific experimental setup. Actually, many factors are assumed to vary this constant, such as

- dimensions of the component,
- reinforcement ratio,
- concrete mix and
- material properties.

The proximity to the moment-curvature relationship, which likewise depends on these factors, strengthens the conjecture that they have an influence.

Chapter 2

A Comparative Evaluation of Strain Measurement Techniques in Reinforced Concrete Structures—A Discussion of Assembly, Application, and Accuracy

The following chapter is taken verbatim from:

> CLAUß, F.; AHRENS, M. A. and MARK, P. *A Comparative Evaluation of Strain Measurement Techniques in Reinforced Concrete Structures—A Discussion of Assembly, Application, and Accuracy*. Structural Concrete, 2021. 22(5): pp. 2992–3007. doi: 10.1002/suco.202000706.

Text and figures have been adjusted to the format and layout of this thesis. The content remains identical. The literature used is jointly referred to at the end of the thesis.

Abstract

The measurement of strain in structural elements is a necessary means of investigating the condition of a structure, both in research and in practice. The measurement methods for recording strain considered in this work represent both well-established techniques (strain gauges), as well as techniques that are part of rather current research streams (fiber optic sensors, digital image correlation). This work's contribution lies in providing an overarching comparison of these approaches, thereby informing practitioners and researchers as to parameters concerning their assembly, application, and their accuracy. To such ends, two test series were carried out, one on RC tension rods and another on an RC beam in a four-point bending test. From the latter scenario, for example, certain generalizations were to be deduced for varying load levels: low strains are measured well using the fiber optic technique. Conversely, digital image correlation was discovered to be an adequate choice when assessing higher strain levels and concomitant concrete cracking, as this non-contact technique avoids imprecisions caused by adhesives. Findings are to assist the future user by contrasting the three techniques in terms of assembly, handling, application and resilience of sensors, external influences as well as measurement resolution and accuracy. Such practice-oriented remarks should simplify a selection of the suitable measurement techniques catering to the respective, context-dependent testing scenario.

2.1 Introduction

Faced with an aging body of infrastructure, [77] for example, bridges are subject to constant changes in current standards, the field of structural health monitoring continues to attract significant attention [51, 131, 199, 205]. Within this domain, not only bridges, [116, 120, 164] but tunnels [143] get into the center of research attention. In this context, deformation, strain, and temperature [78, 117, 165] are often measured.

Rather recent developments in measurement technology (e.g., [23, 28, 111, 140, 147, 190]), such as the advent of fiber optic sensor (FOS) or digital image correlation (DIC), have opened up new avenues for research and practice. Said new devices constitute a significant addition to long-established measuring techniques. Among these, strain gauges have gained particular prominence in the past due to their ease of handling, high robustness, and high accuracy. When juxtaposing these three options for their efficacy and appropriateness in testing real structures, [131] questions as to their (ease of) handling, as well as their measurement resolution/accuracy arise (and are to be explored in this work). Influencing factors arising in field applications are in many cases even more extensive. Temperature changes as an example among a variety of environmental influences are often to be taken into account in measurements or even to be corrected [63].

In addition to their use in practical scenarios, which are self-evidently particularly concerned with the respective technology's (ease of) applicability/handling, the three measuring techniques (FOS, DIC, strain gauges) are also suitable for detailed measurements under laboratory conditions. However, these often desired precise measurements up to the assumed exact measurement of quantities such as displacements or, in this case, strain, can suffer immensely different means and quality of application.

Influencing factors that are difficult to capture, for example, the quality of the bonding of sensor (strain gauges and FOS) and the respective surface or even the thickness of the adhesive layer, affect the measured results.

Recently, a significant volume of research has been carried out on the application of FOS [56, 57, 182] and DIC technology in reinforced concrete (RC) context [26]. Here, the focal point is set on optimizing and extending the ways in which these technologies are put to use—for example, improving the application of the measuring techniques (onto the testing object).

As an extension of the existing body of knowledge and in attempting to provide useful guidelines for differentiating between and selecting a technology, a comparative evaluation of the techniques' accuracy is needed. For this purpose, this work will primarily concentrate on measurements with the mentioned techniques in RC. In addition, occasional remarks on their application on pure steel, that is, a scenario with less influencing factors, are offered. Therefore, two test series were carried out first on RC tension rods and secondly on an RC beam in a four-point bending test. On such basis, the results can be used to derive practicable recommendations for the application of the respective measuring technique. Ensuingly, an explanation of various influencing factors ushers in the comparison of the accuracies of the different measuring techniques. Hence, recommendations for strain measurement are finally deduced.

2.2 Underlying Principles of Strain Measurement Techniques

2.2.1 Strain Gauges

Apart from displacement transducers in engineering-specific structural tests, strain gauges are the most frequently used measuring technique. Strain gauges (cf. Figure 2.1) consist of a wire laid in

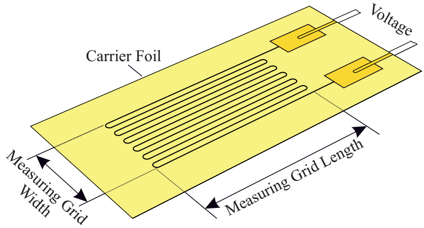

Figure 2.1: Principle sketch of a strain gauge

meanders on a carrier foil. When strain gauges are used to measure strain, the change in electrical resistance of the wire is measured. As this measuring technique has been established for years, we will refrain from describing it in detail. A more comprehensive discussion can be found in [85].

2.2.2 Fiber Optic Sensors

Fiber optic [48, 64, 104, 148, 194] devices permit the measurement of strain or temperature changes by evaluating the backscatter of an induced light beam in the fiber under test. Since the used fiber optic device (ODiSI-B, Luna Inc.) detects the Rayleigh backscattering, further explanations are limited to said share. The Rayleigh backscatter of an induced light beam, which is thus caused by the variable refractive index along the fiber, is recorded by detectors in the fiber optic device. This measurement is performed in the unloaded state, as well as during loading, as shown in Figure 2.2.

This procedure results in two outgoing signals, that is, one for each scenario. Converted into frequency domain and then assessed in smaller evaluation windows (cf. Figure 2.2), the frequency shift Δf (unloaded vs. loaded) in an evaluation window can be directly related to both change in strain $\Delta\varepsilon$ and temperature ΔT, using the coefficients for strain K_ε or temperature K_T

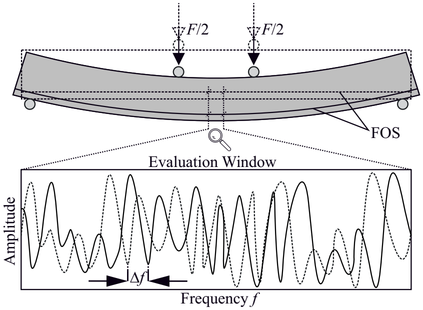

Figure 2.2: Measurement of a frequency shift Δf caused by strain in a FOS (modified with reference to [26])

and the center wavelength λ and the speed of light c. [122, 124]

$$\Delta f = \Delta\varepsilon \cdot \left[-\frac{c \cdot K_{\varepsilon}}{\lambda} \right] + \Delta T \cdot \left[-\frac{c \cdot K_{\mathrm{T}}}{\lambda} \right] \quad (2.1)$$

As specified in Equation 2.1, frequency shifts can be caused by a change in temperature, a change in strain, or both. Hence one of these influences must be kept constant or controlled by a second measurement.

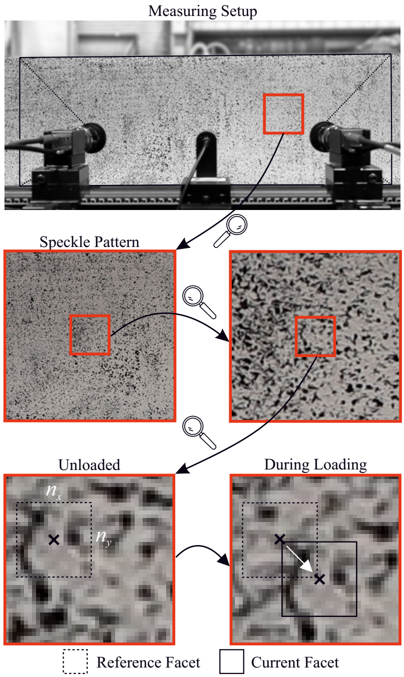

Figure 2.3: Principle strain measurement of DIC (modified with reference to [26])

2.2.3 Digital Image Correlation

With DIC, [18, 24, 146, 188] a displacement field of a surface can be calculated from juxtaposing detailed photos of a test specimen before and during different stages of loading. For this purpose, a preferably random speckle pattern is applied to the surface to be examined. As shown in Figure 2.3, the speckle pattern is then divided up into facets at pixel level. Each facet consists of matrices of $n_{\mathrm{x}} \times n_{\mathrm{y}}$ gray tones—the center of each facet is thus assigned a unique set of gray tones. In turn, comparing images detected before and during loading, said facets form the basis for calculating displacements (of each facet) and finally strains for a meta area. In short, while an applied load deforms the test specimen, each facet undergoes movement from its initial position. [65]

The aim is to locate the set of gray tones from the unloaded state (reference facet) in each image during loading. When strain is applied, each facet and thus its individual set of gray tones cannot only be shifted but also be rotated or experience slight modifications due to altered exposure to lighting. To reduce complexity, however, the facet shown in Figure 2.3 is only shifted.

By applying the least-squares method, [208] each facet center's displacement is determined. Using the deformation results from the immediate vicinity of each point, strain can be calculated for a meta area.

2.3 Experiments

2.3.1 Tension Rod

Test Set-Up

In a first test series, different types of fibers (FOS), as well as adhesives, were tested regarding their precise strain measurement qualities in concrete structures. Tested were nine identically shaped RC tension rods with cross-sectional dimensions of 70 mm × 70 mm. As depicted in Figure 2.4, the test specimens, through which a reinforcement bar (1 Ø 12 mm) passes centrally, exhibit a length of 550 mm. To apply load to the test specimens, the reinforcement bars—protruding 175 mm on both sides—were later clamped into the testing machine.

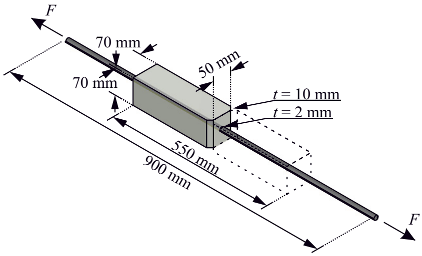

Figure 2.4: Test set-up of tension rods

In order to predetermine the location of the initial damage, two notches in each of the concrete structures and reinforcement bars were prepared facing each other. These intended weak points were placed centrally of the longitudinal axis of the test specimens, and therefore the first crack in the concrete was to emerge right at this point. In addition to the two aforementioned ones, a notch along the entire reinforcement bar was added. Such modification rendered it possible to place the first of the two FOS within said notch, thereby enclosing and protecting it from heightened exposure to surrounding concrete. The other FOS was installed along the web of the reinforcement bar, that is, the exact opposite side of the bar. In this way, by comparing strain measurements produced by one enclosed and one non-enclosed FOS, the difference between both placements could be assessed.

Table 2.1 lists the examined adhesives and fibers. Generally, polyimide fibers and cyanoacrylate present common materials for fiber optic applications [100]. Besides, fibers with acrylate and titanium doped coatings were investigated. Especially the inevitably rough handling of the fiber itself during concreting motivates the test of a stiffer fiber, that is, fiber with a titanium doped coating. In addition to a standard 5 min-epoxy resin, the AC2411 adhesive by Polytec PT was also investigated.

At a tensile strength of the concrete of approx. 4 N/mm^2, according to Eurocode 2, the tensile force causing the theoretical first crack in the middle of the test specimen is 14 kN.

Results

In the following, the selected results of the tests on the RC tension rods are presented in accordance with the objectives set for this work. Figure 2.5a shows the strain curves for a load of 5 kN, which corresponds to approximately 30 % of the force required to produce the first crack at the, as described preset location at the center of the longitudinal axis of the rod.

For all three strain curves, it can be observed for the protrusions of the reinforcement, symmetrically on both sides of the rod, there are almost constant strain levels. The strain of approx. 230 µstrain measured here corresponds to the calculated strain in the rebar under the assumption of Hooke's law. In between the plateaus on each side, the stress detected in the reinforcement bar decreases due to the bonding behavior with the surrounding concrete. In a crack, however, the

Table 2.1: Overview of investigation on RC tension rods with different fibers and adhesives

		Adhesive		
		Cyanoacrylate	Epoxy resin	AC2411
Coating	Polyimide	X	X	X
	Acrylate	X	X	X
	Titania 125-9	X	X	X

concrete's participation is interrupted abruptly. Not all combinations of fiber type and adhesive are able to capture the steep course (large gradient) precisely. At this point, a distinction has to be made between different characteristics resulting from a soft or stiff adhesive and coating as follows. When using the cyanoacrylate adhesive, areas are identified where no strain can be measured ($x = 130-180$ mm and $x = 650-710$ mm). Since this fiber optic measuring device can record strain gradients of approx. 150 µstrain of neighboring points, areas exceeding this limit are excluded from measurement entirely. One option to counteract such failure is to reduce the size of the evaluation window. A reduction in the size of the evaluation window, therefore, has the consequence that larger strain gradients can be recorded due to the finer resolution of the measurement.

The strain curve representing the standard epoxy resin displays similar characteristics. One notable exception is that strain results measured along their path are much smoother and continuous (without measurement failures). That is, the strain gradients between adjacent points do not exceed 150 µstrain. Furthermore, a slightly increased strain can be seen at the center longitudinal axis of the concrete structure, that is, notched area predetermined to crack first.

The results of the AC2411 adhesive features high

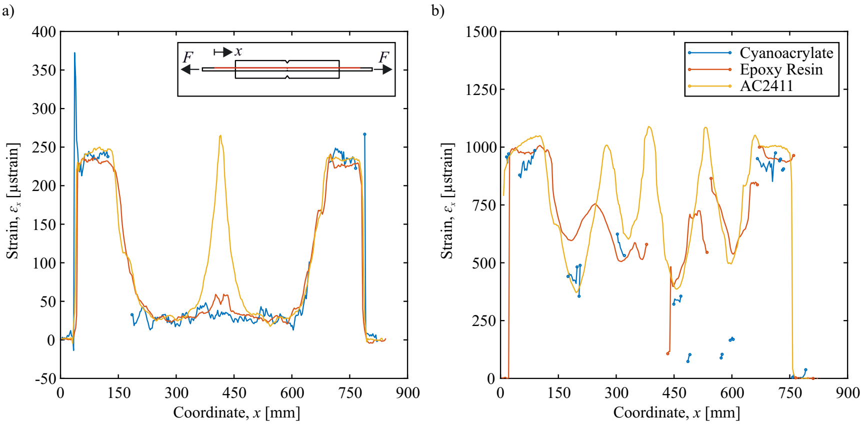

Figure 2.5: Strain measured by FOS using cyanoacrylate, epoxy resin and AC2411 at a load level of a) 5 kN $= 0.30\,F_{\mathrm{cr}}$ and b) 20 kN $= 1.30\,F_{\mathrm{cr}}$

similarities with the results of the standard epoxy resin. The main divergence is to be detected at the aforementioned location. Said difference occurs when a crack develops, the reinforcement in the axis of the crack takes over the force exerted upon it. The strain peak at the middle indicates the reinforcement beam's complete takeover of the acting force of approx. 255 µstrain. Due to the formation of a crack in merely one of the three test specimens shown, the strain in this area is no longer quantitatively comparable. The integration of the strain to a total elongation of the test specimen thus yields different values.

The tested cyanoacrylate adhesive exhibits a higher stiffness than the standard epoxy resin and AC2411. This characteristic conditions that strains are transferred into the fiber at the very point where they occur. This direct force transmission from the structure into the fiber allows for the most accurate and realistic results. Vice versa, as can be seen in the results of the epoxy resin and AC2411 adhesive, the strains are not directly transferred into the FOS but are first diffused by and transported via a larger area of the adhesive. Such spreading behavior, as displayed in Figure 2.5a, results in a slight distortion of the results. Submitted to augmented levels of force, such a falsifying effect could increase drastically and, for example, cause a drop of the measured strain peak at the position of crack emergence. Hence, the adhesive's lack of stiffness not only engenders a smoothing of the measured strain points at any load (e.g., compared cyanoacrylate) but, more importantly, corrupts the detection of peak strain measurements in areas of crack emergence in increased load scenarios. Here, said adhesives with lower stiffness would therefore condition a decrease in the detected strain at the crack itself and redistribute strain to and past the crack's shores—effectively a de-localization.

Figure 2.5b illustrates the strain results using the different adhesives for a load of 20 kN (i.e., approx. $1.30\,F_{\mathrm{cr}}$). The measured strain peaks present in the midsection of the rod (between $x = 225$ and 550 mm) indicate several cracks in the concrete. Again, the force supposedly carried by the concrete is locally taken over by the reinforcing steel. In the scattered results of the cyanoacrylate, it can be seen that due to the increasing load and the associated progressive crack occurrence and growth, the limit value of 150 µstrain of adjacent strain results is often exceeded, and strain measurements for the rebar fail to a large extent. Such areas are likewise partially present in the depiction of results for the epoxy resin. Nevertheless, the course of both graphs suggests broadly similar strain measurements for said adhesives.

The variance in stiffness of the layer of adhesive around the FOS (as was detailed for various adhesives), therefore, always causes a spreading of the strain over immediately adjacent areas and slightly distorts the absolute measured values. The highest degree of smoothing and distortion thus occurs with AC2411, that is, the softest adhesive, followed by epoxy and cyano. AC2411 conversely, however, features the highest degree of continuity in measurements, that is, avoids measurement failures. Therefore, in theory, a trade-off between measurement accuracy and continuity, particularly relevant in higher load scenarios, must be taken into account when selecting an adhesive. In practice, however, AC2411 clearly lends itself best to test set-ups with gradually increasing load levels.

Similar findings can be derived from comparing the results of glass fibers with different coatings (cf. Table 2.1). A rather soft layer around the glass fiber, as is the case for acrylate or titanium coating, also manipulates the measured strain levels. In a process parallel to the detailed behavior of differently stiff adhesives, this transfer of strain to surrounding areas rises with increasing load levels. Overall, observation of strain measured by FOS seems to be promising and of sufficient quality up to about $1.3\,F_{\mathrm{cr}}$ as a rule of thumb. While $1.0\,F_{\mathrm{cr}}$ is associated with the first crack of the specimen, $1.3\,F_{\mathrm{cr}}$ characterizes a completed crack pattern with all primary cracks at regular distances. For loads above that level, an increasing smoothing and transfer of strains into adjacent regions happens due to the low stiffness of the adhesive. At higher loads, overlapping of impaired regions and must be taken into account.

2.3.2 Four-Point Bending Test

Method of Investigation

Now that the preliminary investigations for FOS have been carried out on one of the simplest structures, that is, tension rod, the next step is to increase the complexity of the system (test specimen under test) to obtain further results. The static system to be examined should satisfy various requirements. As such, the basic structure should allow for simple derivation of results and feature both compressive and tensile strains in the cross-section. Also, the specimen's characteristics as to spatial dispersion of the strain state over the height and the resulting moderate strain gradient should allow for optimal comparability of the strain measurement techniques. Precipitating from such requirements, the choice of the static system for this testing scenario is a single-span beam, which is loaded in a four-point bending test. The RC beam is successively loaded up to 160 kN, with the load levels being held at a constant level every 5 kN for a short period of time. By being able to assess the respective technique's measurements during such (temporarily) constant load levels as steady, the repeatability of the strain measurement techniques can be investigated.

Test Set-Up

An RC beam of the dimensions of 150 mm / 400 mm / 2400 mm ($b\,/\,h\,/\,l$) was concreted at Ruhr University Bochum. The test specimen was tested in a four-point bending test with a span length of 2000 mm. The two concentrated loadings were placed right in the middle between the supports with a distance of 660 mm to each other (cf. Figure 2.6).

This loading scenario necessitates a bending reinforcement of 2 Ø 16 mm and stirrups Ø 10 mm / 20 cm / 2. Additionally, a constructive reinforcement of 2 Ø 8 mm in the compressive zone was added. Excluded from the ensuing remarks on test set-up and arrangement of measurement technology in the test specimen are the ultrasonic transducers. As was discussed in earlier works, [26] they were installed, especially in the shear-free area between the point loadings. In order to position these ultrasonic transducers, the otherwise obsolete stirrups are also extended to the shear-free zone.

For better compaction, the beam was concreted on the side surface. This process offered the additional advantage of a smooth management of all sensors during concreting. This rather unusual concreting orientation is not expected to have any influence on the load-bearing behavior and thus on the strains investigated. But against the background of installing multiple measurement techniques, it made things much easier.

As detailed above, three different methods were employed for strain measurement. To reiterate, one can distinguish between standard strain gauges (SG), FOS, and DIC.

In order to ensure that the different technological (measuring) devices do not influence each other, their positioning was construed in a way limiting interference to a minimum. By means of an example, the cameras used for DIC collected imagery on one side of the RC beam, while FOS and

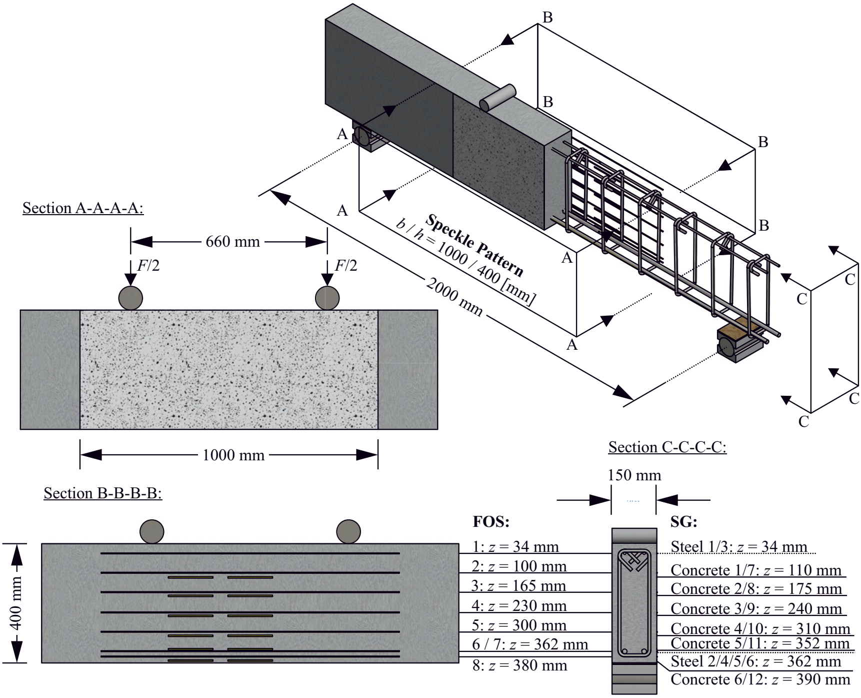

Figure 2.6: Test set-up of the four-point bending test (modified with reference to [26])

SG were arranged on the other side of the body. The speckle pattern (DIC) is thus only applied to the front-side (cf. Figure 2.6 top and Figure 2.7) and captured by the cameras, which are placed at the shortest possible distance between them and the test specimen. This is to procure the highest possible pixel density (number of pixels per area), and therefore the highest possible information density for calculating surface strains while simultaneously avoiding a loss of camera focus. At such a distance, the maximum recordable width of the camera lenses employed here, 1000 mm, is fully exploited. Due to the fixed aspect ratio of the captured images, the height of the beam is also captured completely.

The FOS, by contrast, were attached to the back of the beam. In this experiment, the system ODiSI-B of Luna Inc. was used and combined with an eight-channel fiber optic switch. Said switch permits the utilization of up to eight sensors in this test, however, only in (short) succession of one another. However, by means of suitable programming in C++ in the Software Development Kit (SDK), a quick-paced, automatized change among the eight channels is possible. This shortcoming is offset by the design of the load scenario. As pointed out earlier, the stepwise increasing load levels, which are held constant for a short period of time, allow for each channel to be triggered at every load level.

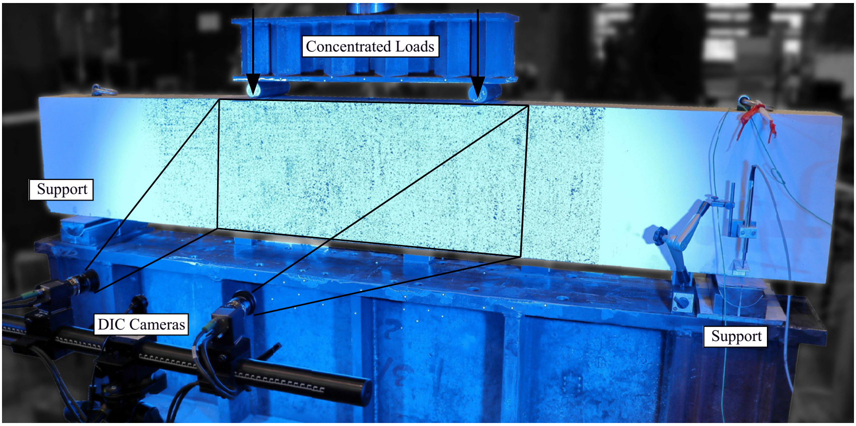

Figure 2.7: Front-side of the test set-up with the cameras for DIC in the foreground (modified with reference to [26])

Such a progression leads to quasi-simultaneous measurement across all eight channels, that is, all eight FOS. Since creeping effects within the RC beam cannot be avoided, the measurement of the first fiber was repeated at the end of the 8-channel succession on each load level to quantify these effects. As to the precise arrangement of the FOS, one sensor was attached in a notch along the reinforcement bar, while another seven FOS were attached distributed over the height of the surface of the test specimen (cf. Figure 2.6).
Moreover, conventional strain gauges were to be installed. In the set-up discussed here, a distinction must be made between strain gauges that are applied to the reinforcing steel on the one or to the concrete on the other hand. In this context, strain gauges with a length of 3 mm were used for measuring the strain of the reinforcement. In contrast, much longer strain gauges, measuring 100 mm in grid length, were used for measuring concrete strain. This distinction is necessary because the true strain state along the entire grid length is integrated into one strain value. In order to avoid deviations in recorded strain measurements caused by detection of fluctuating strain, attributable to the inhomogeneity of the concrete, a larger grid is used (cf. Figure 2.6).

Results

Figure 2.8 shows strains recorded by FOS and strain gauges (Figure 2.8a), as well as DIC (Figure 2.8b). The unprocessed values produced by the FOS are illustrated in gray. In order to smooth out these highly fluctuating, scattered values, a stepwise robust linear regression was applied to the data points. Such a process always entails a loss of local information. Hence, the window length must be weighed against this loss of data. However, as depicted in Figure 2.8a, the measured strains of the FOS and the strain gauges match well.
The imagery produced by DIC for a facet size of 19×19 pixels $= 19^2$ pixel^2 and a load of 160 kN (Figure 2.8b) displays the alternating crack pattern of primary and secondary flexural cracks. In addition, flexural shear cracks are indicated at the edges, while for the rest of the test specimen a mélange of neutral, tensile, and compressive

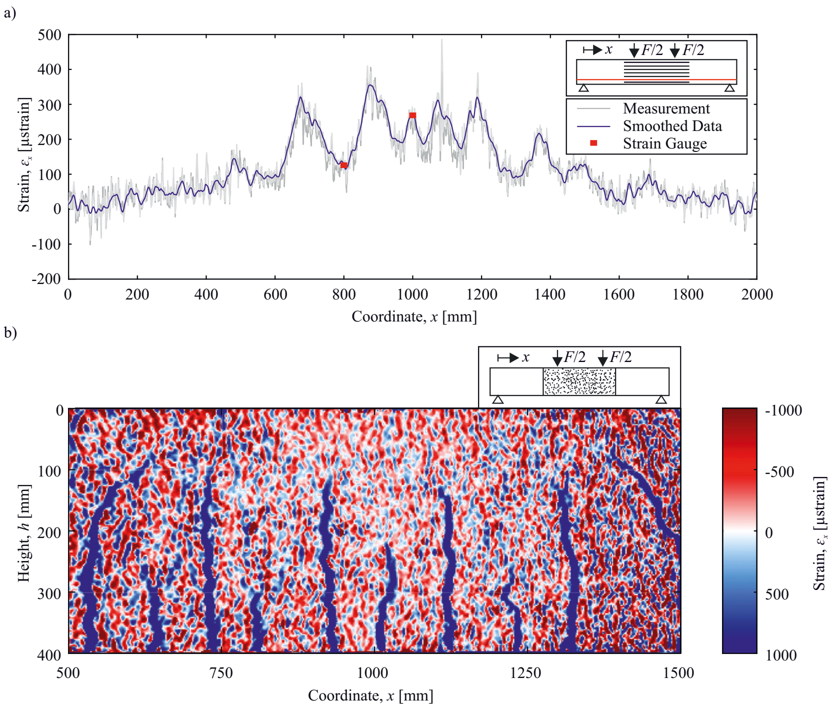

Figure 2.8: Strain results from a) FOS and strain gauges as well as b) DIC at a load of 160 kN (modified with reference to [26])

strains appear to have occurred. However, as will be detailed further in the following, such scattered values result from measurement noise and therefore do not represent the true forces operating in the test specimen.

2.4 Comparison of Strain Measurement Techniques

2.4.1 Assembly and Application

Strain Gauges

Since strain gauges are a measuring technique whose mode of operation is based on the change in electric resistance levels under changing external influences, protection against water ingress, for example, is a matter of course. Ex factory, SG are usually purchased fully assembled from the respective manufacturer. The measuring grid with the corresponding polyimide film is applied using a suitable adhesive—for steel applications, such as on reinforcing steel, for example, a cyanoacrylate has been proven to be adequate. In contrast to the application on steel, a two-component epoxy resin is used for concrete. This difference in the utilized adhesives can largely be attributed to the porosity of the concrete surface. A thin adhesive layer between the strain gauge and the measured object ensures that the force is transmitted mostly unaltered by the adhesive. More specialized variants of strain gauge technology also enable underwater measurements. Generally, however, they are usually covered with an aluminum foil, including a plasticine compound to protect it against, for example, mixing water.

Fiber Optic Sensors

As shown in Figure 2.9a, the glass fiber of a FOS consists of a core, a cladding, and a coating. In order to splice different glass fibers together, the outer coating must be removed mechanically. In analogy to strain gauges, FOS can also be purchased fully assembled. However, it is also possible to assemble a FOS from the three components shown in Figure 2.9b. For this purpose, the three components (pigtail, sensor fiber, and termination) are spliced together in the depicted order. The corresponding splice loci (ends spliced together utilizing an electric arc) are considered to be particularly brittle and are therefore protected by a tube equipped with metal pin reinforcements.
Since FOS technology executes measurements of the Rayleigh component of the backscattered light spectrum, it is necessary to completely eject the emitted light from the core at the end of the sensor. To such ends, one aspect of the termination fiber's light transmission characteristics is exploited. Contrary to the sensor fiber, which is, in fact, specifically designed to do so, the termination fiber does transmit light inadequately when arranged in a loop with a small bend radius. The physical process underlying such behavior can be described as follows: the induced light beam within the termination fiber's core strikes the interface between the core and the surrounding cladding at an angle that prevents total reflection of the light and thus gradually channels the emitted light out. Therefore, the fiber of the termination is laid in short loops in order to ensure the complete ejection of the induced light.
In contrast to the application of a strain gauge to a concrete or steel surface, the previously introduced tests and the respective investigations (Chapter 2.3) indicated that the application of the AC2411 adhesive provides good results both for embedded reinforcing bars (see also Figure 2.10) and for the direct application to concrete surfaces. The employed adhesive (AC2411) solves the tradeoff between measurement failures in certain areas (i.e., stiffer adhesive) and an excessive smoothing of the measured values (i.e., less stiff adhesive) well. However, this specific adhesive proves useful for applications of FOS in testing scenarios where the sensor is cast within the concrete specimen. If such direct contact is avoided (cf. [99]), the use of cyanoacrylate is the better choice due to its high stiffness and the associated

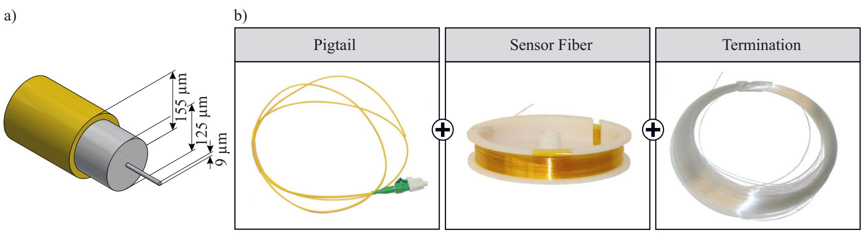

Figure 2.9: a) Glass fiber consisting of core, cladding, and coating, b) components of a FOS

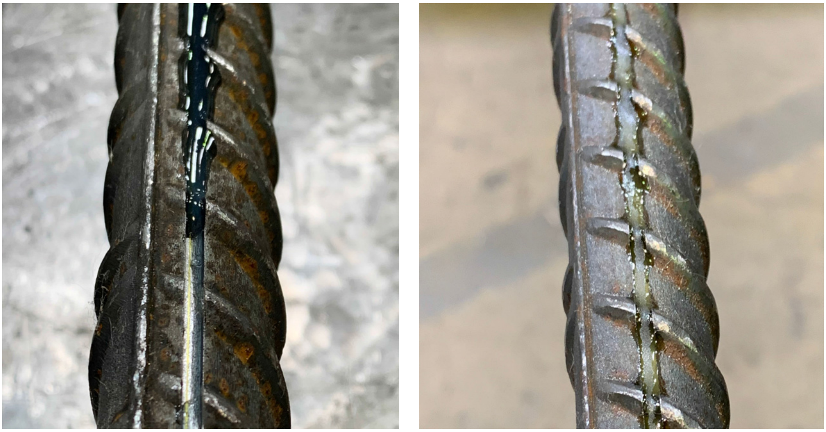

Figure 2.10: a) Partially and b) completely glued FOS into a notch along a rebar

accurate strain measurement. This knowledge can, therefore, be transferred analogously to steel component contexts. The absence of strain peaks on smallest areas, as it occurs in case of cracking of concrete, allows the advantageous use of cyanoacrylate. Among epoxy resins, AC2411 has proven to be the most useful adhesive.

At the onset of the experiment a reference measurement, for example, in a load-free scenario, is executed. Such result is employed as a comparative measurement to subsequent strain recordings (cf. Figure 2.2).

Digital Image Correlation

In contrast to the two measurement techniques described above, DIC does not require profound assembly or specific application of the measuring technology within or onto the test specimen. Instead, the distances between the cameras themselves, as well as the distance to the test specimen must be modified in accordance to the individual scenario's requirements. Moreover, the grain structure of the employed speckle pattern is pivotal and executed as follows. As depicted in Figure 2.11, the sample to be examined is first painted white, and then a black speckle pattern is applied. Upon said application, both the random arrangement of the speckle pattern (allowing for the retrieval of a section [facet] in different load scenarios via mathematical optimization) and the adequate distribution of individual speckles (preferably in a unique pattern of gray-scale pixels within the image section) are to be closely monitored.

Also, accurate positioning of the cameras, especially concerning the parallel arrangement of cameras' plane and measuring plane, surrounding lighting conditions, and, for example, possibly changing heat sources are of crucial importance.

2.4.2 Accuracy and Error Evaluation

Strain Gauges

As can be observed for the FOS (cf. ensuing segment), (uniaxial) strain gauges likewise only measure strain in one designated direction. Consequently, a small (unplanned) skew of the strain gauge (or the FOS) is more likely to occur when,

Figure 2.11: Speckle pattern and cameras for DIC strain measurements

for example, a rather small strain gauge is applied to a large reinforcement steel body. Here, applying the gauge in geometric accordance parallel to the body's longitudinal axis is a true challenge and may quickly result in angular errors. Due to the geometric dimensions of the object under test, however, this error is often difficult to quantify. An imprecise application can be avoided by using larger strain gauges (cf. Figure 2.1). In doing so, manual application is facilitated, and the correct position can be best approximated optically. Inaccuracies that cannot be detected by the eye only engender slight angular errors leading to negligibly distorted results.

Equally difficult to evaluate is the correct amount of adhesive overall and below the sensor. If the adhesive layer is too thick, the strain can be spread, producing results described above.

In addition to measurement errors resulting, for example, from an inadequate application (such as an increased thickness of the adhesive, angle errors during the application, or improper insulation against moisture penetration), the following section focuses on measurement errors on the part of the respective measuring instrument. If negative influences are assumed, for example, self-heating of the strain gauge and a residual error due to exclusively linear temperature compensation, the zero point-related measurement error can be estimated at approx. 10 – 15 µstrain. Besides, there is measuring inaccuracy resulting from the measuring device itself as well as the tolerance within the strain gauges' k-factor. The non-zero point error can be estimated at 1 %. It should be noted, however, that the context-relevant factors were calculated using conservative estimates.

A dispersion of the measured values around a constant value could be measured in tests on polished stainless-steel tension rods. A scattering of less than 1 µstrain was observed here (cf. [99]).

Fiber Optic Sensors

Similar to the observations made for strain gauges, measurement errors are also to be expected with FOS results stemming from, for example, an inadequate application within the test specimen (inappropriate adhesive layer or corrugated, non-linear application).

Furthermore, as discussed in Chapter 2.2, the measured frequency shift simultaneously depends on both strain and temperature [124]. The assessment of strain and temperature coefficient underlines that strain changes have a more significant influence on the frequency shift. When measuring mechanical strain and impact by an un-

expected temperature, the latter influence is usually rather small. On the other hand, the recorded measurement values are strongly distorted when measuring temperature and an unexpected mechanical strain.
As stated in [100] and [124] and depicted in Table 2.2, the measurement's repeatability, that is, the scattering of the measured values around a constant level, can be specified with ±20 µstrain or ±5 µstrain depending on the mode of operation. For the experiments elucidated here, the measurement mode with the smallest point distance of 0.65 mm was selected (repeatability ±20 µstrain). For the following testing scenarios, smaller point spacing and even more importantly the thereby decreased number of measurement failures is selected, despite the disadvantages of (1) lower measurement repeatability and (2) lower measurement frequency:

- for quasi-static tests,
- tests in which high fluctuations in the strain results are to be expected (such as measurements of steel strains in a concrete body or concrete strains),
- tests in which a high point-density in the results is necessary and
- tests where strains can be recorded, which exceed the repeatability many times over.

Accuracy of the strain measurement can be specified at ±25 µstrain regardless of the selected mode of operation.

Digital Image Correlation

The advantage of DIC is constituted by the fact that measured results are not reliant on fixations such as adhesive or an improper misalignment of the sensor. Similar to both measurement methods discussed before, the generalization of an absolute measurement deviation or a measurement error is difficult to achieve with DIC. Here, variety of (environmental) variables influencing recordings produced via DIC, such as changing light or temperature conditions, or, for example, a deterioration of the imaging performance in the edge areas of an image, obstruct such generalized assertions. Furthermore, the results also depend on the generated information density. Significant factors in this context are the distance between the cameras and the object to be measured, as well as the resolution of the camera(s) used.
The load on the RC beam in the four-point bending test was increased sequentially in 5 kN steps. Approx. 30 pictures were taken with both cameras. For Figure 2.12 (below), the standard deviation (SD) of the strain on one load level was calculated. It is to be stressed that the SD and thus also the scattering of the measured values in the horizontal edge areas increase. On the other hand, an approximately constant SD along the

Table 2.2: Modes of operation of the used fiber optic device (ODiSI-B, Luna Inc.)

Mode of operation		High resolution	Extended length
Data acquisition rate	[Hz]	23.8	50
Maximum sensor length	[m]	10	20
Gauge length	[mm]	1.3	5.2
Gauge pitch	[mm]	0.65	2.6
Repeatability at zero strain	[µstrain]	< ±20	< ±5
Repeatability across full strain range	[%]	±0.55	±0.10
Accuracy	[µstrain]	±25	±25

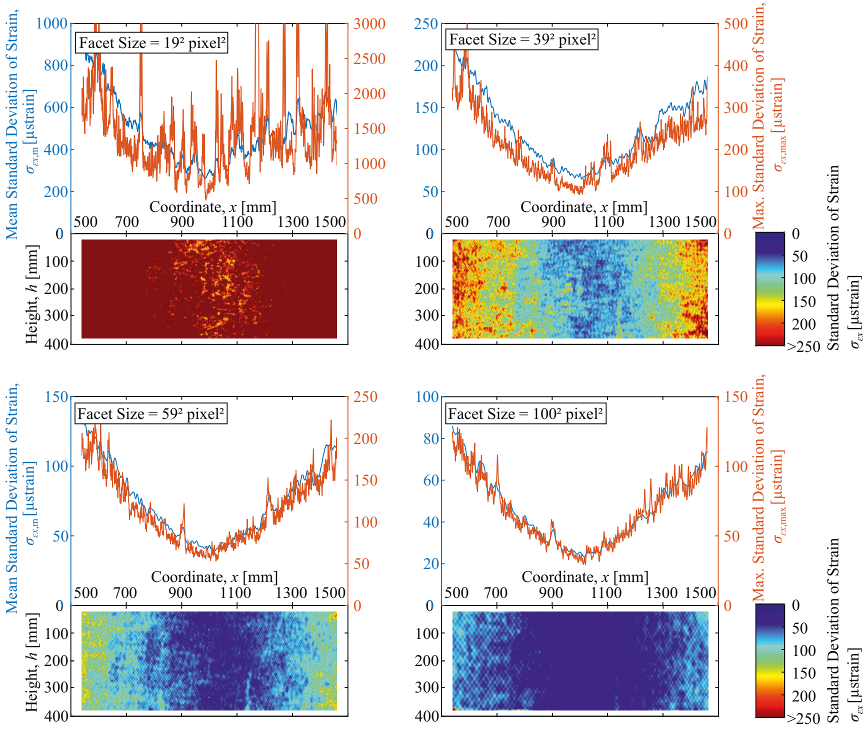

Figure 2.12: Spatial standard deviation from DIC strain measurements

vertical axis can be deduced.

Figure 2.12 juxtaposes SD values of measurements recorded by DIC for four different facet sizes (19^2, 39^2 , 59^2, and 100^2 pixel^2). It is evident that the scattering decreases with increasing size of the facets. As was to be expected, increased facet size produces lower resolution. Such loss of information allows for less specific assertions on local deviations, that is, phenomena indicating local strain concentrations.

As stated before, the SD of the recorded behavior of different facets compared along the vertical axis remains very similar. The color schemes presented in Figure 2.12 clearly underscore this highly analogous state, for example, along the vertical axis in the edge areas. In this way, the SD can be averaged over the height (blue graph), or the maximum value (red graph) can be evaluated (Figure 2.12 above).

Table 2.3 compares different SD values (mean and max. SD of strain) from Figure 2.12 for the four facet sizes at the center of the concrete beam, that is, at $x = 1000$ mm. At this specific location, both mean (blue) and max. (red) SD graphs reach global minima. Since the two cameras employed here both focus on one facet at the true center of the recorded plane, that is, $x = 1000$ mm; $y = 200$ mm, the imagery generated

Table 2.3: Mean and max. SD of strain read from Figure 2.12 for $x = 1000$ mm

Facet size [pixel^2]	Mean SD of strain $\sigma_{\varepsilon x,m}$ [µstrain]	Max. SD of strain $\sigma_{\varepsilon x,max}$ [µstrain]	$\sigma_{\varepsilon x,m}/\varepsilon_{cr} = \sigma_{\varepsilon x,m}/100$ µstrain [-]	$\sigma_{\varepsilon x,max}/\varepsilon_{cr} = \sigma_{\varepsilon x,max}/100$ µstrain [-]
19^2	300	500	3	5
39^2	75	150	0.75	15
59^2	40	60	0.4	0.6
100^2	25	35	0.25	0.35

here is of the highest repeatability possible—as discussed, the cameras' performance deteriorates toward the edge of the images. Thus, the DIC-recorded strain measurements and their SD not only allows for inferences on repeatability but also provides the basis for assessing the viability of different facet sizes for measuring concrete strain.

As initial cracking in concrete occurs at 100 µstrain, the ratio between said strain level and the (lowest) SD recorded in a facet ($\sigma_{\varepsilon x,m}/\varepsilon_{cr} = \sigma_{\varepsilon x,m}/100$ µstrain). If the ratio is $= 1$ or $\gg 1$, the facet is impracticable for measuring concrete tensile strain, if it is $\ll 1$ it is suitable for doing so—values in between must be assessed individually. Here, regarding the issue of repeatability, the largest facets size of 100^2 pixel^2 offers the highest repeatability and, at least concerning this characteristic, outperforms the other variants. This is to be considered as a useful point of reference but cannot be fused into a general principle.

Comparison

As discussed throughout this work, the test specimen was equipped with the three types of measuring techniques for repeated strain measurements—SG, FOS, and DIC. In order to contrast and critically discuss their characteristics, measurements produced by all three technologies were collected at a load level of $F = 160$ kN—representing approx. 80 % of the ultimate bearing capacity. Said load level ensures distinct strains. Figure 2.13 depicts six normal distributions generated via the parameters of the expected value μ, as well as standard deviation σ. In this context, SGs, due to their performance as to repeatability (here: $\sigma_{SG} = 0.23$ µstrain) and accuracy, as well as due to their long-established utilization are designated as the reference technology. That is, the parameter μ_i for both FOS and the four facet sizes (DIC) is relative to the SG probability function: *related precision* $= \mu_i - \mu_{SG}$.

Here, 19^2 pixel^2 facet best approximates the reference SG value in terms of *related precision* ($\mu_{FS19} = 16.16$ µstrain), while FOS, at 45.57 µstrain produce the largest *related precision*. However, it is crucial to be aware of the fact that all *related precision* values are indeed calculated using the SG parameter. Therefore, the *related precision* values illustrated in Figure 2.13 do not allow for simple, quantitative comparison among one another. Consequently, expected values ought to be compared in their absolute form: $\mu_{FS19}/\mu_{SG} = 771.32/755.16 = 0.98$ and $\mu_{FOS}/\mu_{SG} = 800.73/755.16 = 0.94$. The ratios presented here nicely emphasize the negligible spread between the considered measurement techniques in terms of their produced accuracy (i.e., μ_i). This insight prompts closer scrutiny of the repeatability performance of the three measurement techniques.

Having discussed the standard deviations for different facet sizes in DIC earlier (remarks on

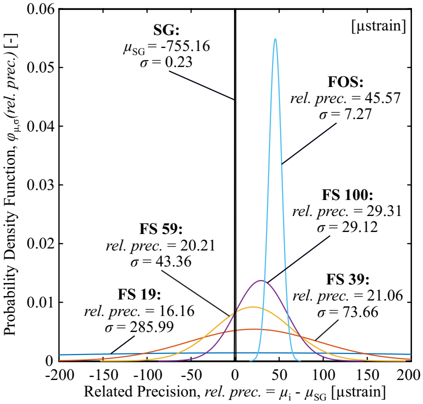

Figure 2.13: Idealized distribution of the measured values at a load of $F = 160\,\mathrm{kN}$ in a four-point bending test

Figure 2.12 and Table 2.3), Figure 2.13 displays and contextualizes the three techniques' repeatability performance—and highlights the immense spread in this regard. While σ_{SG} clearly ranges top of the list at 0.25 µstrain, σ_{FOS} follows close behind at 7.27 µstrain. Again comparing this to the smallest facet of DIC (19^2 pixel^2), the ratio is almost 40-fold ($\sigma_{\mathrm{FS19}} = 285.99$ µstrain). While all three types of measurement display relative similarity in terms of accuracy (1 vs. 0.94), the spread in repeatability is much larger and requires a weighing of interests.

2.5 Conclusions

In this work, the quality of strains in RC components recorded with different techniques is assessed. The applied techniques comprise common strain gauges for reference and more sophisticated technologies, namely FOS and DIC. Based on two test series on simple tension rods and a beam subjected to four-point bending general recommendations concerning device handling, sensor application (adhesive or non-contact), as well as material resilience, accuracy, repeatability, and measurement resolution on RC members are derived.

- Strain gauges exhibit the highest repeatability of strain readings ($\sigma_{\mathrm{SG}} < 1$ µstrain) but with the lowest spatial resolution (0D). Since the accuracy of this long-established measurement technique is well-known and does not require further evaluation, it serves as a reference for the others. Severally repeated strain readings on constant load levels deliver stable means μ_{SG} required to get and assess the performance of other techniques (i) by means of their relative precision (*rel. prec.* $= \mu_{\mathrm{SG}} - \mu_{\mathrm{i}}$).

- In comparison FOS are less robust, quite tricky to apply and prone to damage during casting and testing but yield 1D quasi-continuous strains in concrete and steel along directed fibers. Especially a sound combination of fiber type and adhesive turns out decisive to get valuable strains. Testing of the tension rods revealed Polytec PT's AC2411 adhesive combined with a polyimide-coated fiber most promising for RC. With this combination testing in four-point bending yields a *rel. prec.* $\approx$ 46 µstrain along with a repeatability of $\sigma_{\mathrm{FOS}} \approx$ 7 µstrain.

- With DIC technology, strain maps (2D) are calculated by correlating images recorded with two cameras. As a non-contact method external factors (heat sources, air currents, lighting conditions) and the installation of equipment (orientation of the cameras, quality of the speckle pattern) gain importance. Even more important is data smoothing driven by the facet size. With rising facet size from 19^2 to 100^2 pixel^2, the repeatability is found increasing from $\sigma_{\mathrm{DIC}} \approx$

286 to 29 μstrain, while the relative precision is *rel. prec.* ≈ 16 to 29 μstrain.

Practically the *rel. prec.* of all alternatives is seen on an equivalent level and thus rated well-suited to record strain data in RC structures. Repeatability of the readings decreases with increasing dimensionality. As a rule of thumb, it decreases by one power per dimension.

If more dimensional measurement techniques are to be applied in a project, the installation effort truly rises, which can be justified with higher information density and spatial data. Nevertheless, the use of a few strain gauges for reference is strongly recommended and allows assessing measuring accuracies. Especially, repeated measurements on constant load levels enable to rate the robustness.

Chapter 3

Temperature Induction into RC Structures

The following chapter is taken verbatim from:

> CLAUß, F.; LÖSCHMANN, J.; AHRENS, M. A. and MARK, P. *Temperaturinduktion in Betontragwerke – Experimentelle Untersuchungen zur Methode*. Beton- und Stahlbetonbau, 2021. 116(7): pp. 539–550. doi: 10.1002/best.202100010.

Text and figures have been adjusted to the format and layout of this thesis. The content remains identical. The literature used is jointly referred to at the end of the thesis.

Abstract

De-icing of bridge decks, control of hardening or concrete strengthening through tempering are promising applications for active temperature induction into RC structures. The paper introduces fundamental approaches and devices: heating with infrared radiators, heating pads, heated water and Peltier elements, cooling liquids and dry ice, are discussed by means of nominal electric powers, attachment to the structure, interaction of device and structure, temperature control and potential losses. The characteristics of the approaches are analyzed and rated.
A test series on insulated beams serves for reference. The alternative approaches are separately applied and combined to induce temperature gradients. Heating pads and infrared radiators are most suited for heating while Peltier elements and liquids are beneficial for cooling. From comparison recommendations for practical application are derived.

Temperaturinduktion in Betontragwerke

Experimentelle Untersuchungen zur Methode

Das Enteisen von Brückenfahrbahnen, die gesteuerte Erhärtung von Beton oder die Tragwerksverstärkung bei Temperierung sind Anwendungen für eine gezielte Temperaturinduktion in Betontragwerke. Der Beitrag behandelt dazu grundlegende Methoden. Dies sind das Erwärmen mit Infrarotstrahlern, Wärmematten oder erhitztem Wasser und das Kühlen mit Peltier-Elementen, Kühlflüssigkeiten oder Trockeneis. Diskutiert werden die nominellen elektrischen Leistungen, die Fixierung am Bauteil, Interaktionen zwischen Temperierung und Bauteil, die Temperaturregelung und mögliche Verluste. Die Verfahren werden mit ihren Eigenschaften vorgestellt und bewertet. Als Basis dient eine Versuchsserie an Balken mit Einhausung durch Wärmedämmung. Die einzelnen Temperierverfahren werden separat untersucht und zur Erzeugung eines Temperaturgradienten kombiniert. Es zeigt sich, dass besonders Wärmematten oder Infrarotstrahler für das Heizen und die Peltier-Kühlungen bzw. Kühlwasser für das Kühlen geeignet sind. Für die praktische Anwendung werden Empfehlungen abgeleitet.

3.1 Einleitung

Temperaturen aktiv in Tragwerke einzubringen, ist im Bauwesen weitgehend unbekannt. Tragwerke ertragen reaktiv die auf sie einwirkenden Temperaturzustände und entwickeln daraus Verformungen oder Zwängungen bei Verformungsbehinderung. Temperaturen zu steuern oder zu regeln ist unüblich. Ganz anders stellt sich das z. B. im Maschinenbau dar. Klimatisierung, der Einsatz von Formgedächtnismaterialien oder ein gezieltes Wärmen von Metallen zur Verformung sind gängige und bewährte Verfahren aktiver Temperaturregelung [74, 95, 168].

Das Potential der Temperaturregelung für das Bauwesen ist groß. Erste Ansätze liegen in der Erwärmung von Brückenfahrbahnplatten zur Enteisung [45, 221], der Konditionierung von Beton während der Erhärtung [176, 189, 198] oder seit kurzem auch zur gezielten Einbringung von günstigen Zwangskräften [117, 119]. Bei Verstärkungen von Bestandsbauwerken [82, 132, 204], wie etwa ermüdungsgefährdeten Brücken [164] oder Deckenplatten, erhöht eine Temperaturinduktion erheblich die Effizienz [117]. Dabei werden die Zwangskräfte geregelt und

Schnittgrößen gezielt voreingestellt. Solch eine Voreinstellung ist auch im Brückenbau hilfreich, wo Zwang aus Bauzuständen reduziert oder gänzlich eliminiert werden kann [119]. Darüber hinaus ist der Einfluss von Temperaturänderungen [78] auf beispielsweise Ultraschallwellen [26] und damit auch die experimentelle Induktion in Stahlbetontragwerke Gegenstand aktueller Forschung.

Der Beitrag stellt den technischen Aufbau verschiedener Methoden zur Temperaturinduktion dar. Temperierungen werden hinsichtlich ihrer Leistung, Grenzen und Randbedingungen diskutiert und an Betonbalken angewendet. Ziel ist es, geeignete Methoden und ihre Kombinationsmöglichkeit vorzustellen, ihre Einsatzbereiche aufzuzeigen und letztendlich eine Entscheidungsgrundlage für praktische Anwendungen zu schaffen. Die Anwendung am Bauteil erfolgt durch die Erzeugung eines linear veränderlichen Temperaturgradienten. Dazu wird die Oberseite erwärmt und die Unterseite gekühlt. Die Temperierungen beeinflussen sich dabei gegenseitig.

3.2 Methoden zur Temperaturinduktion

3.2.1 Auswahl der Methoden

Bei den Methoden ist prinzipiell zwischen Heizen (Wärmen) und Kühlen zu unterscheiden. Die Termini beziehen sich auf die Ausgangstemperatur T_0 (Referenz) des Bauteils. Beim Heizen wird Wärmeenergie zugeführt, sodass die Temperatur im Bauteil ansteigt. Kühlen hingegen bedeutet ein Absenken der Temperatur. Typische Heizmethoden sind:

- Wasserheizung
- Peltier-Heizung
- Heizmatten
- Heißluft
- Infrarotstrahler

Unter Ausschluss der Methoden, welche keine präzise Temperaturregelung (Heißluft) oder effiziente Anwendung (Peltier-Heizung) zulassen, werden im Beitrag ausschließlich Wasserheizungen, Heizmatten und Infrarotstrahler behandelt. Zum Kühlen stehen folgende Methoden zur Verfügung:

- Wasserkühlung
- Peltier-Kühlung
- Verdunstungskühlung
- Kältemischungen von Stoffen
- Trockeneis

Auch hier werden Methoden (Peltier-Kühlung, Wasserkühlung) hinsichtlich ihrer praktischen Realisierbarkeit und Regelbarkeit ausgewählt. Die Anzahl an Kühlmethoden ist begrenzt. Daher werden Peltier-Elemente trotz ihres hohen technischen Aufwands hier berücksichtigt. Bild 3.1 gibt einen Überblick über die mit den ausgewählten Methoden realisierbaren Temperaturbereiche mit Referenz bei ca. 20 °C [70, 71, 89]. Aufgrund der vielen Einflussfaktoren auf die eingetragene Wärmeenergie sind die Grenzen als Orientierung anzusehen.

3.2.2 Temperiertes Wasser

Unter atmosphärischen Bedingungen kann Wasser Temperaturen zwischen fast 0 °C und 100 °C annehmen, ohne dass ein Wechsel des Aggregatzustands auftritt. Wasser ist somit zum Kühlen und Heizen geeignet. Der Wärmeübergang vom Wasser in ein Bauteil erfolgt mittels

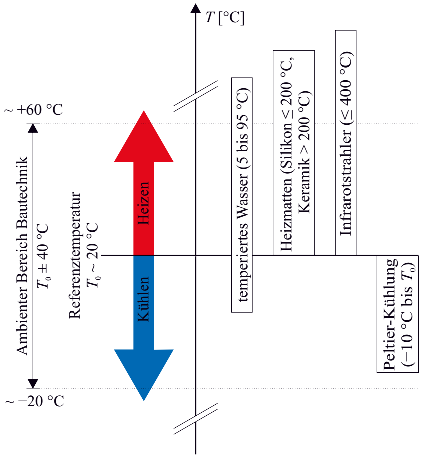

Bild 3.1: Ausgewählte Temperiermethoden zum Heizen und Kühlen mit erzielbaren Temperaturbereichen

Figure 3.1: Selected tempering methods for heating and cooling with achievable temperature ranges

Wärmeleitung. Er kann direkt oder indirekt realisiert werden. Ein Beispiel für eine direkte Temperierung ist durch ein Bauteil hindurchfließendes Wasser. Bei indirekter Temperierung mittels Kühl- bzw. Heizkörper ist zwischen einem offenen (freier Wasserspiegel) und einem geschlossenen System zu unterscheiden. Da ein großer Wärmeaustausch eine hohe Fließgeschwindigkeit erfordert, ist eine geschlossene Bauweise zu bevorzugen (vgl. Bild 3.2). Der Transport des Wassers erfolgt dann unter Druck. Darüber hinaus beschränken sich offene Systeme aufgrund des freien Wasserspiegels auf die Temperierung von oben. Mit geschlossenen Systemen können Bauteile allseitig (vgl. Bild 3.2) temperiert werden. Um einen optimalen Wärmetransport zu gewährleisten, ist eine von der Bauteildimension abhängige Fördermenge erforderlich.

Die Temperierung des Wassers kann über Kühlaggregate (z. B. gwk weco) bzw. Heizaggregate (z. B. gwk teco) realisiert werden. Im Kälteaggregat wird dem Wasser beispielsweise mithilfe von Druckänderungen eines Kältemittels Wärmeenergie entzogen (Kompressionskühlung) oder im Heizaggregat Wärmeenergie elektrisch zugeführt.

Der in Bild 3.2 dargestellte Druckbehälter einer geschlossenen Wassertemperierung besteht aus zwei Rechteckhohlprofilen aus Stahl. Stirnbleche an beiden Enden mit einem Zu- und einem Abfluss verschließen den Behälter. Dieser ist über Druckschläuche mit dem Heiz- bzw. Kühlaggregat verbunden, sodass ein geschlossener Wasserkreislauf entsteht. Eine Ausnehmung in den Profilen ermöglicht eine doppelte Durchströmung des Behälters. Dadurch können größere Querschnittsbreiten temperiert werden, ohne dass Totbereiche in der Wasserströmung entstehen. Das Prinzip sorgt für eine homogene Einleitung der Temperatur in das Bauteil. Die Temperierung erfolgt mittels Zweipunktregelung. Das Kühl- bzw. Heizaggregat regelt die Temperatur nach, sobald die Wassertemperatur im Rücklauf die Solltemperatur um 1 °C über- bzw. unterschritten hat.

3.2.3 Heizmatte

(Silikon-)Heizmatten können zum Heizen von Bauteilen von bis zu 200 °C verwendet werden [89]. Die Wärme wird durch elektrischen Strom erzeugt. Dazu sind Heizdrähte mäanderförmig zwischen zwei Silikonschichten verlegt. Über den Abstand der Schlaufen wird bereits beim Bau der Matten die Heizleistung eingestellt. Die Temperierung eines Bauteils erfolgt immer von außen mittels Wärmeleitung. Dazu werden die elastischen Matten auf die Oberfläche gelegt bzw. bei einer Temperierung von unten oder der Seite

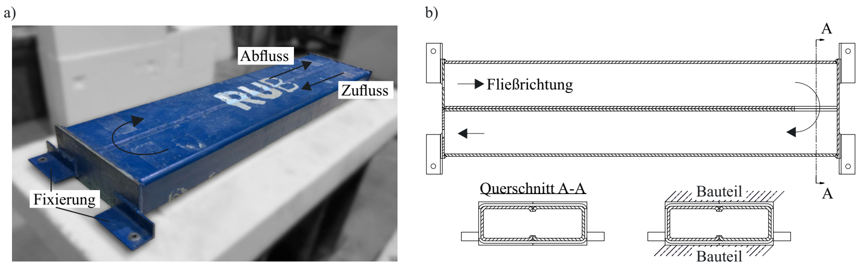

Bild 3.2: a) Stahldruckbehälter einer Wassertemperierung, b) Skizze des Druckbehälters

Figure 3.2: a) Steel pressure vessel for tempering with water, b) sketch of the vessel

gegen die Oberfläche gepresst. Für die in Bild 3.3 dargestellte Silikonheizmatte beträgt der Abstand der Heizdrähte ca. 3 mm. Es ergibt sich eine Leistung von 3000 W. Mittels PID-Regelung und Temperaturfühler (PT100) kann die Temperatur auf der Oberseite eingestellt werden.

3.2.4 Infrarotstrahler

Gängige Infrarotstrahler können Temperaturen von bis zu ca. 400 °C erzeugen. Die Funktionsweise basiert auf Wärmestrahlung. Infrarotstrahlung ordnet sich im Spektralbereich der elektromagnetischen Wellen direkt oberhalb des sichtbaren Lichtes bei 0,78 µm bis 1000 µm an. Daraus ergeben sich gemäß Wienscher Verschiebungsgesetz $\lambda_{max} \cdot T = 2898\,\mu\text{m}\,\text{K} = \text{konst.}$ [83] Temperaturen von über 3000 K bis ca. 3 K [35, 83]. Im Gegensatz zu den anderen Temperiermethoden erfolgt die Wärmeeinleitung in das Bauteil mittels Strahlung, sodass kein mechanischer Kontakt zur Oberfläche vorhanden ist. Ein einzelner Infrarotstrahler wird beispielsweise in einem Modul bestehend aus Hochleistungsreflektoren und Lüftern (Bild 3.4) positioniert. Der Infrarotstrahler (hier Doppelrohrstrahler) besteht aus metallischen Heizwendeln, welche innerhalb eines Quarzglasrohres atmosphär verlegt sind.

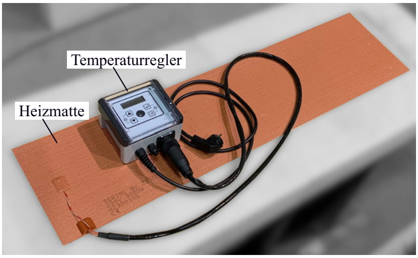

Bild 3.3: Silikonheizmatte (ISOHEAT MIL-SM) mit Temperaturregler

Figure 3.3: Silicone heating pad (ISOHEAT MIL-SM) and controller

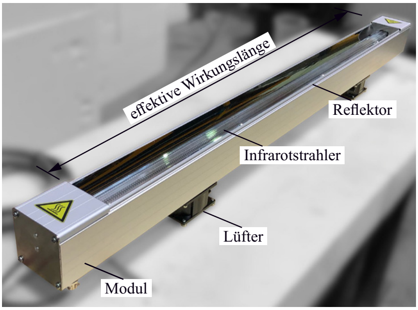

Bild 3.4: Infrarotmodul (IBT.InfraBioTech GmbH SIR-Strahler DRS 1000 × 80/4,0) mit zwei rückseitigen Lüftern

Figure 3.4: Infrared module (IBT.InfraBioTech GmbH SIR emitter DRS 1000 × 80/4.0) with two fans at rear

Die Nennleistung des Strahlers beträgt 4000 W [87]. Mit einer Regeleinheit (Zweipunktregler) kann die Leistung des Strahlers unter Verwendung eines Temperatursensors (Thermoelement Typ K) gesteuert werden.

3.2.5 Peltier-Kühlung

Peltier-Kühlungen nutzen den bei der Temperaturmessung mit Thermoelementen auftretenden Seebeck-Effekt [113] in seiner Umkehrung (Peltier-Effekt), um durch eine elektrische Spannung eine Temperaturdifferenz in einem Leiter zu erzeugen. Dazu werden Halbleiter mit unterschiedlicher Dotierung (Einbringung von Fremdatomen zur Veränderung der elektrischen Leitfähigkeit) alternierend in Reihe geschaltet (Bild 3.5). In die Halbleiter eingeleitete Elektronen gelangen abwechselnd von einem energetisch höheren Leitungsband (p-dotiert) in ein geringes (n-dotiert) und nehmen dabei Wärme auf bzw. geben sie ab. Es entsteht ein Wärmetransport zwischen den beiden Seiten des Peltier-Elements. Durch Umkehrung des Stromflusses ist mit Peltier-Elementen sowohl Heizen als auch Kühlen möglich. Dabei sind Temperaturdifferenzen zwischen der warmen und der kalten Seite von bis zu 75 °C erzielbar [113].
Wärmeleistung wird neben dem Peltier-Effekt ($\dot{Q}_{\mathrm{PE}}$) auch durch den elektrischen Strom ($\dot{Q}_{\mathrm{el}}$) erzeugt. Zudem reduziert Wärmeleitung $\dot{Q}_{\mathrm{WL}}$ zwischen den beiden Seiten (warme und kalte Seite) die Kühlleistung $\dot{Q}_{\mathrm{c}}$ [75, 129]. $\dot{Q}_{\mathrm{c}}$ ergibt sich dann additiv zu Gl. 3.1, wobei Kühl- und Wärmeeffekte unterschiedlichen Vorzeichens sind.

$$\begin{aligned}\dot{Q}_{\mathrm{c}} &= \dot{Q}_{\mathrm{PE}} + \dot{Q}_{\mathrm{el}} + \dot{Q}_{\mathrm{WL}} \\ \dot{Q}_{\mathrm{c}} &= \alpha \cdot I \cdot T - \frac{R \cdot I^2}{2} - \lambda \cdot \Delta T \cdot \frac{A}{d}\end{aligned} \tag{3.1}$$

mit:

α	Seebeck-Koeffizient [V/K]
I	Stromstärke [A]
T	Temperatur des Peltier-Elementes [K]
R	Ohm'scher Widerstand [Ω]
λ	Wärmeleitfähigkeit [W/(m K)]
ΔT	Temperaturdifferenz [K]
A	Fläche der Halbleiter [m]
d	Höhe des Peltier-Elementes [m]

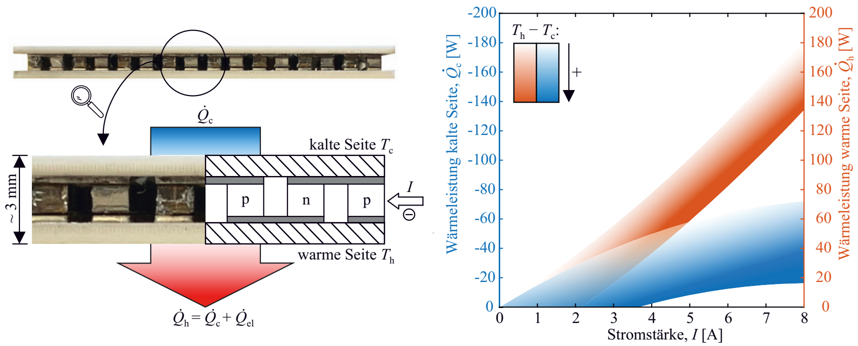

Bild 3.5: Aufbau und Wirkungsweise von Peltier-Elementen sowie Entwicklung der Wärmeleistung auf der kalten bzw. warmen Seite in Abhängigkeit von der Stromstärke [192]

Figure 3.5: Setup and mode of operation of Peltier elements and development of the heat output on the cold and hot side as a function of the current strength [192]

Mit ansteigender Stromstärke übersteigt die Wärmeleistung auf der warmen Seite (Index h) zunehmend die Kühlleistung (Index c) der kalten Seite $\dot{Q}_\mathrm{h} > \dot{Q}_\mathrm{c}$ (Bild 3.5).
Um einen Temperaturanstieg im gesamten Element zu vermeiden, ist eine adäquate Kühlung der warmen Seite erforderlich. Die Wärmeleistung auf der warmen bzw. kühlen Seite des Peltier-Elementes kann mithilfe von Bild 3.5 näherungsweise in Abhängigkeit der verwendeten Stromstärke I bestimmt werden. Zudem wird deutlich, dass die Wärmeleistung mit ansteigender Temperaturdifferenz zwischen der warmen T_h und kalten Seite T_c absinkt. Das Verhältnis zwischen der erreichten Kühlleistung und der entstehenden Wärmeleistung aus dem elektrischen Strom wird als Performance-Koeffizient (engl. *coefficient of performance, COP*) bezeichnet und beschreibt die Effizienz der Kühlung. Eine hohe Effizienz, proportional zu einer moderaten Wärmeentwicklung auf der warmen Seite, wird bei ca. 50 % der maximalen Stromstärke erreicht [193].
Bild 3.6 zeigt eine mögliche Verschaltung von Peltier-Elementen als Reihenschaltung mit jeweils 3 Peltier-Elementen und einer Parallelschaltung in 12 Gruppen. Die verwendeten silikonversiegelten Peltier-Elemente haben eine maximale Stromstärke von 8,6 A bei einer Spannung von 15,7 V. Aus der Gleichspannung der Netzteile von 24 V ergibt sich infolge der Reihenschaltung eine Spannung von 8 V an jedem Peltier-Element. Jedes Element wird dadurch mit ca. 4,4 A Strom versorgt. Es ergibt sich der erwähnte effiziente Betrieb bei ca. halber Stromstärke. [193]
Für die Abführung der freigesetzten Wärme-

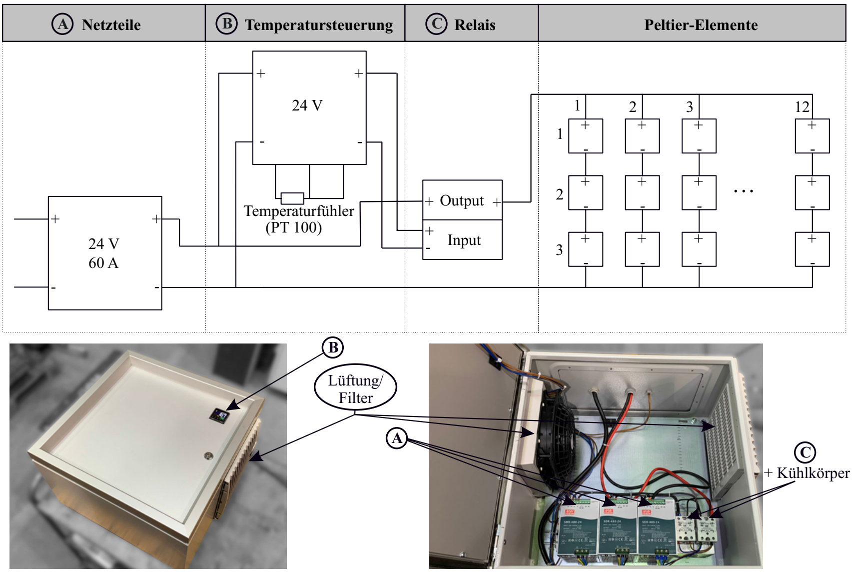

Bild 3.6: Verschaltung und Schaltschrank der Peltier-Kühlung

Figure 3.6: Wiring and control panel of the Peltier cooling

energie wird die in Abschnitt 3.2 vorgestellte Wasserkühlung verwendet. Die Peltier-Elemente werden dazu, wie in Bild 3.7 dargestellt, mit ihrer warmen Seite auf dem mittels einer CNC-Fräse planierten Deckblech eines Kühlkörpers angeordnet. Taschen aus Moosgummi dienen der Lagesicherung und isolieren die kalte und die warme Seite der Peltier-Elemente voneinander. Auf die kalte Elementseite werden gegliederte Aluminiumbleche zur Temperaturverteilung und -einleitung in das zu kühlende Bauteil aufgelegt. Auf den Kühlkörper und die Aluminiumbleche geklebte Grafitfolien (Wärmeleitfähigkeit in der Ebene von $\lambda_{xy} = 1600\,\mathrm{W/(m\,K)}$) dienen der horizontalen Wärmeverteilung (heat spreading). Die beidseitig von jedem Peltier-Element gesetzten Verschraubungen im Deckblech und den Aluminiumblechen gewährleisten eine zentrische Pressung. Dabei verhindern unter den Schraubenköpfen angeordnete Tellerfedern Schiefstellungen oder Verformungen der Bleche, welche zu einer schlechteren Wärmeübertragung führen würden. Wie in Bild 3.6 dargestellt, wird das System aus 36 Peltier-Elementen mit einem Temperaturregler verbunden. Die Zweipunktregelung erfolgt über einen Temperaturfühler (PT100), welcher mittig in ein Aluminiumblech eingelassen ist.

3.3 Diskussion

3.3.1 Elektrische Leistung

Tab. 3.1 fasst die wesentlichen Merkmale der Temperiermethoden zusammen. Die elektrische Leistung gibt Aufschluss über den Stromverbrauch. Die Silikonheizmatten weisen den niedrigsten Verbrauch aller ausgewählten Heizmethoden auf. Bei den Kühlmethoden verbraucht das temperierte Wasser am wenigsten Strom. Grund für die höhere elektrische Leistung der Peltier-Kühlung ist vor allem das zusätzlich erforderliche Kühlaggregat (siehe (d) 9000 W).

3.3.2 Temperaturregelung

Aus der Regelungsart, der Lage des Temperatursensors sowie der Leistung der Tempe-

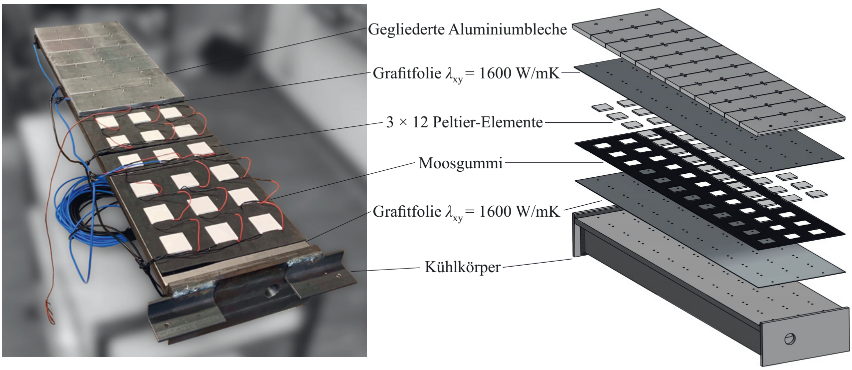

Bild 3.7: Peltier-Elemente mit zugehöriger Wasserkühlung, im hinteren Bereich bereits durch Aluminiumbleche verpresst

Figure 3.7: Peltier elements with corresponding water cooling and already installed aluminum sheets in the back

Tab. 3.1: Überblick über die vorgestellten Methoden zur Temperaturinduktion

Table 3.1: Summary of the methods presented for temperature induction

	Heizen			**Kühlen**	
	(a) Temp. Wasser	(b) Heizmatte	(c) Infrarot-strahler	(d) Temp. Wasser	(c) Peltier-Kühlung
Wärmeübergang	Wärme-leitung	Wärme-leitung	Wärme-strahlung	Wärme-leitung	Wärme-leitung
Temperaturbereich [°C]	≤ 95	≤ 200	≥ 100	≥ 5	≥ -10
Elektr. Leistung [W]	18000	3000	3×4000	9000	$1500 + 9000$
Verformungsfähigkeit	nein	ja	ja	nein	nein
Temperaturregelung (alternativ möglich)	on/off	PID	PID (on/off)	on/off	on/off (PID)
Toleranzband (tatsächliche Amplitude) +/– [°C]	1 (< 0,1)	0,5 (1,5)	1 (0,75)	1 (0,3)	1 (< 0,1)

rierung ergeben sich erhebliche Unterschiede in der Frequenz und der Amplitude der Heiz- bzw. Kühltemperaturkurven. Bild 3.8 zeigt dies für die vier Temperierarten Wasser, Infrarotstrahler, Heizmatte und Peltier-Kühlung an einem Betonkörper. Dabei ist zwischen moderaten ($\approx 5\,/\,30\,°C$) und hohen Temperaturen ($\approx -10\,/\,75\,°C$) zu unterscheiden und die Position der Temperaturmessung (blaue Punkte) und Regelung (rote Punkte) zu beachten. Die Temperaturbereiche orientieren sich an den später vorgestellten *Benchmark* und *Stress Tests*.

Die Temperaturverläufe der Heizmatte und der Peltier-Kühlung weisen eine hohe Frequenz auf. Gründe hierfür sind

- eine schnelle Wärmeabgabe (hohe Wärmeleitfähigkeit) oder
- eine niedrige Wärmekapazität der Systeme und
- eine Temperaturregelung in unmittelbarer Nähe zur Heiz- bzw. Kühlquelle.

Erwärmungs- und Abkühlphasen folgen im schnellen Wechsel. Ihre Dauer verringert sich mit ansteigender Differenz von Temperier- und Umgebungstemperatur. So erhöht sich die Frequenz der Heizmatte bei höheren Temperaturen aufgrund des schnellen Abkühlens des Silikons. Beim Annähern an die Leistungsgrenze ist kein alternierender Verlauf mehr zu erkennen. Dies zeigt sich bei der Peltier-Kühlung mit einer kontinuierlichen Zufuhr an Kühlleistung. Die Frequenz der Wassertemperierung ist aufgrund der Lage des Temperatursensors im langen Wasserumlauf deutlich geringer. Der Temperaturverlauf der Infrarotstrahler zeigt kein einheitliches Bild. Durch Luftströme entlang der freien, bestrahlten Bauteiloberseite kommt es zu Temperaturschwankungen.

Die Heizmatte erzeugt aufgrund ihrer hohen Leistung (3000 W) und der geringen Wärmekapazität des Systems große Amplituden. Heizmatten bieten sich daher vor allem für Temperaturen oberhalb von 50 °C an. Infrarotstrahler sind aufgrund der durchgehenden Überschreitung des Sollwertes der Zieltemperatur erst ab 100 °C zu empfehlen. Grundsätzlich ist bei hohen Leistungen die Verwendung einer stetigen Regelung (hier: PID-Regelung) erforder-

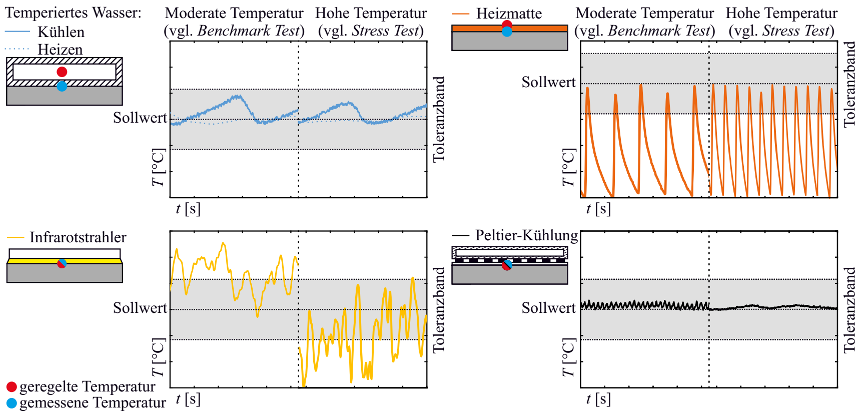

Bild 3.8: Temperaturverlauf der Temperierung in Abhängigkeit von den einzelnen Methoden zur Temperaturinduktion

Figure 3.8: Variation of the temperature dependent on the alternative methods of temperature induction

lich, um Amplituden zu reduzieren. Trotz dieser Regelung verlassen Heizmatte und Strahler ihre Toleranzbänder, bei der Heizmatte unterschreitend, bei den Strahlern in beide Richtungen. Wassertemperierung und Peltier-Kühlung halten die Toleranz. Die Amplitude der leistungsstarken Wassertemperierung (Tab. 3.1) wird durch das große Wasservolumen und die verzögerte Wärmeübertragung zum Bauteil gedämpft. Die verwendete Zweipunktregelung (on/off) bewirkt eine Amplitude einseitig des Sollwertes. Somit wird im Mittel eine niedrigere Temperatur eingeleitet. Unabhängig von den gezeigten Variationen direkt am Temperiermedium bleiben die Temperaturen im Bauteil (Tiefe > 2 cm) aufgrund der Trägheit der Wärmeleitung im Beton unbeeinflusst. Allein große Amplituden sind durch hohe Frequenzen auszugleichen.

3.3.3 Temperaturübergang

Der Temperaturübergang erfolgt bei den vier Methoden (a, b, d, e) mittels Wärmeleitung, beim Infrarotstrahler über Wärmestrahlung (c). Bei Wärmeleitung muss das Temperiermedium der Bauteiloberfläche folgen, auch wenn ein Bauteil sich verformt. Luftschichten sind ungünstig und wirken deutlich isolierend. Beim Infrarotstrahler (c) spielen übliche Bauteilverformungen hingegen keine Rolle.

3.3.4 Fixierung am Bauteil

Die Art der Wärmeübertragung bedingt die Positionierung und Fixierung der verschiedenen Heiz- und Kühlsysteme. Bei Wärmeleitung ist eine mechanische Ankopplung zwischen der Betonoberfläche und dem Temperiersystem nötig. Bei Wärmestrahlung (Infrarotstrahler) ist das System mit Abstand zur Bauteiloberfläche zu positionieren. Die Fixierung hängt dabei von der Ausrichtung der zu temperierenden Fläche ab. Liegt sie an der Bauteiloberseite, ist ein reines Auflegen der Systeme (a, d, e) möglich. Heizmatten (b) sind durch ihr geringes Gewicht und ihre Flexibilität anfällig für nicht vollflächige Auflagen.

Sie sollten daher zusätzlich beschwert werden, beispielsweise mit Blechen. An der Unterseite oder an den Seitenflächen können die Systeme mithilfe von Winkeln (vergleiche Bild 3.2a und 3.7) und Gewindestangen (Bild 3.9) gegen das Bauteil gepresst werden.

3.3.5 Interaktion mit dem Bauteil und Verluste

Der direkte Kontakt von Temperiersystem und Bauteil ist entscheidend für eine gute Wärmeübertragung. Diese verbessert sich mit steigendem Anpressdruck (vgl. effektive Wärmeleitfähigkeit λ_{eff} und thermischer Kontaktkoeffizient k_{K} [68]), da sich Lufteinschlüsse in der Kontaktfläche und dadurch auch Verluste bei der Wärmeeinleitung reduzieren. Bei Aufhängungen mit Winkeln lässt sich der Anpressdruck über die Gewindestangen regulieren, bei aufliegenden Systemen mit Auflasten.
Durch den Anpressdruck in Kombination mit steifen Temperiersystemen (a, d, e) können Verformungen des Stahlbetonbauteils, resultierend aus äußeren Einwirkungen oder der Temperierung selbst, behindert werden. Es kommt zu Zwängen und ungewollten Einflüssen auf das Tragverhalten. Dies spielt bei elastischen Heizmatten (b) und Infrarotstrahlern (c) keine Rolle. Bei allen anderen Systemen sind Maßnahmen vorzunehmen, um eine freie Verformbarkeit des Bauteils bei gleichzeitigem Erhalt der Wärmeeinleitung zu gewährleisten. Planmäßige Luftschichten sind dazu kaum brauchbar, da sie die Wärmeleitung stark verringern. Besser geeignet sind Wärmeleitpads mit hoher Verformungsfähigkeit als Zwischenschicht (Bild 3.9). Sie besitzen geringe Eigensteifigkeit und gute Wärmeleiteigenschaften. Herkömmliche Stärken von $< 1\,\text{mm}$ sind in der Regel nicht ausreichend. Abhängig von den erwarteten Bauteilverformungen sind Stärken von $> 5\,\text{mm}$ zu empfehlen. Neben einer möglichen Verformungsbehinderung ist die zusätzliche Last aus dem Eigengewicht einer Temperiermethode zu berücksichtigen. Heizmatten können aufgrund des geringen Eigengewichts vernachlässigt werden. Kühlen ist in der getroffenen Auswahl mit einer zusätzlichen Last aus dem Temperiersystem verbunden.

3.3.6 Fazit

In diesem Kapitel wurde die elektrische Leistung, die Temperaturregelung, der Temperaturübergang, die Fixierung am Bauteil und

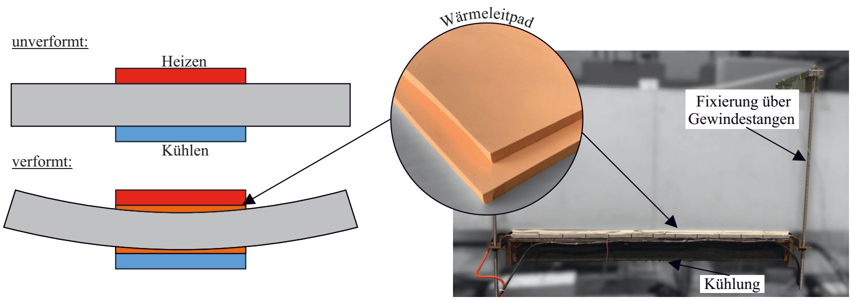

Bild 3.9: Ausgleich von Bauteilverformungen und Fixierung einer Kühlung am Bauteil

Figure 3.9: Compensation of structural deformation and attachment of a cooling system to the component

die Interaktion mit dem Bauteil diskutiert. Während die Regelung keinen signifikanten Einfluss auf die Temperaturinduktion hat, sind die übrigen Faktoren gegeneinander abzuwägen. Um den Wärmeübergang zu optimieren, sind Luftschichten durch einen hohen Anpressdruck auszuschließen. Das Anpressen beeinflusst nachteilig die Verformungsfähigkeit des Bauteils, was durch Wärmeleitpads bei Erhalt des Wärmeübergangs ausgeglichen werden kann.

3.4 Anwendung: Erzeugung eines Temperaturgradienten

3.4.1 Versuchsaufbau und -durchführung

An einem Betonbalken mit Rechteckquerschnitt wurde ein vertikaler Temperaturgradient erzeugt. Dazu wurde ein Heizsystem an der Oberseite mit einem Kühlsystem an der Unterseite kombiniert (Bild 3.10). Dies erfolgte für verschiedene Kombinationen aus Wasserkühlung sowie -heizung, Silikonheizmatten, Infrarotstrahlung und Peltier-Kühlung. Zur Isolierung war der Versuchskörper allseitig mit 100 mm starkem extrudiertem Polystyrol umschlossen. Bei den Infrarotstrahlern entfiel die Isolierung der zu heizenden Oberseite. Der Versuchskörper wies Abmessungen von $b\,/\,h\,/\,l = 250\,/\,160\,/\,1000$ [mm] auf. Die zu heizenden bzw. kühlenden Flächen nahmen die komplette Ober- bzw. Unterseite ein. Vier Thermoelemente (T_1 bis T_4, Bild 3.10a) messen das veränderliche Temperaturfeld [100] über die Höhe. Durch die geringe Wärmeleitfähigkeit von Beton ($\lambda \approx 2$ W/m K) stellte sich der stationäre, lineare Temperaturgradient selbst bei der Balkenhöhe von 16 cm erst nach Stunden ein.

Es wurden zwei Versuchsserien durchgeführt, und zwar *Benchmark Tests* und *Stress Tests*. Tab. 3.2 zeigt dazu die in den Regeleinheiten eingestellten Temperaturen. Im *Stress Test* wurden die Kühlmethoden auf die jeweils minimal erzielbare Temperatur (Wasserkühlung: 5 °C, Peltier-Kühlung: -10 °C) eingestellt. Die Heiztemperatur wurde auf 35 °C bzw. 75 °C fixiert. Höhere Temperaturen ($\gg$ 75 °C) könnten die Isolierung und den Beton schädigen.

3.4.2 Versuchsergebnisse

Bild 3.11a zeigt den Temperatur-Zeitverlauf beispielhaft für den Versuch mit einer Silikonheizmatte und einer Peltier-Kühlung. Dabei wurden Temperaturen an den temperierten Oberflächen mit Thermoelementen gemessen. Zunächst wurde der *Benchmark Test* durchgeführt. Nach Erreichen eines stationären Zustands wurden die Temperaturen auf die des *Stress Tests* angepasst.

Bild 3.11b stellt die korrespondierenden, internen Temperaturmessungen über die Höhe dar. Die gestrichelt gezeigten Randbereiche werden extrapoliert. Neben den gemessenen Temperaturen werden in Bild 3.11a ebenfalls ein gleitender Mittelwert der fluktuierenden Temperatur der Silikonheizmatte sowie die in der Regeleinheit eingestellte Temperatur gezeigt. Die Differenz dazwischen lässt auf Verluste an die Umgebung und insbesondere infolge von Wärmedurchlasswiderständen zum Bauteil schließen. Im *Benchmark Test* der Peltier-Kühlung wurde die eingestellte Temperaturdifferenz erreicht. Dies ist auf den hohen Anpressdruck durch das Aufliegen des Betonbalkens (Bild 3.10a) in Kombination mit Reserven in der Kühlleistung (eingestellte Temperatur 5 °C $>$ minimal erzielbare Temperatur -10 °C) zurückzuführen.

Bild 3.12 zeigt die mit den einzelnen Temperiermethoden erreichten Temperaturdifferenzen im

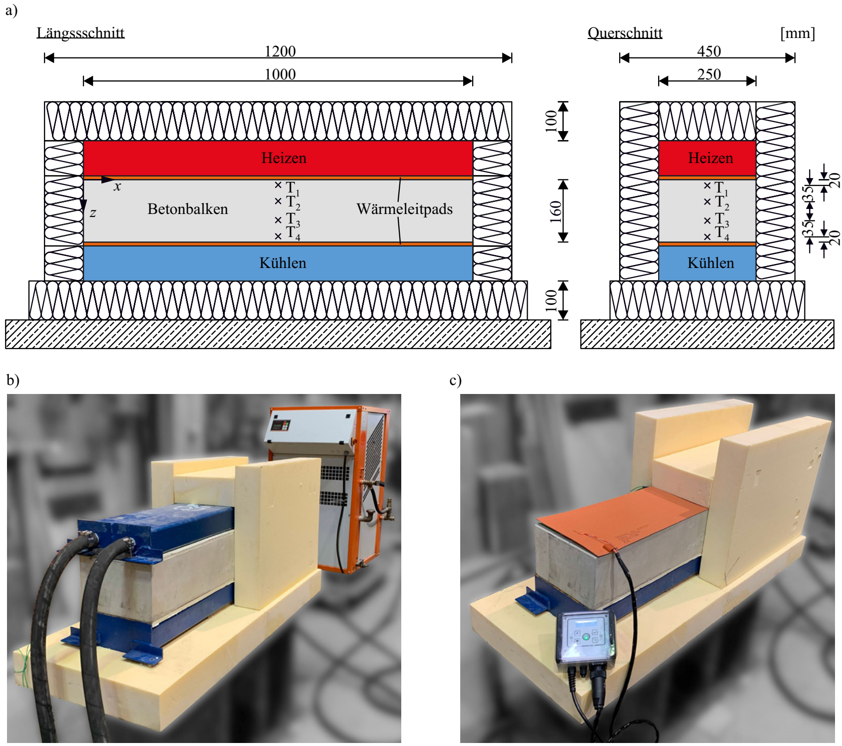

Bild 3.10: a) Zeichnung des Versuchsaufbaus; Fotos der Temperierversuche mit b) temperiertem Wasser zum Heizen und Kühlen und c) temperiertem Wasser zum Kühlen und einer Heizmatte

Figure 3.10: a) Sketch of the test setup; photos of the experiments with b) tempered water for heating and cooling and c) tempered water for cooling and a heating pad

Tab.: 3.2: Eingestellte Temperaturen für die *Benchmark* und *Stress Tests*

Table 3.2: Temperatures set for *benchmark* and *stress tests*

			Temperiertes Wasser	Heizmatte	IR-Strahler	Peltier Kühlung
Benchmark	T_{Heizen}	[°C]	35	35	35	
Test	$T_{\text{Kühlen}}$	[°C]	5			5
Stress	T_{Heizen}	[°C]	75	75	75	
Test	$T_{\text{Kühlen}}$	[°C]	5			-10

stationären Zustand für beide Testarten. Die Versuche werden stets anhand der Kombination aus Heiz-Kühlsystem (z. B. SH-W) benannt. Die Differenzen ergeben sich aus den extrapolierten Messwerten der internen Thermoelemente T_1 und T_4 (vgl. Bild 3.11, gestrichelt). Neben den erzielten werden auch die eingestellten Differenzen und der prozentuale Unterschied dazwischen angegeben. Es sei darauf hingewiesen, dass kein vollfaktorieller Versuchsplan durchgeführt wurde. Ergebnisorientiert wurden getestete Temperiersysteme durch leistungsstärkere ersetzt. Die größte Temperaturdifferenz wurde sowohl für die *Benchmark* als auch die *Stress Tests* durch die Kombination von Infrarotstrahlern und Peltier-Kühlung erreicht (19 bzw. 52,5 °C). Bei den *Benchmark Tests* ($T_0\pm$ 15 °C) verhielten sich die weiteren Temperiersysteme bezüglich der einzubringenden Differenzen vergleichbar (ca. 13 bis 15 °C), da die Leistung keines Systems

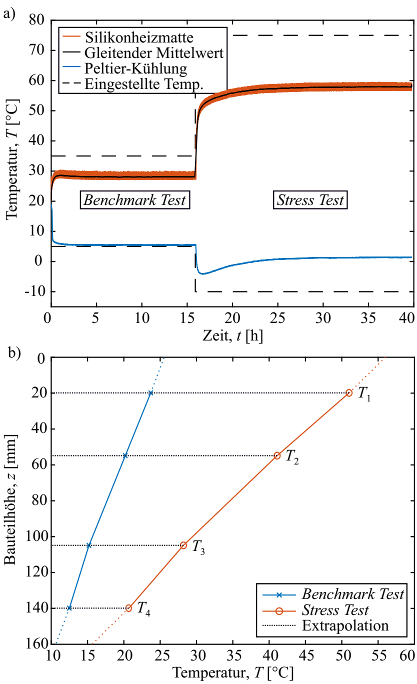

Bild 3.11: a) Temperatur-Zeitverlauf von Thermoelementen auf der Oberfläche für den Versuch mit Silikonheizmatte und Peltier-Kühlung und b) Temperaturprofil über die Höhe

Figure 3.11: a) Temperature versus time of thermocouples on the surface for heating with silicone pads and Peltier cooling and b) temperature profile over the depth

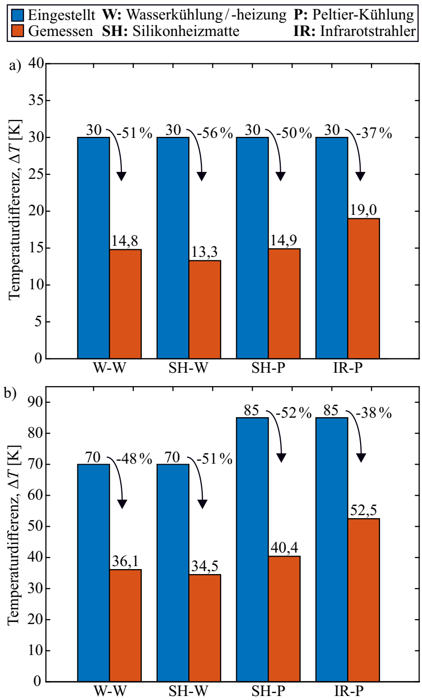

Bild 3.12: Extrapolierte Temperaturdifferenzen für a) die *Benchmark Tests* und b) *Stress Tests*

Figure 3.12: Extrapolated temperature differences for a) *benchmark tests* and b) *stress tests*

ausgeschöpft wird. Kleine Unterschiede resultieren aus der Fixierung am Bauteil (Anpressdruck) und der Position des Temperaturfühlers. Größere Abweichungen zwischen den Methoden zeigen sich bei den *Stress Tests*. Günstig zeigt sich die Peltier-Kühlung (ca. 40 °C erzeugbare Temperaturdifferenz im Balken), die niedrigere Temperaturen als die Wasserkühlung (ca. 35 °C) ermöglicht.

Für alle Kombinationen aus temperiertem Wasser, Silikonheizmatten und Peltier-Kühlung sind Verluste bei der Temperatureinleitung von mindestens 50 % feststellbar. Sie sind bei den Infrarotstrahlern durch die Regelung direkt an der Bauteiloberfläche günstiger (37 %). Neben der Position des Temperaturfühlers der Regelungseinheit und der Ankopplung des Temperiersystems spielt der eingebrachte Wärmestrom $\dot{Q}$ (Leistung) der Temperierung eine entscheidende Rolle. Bild 3.13 zeigt dies für die beiden Testarten (links *Benchmark*, rechts *Stress Test*) anhand von numerischen Vergleichsrechnungen nach [165]. Die aufgebrachten Wärmeströme sind frei gewählt. Exemplarisch soll die Abhängigkeit des Temperaturgradienten von den eingestellten Sollwerten und den maximalen Leistungen gezeigt werden. Dargestellt sind die stationären Temperaturverläufe über die Höhe, die sich bei verschiedenen Werten $\dot{Q}$ einstellen, wobei die Wärmeströme beim Erreichen der Sollwerte der Oberflächentemperaturen jeweils ausgesetzt ($\dot{Q} = 0$) werden. Erwartungsgemäß definiert der eingebrachte Wärmestrom die erzielte Temperaturverteilung. Mehr Leistung führt zu höheren Temperaturgradienten und umgekehrt. Dies gilt bis zu gewissen Grenzwerten (hier: *Benchmark* $>$ 3750 W/m, *Stress Test* $>$ 11000 W/m), wo der gewünschte Gradient erreicht ist. Weicht der Mittelwert aus den Sollwerten (oben und unten) von der Ausgangstemperatur ab, entsteht ein unsymmetrischer Temperaturgradient. Dies gilt auch für ungleiche Wärmeströme auf der Ober- und Unterseite.

3.4.3 Empfehlungen

Bild 3.14 zeigt Empfehlungen zur Verwendung von Heizmethoden in Abhängigkeit von der er-

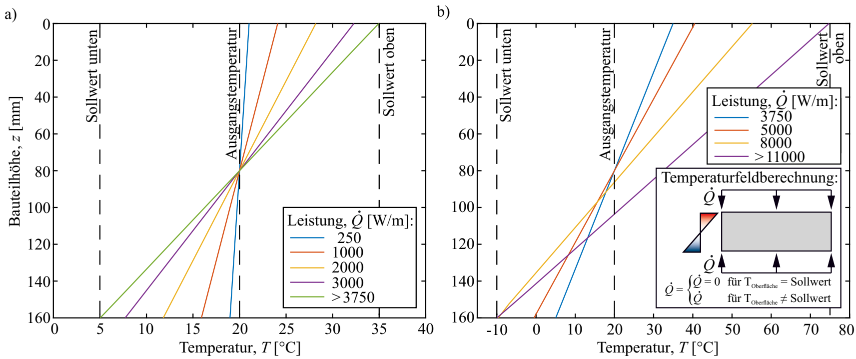

Bild 3.13: Aus Temperaturfeldberechnungen [165] resultierende stationäre Temperaturprofile über die Höhe für a) die *Benchmark Tests* und b) die *Stress Tests* als Funktion des eingebrachten Wärmestroms

Figure 3.13: Temperature profiles over the depth obtained from temperature field simulation [165] for a) *benchmark tests* and b) *stress tests*

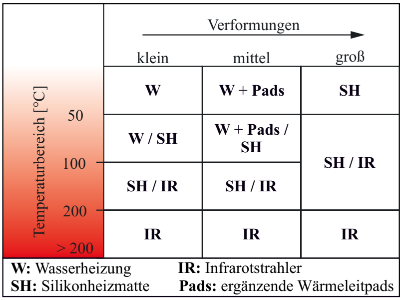

Bild 3.14: Empfehlungen zur Verwendung von Heizmethoden

Figure 3.14: Practical recommendations for heating

warteten Verformung des Bauteils (von klein nach groß) und der erforderlichen Temperatur (von niedrig nach hoch). Dabei werden neben der Leistungsfähigkeit des Temperiersystems auch weitere diskutierte Einflussfaktoren wie Temperaturübergang und -regelung sowie die Fixierung am und Interaktion mit dem Bauteil berücksichtigt. Wassersysteme bieten sich bei geringen Temperaturen deutlich unter 100 °C an. Ab rund 50 °C sind Heizmatten geeignet, bei Temperaturen jenseits von ca. 100 °C Infrarotstrahler. Wassersysteme benötigen Wärmeleitpads, um mittlere Verformungen (ca. 5 mm) auszugleichen. (Silikon-)Heizmatten und Infrarotstrahler kommen ohne diese aus und eignen sich deshalb bei großen Verformungen. Als Kühlmethode bieten sich Peltier-Elemente bis rund -10 °C an. Kühlwasser ist bis ca. 5 °C einsetzbar.

3.5 Schlussfolgerung

Es wurden die Temperiermethoden temperiertes Wasser, Heizmatten, Infrarotstrahler und Peltier-Kühlung hinsichtlich Regelung, Wärmeübergang, Fixierung am Bauteil, Interaktion mit dem Bauteil und thermischer Verluste konzeptionell sowie experimentell untersucht. Folgende Schlüsse lassen sich ziehen:

- Grundsätzlich entscheidet die Leistung eines Temperiersystems über erzielbare Temperaturen. Ist sie ausreichend hoch, entspricht die tatsächlich erreichte Temperatur (fast) der Solltemperatur. Ansonsten müssen die Sollwerte in der Regelung übersteuert oder Verluste gegenüber der gewünschten Temperaturgröße hingenommen werden.

- Bei der Ankopplung der Temperiereinheit an ein Bauteil sind zwei gegenläufige Auswirkungen zu beachten: Zum einen ist für die Wärmeeinleitung ein direkter Kontakt mit hohen Anpressdrücken zu gewährleisten. Zum anderen muss sich das Bauteil – mechanisch entkoppelt von der Temperiereinheit – weiter frei verformen können. Bei steifen Temperiersystemen wie Wasserdruckbehältern sollten daher verformungsfähige, wärmeleitfähige Weichschichten wie Wärmeleitpads zwischengelegt werden.

- Elastische bzw. kontaktlose Temperiersysteme wie Heizmatten und Infrarotstrahler lassen Bauteilverformungen zu, ohne den Wärmeeintrag zu verschlechtern.

- Infrarotstrahler liefern die effizienteste Heizmethode mit den geringsten Verlusten bei der Wärmeeinleitung (37 %). Sie übersteuern leicht bei ihrer Regelung und eignen sich besonders für Temperaturen über 100 °C. Für Temperaturen bis 100 °C bieten sich Heizmatten und Wassertemperierung an.

- Kühlen von Bauteilen ist gegenüber dem Wärmen grundsätzlich mit größerem technischem Aufwand verbunden. Die entwickelte Peltier-Kühlung erreicht Temperaturen bis -10 °C.

(Silikon-)Heizmatten bzw. meanderförmig verlegte Heizdrähte können, wie auch Wasserkreisläufe zur Enteisung von Brückenfahrbahnplatten, verwendet werden. Sie bieten sich auch bei der nachträglichen Verstärkung mit Temperaturinduktion an. Zur serienhaften Konditionierung von Beton sind Temperierstraßen mit installierten Infrarotstrahlern (in Analogie zu Trocknungsöfen) denkbar. Ein Temperiersystem sollte – individuell zugeschnitten auf den Anwendungsfall – unter Einbezug aller eingangs genannter Faktoren ausgewählt werden.

Chapter 4

Thermo-Mechanical Experiments on Reinforced Concrete Beams—Assessing Thermal, Mechanical and Mixed Impacts on Fiber Optic Measurements

The following chapter is taken verbatim from a manuscript submitted to the journal "Structural Concrete" (Online ISSN: 1751-7648):

> CLAUß, F.; AHRENS, M. A. and MARK, P. *Thermo-Mechanical Experiments on Reinforced Concrete Beams—Assessing Thermal, Mechanical and Mixed Impacts on Fiber Optic Measurements*. Submitted to Structural Concrete in December, 2021.

Text and figures have been adjusted to the format and layout of this thesis. The content remains identical. The literature used is jointly referred to at the end of the thesis.

Abstract

Strain and temperature measurements on reinforced concrete structures with Rayleigh-based FOS promise dense data networks of crucial structural parameters. In this context, the measurement of temperature and mechanical strain is invariably intertwined, precipitating in a frequency shift recorded via FOS. Consecutive experiments were carried out on reinforced concrete beams under mechanical, thermal, and thermo-mechanical loading. Basic analysis of fiber optics equations indicates the sensitivities toward both influences. These are quantified and juxtaposed in experiments, first separately and subsequently combined. As concerns temperature measurement, the slightest tensile forces exerted onto the FOS may engender distortions of several degrees Celsius. Conversely, strain measurements are affected by temperature changes to a lesser degree. Nevertheless, the level of strain to be sensed and the severity of corrupting temperature shifts must be carefully weighted. The article raises awareness for the coupling of temperature and strain and enables the practitioner to identify and assess perturbations.

4.1 Introduction

As with people, infrastructure is aging. Detecting the signs of the times in our structures as early as possible requires more than a keen eye. There is a wide range of approaches to monitoring structures, subsumed under the concept of Structural Health Monitoring. These range from classical electrical [131, 163, 164], to acoustic [167, 203], to fiber optic methods [5, 6, 157]. Fiber optic sensors (FOS) offer the advantage of measuring strain [58] and temperature [64, 181] at a pitch of less than one millimeter and high frequency over a length of tens of meters [153, 161]. These advantages have qualified fiber optics not only for practical research (e.g., [56, 142]) but also for investigations with basic research underpinnings [66, 99, 195]. In addition to applications in civil engineering, this technique is gaining traction in other disciplines such as geotechnics [97], hydrology [169], and tunneling [130]. Unlike strain measurement, temperatures are rarely measured in applications involving FOS [117, 119, 144, 184].

FOS simultaneously respond to strain and temperature changes. Both effects are coupled. This inherent property, which appears to be an advantage at first glance, implies a challenge in FOS application. Depending on the task, one measured variable, i.e., strain or temperature, must be isolated. For temperature measurements, sensors are mechanically decoupled. Residual strain not decoupled, e.g., due to friction, may falsify temperature measurement. In contrast to laboratory tests, temperature changes during the diurnal or annual cycle are constitutive elements of practice contexts. This natural temperature change must be recorded and eliminated from analysis in structural applications. To such ends, a supplemental FOS is commonly employed in order to compensate for temperature effects.

The engineer must deal with such corrupting cross-effects (temperatures in strain measurements and strains in temperature measurements). As mentioned above, one option consists of compensating for them in strain measurements. An alternative course of action lies in quantifying the corrupting temperature shift and, if necessary, estimating and accepting an error. In either case, detailed knowledge of the extent of strain and temperature coupling is required to apply the technique deliberately.

This is where this article comes in. First, necessary explanations of the temperature and

strain calculations from the initially measured frequency shift are given. Then, three own experiments (mechanical, thermal and thermo-mechanical loading of the test specimen) are outlined and evaluated. These experiments usher in the investigation of fiber optics with regards to the specific measurement of the primary influence and the quantification of the respective cross-effect.
As will be presented in the ensuing chapter, the *mechanical* test lays the foundation for this. The temperature influence is comparatively easy to minimize due to control over environmental conditions in the laboratory setting. In the *thermal* test setting, the interaction of temperature and strain can be deduced from the temperature recordings of the FOS. Cross-effects are detected and quantified. Finally, the thermo-mechanical test serves to ascertain the corrupting impact of temperature on strain measurements.

4.2 Fiber Optics

The technological antecedent to the quasi-continuous measurement offered by FOS lies in the distributed measuring technique of fiber Bragg grating (FBG) sensors [84, 96, 105, 112]. The fiber's material (the refractive index) is changed at a singular point (Bragg grating) using UV radiation. Consequently, employing measurements of the reflected light's wavelength λ at said point (or its change $\Delta\lambda$), strains $\Delta\varepsilon$ or temperature changes ΔT can be calculated. The strain response (Equation 4.1) results from both the physical elongation affecting the sensor and the change in refractive index due to photoelastic effects ($(n^2/2)\cdot p_\mathrm{e}$). The thermal response results from the inherent thermal expansion of the fiber material (α) and the temperature dependence of the refractive index ($(\mathrm{d}n/\mathrm{d}T)/n$). [4, 96, 128]

$$\frac{\Delta\lambda}{\lambda} = \left[1 - \left(\frac{n^2}{2}\right)\cdot p_\mathrm{e}\right]\Delta\varepsilon + \cdots \left[\alpha + \frac{\frac{\mathrm{d}n}{\mathrm{d}T}}{n}\right]\Delta T \quad (4.1)$$

with:

$\Delta\lambda$	Shift in Bragg wavelength, [nm]
λ	Bragg wavelength, [nm]
n	Refractive index
p_e	Photoelastic coefficient
$\Delta\varepsilon$	Strain change, [$\mu\varepsilon$]
α	Coefficient of thermal expansion
ΔT	Temperature change, [°C]

In the quasi-continuous measurement system employed here [153], i.e., FOS, a laser directs light into glass fiber. Microscopic imperfections of the glass caused by melting during its production process lead to slight variations of the refractive index along the fiber [47, 48]. The resulting Rayleigh backscatter of the emitted light is measured. The signal contains location-dependent frequencies that rise with increasing distance from the detector (measuring system) [161].
Analogous to the measured wavelength shift in FBG sensors ($\Delta\lambda/\lambda$), with FOS, changes in temperature and strain lead to a frequency shift ($\Delta\nu/\nu$) [161]. In most practical cases, the effects of temperature and strain will dominate the spectral response of Rayleigh backscatter [121, 122]. Nevertheless, the measurement results are additionally affected—although to a lesser extent—by environmental conditions such as pressure, humidity, and electromagnetic fields [104]. The similarity of FBG and quasi-continuous FOS approaches may be demonstrated in mathematical expressions. When the terms in brackets of Equation 4.1 (FBG) are transformed into constants and the wavelength (shift) is replaced by the frequency (shift), Equation 4.2 (FOS) is obtained,

which is well known from quasi-continuous metrology:

$$-\frac{\Delta\nu}{\nu} = K_\varepsilon \cdot \Delta\varepsilon + K_\mathrm{T} \cdot \Delta T \tag{4.2}$$

with:

$\Delta\nu$	Frequency shift, [GHz]
ν	Mean optical frequency, [GHz]
$K_\mathrm{T} = 6.45 \cdot 10^{-6}$	Temperature coefficient, [1/°C]
$K_\varepsilon = 0.78 \cdot 10^{-6}$	Strain coefficient, [1/$\mu\varepsilon$]

By mathematical conversion and the introduction of the relationship between the frequency ν, wavelength λ and velocity c, we obtain:

$$\begin{aligned} \Delta\nu &= -\left[\frac{K_\mathrm{T} \cdot c}{\lambda} \cdot \Delta T + \frac{K_\varepsilon \cdot c}{\lambda} \cdot \Delta\varepsilon\right] \\ &= \frac{1}{k_\mathrm{T}} \cdot \Delta T + \frac{1}{k_\varepsilon} \cdot \Delta\varepsilon \end{aligned} \tag{4.3}$$

with:

$\nu = \frac{c}{\lambda}$

c	Speed of light, [m/s]
λ	Mean optical wavelength, [nm]
$k_\mathrm{T} = -\frac{\lambda}{K_\mathrm{T} \cdot c} = -0.638$	Conversion factor, [°C/GHz]
$k_\varepsilon = -\frac{\lambda}{K_\varepsilon \cdot c} = -6.67$	Conversion factor, [$\mu\varepsilon$/GHz]

Equations 4.1 and 4.2 as well as Figure 4.1 illustrate the duality, i.e., the coupling of the influences—changes in strain and temperature. The effect of both influences considered (a) separately and (b) in combination leads to a change in frequency shift. A comparison of conversion factors elucidates to the different weighting of the two influences with respect to the frequency shift. Their coupling means that as soon as temperature and strain influences are present simultaneously, additional steps for making inferences as to each individual factor are rendered necessary.

In this vein, available mathematical approaches are suggested by [4, 59]. A convenient solution is the separate isolated measurement of temperatures using an additional fiber. For strain measurement, the FOS is mechanically coupled to the desired component (usually by bonding). In addition to mechanical strain, this sensor simultaneously measures elongation due to temperature (mixing effects). A second sensor, which does not pick up any strain due to its freely movable position in a tube, ideally solely measures temperature-related frequency shifts. The latter result is finally subtracted from the mixed frequency shift. The result is a temperature-compensated strain measurement.

The right part of Equation 4.3 can be transformed to calculate strain (Equation 4.4) or temperature (Equation 4.5). Usually, it is assumed that the respective other influence has ideally been excluded and is therefore equal to 0. However, the rear term of Equations 4.4 and 4.5 can quantify how far the target measurand is influenced by the respective other quantities (cross-effect).

An indication of this is provided by the ratio $k_\varepsilon/k_\mathrm{T}$ or $k_\mathrm{T}/k_\varepsilon$. In Sections 4.4.3 and 4.4.4 this cross-effect in the measurements will be discussed in more detail.

$$\Delta\varepsilon = k_\varepsilon \cdot \Delta\nu - \frac{k_\varepsilon}{k_\mathrm{T}} \cdot \Delta T \tag{4.4}$$

$$\text{with}: \quad \frac{k_\varepsilon}{k_\mathrm{T}} \approx 10\,[\mu\varepsilon/^\circ\mathrm{C}]$$

$$\Delta T = k_\mathrm{T} \cdot \Delta\nu - \frac{k_\mathrm{T}}{k_\varepsilon} \cdot \Delta\varepsilon \tag{4.5}$$

$$\text{with}: \quad \frac{k_\mathrm{T}}{k_\varepsilon} \approx \frac{1}{10}\,[^\circ\mathrm{C}/\mu\varepsilon]$$

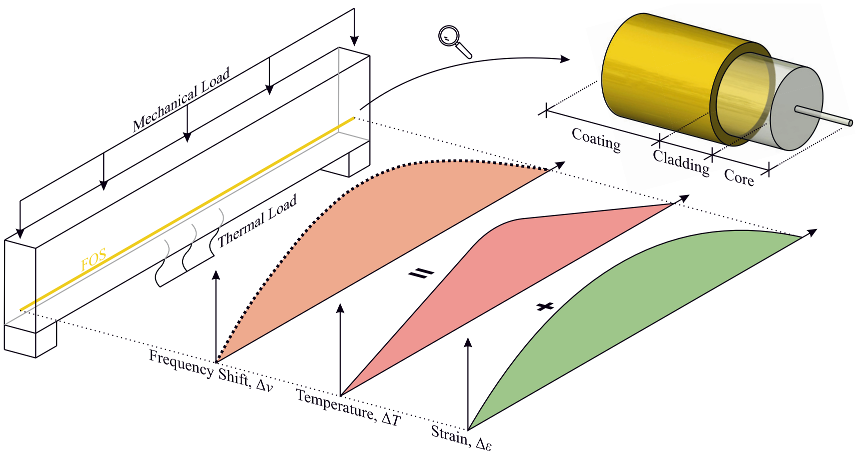

Figure 4.1: Temperature and strain changes induce frequency shift

Equation 4.5, in principle, emphasizes a linear dependence of the temperature on the frequency shift scaled with the factor k_T. In [121, 122] however, a 4th order polynomial approach according to Equation 4.6 is recommended for temperature measurements. Since the relationship between the frequency shift and temperature must be established individually in each application, an accompanying temperature measurement is necessary. Linear regression is then used to find the coefficients β_0 to β_4 that best represent the model of temperature change in a least-squares fashion. β_0 represents the ambient temperature, while the regression coefficient of the linear term adapts the general manufacturer's data concerning k_T to the local conditions. Lastly, the remaining coefficients capture potential higher-order components.

$$\Delta T = \beta_0 + \beta_1 \cdot \Delta\nu + \beta_2 \cdot \Delta\nu^2 + \cdots \\ \beta_3 \cdot \Delta\nu^3 + \beta_4 \cdot \Delta\nu^4 \quad (4.6)$$

4.3 Experiments

4.3.1 Specimens

The objective is to investigate fiber optic measurement technology subjected to coupled thermo-mechanical influences. Following the principle of One-Factor-At-A-Time (OFAT), the effects on the test specimen—mechanical and thermal—are initially examined individually and later in combination. Hence, a total of three tests were performed on two test specimens. In contrast to the mechanical test conducted with the first test specimen, the thermal test on the second one is non-destructive. This allows for an additional experiment to be carried out on the same sample body. A mechanical load follows the initial purely thermal test once a thermal steady state is reached—the thermo-mechanical test results from the loading in the heated state.
Two reinforced concrete (RC) beams with identical external dimensions ($w \times d \times L = 0.25 \times 0.50 \times 3.9$ [m]) and reinforcement layout (flexu-

ral reinforcement 3 Ø 20 mm, structural reinforcement 2 Ø 8 mm and stirrups Ø 12 mm / 30 cm / 2) are fabricated. In the mechanical as well as in the later thermo-mechanical test, the specimens (see Figure 4.2) are loaded by two concentrated loads under four-point bending. With a span of $L_{\text{eff}} = 3.5$ m and a distance between the concentrated loads of 1.2 m, a constant bending moment is generated in the area between.

In analogy to this constant load, the second test specimen is heated to approx. 40 °C in its middle section on both the upper and lower side. The heat is induced via two heating mats ([89]) with a length of 1.0 m and a width of 0.25 m (see Figure 4.2, marked in red). In [27], among other methods, this technique for temperature induction was investigated: the low weight but especially their high flexibility regarding deformations qualifies the heating mats for this application. In order to separate the test specimen to be heated from the colder outside air, it was completely encased in polystyrene of 20 cm thickness. Merely the locations of support and later load application were omitted and designed in such manner that deflection during later loading is rendered possible in unhindered fashion.

4.3.2 Sensor Placement and Installation

Placement

Throughout the experiments, the targeted quantities, i.e., strain and temperature, are recorded. Strain gauges and FOS were used to record strain, and thermocouples (TC) and FOS were used to record temperature. Figure 4.3 shows the consistent sensor placement for the experiments.

During mechanical testing, FOS 1 and 2 measure the concrete strains along a lateral surface. Here, they are glued on. Expecting a linear strain profile over the depth of the specimen due to the (constant) bending moment, the FOS were placed in the direction of the beam's longitudinal axis and staggered over its depth. The loops result in nine layers (e.g., FOS 1 and 2 in Fig. 4.3). Strain measurements varies significantly along the body's length due to concrete cracking and are therefore recorded in finely grained millime-

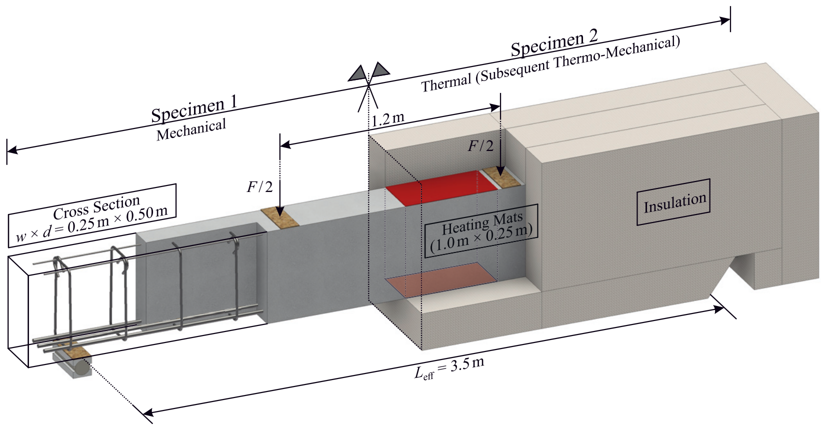

Figure 4.2: Test specimens for the mechanical, thermal and thermo-mechanical tests

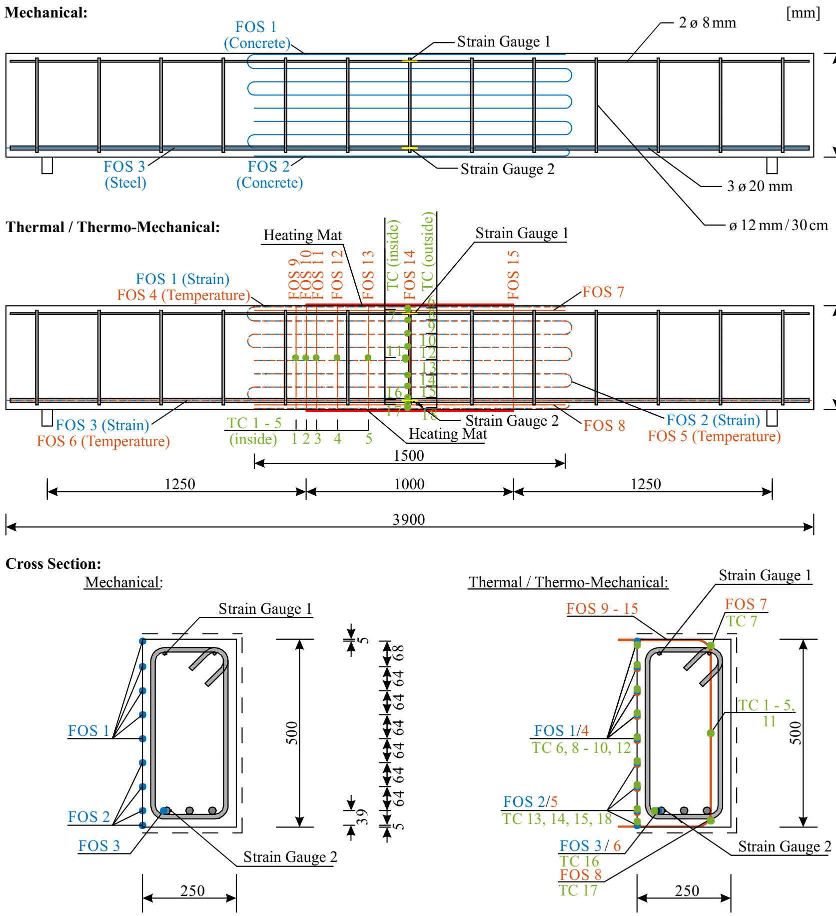

Figure 4.3: Geometry, reinforcement and sensor layout

ter range intervals (0.65 mm spacing of the measuring points). Conversely, strain measurements along the body's depth (e.g., FOS 1 & 2) vary less intensely, allowing for a coarser gradation and more space between measuring points. Finally, FOS 3 measures the strain of the reinforcing steel. For reference, strain gauges were attached to the reinforcing steel (top and bottom) in the middle section of the specimen.

In order to only record the temperatures in the thermal test, FOS 7 and 8 were placed horizontally and FOS 9 to 15 vertically in the specimen. These FOS are guided through plastic capillaries inside the specimen as to avoid tensile forces. Their insertion is oriented along the points at which the largest temperature changes in the beam are to be expected.

Since the optical fibers always detect strain and temperature changes simultaneously, measuring strain requires quantifying the corrupting cross-effect exerted by temperature shifts. Hence, installing a separate fiber recording temperature only allows for temperature compensation. Said FOS is placed directly next to the fiber for strain measurement. Parallel to FOS 1 to 3 for the strain measurement from the mechanical test, the capillary-guided FOS 4 to 6 are added in the thermo-mechanical test. They can be used to compensate for the corrupting temperature cross-effects in the strain measurement values (cf. Section 4.2).

In addition to the 15 FOS, 18 thermocouples are installed. Except for the looped FOS 4 and 6, they are always located in the center of the sensor. For these two, however, one thermocouple is placed in the center of each layer. Table 4.1 links the individual FOS and TC and assigns their numbering to the experiments.

Beyond the fiber optics and conventional measurement techniques (strain gauges and thermocouples), the spackle pattern for digital image correlation (DIC) is added to the opposite lateral surface (opposite to the surface shown in Figure 4.3). Although the results of this measurement technique are not part of the following analysis, their collection nevertheless influences the experimental procedure. The load increase must be gradual. At each level, the test is stopped, the insulation is opened, a photo is taken and the insulation is closed again.

Installation

The FOS must be firmly bonded to the concrete component for strain measurement. As described in [25], the Polytec PT AC2411 adhesive is suitable for this purpose. First, a longitudinal groove is milled into the rebars. Afterward, the FOS is bonded into this groove. The FOS leaves this

Table 4.1: Objectives of the individual FOS

Test	FOS Strain	FOS for Temperature Compensation	FOS Temperature	TC Temperature
Mechanical	1 2 3			
Thermal			7 8 9 10 11 12 13 14 15	7 17 1 2 3 4 5 11
+ Mechanical	1 2 3	4 5 6		6 / 8 / 9 / 10 / 12 13 / 14 / 15 / 18 16

groove at each end of the rebar and is guided out of the formwork. These areas (from the point where it leaves the rebar until it is completely guided out of the formwork) are protected by plastic capillaries. The fibers coming out of the formwork then lead into tubes outside the formwork and are thus protected (see Figure 4.4, left). After curing, FOS 1 and 2 are bonded to the surface of the concrete specimen in loops as described in [100] in Figure 4.3 to record the strain field.

To measure temperatures with FOS, they are either installed in plastic capillaries and (a) glued on or (b) embedded directly in concrete (see Figure 4.4, right). The FOS remain freely movable within the capillaries when installed (e.g., after concreting). Employing this technique, encapsulating and thereby protecting the FOS tasked with only measuring temperature, strain transfer from the component into the fiber, which would here constitute a corrupting cross-effect, is avoided. For referencing and later calibration (see Section 4.4.3) of the temperature measurements of the FOS, thermocouples (see Figure 4.4, right) are attached to the capillaries.

4.3.3 Test Set-Up and Experimental Procedure

The test specimens are loaded externally by four-point bending. As shown in Figure 4.5, a load induction traverse spreads the force of the servo-hydraulic cylinder evenly over the two load application points. DIC measurements are carried out in conjunction with the fiber optical and conventional measurements. The thermo-mechanical test requires a gradual increase in load and interruption at regular intervals to remove the insulation in front of the speckle pattern. Following the capture of the photos, the insulation is closed again, the load is further increased, and the process is repeated. On the other hand, in the mechanical test, the DIC measurement takes place continuously with a permanently unobstructed view as no insulation is required.

The first test specimen is subjected to load-controlled force in the mechanical test, increasing across gradual 5 kN steps initially until 100 kN is reached, and ensuingly 10 kN steps until reinforcement yielding occurs at a load of approx. 330 kN. The second test specimen is subjected

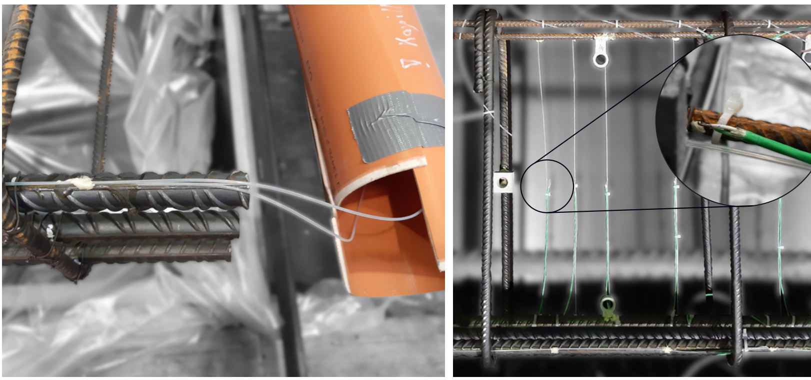

Figure 4.4: Left: Protection of the FOS in capillaries and pipes for concreting, right: mounting of the FOS and thermocouples

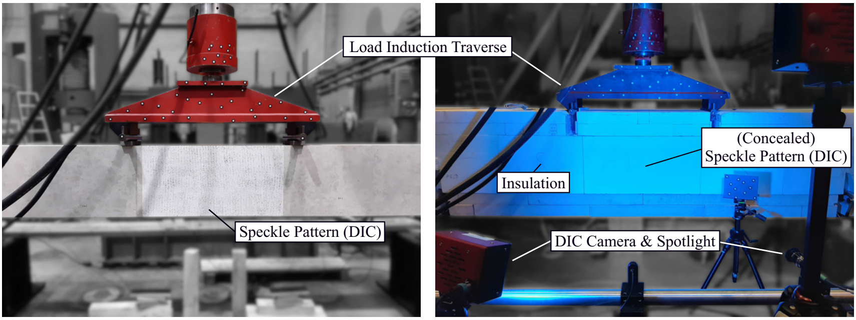

Figure 4.5: Set-up of the mechanical (left) and the thermo-mechanical (thermal) test (right)

to 40 °C in the thermal test on the top and bottom sides (see Figure 4.2). This temperature is maintained for seven days (168 h) until a thermal steady state is reached in the interior. Subsequently, the test specimen is subjected to a stepwise loading procedure identical to the purely mechanical test.

4.3.4 General Results

FOS 1 and 2 are attached in loops to the lateral surface of the first test specimen (mechanical test). Only the longitudinal sections of these FOS are considered in the evaluations. In accordance with Figure 4.3, there are nine layers along the depth. In these nine sections, a strain measurement is recorded every 0.65 mm of the fiber. Consequently, measured values are obtained on nine levels of the specimen, every 0.65 mm. These measured values can be processed as a two-dimensional strain field, as shown in Figure 4.6 on the top. In order to display the strain field over the entire depth (0.5 m), the boundary values are extrapolated (from the uppermost or lowermost level, extrapolation length: 5 mm).

The red regions represent the compression zone and the light blue ones the tension zone of the beam under applied loading. Dark blue areas indicate cracks. A black line delimits the compression zone. This represents the zero crossing between compressive and tensile strains over the depth. Due to the coordinate system starting at the top of the bar (depth [d] increases towards the bottom), the black line simultaneously indicates the compression zone height.

It is evident that compressive strains (or stresses) occur at the top and tensile strains at the bottom, corresponding to the positive bending moment. As expected, the cracks (dark blue) form in the tension zone. They form in regular intervals of about 30 cm and grow or propagate from bottom to top. The largest crack in the center at about 2.0 m already slightly reduces the compression zone height. This can be seen by the smaller red region in the vicinity and the black line moving upward in Figure 4.6.

It should be noted that the width of the dark blue area does not indicate the crack widths. The relative displacement of the crack edges (originating from zero in the uncracked state) locally leads to high strains, which are also carried into neighboring parts due to a certain softness of the adhesive of the FOS. Further details can be found in [25, 26].

The lower section of Figure 4.6 exhibits the mea-

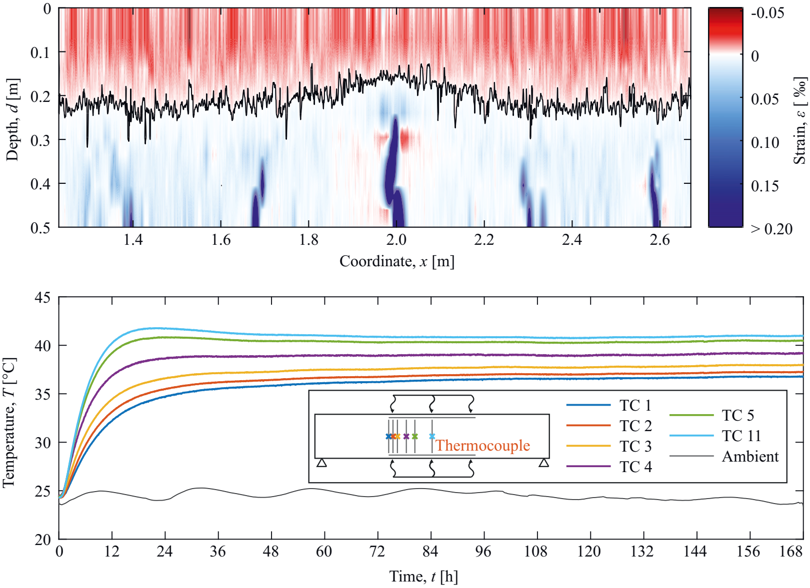

Figure 4.6: Strain field derived from the nine levels of FOS 1 and 2, bottom: temperature development in the thermal test

sured temperatures of the TC 1 to 5 and 11, as well as the ambient temperature. It is to be pointed out that the heating has taken place over 168 h. In the first 12 h, the temperature measured at all TC locations increases sharply. From about 36 to 48 h, on the other hand, hardly any temperature change can be seen. The small fluctuations in the ambient temperature obviously do not affect the component temperature.

Comparison of the thermocouples indicates that the highest temperature is consistently measured in the center of the test specimen (TC 11). The measured temperatures decrease towards the beam's longitudinal end faces, where most temperature loss occurs. Toward both end faces, the influence of the non-tempered areas increases.

Overall, the curves (Fig. 4.6 bottom) run affine to each other and consolidate at a constant level after 36 to 48 hours. After 168 hours, the load increase occurs as part of the thermo-mechanical test.

4.4 Individual Impacts and Interaction

4.4.1 Preface to the Discussion

Parallel to the mechanical, thermal, thermo-mechanical tests (themselves), a discussion of said scenarios is presented separately in the ensuing subchapters. In the laboratory, purely mechanical testing against unintended temperature changes is easier to achieve than vice versa. Not only do controlled environmental conditions (e.g., solar radiation or air temperature) limit its influence but also the inertia of thermal conduction of concrete contributes to it. However, solely measuring strain as an isolated quantity is a physical impossibility in real-life scenarios. Temperature changes are inherent to the diurnal cycle. Therefore, the explanations first address mechanical strains only and then transition to isolated temperature measurement with FOS. The interaction of targeted measurand and corrupting cross-effects in the thermal test are then analyzed. As a synthesis of said two preceding experiments, the concluding thermo-mechanical test comprises both temperature and strain, as well as their interaction. It provides information about the accuracy of strain measurements under the influence of temperature and enables a discussion of real application scenarios for FOS.

4.4.2 Mechanical Load

Figure 4.7 depicts the strain curves of the reinforcement under a load of 100 kN (left) and 300 kN (right). In both diagrams, the strain curve increases from the supports (end faces) to the center and displays some distinct peaks. In the load area between $x = 1.35$ m and 2.55 m, a plateau is formed despite further peaks. Each peak (local increase in strain in the reinforcement) indicates a crack in the concrete at this point. Here, the reinforcement has to absorb the force released by the cracking concrete. As a result, the strain increases locally by leaps and bounds.

For deformation computations of RC members in the cracked state, the average steel strain ε_{sm} (e.g., [29, 222]) can be formally calculated using the course of the reinforcing steel strain according to Equation 4.7.

$$\varepsilon_{\text{sm}} = \frac{1}{l_{\text{T}}} \int_0^{l_{\text{T}}} \varepsilon_{\text{s}}(x)\,\mathrm{d}x \tag{4.7}$$

with:

l_{T}	A transfer length of the released force from the reinforcement into the concrete
$\varepsilon_{\text{s}}(x)$	Steel strain

It is obtained by integrating the strain curve in

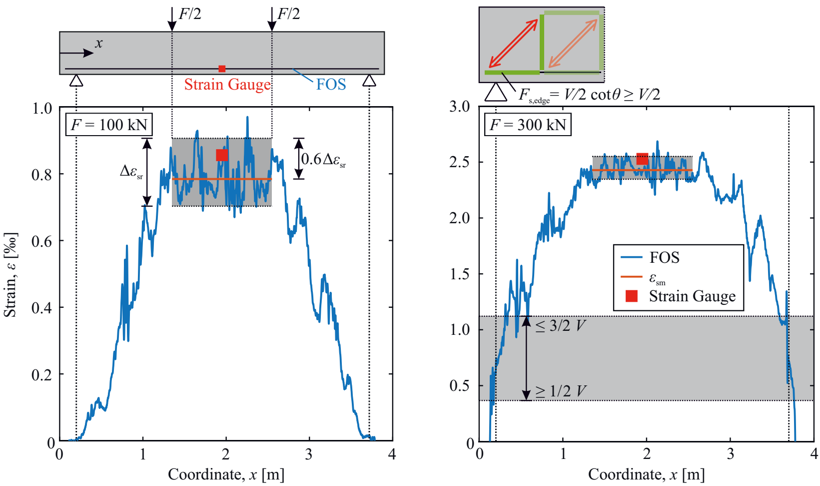

Figure 4.7: Strain measurement with FOS on the reinforcement for 100 kN (left) and 300 kN (right)

the affected area and is related to its length. Consequently, it idealizes this area via its average value as a constant. This is shown in Figure 4.7 (left and right) based on the fiber optic measurements between the concentrated loads ($x = 1.35$ to 2.55 m), i.e., the area of constant bending moment.

Furthermore, the strain increment in the reinforcement $\Delta\varepsilon_{sr}$ during cracking can be formally calculated according to Equation 4.8. It links the average steel strain, the strain in the crack as well as the strain increment.

$$\varepsilon_{sm} = \varepsilon_{s2} - \beta_t \cdot \Delta\varepsilon_{sr} \tag{4.8}$$

with:

ε_{s2}	Steel strain at the location of a crack
$\Delta\varepsilon_{sr}$	Steel strain increment due to cracking of the concrete

β_t is derived from the bond relationship between the reinforcement and the concrete and can be assumed to be 0.6 for short-term exposure to load [222]. If the average strain is thus raised or lowered, the maximum and minimum strain levels of the reinforcing steel shown in Figure 4.7 are obtained. The juxtaposition of both load levels depicted in Figure 4.7, underlines how the maximum and minimum levels are compatible with the measured strains.

The local strains detected by the strain gauges in the center of the reinforcement also coincide well with the curves of both loads (100 kN and 300 kN).

In addition, the right of Figure 4.7 shows that the strain at the supports (dashed line) does not decrease to 0. In cracked RC beams, a truss-like load-bearing behavior develops. In equilibrium, the applied force is transferred to the support by concrete compressive and steel tensile struts (the reinforcement). This results in a constant base level of strain at the support following, even if the corresponding bending moment at this location is equal to 0. Emanating from equilibrium considerations, it is to be deduced that the tensile force at said point always falls between:

$$\frac{V}{2} \cdot \cot(\theta) \geq F_{s,edge} \geq \frac{V}{2} \tag{4.9}$$

With the general restrictive range of compressive struts' inclination at approx. 18 ° to 45 °, the edge tensile force must settle between $3/2V$ and $1/2V$. Transformed into strain, these limits are plotted in Figure 4.7 on the right. The comparison again underlines that the measured values fall within the calculated edge tensile force limits.

4.4.3 Thermal Load

Figure 4.8 plots the temperature curves measured by FOS and TC at all eight measuring points over the full test duration of 168 h. The measuring points are the locations where the TC are attached to the corresponding FOS (cf. Figure 4.3 and Figure 4.4). To reiterate statements made earlier, all FOS only tasked with temperature measurement are guided in capillary fashion in plastic tubes, thereby avoiding contact between fiber and con-

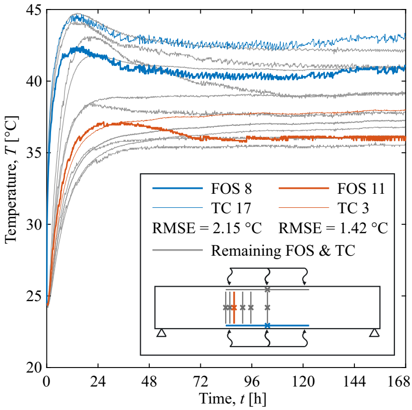

Figure 4.8: Temperature-time courses of FOS 8 and 11 paired with thermocouples 17 and 3

crete. Two selected pairs of curves without (FOS 8 / TC 17) and with (FOS 11 / TC 3) influence of moisture changes are highlighted in color. Especially the temperature curves of FOS 8 and TC 17 display affinity to each other. Nevertheless, an almost constant absolute temperature difference of approx. 2.5 °C can be observed.

For practical application, such offset must be eliminated. For this purpose, a scaling coefficient, i.e., conversion factor, adjusts the functional relationship between the temperature change ΔT and the actual measured variable frequency shift v according to Eq. 4.5 or Eq. 4.6.

In practice, such implies that the factor k_T offered by the general specifications of the fiber manufacturer (default) must be calibrated and specified for each individual test to produce accurate temperature measurements.

Mathematically, such is undertaken by linear regression [134], either simplified using the linear approach according to Eq. 4.5, or employing the 4th order polynomial approach according to Eq. 4.6. The latter offers greater flexibility and a more precise conversion. The computational power required for said regression is easily covered by modern tools. Therefore, said approach is used exclusively in the following.

Contrary to the pairing of FOS 8 and TC 17, a comparison of the trajectories of FOS 11 and TC 3 uncovers lesser degrees of similarity. Initially, both courses of temperature measurements are close to each other. However, in the time span between 36 h to 84 h, they diverge. Finally, beginning approx. at 84 h, they again show a quasi-constant offset of 1.5 °C from one another. While the unadulterated, more precise measurement temperature in TC 3 follows a constant after about 36 h, FOS 11 exhibits temperature changes during this period. Hence, fiber optic measurement must be influenced by another effect here. Said effect may reside in what may be coined parasitic strains, which stem from friction, e.g., an overly narrow bending radius, between FOS and plastic tube. However, differences in humidity or transverse pressure from compression are also known to influence, albeit to a lesser degree, the frequency shift [104, 121, 122]. The aging of the coating also exerts potential influence. In order to be able to exclude time-dependent reasons, the regression was therefore limited to the first 48 hours during which the deviations are consistently small. The calibration here is thus adapted for a short-term measurement scenario. If a long-term observation, e.g., while monitoring, is to be carried out, the exact influences corrupting must be accounted for to ensure.

The top section of Figure 4.9 depicts the regression of the data measured with TC and the frequency offset of the FOS utilizing the 4th order polynomial approach. Measures of determination close to 1 and low RMSE prove the high quality of the conversion. In both cases, the graphs follow a quasi-straight progression. The somewhat clearer curvature of TC 3 and FOS 11 demonstrates that a higher-order approach produces small gains in accuracy here.

The regression is performed for each fiber and the corresponding thermocouple. If the temperatures deduced from FOS frequency shift measurements are computed employing a conversion based on said new relationships, the temperature-time courses on the bottom of Figure 4.9. Resultingly, temperature measurements produced by respective TC and FOS pairings are almost congruent.

By means of an example, the temperature measurements produced by FOS 7 and 8 along the test specimen's central section are illustrated in Figure 4.10. Hence, FOS 7 and 8 (length of 1.20 m) extend 10 cm past the central section covered by the heating mat (length of 1 m). This is to ensure temperature detection for the entire heated

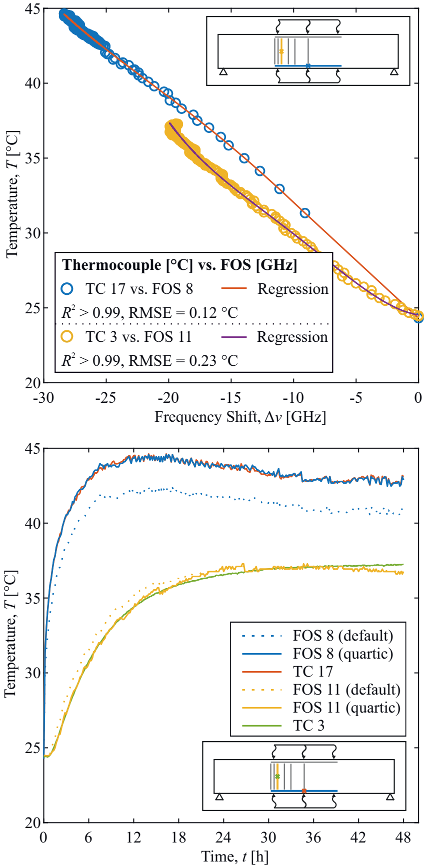

Figure 4.9: Temperature-time courses after regression of the frequency shifts to the actual temperatures

segment.

After two hours of heat exposure, areas of decreasing temperature appear toward the edges, resulting from the unavoidable heat loss into the non-tempered edge segments of the beam. While the course of FOS 8 already appears symmetrical to the center and suggests a plateau, the course of FOS 7 shows substantial deviations, especially on the left side. Moreover, less pronounced local deviations are evident on the right side. Due to the constant temperature field with uniform heating of the upper and lower side of the beam via the heating mat, the course of measurements produced by said fibers would a priori be expected to proceed in a congruent fashion. Said expectation is fulfilled when regarding the produced measurement curves of FOS 7 and 8 after 168 h of test duration (in the background, gray). However, since short-term measurements are prioritized here, it is necessary to discuss the reasons for potential deviations, to quantify their magnitude to be able to estimate the magnitude of error in the measurement.

Since the plot of FOS 8 after 2 h is largely as expected, it is the reference of an error estimate in Figure 4.10, right. For this purpose, it was first smoothed by robust linear regression, which fits each section of 160 measured values with a 2nd order polynomial and reduces the inherent measurement scatter. It was then shifted in the axis of symmetry to the center of the field and brought into agreement with the course of FOS 7. This ensures that only local residuals remain and global deviations, e.g., due to non-uniform heating of the top and bottom surfaces throughout the measurement range, are eliminated. In Figure 4.10, bottom right, this residual was finally transformed into strain using the known relationships via the frequency shift and projected onto the gauge length.

This residual strain is interpreted as a parasitic strain, which is not due to temperature influences. Rather, its origin is assumed to be unplanned influences such as friction between the FOS and the capillaries, bending radii that are too tight, or strain induced by deformations of the component. In the case of friction, they can build up over time and also degrade, e.g., due to post-slip. It

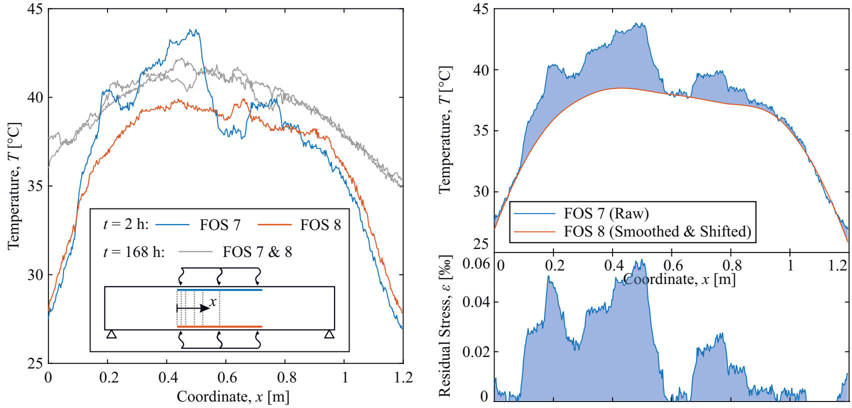

Figure 4.10: Left: strain affected temperature readings of FOS 7 and 8, right: residual strains in FOS 7 impair temperature readings

would be wrong to interpret the size of the residual strain as temperature. The maximum value is 0.06 ‰ at the point $x = 0.5$ m, which corresponds to the temperature deviation of 6 °C in the diagram above.

To improve the classification of the magnitude, the residual strain can be converted further into a force acting on the fiber. If, for the sake of simplicity, the polyimide coating ($E = 2{,}400$ N/mm^2), which is significantly softer than the core and cladding (silicate glass: $E = 73{,}000$ N/mm^2), is according to [7, 128] neglected, force of only 0.05 N results employing a fiber diameter of 0.125 mm. This corresponds to a weight of approx. 5 g. Even said minimal force leads to an error of approx. 6 °C, consequently, larger forces to correspondingly larger errors.

4.4.4 Combined Thermo-Mechanical Load

In principle, thermo-mechanical tests can be carried out in two ways. On the one hand, actions are applied one after the other, as in this case. First, the influence of temperature and afterwards of mechanical load on the measurement can be examined. On the other hand, in terms of real-world application, the second possibility of a contemporary mixed load, as is usually the case on structures (e.g., traffic load and change of temperature in the diurnal cycle) is more representative. It presupposes that the effect of all influences and, if necessary, their interaction is known in advance to ensure a clear assignment of cause and effect. Otherwise, false conclusions might be drawn. The temperature error caused by even small parasitic strains was shown earlier.

Considering the inverse scenario, temperature errors are to be transformed into equivalent strain errors and evaluated. The central question remains, which findings result from this for the measurement practice.

For the DIC measurements, the load had to be increased stepwise in the thermo-mechanical test. The insulation was briefly removed at each load level on one side, a photo was taken, and the insulation was closed again. The effect of the repeated opening is revealed by the temperatures in Figure 4.11. Both TC 11 and TC 16 are located in the middle of the beam, TC 11 in the center, TC 16 at the edge in close proximity to the heating mats. The temperature in the interior is more affected by the multiple openings than near the edge. In the center (TC 11), a temperature difference of 0.8 °C accumulates. At the edge, the proximity to the heating mat results in only 0.2 °C.

To assess non-consideration of such temperature changes on strain measurements with FOS, the temperature changes were transformed from frequency shifts into strains via the known conversions. In Table 4.2, in addition to the maximum temperature drop due to the opening of the insulation of 0.8 °C, representative temperature differences in the diurnal cycle at structures in summer and winter are given for comparison purposes. The resulting strain error is small in all cases, which explains why strain measurements with FOS are practically much more common than temperature measurements. Their error potential due to mutual influence is much smaller.

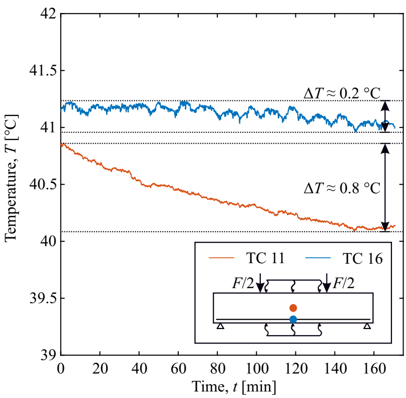

Figure 4.11: Development of temperature over time in the thermo-mechanical test

Table 4.2: Strain error due to temperature change

Residual Temperature [°C]	Strain Error [‰]
0.8	0.008
5 (winter)	0.05
12 (summer)	0.12

Before the start of the load increase, the strain measurement in the test was zeroed. Consequently, purely mechanically induced strains were measured in isolation. Previous temperature changes (in the thermal test), therefore, no longer play a role. Figure 4.12 shows such a strain measurement of the FOS 3 on the longitudinal reinforcement as a white line along the entire beam length. The strain errors listed in Table 4.2 are plotted as scatter bands around this line. The narrow white band indicates the scatter of the measurement due to the opening-based temperature change, the other gray bands those due to not taking into account hypothetical temperature changes in winter and summer, respectively. Even the more severe summer case ultimately affects the strain measurement only slightly.

For classification, this temperature-related strain scatter can first be compared with the measurement system's (Luna ODiSI 6108) accuracy specifications and the selected measurement mode (High Resolution, Gage pitch 0.65 mm) according to the manufacturer's specifications [153]. A total scatter of 0.047 ‰ is obtained from the sum of accuracy (±0.025 ‰) and repeatability (±0.022 ‰). This but also the absolute magnitude of the strain to be recorded is to be used for the evaluation.

A temperature-related deviation in strain of 0.008 ‰ (0.8 °C) accounts for only 20 % of the total uncertainty of the measurement system. At 5 °C unintended temperature change, the scatter

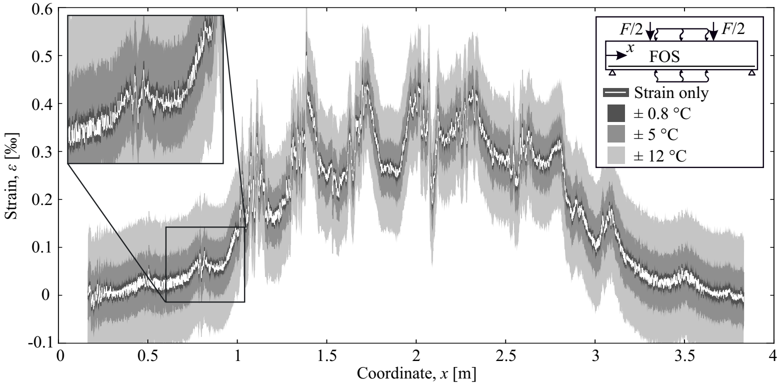

Figure 4.12: Reinforcement strains in the thermo-mechanical test along with scatter bands for residual temperatures of 0.8, 5 and 12 °C

is about as large as the total scatter of the measurement system, at 12 °C more than twice as large (see Table 4.3). In the worst case, errors from both scatter add up, the total scatter of the measuring system and from unintended temperature deviation, which in turn must be taken into account when determining the acceptable scatter size of the measurement.
In addition to the relative consideration, the absolute magnitude of the strain to be measured also determines whether such scatter plays a role or is negligible. An individual decision for each measurement task seems indispensable. Especially for RC, the considerations are complex. Normal strength concrete cracks at a tensile strain of about 0.1 ‰. A temperature error of 5 °C would account for 50 % of this strain. However, scatter of the same size has hardly any influence on the measurement or testing of the yield strain of reinforcing steel (2.5 ‰).

4.5 Conclusions

Rayleigh-based FOS measurements of RC structures promise fine-mesh data networks of substantial structural-mechanical quantities, i.e., strain and temperature. Such pertains to both laboratory and real-life application scenarios. With interest in the coupling and corrupting interplay of temperature and mechanical strain measurements, consecutively executed tests were carried out on RC beams under mechanical, thermal and thermo-mechanical loading, respectively. In addition to

Table 4.3: Comparison of deviations from unplanned temperature changes with characteristic strains [‰]

Strain Error from Temperature Change 0.8 °C	5 °C	12 °C	Measuring System Repeatability + Accuracy	Strain at Cracking of Concrete	Strain at Yielding of Reinforcement
0.008	0.05	0.12	0.047	0.1	2.5

general quality and plausibility checks of the measured quantities, the investigations focused on the mutual influence of strain and temperature. Both the influence of parasitic strain on temperature measurement and that of temperature variance on mechanical strain measurement could be quantified. Produced findings are in line with the theoretical magnitude of the cross-effects deduced from simplification and mathematical conversion of fundamental equations of fiber optics.
In more detail, the following could be ascertained and contributed:

- Under laboratory conditions, strain can be recorded in an isolated, precise and quasi-continuous manner in place and time using FOS. The quality is sufficient to identify average component strains for deformation measurements and to track strain transfer during cracking in the composite region. Residual strains and resulting residual tensile forces at the support are obtained within normatively justified limits and consistent with established model concepts.

- It was demonstrated how the conversion of FOS-produced measurements may be calibrated more precisely with the assistance of TC, so as to obtain high-resolution temperature measurements across structures.

- In temperature measurement, the significant corrupting influence of involuntary strain effects, e.g., from friction or contact, were emphasized.

- In absolute terms, the ratio of the conversion factors of temperature causes larger errors in strain measurement than the other way around (rule of thumb: 1 °C leads to strain deviations of 10 µstrain or 1 µstrain to 0.1 °C temperature deviation). This must be put into perspective for applications in practical construction since strain conventionally ranges between 100 to 1000 µstrain, whereas temperature changes only account for few °C.

- Even with capillary installation of FOS intended to isolate the temperature effect, parasitic strains of significant magnitude can occur. Even strain corresponding to a force of only 0.05 N (5 g weight force) produces temperature measurement adulterations of about 6 °C. This must be considered a key explanation as to why temperature is rarely measured employing Rayleigh-based fiber optic systems, as opposed to strain measurement contexts.

- Strain measurement in real-world scenarios must account for the corrupting influence of temperature. A temperature change of 5 °C (diurnal cycle winter) already reaches the order of magnitude of the general measurement accuracy of the fiber optic system. If the system accuracy and the temperature-related variance of 5 °C add up, cracking can no longer be detected reliably—entailing consequential implications for construction monitoring purposes. Since both temperature variance and system accuracy remain invariable across testing scenarios, their corrupting impact on the respective measurement scenario decreases in relative terms, with increasing strain levels.

- With respect to the highly complex material behavior of RC, the permissible error size must always be checked for the specific measurement context.

Chapter 5

Comparison of Experimentally Determined Two-Dimensional Strain Fields and Mapped Ultrasonic Data Processed by Coda Wave Interferometry

The following chapter is taken verbatim from:

> CLAUß, F.; EPPLE, N.; AHRENS, M. A.; NIEDERLEITHINGER, E. and MARK, P. *Comparison of Experimentally Determined Two-Dimensional Strain Fields and Mapped Ultrasonic Data Processed by Coda Wave Interferometry*. Sensors, 2020. 20(14): 4023. doi: 10.3390/s20144023.

Text and figures have been adjusted to the format and layout of this thesis. The content remains identical. The literature used is jointly referred to at the end of the thesis.

Abstract

Due to the high sensitivity of coda waves to the smallest structural alterations such as strain, humidity or temperature changes, ultrasonic waves are a valid means to examine entire structures employing networks of ultrasonic transducers. In order to substantiate this ex ante assessment, the viability of measuring ultrasonic waves as a valid point of reference and inference for structural changes is to be further scrutinized in this work. In order to investigate the influence of mechanical strain on ultrasonic signals, a four-point bending test was carried out on a reinforced concrete beam at Ruhr University Bochum. Thus, measurements collected from a network of selected transducer pairings arranged across the central, shear-free segment of the test specimen, were correlated to their respective strain fields. Detected ultrasonic signals were evaluated employing Coda Wave Interferometry. Such analysis comprised the initial non-cracked state as well as later stages with incremental crack depth and quantity. It was to ascertain that the test specimen can in fact be qualitatively compartmentalized into areas of compression and tension identified via relative velocity changes presented in attribute maps. However, since results did not entail a zero crossing, i.e., neither positive nor negative values were to be calculated, only relative changes in this work displayed staggered over the height of the object under test, are discussed. Under the given methodological premises, additional information is currently required to make quantitative assertions regarding this correlation of ultrasonic and strain results. This holds true for the comparability of the ultrasonic and strain results for both non-cracked and even the cracked state.

5.1 Introduction

With constantly growing traffic volumes, especially pertaining to cargo and heavy goods transport, putting increasing stress levels on an aging stock of transportation infrastructure (e.g., bridges [77, 116, 120]) and various changes in current standardizations looming large, calls for the development of a simple and comprehensive monitoring system are growing louder. Such a system, which must be designed for both new and existing structures, therefore needs to be able to carry out real-time damage assessments [143] in order to inform better-advised decision-making by public officials, for example, commissioning necessary strengthening of decaying structures. Ultrasound, as a signal that propagates through significant volumes or even entire structural elements, ushers in the possibility of achieving spatial results with a limited number of sources and receivers making it a potentially viable foundation for designing such versatile monitoring systems.

Ultrasonic (US) transmission measurements are in common use for determining local defects, for the assessment of freeze-thaw resistance, in concrete fatigue tests and even in monitoring load tests of pre-stressed bridge girders [139]. The assessment of freeze-thaw resistance is a common example for the evaluation of the direct wave (time of flight). By evaluating not only the first wave but also later arrivals—the coda—it is possible to take parts of the US signal under consideration that have interacted with larger areas of the concrete structure.

Because of inhomogeneities on the micro- and meso-level of concrete—like aggregates, pores or (micro-) cracks—the US signal is scattered multiple times and the wave is deflected from the direct path. By not only passing this direct path between a source and receiver, the coda contains information about an array of undergone volumes. It has been shown that stress, temperature [78, 165] and moisture modifications as well as (micro-) cracks affect the coda signal. Due to the aforementioned sensitivity of US signals to small changes in the structure to be examined, it is possible to investigate the relation between these deviations on the one, and variation of the latter segment of the signal, i.e., the coda, on the other hand. Based on these results, real time assessments [162, 164, 165] of civil engineering structures seem possible. Depending on the geometric spreading of the US signal, it may enable not only real time assessment of structures but even early detection of possible future weak points and determination of areas where maintenance is required.

Recently, Coda Wave Interferometry (CWI) [179], a technique originating from the field of seismology, was also applied to civil engineering problems. It is based on the comparison of a reference signal and a signal including a modification of one or multiple of the aforementioned factors. By using a two-dimensional network of transducers (in this context, devices that are able to both send and receive ultrasound), it is possible to aggregate single results and map them as plane fields (in the following, used interchangeably with areas or zones indicating the two-dimensionality of data).

Beyond strain gauges, other measurement techniques, such as Digital Image Correlation (DIC) or Fiber Optic Sensors (FOS) have emerged in recent years. These offer the opportunity of not only measuring strains at one specific point, but also of investigating overall structural behavior via more encompassing field-like zones. However, the characteristics of concrete—for example, little tensile strength and the emergence of cracks—complicate the evaluation further. Nonetheless, there are recent studies [56, 57] on calculating the crack width by integrating measured strains from FOS. Other research [182] has shown another advantage of this novel measuring technique so that the triaxial behavior of concrete can be further scrutinized via an adequate application of FOS. DIC, generating and contrasting photos of two-dimensional character, initially produces data on deformation fields, which subsequently provide the basis for computing strain fields. In contrast to these results, strains detected via FOS are initially measured solely along the fiber itself and therefore have to be pre-processed in order to generate areal, plane data for distinguishing between zones of, for example, compression or tension.

In this work, an experiment on a reinforced concrete (RC) beam subjected to four-point bending is presented. In addition to a network of US transducers, the test specimen was equipped with different, aforementioned techniques for strain measurement. Hereby, the focus lies on results produced by DIC and FOS. The calculated two-dimensional strain fields will be compared to mapped US data. For this purpose, CWI methodology was applied with a stepwise reference.

5.2 Principles of Measuring Methods

5.2.1 Strain Measurements

Fiber Optic Sensors

Fiber optic devices enable detection of strain or temperature changes by evaluating the backscattering of an induced light beam in the fiber under test. Apart from the Rayleigh component of the backscattering, one can distinguish between Brillouin and Raman backscattering. As the fiber optic device employed here utilizes Rayleigh backscattering, further explanations will here be limited to this very component.

Rayleigh backscattering can be attributed to quasi-stationary entropy fluctuations of anisotropic molecules [86]. Thus, when a light beam is emitted into a glass fiber, Rayleigh backscattering, which is hence caused by the variable refractive index along the fiber, is recorded by detectors in the fiber optic device. This measurement is done once in a reference state, such as the unloaded state, and during loading as shown in Figure 5.1. Two emerging signals result from this procedure. By performing a Fast Fourier Transformation, the two signals are converted into a frequency domain and afterward evaluated in smaller windows. The frequency shift Δf in an evaluation window can be related directly to the change in strain $\Delta\varepsilon$ and simultaneously in temperature ΔT, employing the coefficient of expansion K_ε and temperature K_T, respectively, as well as the center wavelength λ and c the speed of light [124].

$$\Delta\varepsilon \cdot \left[-\frac{c \cdot K_\varepsilon}{\lambda}\right] + \Delta T \cdot \left[-\frac{c \cdot K_\mathrm{T}}{\lambda}\right] = \Delta f \quad (5.1)$$

As stated and depicted in Equation 5.1, frequency shifts are caused by a change in temperature as well as in strain. Therefore, one of these effects has to remain constant or has to be controlled by a second measurement. The values of the coefficients K_ε and K_T depend on the doping level of the fiber core as well as, to a lesser degree, on the composition of the cladding and coating [124]. The strain coefficient is, by a power of ten, greater than the temperature coefficient. This demonstrates that a small temperature change during a strain measurement is of minor importance. Conversely, a change in strain during a temperature measurement can lead to skewed results. It is here to be noted that the approach using a linear relationship between temperature and strain is simplified and should only be used for pure strain measurements. For real temperature measurements, a quartic polynomial is preferable, to be chosen according to [122]. Further sophisticated remarks on the application of FOS to test specimens can be found in [100].

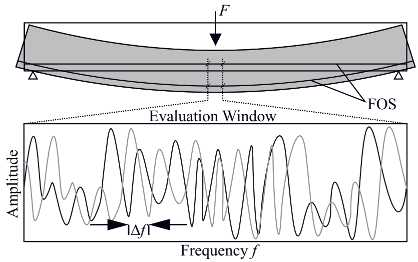

Figure 5.1: Frequency shift in the evaluation window caused by an exemplary loading.

Digital Image Correlation

With DIC, surface strains can be calculated from detailed photos of a test specimen. Hence, a preferentially random speckle pattern is sprayed on the surface of interest. As shown in Figure 5.2, the speckle pattern is then divided into squares (i.e., facets) on the pixel level. These facets are the basis for the calculation of displacements (at each facet) and strains for a meta area. Dividing the speckle pattern into facets results in matrices consisting of $n_\mathrm{x} \times n_\mathrm{y}$ gray tones. Thus, a unique set of gray tones is assigned to the center of each facet. After the test specimen is deformed by an applied load, the facet experiences movement from the position it held prior to the application of loading—it is moved from its initial position. The aim is to retrieve the reference set of gray tones (reference facet) from the unloaded state, in the current, post-load image. During loading, each facet, and therefore its individual set of gray tones, can be shifted, rotated and slightly changed by modified light exposure at its updated position. For purposes of reducing complexity, however, the facet depicted in Figure 5.2

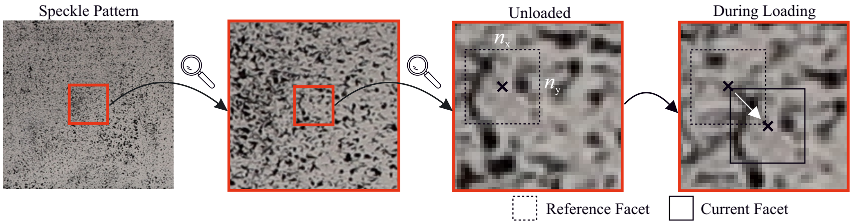

Figure 5.2: Speckle pattern and schematic representation of facet matching.

is only shifted. [65]

In facet matching, various factors such as shifting, rotation and perspective distortion of the facet itself or possible contrast and lightning changes of the facet in its updated, potentially altered position have to be taken into consideration. Therefore the gray tone matrix of the reference facet $g_M(x_i, y_i)$ and a search matrix $g_{Si}(x_{it}, y_{it})$, which contains the current (loaded/transformed) facet, are interpolated to determine deformations smaller than one pixel. The application of the least squares method to these matrices leads to Equation 5.2 [65, 208]. The coefficients r_0 and r_1 describe the relative camera offset and relative camera gain, respectively.

$$\min \sum_{i=1}^{n} |g_M(x_i, y_i) - \cdots \\ (r_0 + r_1 \cdot g_{Si}(x_{it}, y_{it}))|^2 \quad (5.2)$$

Facet matching determines the displacement of each facet center. Using the deformation results from the direct vicinity of each point, strain can be calculated for a meta area.

5.2.2 Ultrasound

The wave speed of an acoustic wave is an inherent property of the medium. While under constant conditions, wave speed—and in fact the entire waveform—of a repeated US measurement should not change at all, changes in the medium, for example, compression, tension or cracking, will however influence parameters like velocity, phase or attenuation. To detect these changes, most state-of-the-art US Non-Destructive Testing (NDT) methods use the first arrival of the direct, ballistic waves between source and receiver. In contrast, CWI uses the later segments, i.e., the coda, of the US recording to determine differences between repeated measurements and calculate velocity changes. Multiply scattered coda waves spend more time in the medium and sense a larger area before they are recorded at the receiver. Such behavior is illustrated in Figure 5.3. While the first, ballistic waves only record changes on the direct path, coda waves have sensed a wider area by the time they reach the receiver. This area—or the area a measurement is sensitive to—can be described by the sensitivity kernel for all times t_n after the source excitation [145]. Therefore, subtle changes in the sensitive zones between and around source and receiver, which would not influence the direct wave investigated in standard NDT-US measurements, can be captured.

In Figure 5.4, the influence of a small load on an US measurement using embedded transducers in a concrete beam is demonstrated. While there is no obvious change visible when looking at the entire recording and while the first arrival and early section of the recording between 0 and 0.25 ms are not changing, a shift of peaks and troughs can

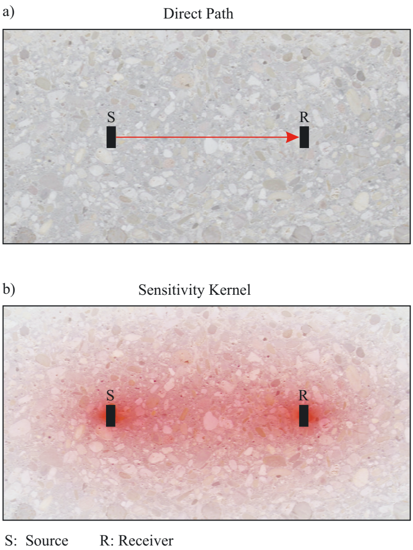

Figure 5.3: In classical US measurements, travel times are recorded and calculated via the ballistic waves. a) Ballistic wave between source and receiver. Using coda waves, changes of travel time within a larger segment, described by b) the sensitivity kernel (red), can be resolved.

be discerned in the coda.
This property is used in CWI to quantify changes in the sensed medium. The technique is based on a comparison of two recordings between the same sources and receivers at different times. As a measure for similarity between waveforms, the correlation coefficient (*CC*) is commonly used as follows:

$$CC(t) = \frac{\int_{\mathrm{T}} u_{\mathrm{u}}(t)\, u_{\mathrm{pt}}(t)\, \mathrm{d}t}{\sqrt{\int_{\mathrm{T}} u_{\mathrm{u}}^2(t)\, \mathrm{d}t \int_{\mathrm{T}} u_{\mathrm{pt}}^2(t)\, \mathrm{d}t}} \tag{5.3}$$

The unperturbed wave field u_{u} and the perturbed wave field u_{pt} are compared on a time interval T, where the resulting coefficient is $\{CC| -1 \leq CC \leq 1\}$. If u_{u} and u_{pt} are similar, CC will be close to 1. If they are similar but the phase is shifted by 180 degrees, it is close to -1. In the case of completely different waveforms, the coefficient is zero. As the *CC* is only a measure of similarity, velocity changes need to be calculated with more advanced operations. To such ends, two techniques for the determination of velocity changes are commonly applied. The first one, proposed in [154, 158, 180] compares the signals in small time windows and determines the time shift maximizing the *CC*. This time shift is linked to a relative velocity change ($dt/t = -dv/v$). The second technique, the so-called stretching technique introduced in [107, 115, 177], utilizes the larger parts of the coda on the interval between t_1 and t_2 to determine a stretching factor $\alpha = -dv/v$ rather than a time shift. Therefore, the unperturbed signal is stretched by α, which maximizes the *CC*.

$$CC(t,\alpha) = \frac{\int_{\mathrm{t_1}}^{t_2} u_{\mathrm{u}}(t(1-\alpha))}{\sqrt{\int_{\mathrm{t_1}}^{t_2} u_{\mathrm{u}}^2(t(1-\alpha))\, \mathrm{d}t}} \cdots \frac{u_{\mathrm{pt}}(t)\, \mathrm{d}t}{\int_{\mathrm{t_1}}^{t_2} u_{\mathrm{pt}}^2(t)\, \mathrm{d}t} \tag{5.4}$$

If only the overall velocity of propagation of the sensed medium changes, the US signal recorded after this change is a stretched (or compressed) copy of the original signal. Just the mean velocity but not the scattering properties changes. The α maximizing Equation 5.4 can then be linked to the apparent overall velocity change in the sensed medium. However, there is no direct link to a physical property. Since the latter technique has both produced robust results and been applied frequently in recent years ([139]), it will be applied in the analysis of the US measurements in this paper. In a monitoring set-up, where many consecutive measurements are evaluated, a reference measurement needs to be chosen. This reference can be static, for example, choosing

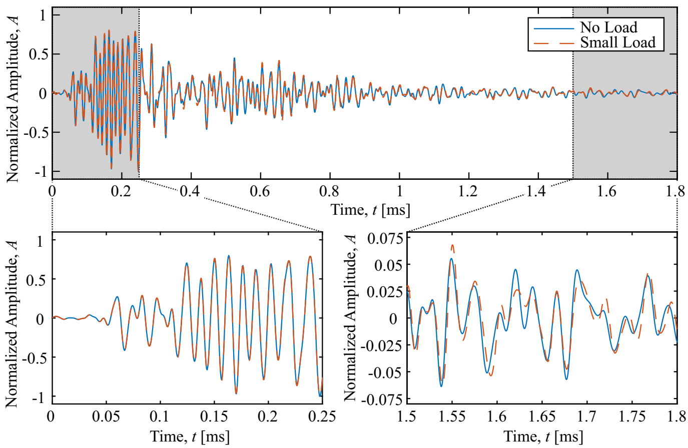

Figure 5.4: A comparison of measurements with embedded transducers in a concrete beam shows the small influence of subtle changes. While in the first arrivals (bottom left) no change is visible, small differences in the later coda part indicate a change in the specimen (bottom right).

the first measurement as the zero-state. dv/v and CC are then calculated with respect to this fixed-reference CWI signal. Alternatively (discussed in [139, 199]), the reference signal can also be changed in a stepwise fashion. This ensures a strong similarity of the compared signals—if no major damages occur—and is thus helpful in long-term experiments, as well as in experiments where the changes to the material are substantial and even destructive. While the fixed-reference method is computationally less expensive, it will fail to produce good results as to long-ranging experiments or experiments where the specimen is destroyed in many cases. If the correlation between two measurements is too small (< 0.7), the calculated dv/v will be unstable and have to be interpreted with caution. The dv/v calculated in the stepwise procedure can be accumulated and linked to the zero-state. A calculation of the total velocity changes throughout the whole experiment is possible, while the CC and dv/v calculations remain stable.

5.3 Experiments

5.3.1 Method of Investigation

As shown in Figure 5.3, the coda part of the US signal consists of information accumulated from sensing a larger undergone area. In the aforementioned CWI, an evaluation window is defined for which CC and dv/v are calculated. By choosing a relatively long evaluation window, for example, from 0.75 ms to 1.8 ms (cf. Figure 5.4), the results of the CWI are calculated as an integral over the full undergone volume.

In order to compare strain fields and US maps and with respect to the integration of results over larger areas, it is advisable to investigate an area with constant strains. Therefore, an RC beam subjected to four-point bending was determined as an appropriate testing specimen. Resulting from such a load scenario, a constant bending moment and thus likewise a constant strain state between the concentrated loads can be generated. Nevertheless, the general difference between static systems and real test set-ups likewise applies to the experiment at hand. Thus, in practice, there cannot be an ideal form of concentrated load induction for the areas underneath. On these grounds the transducers are placed at a distance of 130 mm in order to avoid said area, i.e., the area between an associated source and receiver pair. Furthermore, only the US transducers located between the two concentrated loads are selected and considered in later evaluations.

5.3.2 Test Set-Up

For the execution of such tests, an RC beam was cast at Ruhr University Bochum. Said beam was designed as to the dimensions of 150 mm / 400 mm / 2000 mm (b / h / l_{eff}), specifically suiting four-point bending. This entails a bending reinforcement of (2 Ø 16 mm) and stirrups (Ø 10 mm / 20 cm / 2). An additional constructive reinforcement (2 Ø 8 mm) was arranged in the compression zone. For simplified attachment of US transducers, the stirrups were also arranged in the shear-free zone between the two concentrated loads. The beam was concreted on the side surface, implying multiple benefits. Most notably, such a casting process generated a smooth surface for the DIC, allowed for a simplified handling of all sensors during concreting and contributed to better compaction of the test specimen. In addition to the test specimen, various concrete cubes and cylinders were made to determine the material properties in accompanying tests. All relevant parameters after 28 days of curing are summarized in Table 5.1.

Table 5.1: Material properties of the concrete.

$f_{\text{cm,cube}}$ [N/mm^2]	f_{ctm} [N/mm^2]	E_{cm} [N/mm^2]
35.0	2.5	28,618

In total, eight FOS were placed within the object under test. While one was applied on the bending reinforcement in a notch along the bar, the remaining sensors were attached on the side surface of the RC beam. Along with placements at characteristic heights, such as the upper and lower reinforcement, the remaining FOS were allocated staggered with equal clearance over the beam's height. Their precise positioning is to be found in Figure 5.5. Said FOS were glued onto the reinforcement steel as well as on the concrete utilizing a special epoxy resin. This particular adhesive had been examined in earlier experiments. It had thus become evident that this particular epoxy resin was indeed stiff enough to transfer the strain from concrete or steel directly into the fiber, while simultaneously displaying the benefit of smoothening the otherwise highly fluctuating measured strains.

An addition to the test beam consisted of initially applying white paint to a predetermined area, which, upon subsequently adding a black speckle pattern, was to enable DIC (a field of 1000 mm $\times$ 400 mm $= b \times h$) in latter stages of the experiment. For accuracy reasons, the two cameras were placed in immediate proximity (cf. Figure 5.6), as close as possible to the specimen in order to maximize pixel density.

Besides these strain sensors, US transducers were arranged in the central area of the beam forming a network structure. SO807 transducers from Acoustic Control Systems, Ltd. (Sarrebruck, Germany), with a central frequency of 60 kHz, are utilized. They consist of a piezoceramic cylinder with a diameter of 20 mm and a length of 35 mm. The radiation is characterized in [209], where it is shown that the US signal is emitted almost uniform in all directions of space. By employing small cement clips to position said

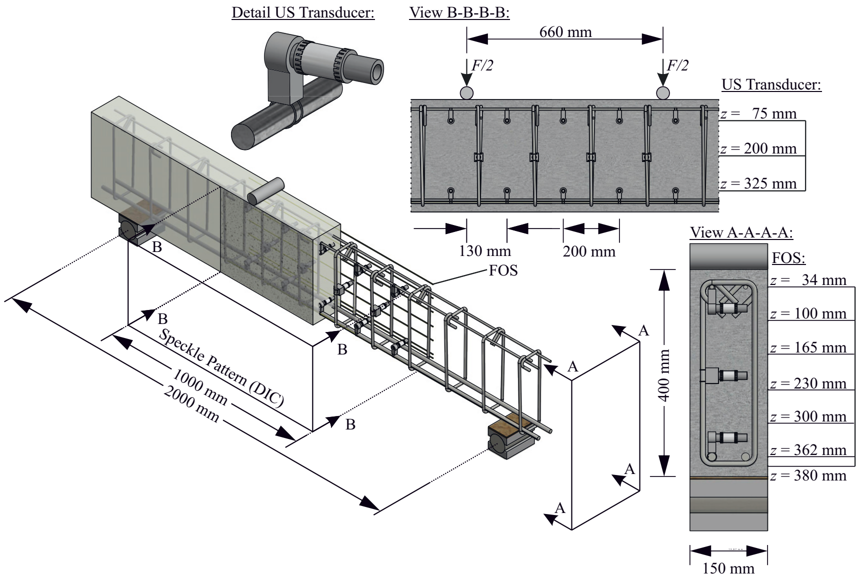

Figure 5.5: Model of the test specimen.

transducers, it was to be ensured that their direct surrounding was constituted by largely homogeneous material. Such clips, in contrast to plastic attachments, for example, exert minimal effect on wave propagation and crack formation during loading. The US transducers were thus in three levels arranged over the height of the RC beam. For the imaging to be applied later, 14 of them were allocated in the middle area of the beam. The transducers of the upper and lower level were attached to the bending or constructive reinforcement, respectively. Precisely between these two, the transducers of the central level were attached to the stirrups. By prior finite element analysis, regions were identified below the steel cylinders (employed to induce the concentrated loads in four-point bending—see Figure 5.5) where the principal stresses in the shear-free, central region are inclined (not horizontally orientated). Here, the stirrups and, in particular, the transducers of the upper layer were shifted inwards by 130 mm. Consequently, no transducers were placed directly below the concentrated loads or in the region affected by load introduction. Thus, the affected region does not overlap the region of the eight central transducers. Nevertheless, measurements through the affected region were performed, too, but are excluded from analysis since they exceed the scope of the recent work.

Loading of the beam progressed in an incremental fashion. Furthermore, on each of the load levels, all types of measurement, i.e., FOS, DIC, US, were performed simultaneously. The US measurements were carried out consecutively between all adjacent pairs of transducers, i.e., for each source-receiver combination, one transducer emits an US signal while the other picks up this signal. Successive switching of all adjacent combinations yields 32 individual measurements between the sensor pairs per load level. Simultane-

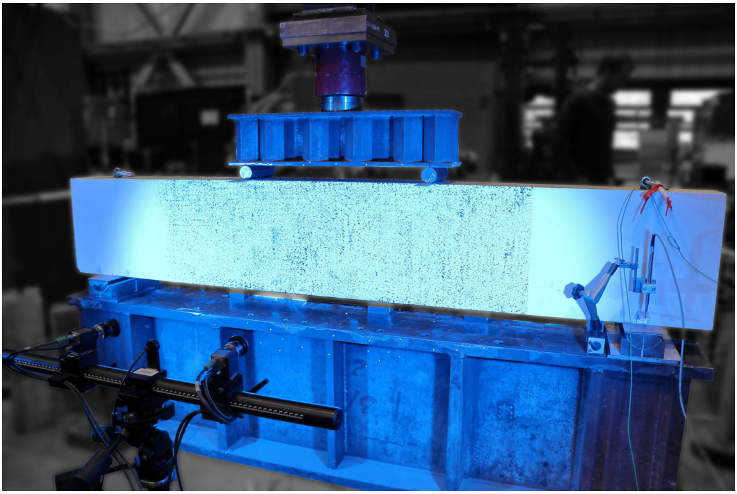

Figure 5.6: Photo of the test set-up.

ous measurements are performed with the FOS as well as with the DIC. This synchronicity results in consistency across said techniques.

Moreover, the ambient temperature in the laboratory was monitored during testing. Taking this into account, the minimal changes in temperature present at the actual testing site were not expected to have any influence on the different measuring methodologies. Mainly due to the relatively low thermal conductivity of approx. $2\,\mathrm{W/(m \cdot K)}$, the heat transfer in concrete is quite inert. During the experiment, the ambient temperature change was $< 0.5\,°\mathrm{C}$. Thus, it is assumed that the spatial temperature variation in the concrete is negligible, which is also confirmed by the temperature measurements.

The investigations in the further course of this project and the associated findings are deemed to enable to lighten the yet quite fine network of transducers (maintaining the high density of results of the CWI) and thus to justify practical application to real structures such as bridges.

5.3.3 Results

Strain

Due to fiber optic technology's general measuring characteristics, a quasi-continuous strain curve is recorded during the experiment. Here, the following mode of operation was selected: length of the evaluation window of 1.3 mm and thus point distance of 0.65 mm. Figure 5.7a depicts the compressive strain measured by an FOS. The FOS is located 34 mm underneath the top of the RC beam (also see Figure 5.5). The unprocessed strains are displayed in gray. Both due to the macroscopic differing Young's modulus of the concrete as well as the measurement noise, highly fluctuating strains are measured. In order to improve their interpretability, the original measured data are smoothed with a piecewise robust regression. As Figure 5.7a displays, the original data (Measurement) are partly in the positive range, although this FOS is allocated in the compression zone. This observation can be traced back

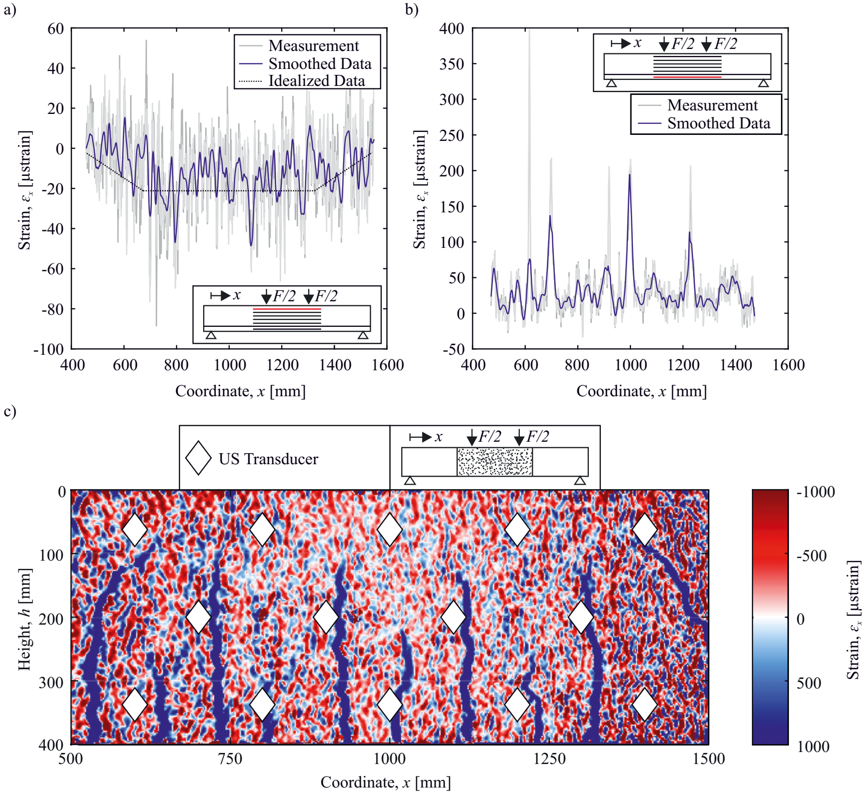

Figure 5.7: a,b) Strain from FOS for an applied load of $F = 10\,\text{kN}$ and c) strain from DIC for an applied load of $F = 160\,\text{kN}$ and marked US transducer positions.

to the measuring noise, which, in relative terms, has a stronger impact during lower loads. Symmetrically originating at both ends, compressive strains are to be observed. Following the constant bending moment between the two concentrated loads, a constant strain level between $x \approx 700\,\text{mm}$ and $x \approx 1300\,\text{mm}$ is highlighted (cf. dotted line in Figure 5.7a).

Analogously, Figure 5.7b illustrates the measured strains for a FOS. However, in contrast to before, this sensor is located in the tensile zone at a distance of 380 mm to the top of the beam. Estimating the concrete strain at the formation of the first crack at $0.1\,‰ \equiv 100\,\mu\text{strain}$, leads to the safe assumption that initial cracks have already emerged. Due to the attachment of the FOS to the concrete surface, the relative shift of the crack edges leads to increasing strains measured at the precise position of a crack. Nevertheless, it is here to be constituted that decreasing stresses and thus also strains towards the crack edges cannot be measured this way.

Figure 5.7c shows the two-dimensional strain field measured by DIC. The underlying displacements used to calculate these strains are estimated for a facet of 19×19 pixels. The measured deformation in a specific facet center (i.e., its displacement) allows for a careful calculation and deduction of strain for meta areas by aggregating the deformation of said facet center itself with deformation data from facet centers in its direct vicinity. Due to this summarizing process, the resolution of DIC strain results suffers, for example, leading to an overemphasis of crack width, as is evident in Figure 5.7c. Furthermore, it is pointed out that, besides the cracks themselves (displayed in continuous blue lines), no strains can be identified because of the strong measuring noise. From the extensive white areas between $x \approx 800$ mm and $x \approx 1200$ mm, it is to be derived that this area exhibits low measurement noise. This can be traced back to the unavoidable picture blur of the image at the horizontal edges of the image. Figure 5.7c displays a regular crack pattern. Two flexural-shear cracks, one on each side, four primary flexural cracks and four secondary flexural cracks in-between can be identified. A more detailed juxtaposition of the crack pattern and the US transducer positions shows that in most cases the cracks did not propagate into the transducers. Therefore, it is to be inferred that in fact no uncoupling of any transducers has occurred. In short, crack propagation and thus the resulting crack pattern is not affected by the transducers, thereby demonstrating that said transducers do not significantly impact load bearing behavior.

The occurrence as well as the propagation of secondary flexural cracks in this experiment are confirmed by general model representations in extant literature. Said models localize secondary flexural cracking in detail. Projecting the point of intersection of the bending reinforcement and a primary flexural crack at an angle of 45 degrees, such projection intersects the upper tip of a secondary flexural crack (cf. [222]).

Ultrasound

On each load level, measurements of all transducer combinations have been carried out. Figure 5.8 illustrates the CC and dv/v calculated with the stepwise CWI. Figures 5.8a,b detail the results of the CWI for exemplary transducer pairs

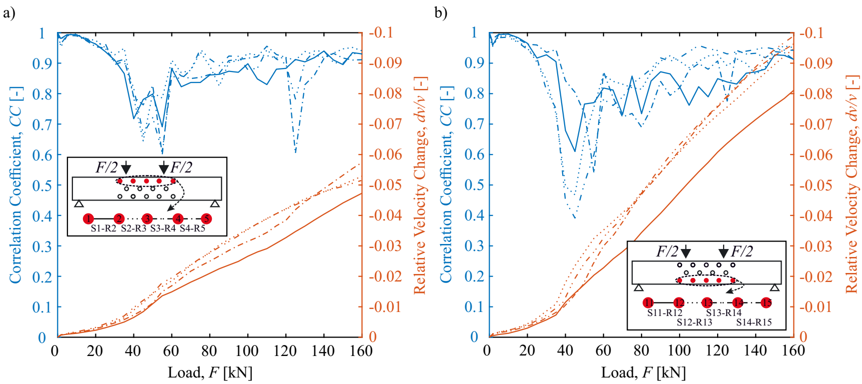

Figure 5.8: Stepwise correlation coefficient CC and cumulative relative velocity change dv/v for selected transducer pairs in the a) compressive and b) tensile zone.

in the compressive (Figure 5.8a) and tensile zone (Figure 5.8b), respectively. As is evident (in Figure 5.8), the *CC* decreases up to a load of approximately $F = 40\,\mathrm{kN}$ to $55\,\mathrm{kN}$. This global minimum can be confirmed for every transducer pair. The *CC* for transducer pairs in the compressive zone decreases to the range [0.60, 0.70], while the one for pairs in tension yields [0.40, 0.60]. Due to micro-cracking in the tensile zone, the decorrelation $(1 - CC)$ is more pronounced here. Based on the tensile strength of the concrete ($f_{\mathrm{ctm}} = 2.5\,\mathrm{N/mm^2}$) and according to the dimensions of the static system, 30 kN constitutes the level of force required to create the first crack. By applying a coefficient of variation of 0.3, i.e., concrete's tensile strength, a completed crack pattern can be expected to emerge at a force level of around 40 kN (cf. [91, 222]). Such theoretical considerations can here be confirmed employing the strain measurement results of the fiber optics. Therefore, it can be concluded that the initial formation of cracks has a higher influence on the correlation than the subsequent crack expansion. Moreover, in contrast to the aforementioned fixed-reference CWI, the *CC* calculated via stepwise CWI is in fact able to recover from and even increase after a temporary decline.

Within a range of approximately $F = 40\,\mathrm{kN}$ to $160\,\mathrm{kN}$, multiple local minimums of the *CC* are identifiable. Furthermore, it can be observed for both cases that the *CC* decreases by several percent right at the beginning. In this context, such *CC* behavior is largely attributable to the relocation from a continuous supporting on elastomer bearings to the supporting in the four-point bending test set-up right before the test.

Because the dv/v in stepwise CWI is only calculated with respect to the previous US measurement, results need to be accumulated. Said fact constitutes the reason why the dv/v continuously increases during loading. It is to be noted that the gradients of the transducer pairs in the compressive as well as in the tensile zone increase after a load of $F = 40\,\mathrm{kN}$. Furthermore, it can be ascertained that a smaller dv/v is calculated in the compressive than in the tensile zone.

5.4 Comparison of US Results and Strain Fields

5.4.1 Non-Cracked to Slightly Cracked State

As previously discussed, the FOS were attached onto the concrete beam, staggered in equal clearance over its height. The measurement output of one fiber consists of one-dimensional strain data with a point distance of 0.65 mm. Assigning the strain from multiple FOS to their respective positionings and heights on the RC beam, allows for an aggregation of the one-dimensional strain data points forming two-dimensional strain fields. Figure 5.9a,c depict such mapped strain data. Values in-between the support lines (FOS data with given height) were linearly interpolated. Since no extrapolation is carried out, the outer FOS (at a height of 34 and 380 mm) represent the limits of the strain field.

Figure 5.9b,d show the dv/v presented as a two-dimensional map (attribute map, cf. [137]). The solitary results of each transducer pair were located right in the middle between them and intermediate values were linearly interpolated. Positioning the results in the middle of two transducer pairs leads to an attribute map with the y-limits of 75 and 325 mm. Note that the color scale (e.g., limits of dv/v) differs for the subsequent representation of attribute maps due to the large variation of dv/v with raising load.

The juxtaposition of strain field and attribute map anew reiterates that the tensile zone shows larger

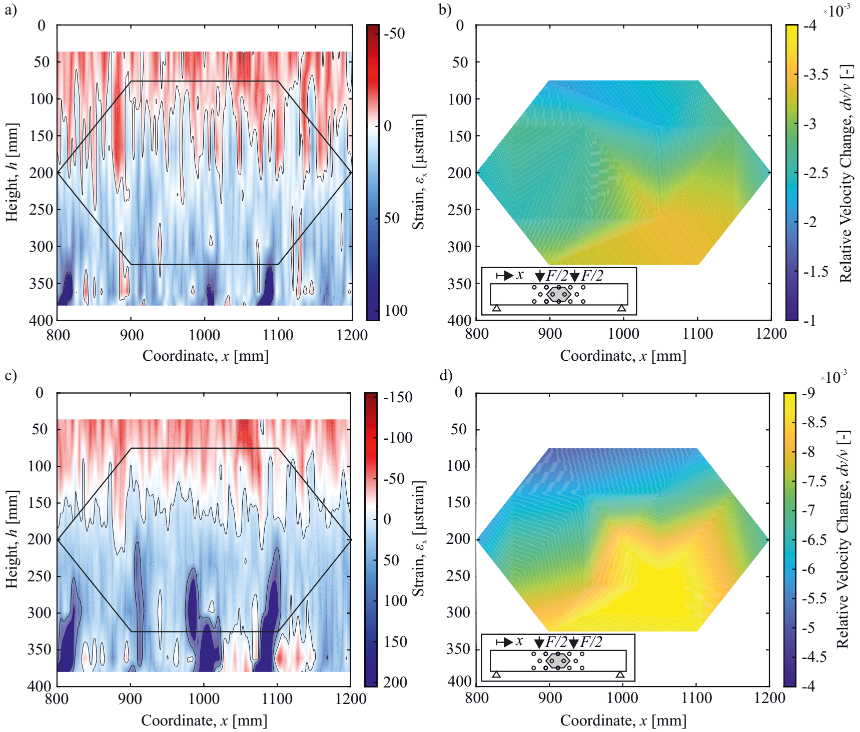

Figure 5.9: a,c) Strain fields derived by FOS measurements assigned to their respective heights, b,d) relative velocity change presented as attribute maps. The two upper figures show the respective results for a load of $F = 10\,\text{kN}$, while the two lower Figures do so for $F = 25\,\text{kN}$.

dv/v than the compressive zone. When the test specimen at hand cracks, the height of said tensile zone approximately equals the depth of primary flexural cracks. Also, the enhanced right-sided crack occurrence is to be identified by the attribute map. A comparison of Figure 5.9b,d reveals how dv/v rises with increasing tensile strain and therefore likewise with growing load. Figure 5.9a,b represents strain and US data for a load level of 10 kN. Because of the low strain values and the, in relative terms, high measuring noise, no definite compressive zone can be identified in Figure 5.9a. However, the height of the compressive zone at a load of 10 kN is estimated to range between $h = 200\,\text{mm}$ and $h = 150\,\text{mm}$. Furthermore, in the tensile zone, at $x \approx 800\,\text{mm} / 1000\,\text{mm} / 1100\,\text{mm}$, small strain peaks are visible, reaching approximately 100 µstrain (noted earlier as the approximate strain level at which concrete first cracks). Further scrutiny of the coordinates of said strain peaks again emphasizes that higher tensile strain is present on the beam's right side.

Figure 5.9b demonstrates greater dv/v present in the lower part of the test specimen compared to the upper part. The dv/v ranges from approximately $-2.25 \cdot 10^{-3}$ in the compressive to $-4 \cdot 10^{-3}$ in the tensile zone of the beam. In addition, a right-sided concentration of the largest dv/v can be observed. Due to the missing zero crossing of the dv/v, measured results can only be interpreted in relation to one another, i.e., as relative change over height. In order to be able to deduce the strain state from the attribute maps, additional information, such as the type of external force, is required. Based on a juxtaposition of strain fields and attribute maps, later analyses of data presented in the attribute maps allow for distinguishing tensile from compressive strains present in the beam. Thus, in relative terms, tensile strains overall cause a greater change in dv/v than compressive strains. The aforementioned clustering of strains on the right side, is likewise underpinned by the US results. As discussed earlier, Figure 5.9c,d exhibits the strain and attribute map for a load of 25 kN. Both depictions point out that, with increasing load and the associated increase in strain, measurement noise plays a lessened role compared to the lower strain levels presented earlier (cf. Figure 5.9a). Thus, such relatively low measurement noise at higher strain levels renders it possible to approximate the compression zone height more precisely as lying between 150 and 175 mm. Furthermore, in addition to the points of increased strain from Figure 5.9a, the higher strain level presented in Figure 5.9c also features further areas of increased strain, which continue to expand vertically in a linear manner. The structure of results for the zones in which increased strain of over $+100$ µstrain occurs, indicates concrete cracking in these areas. It should be noted that strains exceeding $+100$ µstrain are only measured due to the crack edges moving relative to one another (cf. Figure 5.7). In said cracked sections, dv/v analogously also increases, as evident in the strain field. The previously identified phenomenon of tensile zones showing larger dv/v than compressive zones, can also be deduced from Figure 5.9d, so that there are values ranging from $-6 \cdot 10^{-3}$ to $-9 \cdot 10^{-3}$. In accordance with previous results highlighting the right-sided clustering of higher strains, dv/v likewise dominate in this area of the beam.

5.4.2 Completed Crack Pattern and Increasing Crack Widening

In contrast to Figure 5.9, the strain fields are here measured utilizing DIC. Therefore, the measured strain data is presented from $h = 25$ mm to 375 mm. Depending on the rigidity of the epoxy resin adhesive needed to attach the FOS to the rebar or concrete surface, the conjunction of FOS and resin is susceptible to generating slightly skewed results. Here, high strain areas affect FOS measurements in its surroundings, as strain is diverted due to the (inevitably) limited rigidity of the resin. Due to such limitations of FOS-based strain measurements, DIC serves as a vital complement.

In order to calculate strains, DIC measures deformations employing facet sizes of 49×49 pixels as exemplified in Figure 5.10. Due to such resolution, the portrayal of the size of individual cracks (blue line-like strains) appears to be enlarged when depicted in Figure 5.10. By using additional pixels for a facet, additional information is available to the algorithm, which, in turn, is able to determine the displacement of a facet during loading more accurately. Moreover, such an addition (of pixels) encompasses a larger area being available for calculating a meta area's strain levels, so that strain overall can be calculated more meticulously. Thus, notwithstanding the production of more accurate strain results, the density of the results is reduced following this method.

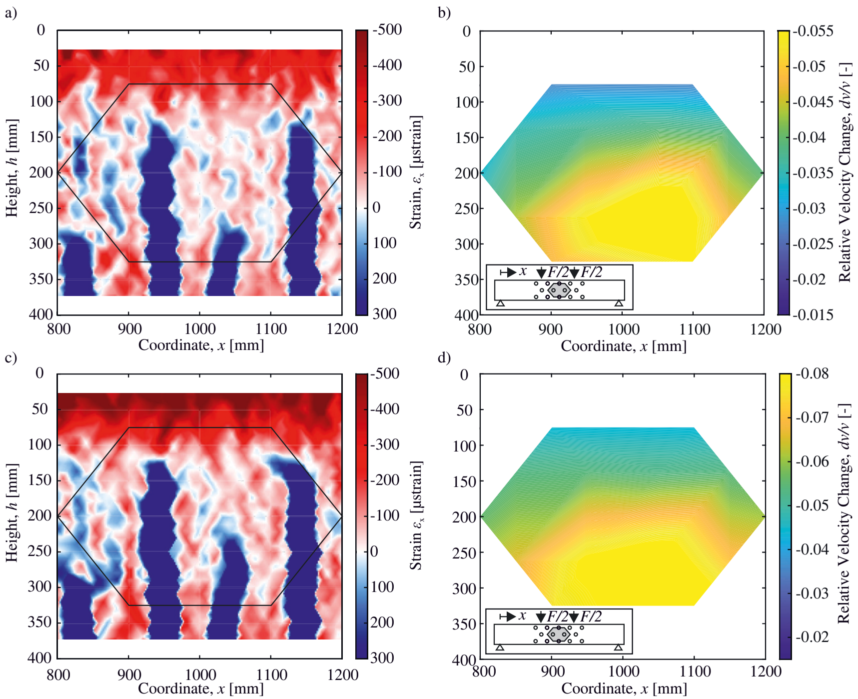

Figure 5.10: a,c) Strain fields from DIC, b,d) relative velocity changes dv/v presented as attribute maps. Figures above show results for a load of $F = 75$ kN, Figures below for $F = 120$ kN, respectively.

Figure 5.10b,d shows an attribute map for the dv/v measured by the eight centrally located US transducers. It is made evident that the qualitative appearance of the attribute map is similar to that of Figure 5.9b,d, whereas only the magnitude of the dv/v differs. As previously discussed, the right-sided concentration of cracking here again finds support in the attribute maps. Consequently, it is to be inferred that even an augmented crack propagation does not hinder the evaluation of the US results. As annotated earlier, the tensile strength of the used concrete requires a force of 30 kN, in order to engender initial cracking. Nevertheless, as Figure 5.7 emphasized, strain peaks, from which cracking is to be expected, can be detected much earlier than 30 kN. Similar to the previous illustration in Figure 5.9, a strain field and an attribute map for a load of 75 kN (Figure 5.10a,b) and 120 kN (Figure 5.10c,d) are displayed. The comparison of Figure 5.10a,c underlines that the strain in the compression zone rises with increasing load. At the same time, the primary flexural cracks propagate only slightly. Due to the progressive crack growth, a compression zone height of approximately 100 to 125 mm can thus be determined for both loads shown here. Due to the high measurement noise present, the low strain zones between cracks cannot be assessed regarding strain distribution.

5.5 Conclusions

In this paper, experiments pertaining to US measuring techniques for the monitoring of large concrete structures performed on an RC beam subjected to four-point bending were presented. To such ends, the test specimen was equipped with a network of US transducers in addition to FOS and DIC systems. In contrast to the results of the DIC, the measurement data of individual FOS must initially be aggregated in order to calculate strain fields. For this purpose, the individual measured values are assigned to the respective placement of the FOS on the test beam and can thus be displayed as strain fields. The US results of respective source-receiver pairings must likewise undergo previous processing employing stepwise CWI, before being assigned to a location along the test object. Finally, the illustration of dv/v in the form of attribute maps creates a representation resembling that of strain fields. A juxtaposition of strain fields and attribute maps eventuates in the understanding that US results can, in fact, serve to qualitatively identify compressive and tensile zones.

Under the given premises, however, the applied evaluation method does not allow for drawing inferences as to a quantitative correlation between the US results and strain fields, derived by means of FOS and DIC data. Nevertheless, it is ascertained that the extent of dv/v grows with increasing load, therefore also strain. Moreover, compression and tension zones as well as locally concentrated cracking measured via US transducers, concurs with measured strain data, rendering it possible to qualitatively attest extensive compatibility of US data on the one hand and FOS and DIC data on the other hand. Consequently, stepwise CWI is able to produce viable results even in spite of increased cracking. Moreover, the evaluation of individual source-receiver pairings has also underlined that even the smallest changes, for example, repositioning the beam from a continuous bearing on elastomers to a bearing in a four-point bending test, can be detected by the US signal. Strains caused by such changes are generally far below the sensitivity of conventional and even novel strain measurement techniques.

Furthermore, FOS results indicate that a mere third of the force, which is customarily deemed necessary to create cracks in concrete (i.e., 30 kN), suffices in practice to generate cracks in the test specimen. As discussed, dv/v measured via US transducers are present in concentrated fashion on the right-hand side akin to strain measured via FOS. Such parallel properties provide reason for assuming that the US signal detected for a force level starting at 10 kN also points toward early cracking. However, such damage cannot be detected through optical inspection.

Therefore, it is here to be concluded that the use of CWI for the early detection of damage to concrete structures has substantial potential for practice.

Chapter 6

Correlation of Load-Bearing Behavior of Reinforced Concrete Members and Velocity Change of Coda Waves

The following chapter is taken verbatim from:

> CLAUß, F.; EPPLE, N.; AHRENS, M. A.; NIEDERLEITHINGER, E. and MARK, P. *Correlation of Load-Bearing Behavior of Reinforced Concrete Members and Velocity Change of Coda Waves*. Materials, 2022. 15(3): 738. doi: 10.3390/ma15030738.

Text and figures have been adjusted to the format and layout of this thesis. The content remains identical. The literature used is jointly referred to at the end of the thesis.

Abstract

The integral collection of information such as strains, cracks, or temperatures by ultrasound offers the best prerequisites to monitor structures during their lifetime. In this paper, a novel approach is proposed which uses the collected information in the coda of ultrasonic signals to infer the condition of a structure. This approach is derived from component tests on a reinforced concrete beam subjected to four-point bending in the lab at Ruhr University Bochum. In addition to ultrasonic measurements, strain of the reinforcement is measured with fiber optic sensors. Approached by the methods of moment-curvature relations, the steel strains serve as a reference for velocity changes of the coda waves. In particular, a correlation between the relative velocity change and the average steel strain in the reinforcement is derived that covers 90 % of the total bearing capacity. The purely empirical model yields a linear function with a high level of accuracy ($R^2 = 0.99$, $RMSE \approx 90\,\mu strain$).

6.1 Introduction

Civil engineers have long been aware of the gradual aging of infrastructure. Global availability of raw materials, ease of workability, almost arbitrary formability, and economic considerations have led to the vast majority of existing structures being made of reinforced concrete (RC). Its increasingly critical state of preservation has driven their activities. Today, regular inspection on-site, i.e., of bridges, is part of the daily business of structural inspectors. However, annual intervals of visual inspection [39] do not reach the root of all problems. Rather, they enable reacting to existing (visible) damage. Until damage becomes visible, time passes by and is lost to take countermeasures early. What can be done in the meantime when damage is not yet visible from the outside? This is where structural health monitoring comes into play. Research streams in in this field are copious (e.g., [9, 135, 185, 220]). Available options to technically equip structures are plentiful (fiber optic sensors (FOS), acoustic emission, strain gauges, displacement transducers, etc.). They address all typical issues of bridges [55] and promise to detect and monitor any changes continuously and is immediately reported if predefined limits are exceeded. Non-destructive techniques are usually preferred since they limit the impact on already weakened structures.

Distinction can be made according to the information content ascribed to a sensor (0D / 1D / 2D / 3D), the number of sensors required in a network to detect and track local or global changes, but also regarding the measuring principle (electrical, (fiber-)optical, acoustic).

Acoustic Ultrasonic (US) measurement methods are characterized by the fact that a wide volume can be investigated already with a single transmitter-receiver pair. Traditional transmission and reflection methods mainly analyze the direct wave between the transmitter and receiver by means of the time of flight [206, 212]. Thus, they provide information on changes or larger defects on the direct path only. Other methods focus on the late part of the US signal that follows the direct wave, the coda. The coda is scattered several times and thus interacts with larger regions. It is known to be sensitive to small changes in mechanical strain (compressive and tensile) [72, 107, 114, 138, 150, 183, 216], temperature [49, 141, 217], moisture [67, 94, 110] as well as cracks or other discontinuities in the concrete [66, 108, 126, 137, 174]. Since strain is the fundamental state variable of RC [125]; it seems most promising to establish a direct correlation between it and the coda to infer the health of structures.

Much effort has been spent on the material level on small compressive strains of concrete in the elastic domain [72, 107, 114, 138, 150, 183]. Using the acousto-elastic effect, good agreement with US results has been found on micro-scale. By contrast, due to concrete's significantly lower capacity in tension, purely tensile strains have seldom been investigated [216]. While the non-cracked domain ends around $30 - 40\,\%$ of the maximum strength in compression (about 350 µstrain), in tension, it already ends at about 100 µstrain. However, from a structural point of view, both is of minor interest on the macro-scale. Basically, RC structures are that successful due to the symbiosis of the two materials, steel and concrete. They are usually subjected to bending, which causes local compressive and tensile zones, and designed in such a way that (tensile) failure is always announced in good time and in a ductile manner. Once concrete cracks in tension, the embedded reinforcement takes all tensile forces (by bond) and enables exploiting RC's capacity far beyond the elastic range. Macro-cracks (of limited width for durability reasons) are thus an elementary part of the construction method and by no means an exclusive indicator of imminent failure. They are inevitable, and thus, proper monitoring must cope them and only alert authorities when critical limits are reached.

The load-bearing behavior of RC after the first crack is crucial. However, previous research could only establish correlations for the non-cracked state. This article is dedicated to the (almost) entire load-bearing behavior of RC, including the cracked state.

Attempts to establish a direct correlation between strain and coda characteristics experimentally beyond the elastic range have failed so far [26]. Employed as an integral coda characteristic, the relative velocity change, obtained from coda wave interferometry (CWI) with step-wise reference, has always shown the same sign independent of stress. Thus, without augmented information employing other techniques for reference, a differentiation between compression and tension remains impossible. Nevertheless, in [26], the course of relative velocity change was found bi-linear and prominent kink at a level of about 1.3 times the cracking force. This indicates a fundamental similarity to the integral load-bearing behavior of RC structures as reflected by the well-known moment-curvature relationship [31, 149, 156, 222].

This similarity shall be used here specifically to establish integral correlation on structural level. Abandoning everywhere highly resolved local strains, this is done in reflection of an integral but representative velocity change of a scanned partial volume between sensor pairs analogous to the specification of an average steel strain. For this purpose, an RC beam subjected to 4-point bending has been tested at Ruhr University Bochum. In addition to US measurements, the strain in the reinforcement is measured with FOS. The results of this experiment are presented here. Focus is laid on the investigation of the load-bearing behavior of RC members. An approach is presented that allows evaluating the almost entire load-bearing behavior of RC members (i.e., up to the cracked range at about 90 % of the maximum load).

The article first introduces the methodology used for US measurements and discusses the key parameter computed thereof. This is followed by a mathematical description of the load-bearing behavior of RC components, and the experiments carried out. Based on these fundamentals, the load-bearing behavior is first analyzed phenomenologically (qualitatively) using various transmitter-receiver combinations. From the similarity to the material behavior of RC, a correlation relationship is developed that enables infering the member condition via US measurements.

6.2 Methods

6.2.1 Sensing Structures with Ultrasound

General Aspects

Elastic-wave-based techniques have become an essential part of the non-destructive testing (NDT) portfolio in civil engineering. Today, methods such as impact echo [22, 170], US transmission and reflection [206, 212] are well-established for material testing [3, 88, 166]. Measurements with US waves—waves featuring frequencies $\geq 20\,\text{kHz}$—are able to analyze the thickness of components and detect major faults. Their application always requires a trade-off between resolution and penetration depth. With higher frequencies, smaller features will be detected; meanwhile, the attenuation of US is increased due to interactions with grains and pores in concrete. [150] distinguish four domains for ultrasound in concrete. Differentiation takes into account the macroscopic size of the specimen L, the US wavelength λ, the concrete grain size d and the intrinsic absorption length l_a. The wavelength is a frequency f and velocity v dependent quantity defined by $\lambda = v/f$. Their four domains are limited as follows:

1. The *low frequency range* and *stationary wave regime*, where the wavelength is greater than the specimen itself. This regime is typically limited to $f \leq 20\,\text{kHz}$.

2. The *single scattering regime* where the wavelength is longer than the grains but smaller than the macroscopic size of the structure ($d < \lambda < L$). In this regime and $20\,\text{kHz} \leq f \leq 150\,\text{kHz}$, intrinsic absorption can be neglected since $l_\text{a} > L$.

3. The *multiple scattering regime* ($f \leq 1\,\text{MHz}$ where $\lambda < d$ but intrinsic absorption does not dominate signal spreading).

4. The *attenuative regime* with $f > 1\,\text{MHz}$ where scattering and intrinsic absorption prevent elastic waves from significant spreading.

Classical transmission-based US NDT techniques analyze ballistic waves—waves that have directly traveled from transmitter (T) to receiver (R) (see Figure 6.1). These techniques are situated on the lower end of the frequency ranges since they transmit significant parts of energy on the direct path. When frequency and scatter in inhomogeneous materials like concrete increase, more wave energy is scattered and no longer travels on the direct path. Then significant portions of energy are recorded at the receiver after the ballistic part. This multiply scattered part of recorded waves is called coda [2].

Researchers in seismology and US have successfully used the coda to detect minute changes in the earth's crust and scattering media such as con-

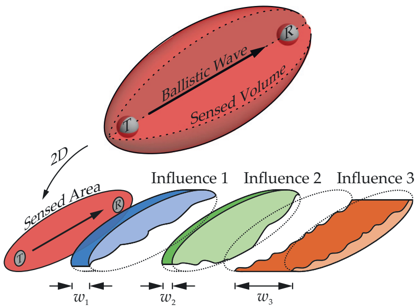

Figure 6.1: Top: Simplified 3D representation of the volume scanned by US. Bottom: Model representation of different influences on the signal. The contribution of these influences to CWI characteristics depends on the affected region and a weighting factor.

crete (e.g., [106, 154, 178]). Multiply scattered coda waves sense a certain volume between transmitter and receiver (Figure 6.1 top). Because they integrate information from the entire volume, the scattering medium acts like an interferometer that merges 3D information to a receiver location. Therefore, the coda probably joins information from different material zones with specific properties and superimposes impacts from, e.g., temperature, moisture, mechanical stress variations and permanent changes such as cracks. All influence the coda to a different degree, dependent on the geometry, the environmental conditions, and the severity of changes (Figure 6.1 bottom). The analysis of such superimposed information stored in the coda is called coda wave interferometry.

The CWI-Method

Small changes in the coda between two consecutive measurements are analyzed by the cross-correlation of the associated signals. Figure 6.2 shows two consecutive measurements, where the influence of a minute change in the material parameters is only visible in the coda, but not in the first arrival. Several techniques are available to calculate characteristic velocity changes from the cross-correlation and to analyze the evolution of velocity changes in a scattering medium such as concrete (see [150]). In recent years, most researchers applied the so-called stretching technique to obtain the velocity change (e.g., [139, 199, 211, 219]):

$$
\begin{aligned}
-\frac{dv}{v} &= \arg\max_{\alpha\in\mathbb{R}} CC(t,\alpha) \\
&= \arg\max_{\alpha\in\mathbb{R}} \cdots \\
&\frac{\int_{t_1}^{t_2} u_1(t(1-\alpha))u_2(t)\,\mathrm{d}t}{\sqrt{\int_{t_1}^{t_2} u_1^2(t(1-\alpha))\,\mathrm{d}t \int_{t_1}^{t_2} u_2^2(t)\,\mathrm{d}t}}
\end{aligned}
\tag{6.1}
$$

As in other techniques, such as the doublet technique [150], this method compares two consecutively recorded signals u_1 and u_2. The level of similarity of these signals in a time window $[t_1, t_2]$ is expressed by the correlation coefficient (CC); $-1 \leq CC \leq 1$. CC close to one indicates very similar signals. If the two signals are $180°$ phase-shifted, CC is close to negative one. If the two signals are not similar anymore, CC approaches zero. To determine a velocity change with Equation 6.1 the signal u_2 is compared to a stretched (or compressed) version of u_1. The stretching factor α that maximizes CC is the relative velocity change dv/v for the sensed volume. In monitoring experiments, where several consecutive measurements are evaluated, either the initial state can be chosen as a fixed reference or the reference is updated step-wise. The latter is advantageous in cases where strong changes are expected, as strong differences between u_1 and u_2 (meaning $CC < 0.7$) are avoided, while the relative velocity change can still be related to the initial state. Therefore, this step-wise procedure is used here throughout.

For analysis, the relative velocity change dv/v has another, yet decisive advantage over the correlation coefficient CC, since it develops strictly monotonically with time or with load. Its evolution can therefore be expected to run affine to that of common structural quantities such as strains.

As mentioned, the US coda is sensitive to small changes in the sensed material (e.g., [107, 114, 141, 150]). When monitoring civil engineering structures, the analysis of stress (strain) changes in a structure is of special interest, as it can be an early indicator of damage. This dependency of US velocity to stress (strain) is covered in the acousto-elastic theory by the inclusion of non-linear elastic laws to the equations of motion. Then the relative velocity change depends on non-

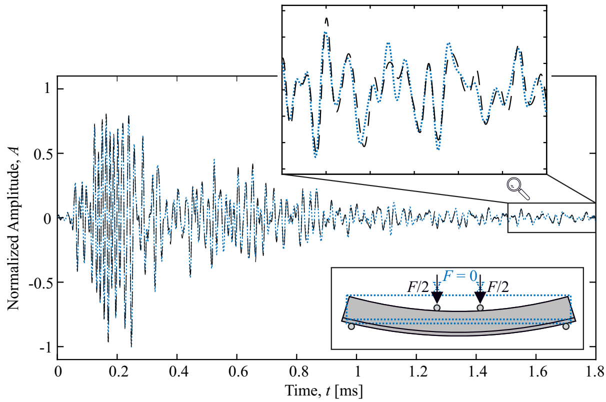

Figure 6.2: US measurement of the same transmitter-receiver combination, before and after an influence has changed.

linear parameters. A detailed description of the acousto-elastic theory can be found in [133, 191].

6.2.2 Load-Bearing Behavior of Flexural RC Members

Due to its low tensile strength that amounts to about 10 % of its compressive strength ($f_{ct} \approx 10\,\%\,f_{ck}$), plain concrete is commonly not used to build structures. Its combination with (reinforcing) steel, which, in contrast, possesses significant tensile strength, compensates for this drawback. Embedded reinforcing steel is designed to take over the stresses released by concrete if necessary. While pouring, it is bonded to the concrete and usually placed in the tensile zone of flexural members (stretched fiber) expected from loading. In structural design, flexural members are commonly denoted as beams, a term that will be used synonymously in the following.

Due to global availability of raw materials, ease of workability, almost arbitrary formability, and costs, RC has become the most frequently used construction material worldwide.

Phenomenological Characterization of RC

The composite RC composed of concrete and steel possesses a complex load-bearing behavior. As far as the top hierarchy is concerned, it can be classified into a non-cracked and a cracked domain (state I / II, cf. Equations 6.3 – 6.6). With increasing load, RC beams pass through these states. Depending on the static system (location of the supports and the external loads) and the point of interest observed along the beam, the internal forces (stresses) also vary. As a result, the beam is usually in different states along its length (x), dependent on the internal stresses.

As the tensile is considerably lower than the compressive strength, the load-bearing behavior is typically classified using the tensile capacity. The non-cracked state ① is characterized by linear elastic behavior. Both concrete and steel are entirely intact and exhibit identical strains on the same level (fiber) in the cross-section (see Figure 6.3 left). Then, bond stresses between the reinforcement and the concrete do not exist.

However, as the load increases, the stresses exceed the tensile strength on a certain level depend-

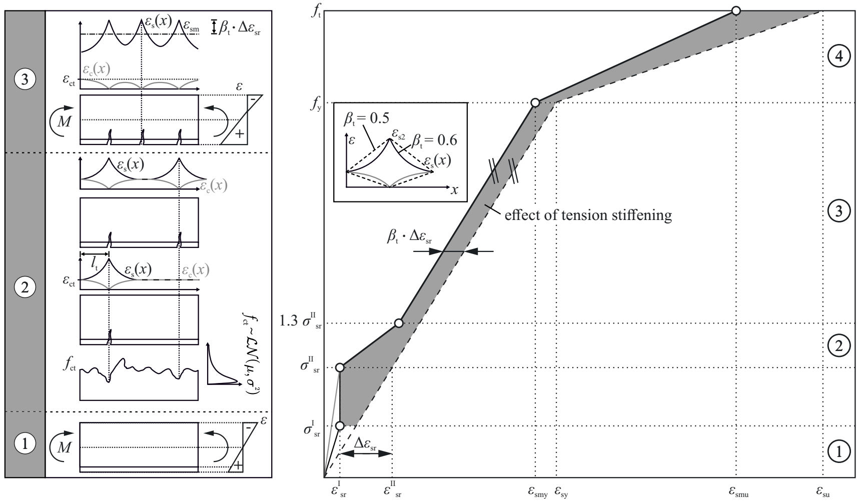

Figure 6.3: Concrete and steel strains (left) for the three ranges of the σ_s - ε_{sm} relation (right).

ing on the concrete grade, the concrete cracks. The bending crack starts from the outermost tensile fiber and runs perpendicular to the neutral axis at center.

Only cracked, RC develops its full potential. Its complex load-bearing behavior is usually further subdivided into three complementary ranges (② – ④, according to e.g., [31, 53, 222]). In the range of cracking (②) and since the tensile strength is subject to inherent variation, the first crack does not inevitably form at the point of maximum load (cf. Figure 6.3 left). Rather, the location of the first crack is always a trade-off between load and tensile strength, and thus depends to some extent on chance.

At cracks, the concrete stress and hence the strain immediately drops to 0. Then, the stress that has been borne by the concrete before is redistributed to the reinforcing steel by the bond. As a result, the stress (strain) in the reinforcement is maximum at the crack. Thus, reinforcement and concrete do no longer exhibit identical strains at the same depth (fiber). Over the transfer length l_t, the bond reintroduces the steel forces into the concrete. Finally, both strains converge on the same level again, while the rest of the beam at a distance l_t from the crack remains non-cracked and still responds linear elastic.

When the reinforcement has transferred the entire force released by the first crack into the concrete again, the next crack emerges at the then weakest location (Figure 6.3 left cf. [91]). Successive cracking repeats until the stress no longer exceeds concrete's tensile strength. This may be caused by: (1) Either the external load is no longer sufficient to exceed the tensile strength or (2) the distance between the cracks becomes too small to transfer enough force into the concrete via bond. The range of cracking (②) ends at approximately another 30 % of the force that has been necessary to generate the first crack ($1.3 \cdot F_{cr}$) cf. [222].

In the third range (③ completed crack pattern), no new cracks form anymore. The crack spacing is final and lies between l_t and $2\,l_t$. With increasing load, the existent cracks widen while the steel strain rises. At some point (④), the yield strength of the reinforcing steel is exceeded in a crack (location is again a trade-off between yield strength and load), the reinforcement yields. No more stresses or forces can be overtaken. From now, load increase goes along with significant elongation and strains and thus crack width. Neglecting potential failure of concrete in the compressive zone (stresses exceed the maximum compressive strength), the beam fails when reaching the tensile strength of the reinforcement at some location. This failure is strongly ductile since it is well-announced by significantly increasing strains before.

Intermediate Resume

Crack before failure is the fundamental design principle of RC. Thus, RC structures are always designed on the safe side, assuming the purely cracked state and neglecting any contribution of concrete to the tensile capacity of the member. In the check of equilibrium of internal forces, all stresses in the compressive zone are ascribed to the concrete while tensile stresses are appointed to the reinforcement. However, what is safe and simple in the design is too extensively idealized regarding realistic deflection prognoses on service level. Taking that simplified assumption, the actual deflection would be strongly overestimated.

Thus, in service conditions, it is of utmost importance to carefully take into account the concrete's contribution to the tensile capacity. That capacity of concrete between the cracks, which increases the total stiffness of the member, is often referred to as tension stiffening. Two alternatives are established to take it into account. One distinguishes a concrete-based formulation [149, 156] from a steel oriented approach [31, 53, 76, 222]. The latter formulation via an average steel strain (cf. Figure 6.3 right) is used here since both the steel strain and relative velocity change, are integral properties of associated characteristic volumes and alter during cracking. This correlation shall be exploited.

Computational Approach

Mathematically, the—due to cracking—fluctuating steel strain along the beam $\varepsilon_\mathrm{s}(x)$ can be averaged. The average steel strain ε_sm is obtained from Equation 6.2 by integration and division through the integration length. That way, realistic steel strains for serviceability conditions can be computed.

$$\varepsilon_\mathrm{sm} = \frac{1}{l_\mathrm{t}} \int_0^{l_\mathrm{t}} \varepsilon_\mathrm{s}(x)\,\mathrm{d}x \tag{6.2}$$

Please recall that the calculation of strains in the non-cracked state ① is elementary. Without cracks, the strain along the beam ε_s^I varies only according to the external forces. On each location, its distribution over the depth is linear and zero at the neutral axis. Upwards, this range is limited by the steel stress associated with concrete cracking σ_sr^I.

$$\begin{aligned} &①: && \varepsilon_\mathrm{sm} = \varepsilon_\mathrm{s}^I \\ &\text{for} && 0 < \sigma_\mathrm{s} \leq \sigma_\mathrm{sr}^I \end{aligned} \tag{6.3}$$

For convenience, the following range of cracking ② is first skipped. First, focus is set on the range of completed cracking ③. When cracked, the force between concrete and steel is transferred by bond. Bond is mathematically captured by a bonding law that generally idealizes the location and slip-dependent shear force transfer between concrete and rebar. It describes how the steel strain in the vicinity of a crack develops. The average steel strain in range ③ follows from Equation 6.4.

$$\text{③:} \quad \varepsilon_{sm} = \varepsilon_s^{II} - \beta_t \cdot \Delta\varepsilon_{sr} \qquad \text{for} \quad 1.3 \cdot \sigma_{sr}^{II} < \sigma_s \leq f_y \tag{6.4}$$

Herein, β_t governs the postulated bonding behavior, i.e., it indicates the steel stress development starting from the crack. Taking the simplest assumption β_t is constant, the bonding behavior is constant, too. This explicitly means: it does not change with load increase. More accurate approaches to account for changing bond properties due to local cracking are published elsewhere [29, 53, 222]. The strain gain in the reinforcement at transition from the non-cracked to the cracked state is denoted $\Delta\varepsilon_{sr}$.

Thus, in view of Equation 6.4 and Figure 6.3 right, it is inferred that the term $\beta_t \cdot \Delta\varepsilon_{sr}$ corrects the purely cracked state for tension stiffening. Moreover, in terms of stress, region ③ is bounded to the top by yielding of the reinforcement ($\leq f_y$). Towards the bottom, it is limited by transition to the range of cracking ($> 1.3 \cdot \sigma_{sr}^{II}$). From compatibility to the ranges ① and ③, the average steel strain in the range of cracking ② is deduced which yields Equation 6.5.

$$\text{②:} \quad \varepsilon_{sm} = \varepsilon_s - \frac{\beta_t \cdot (\sigma_s - \sigma_{sr}^{II}) + \cdots}{0.3 \cdot \sigma_{sr}^{II}} \; \frac{(1.3 \cdot \sigma_{sr}^{II} - \sigma_s)}{} \cdot \Delta\varepsilon_{sr} \qquad \text{for} \quad \sigma_{sr}^{II} < \sigma_s \leq 1.3 \cdot \sigma_{sr}^{II} \tag{6.5}$$

When yielding has occurred (index y), the ultimate load-bearing capacity of the beam associated with f_t is almost reached. With just small gains in the stress level ($f_t/f_y \approx 105 - 110\,\%$), strains and deformation in range ④ grow fast. Then, the average steel strain is obtained from Equation 6.6 wherein δ_d accounts for the ductility of the reinforcement ($\delta_d = 0.8$ high ductility and $\delta_d = 0.6$ normal ductility).

$$\text{④:} \quad \varepsilon_{sm} = \varepsilon_{sy} - \beta_t \cdot \Delta\varepsilon_{sr} + \cdots \; \delta_d \cdot \left(1 - \frac{\sigma_{sr}^{II}}{f_y}\right) \cdot (\varepsilon_s - \varepsilon_{sy}) \qquad \text{for} \quad f_y < \sigma_s \leq f_t \tag{6.6}$$

Considering all four ranges, a piece-wise defined function of the average steel strain is available that covers all phenomenological aspects introduced above. Elsewhere, it has already been applied to compute realistic deformations of a wide variety of RC structures [117, 119, 207]. For this purpose, the average steel strain must first be converted into an average curvature and then (numerically) integrated. Through additional deliberations, the same approach has also been extended to cover other, even more difficult, composite materials such as steel fiber reinforced concrete SFRC [78, 81].

6.3 Experiments

6.3.1 Experimental Setup

To substantiate the supposed principle correlation between the average steel strain and the relative velocity change as a key property of ultrasound obtained from CWI, an experiment has been set up at the lab at Ruhr University Bochum. One simply supported RC beam with rectangular cross-section shown in Figure 6.4 and dimensions 250 / 500 / 3500 [mm] (width / depth / field length) subjected to four-point bending was manufactured. To cover bending and shear demands with respect to EC 2 [41], it has been equipped with longitudinal reinforcement (3 Ø 20 mm) and stirrups (Ø 12 mm / 300 mm / 2). This simple setup meets the experimental objectives quite well

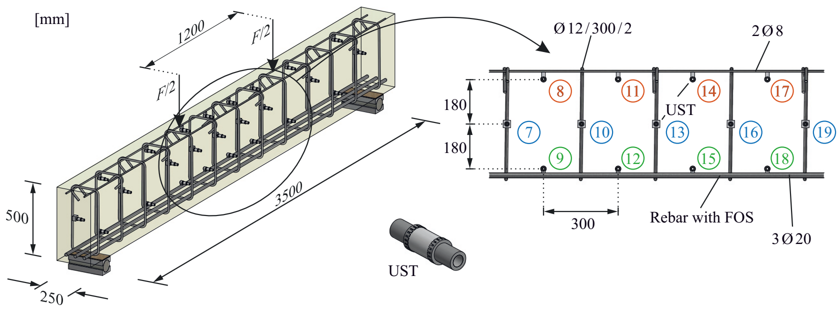

Figure 6.4: Beam geometry, reinforcement layout and loading along with the US transducer (UST) network.

since the central shear-free zone between the two vertical loads yields a plateau of constant bending moment. Herein, pure bending induces constant strains in each fiber and a neutral axis at the center. The strain distribution over the depth is linear. Thus, the principal stresses are strictly orientated horizontally along the beam. Interference with shear (indicated by inclined principal stresses) must not be expected. In this region, a distributed crack pattern with random characteristics as discussed above (cf. Section 6.2.2) will develop while the external load remains simple and controllable. During the test, the load will be increased step-wise and slowly to track all intermediate changes and to record the strains up to bending failure.

6.3.2 Placement of Measuring Equipment

To record US data, a transducer network has been installed all along the beam (Figure 6.4). It covers the central region of the beam on three levels. At the bottom and top layers, the transducers are attached to the longitudinal and constructive reinforcement (2 Ø 8 mm, cf. Figure 6.4), respectively. The central layer is fixed to the stirrups. Embedded US transducers (type SO807 from Acoustic Control Systems, Ltd. (Sarrebruck, Germany)) were used. They consist of a piezoceramic cylinder and have a central frequency of approximately 60 kHz. The radiation was already characterized in [140, 209] and is approximately uniform in the plane perpendicular to the piezo ring. Newly developed fasteners made from quick-cement (see Figure 6.5 left) fix the transducers to the reinforcement. Since their material is similar to the beam's concrete, they do not significantly impair wave propagation and load-bearing behavior.

For reference, a broad spectrum of strain measurement techniques (strain gauges, digital image correlation DIC, FOS, etc.) is available [25]. However, not all methods are equally suited. Conventional strain gauges face difficulties in allocating the measured data to a distinct position. Due to the physical length of a gauge about 3 to 6 mm, the strain is always averaged over that length. So the resolution is limited by the length. Another limiting factor concerns the number and density of individual gauges glued on concrete or steel surfaces and the associated effort. Furthermore, gauges always deliver highly local one-dimensional directed information. Moreover, since the decision where a gauge is to be placed has to be taken in advance (long before the experiment starts), the chance is great to miss the strain hot-spot at a crack whose location is random by

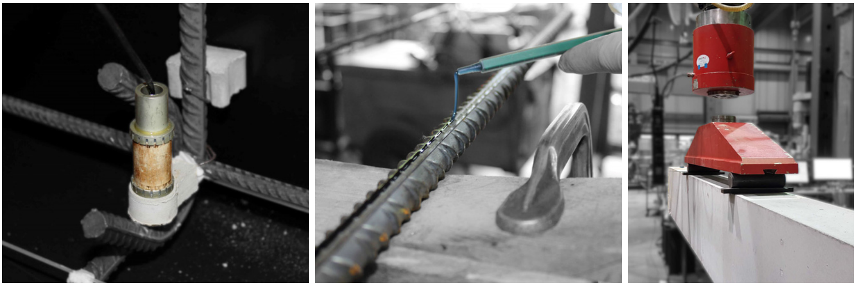

Figure 6.5: Left: US transducer attached to the reinforcement with a quick-cement fastener. Center: Gluing a FOS to the rebar. Right: Beam before the experiment in the test bench.

nature as discussed above (cf. Section 6.2.2). These deficiencies leave strain gauges marginally relevant for the intended application. However, they yield highly precise local strain references to double-check or calibrate other devices.

Thus, measurement techniques that provide higher information density (1D to 3D strain data) seem to be essential. With DIC, exclusively two-dimensional surface strains are observable, which is good for concrete strains but makes the acquisition of steel strains of embedded reinforcement infeasible. Furthermore, strain measurement with FOS is a trade-off. One-dimensional strains along optical fibers are obtained in (sub)millimeter resolution. When appropriately applied (gluing in a groove in the rebar [25, 26, 100], see Figure 6.5 center), strains can be acquired along entire reinforcement bars in high resolution. Installation effort and precision depend on the right combination of core, coating and cladding [25].

6.3.3 Concreting and Curing

Approx. 0.8 m^3 of concrete was mixed for the test specimen and several concrete cubes and cylinders (to determine the material properties). The fresh concrete was poured into the prepared formwork and compacted with the aid of a vibrating table. After 28 days of curing, the test was carried out. On the test day itself, the accompanying material tests (concrete and reinforcement) gave the material parameters listed in Table 6.1. All values are an average of three individual samples tested.

6.3.4 Load Control

Moreover, strain measurements with FOS can be performed quasi continuously (at defined intervals). In contrast, US measurements require load steps during testing since they measure differences between load stages. On each load level (under constant load), the US measurements are conducted transmitting from one US transducer and receiving at another. Successively all other combinations are worked through before the load is increased to the next level.

As discussed above, the time of cracking (end of the range ①, corresponding load F_{cr}) is a tipping point for both the load-bearing behavior of RC

Table 6.1: Material properties of the concrete and reinforcement, respectively.

f_{cm} [N/mm^2]	f_{ctm} [N/mm^2]	E_{cm} [N/mm^2]	f_y [N/mm^2]
33.0	2.8	28,800	552.0

and the results of ultrasound. For this reason, the load is finer graded in the initial range. Up to $2 \cdot F_{cr} \approx 100\,\mathrm{kN}$, it is increased in 5 kN steps. Thereafter, the increment is doubled until the reinforcement yields (end of range ③, corresponding load $F_y \approx 340\,\mathrm{kN}$). The significantly reduced stiffness of the specimen beyond this level rapidly leads to inconstant strains when yielding even on a fixed load level. Then US results can no longer be assigned to a distinct load level without doubt, and testing is consequently stopped.
The environmental conditions in the laboratory are held constant at approx. 22 °C and 52 % relative humidity.

6.3.5 Proof of Concept

With the FOS on the flexural reinforcement, strains are quasi continuously sensed along the entire beam (spacing of measurement points < 1 mm). Figure 6.6 displays such strain readings in the reinforcement (in blue) for a load of $F = 100\,\mathrm{kN}$. Cracks in the concrete are clearly indicated by the peaks. They are induced by the strains transferred from the reinforcement through bond. Their spacing is regular, as can be expected for the range of completed cracking ③. From the strain record, it can be seen that at that load, cracks have occurred almost over the entire specimen, not only in the central region of constant moment between the loads. Besides a rapid increase of the strains around the cracks, the curve is characterized by scatter. However, the magnitude of the scatter is small compared to the strain peaks.
For comparison the average steel strain in the reinforcement (orange) is computed employing Equations 6.3 to 6.6. Throughout the piece-wise defined mean function idealizes the measured course quite well. Depending on the bending moment in longitudinal direction, individual parts of the beam are assigned to the different ranges. The

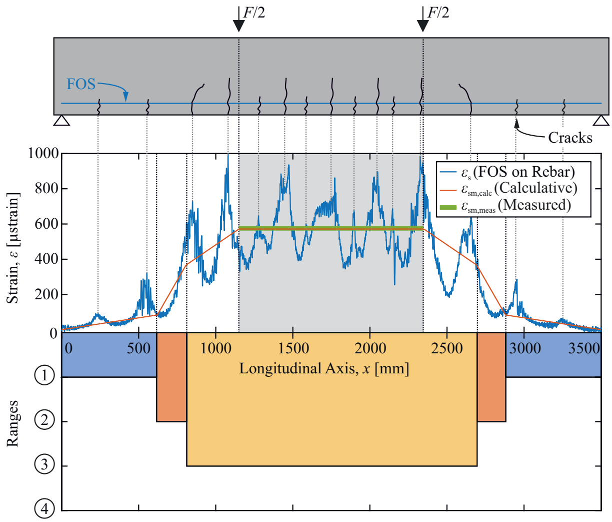

Figure 6.6: Top: Strain records of the FOS on the flexural reinforcement compared to theoretically expected average steel strains. Bottom: Associated ranges employing the σ_s - ε_{sm} relation on an equivalent load level.

non-cracked region close to the supports is followed by the range of cracking ② and the cracked region with completed crack-pattern ③ at center. In the measuring field between the loads, the strain is constant due to the constant bending moment. Here, the average steel strain (green) can be obtained, analog to Equation 6.2, from averaging the FOS readings over the measuring length, too.

$$\varepsilon_{\mathrm{sm}} = \frac{1}{1200\,\mathrm{mm}} \int_{1150\,\mathrm{mm}}^{2350\,\mathrm{mm}} \varepsilon_{\mathrm{s}}(x)\,\mathrm{d}x \qquad (6.7)$$

This average strain ($\varepsilon_{\mathrm{sm,meas}} = 571$ µstrain) is plotted in green in Figure 6.6. It nearly coincides with the theoretically predicted mean from calculation ($\varepsilon_{\mathrm{sm,calc}} = 572$ µstrain, orange). No doubt, at other load levels, the difference may be greater. However, in general computational prediction of material behavior by Equations 6.3 to 6.6, albeit idealizing, seems suitable and in good agreement with the high-resolution measurements by FOS.

6.4 Results and Discussion

6.4.1 Development of the Relative Velocity Change with Time and Load

On the left in Figure 6.7, the force F on the specimen is plotted versus the relative velocity change dv/v from CWI. All results of transmitter-receiver combinations from the compressive (orange) and tensile (green) zones, as well as the neutral axis (blue), are displayed. However, the selection has been limited to the next neighbors (sensor distance 30 cm) of the horizontal combinations only. For each zone, three curves are plotted since one sensor in the neutral axis failed. Due to the constant bending moment between the concentrated loads, all three combinations on each level form a set and theoretically represent identical states. In the non-cracked state, this is more easily recognized, since a homogeneous stress distribution theoretically exists throughout. Certainly, in the cracked state, this expectation seems justified, too, due to the uniformly distributed cracks caused by the load pattern and the integral sensing of the material by the US signal. Consequently, no further distinction must be made between the individual curves on the same level. They all have the same features and show the same characteristics. Deviations of the curves in a set from each other are attributed to inherent scatter, while the differences between the sets are seen significant in view of material response.

In general, all curves in the diagram show two almost linear branches and a range of transition in between. In the range from 0 to 50 kN, they have an initial slope which becomes flatter in transition between 50 and 75 kN and then remains approximately constant until the end. The change in slope is most pronounced for the tensile curves and weakest for the compressive ones. The US signal is more affected in the tensile range than in the compressive range, which is attributed to concrete cracking. Regarding their limits, the three ranges agree with the known limits of the material behavior.

Great similarity to the average strain in the reinforcement computed from the FOS readings according to Section 6.3.5 can be observed in Figure 6.7 on the right. Therein, the evolution of the average steel strain with load is shown. The parallelism between the characteristics of the F - dv/v relation and those of the $\varepsilon_{\mathrm{sm}}$ - σ_{s} relation becomes apparent. The following conclusions are drawn:

1. Cracking strongly affects the US signal and the key quantities computed with CWI, the correlation coefficient CC and the relative velocity change dv/v.

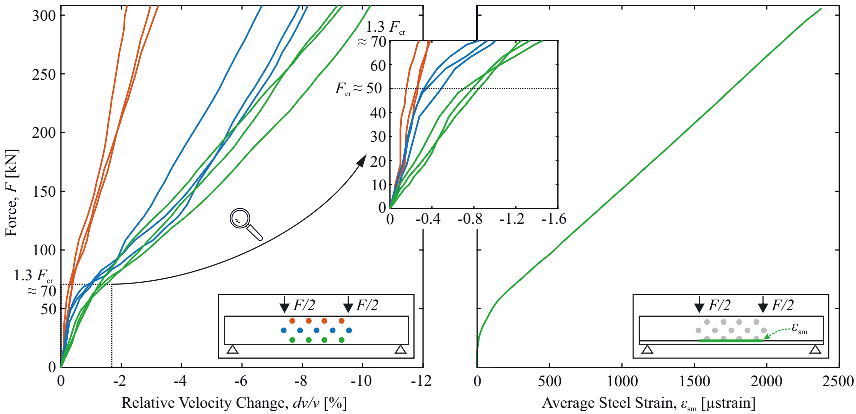

Figure 6.7: Load of the specimen plotted versus the relative velocity change (left) with particular focus on the non-cracked ① and cracking ② range and average steel strain (right).

2. The relative velocity change is always negative.

3. Characteristic points associated with significant changes in the material response F_{cr} and $1.3 \cdot F_{cr}$ can be identified in the F - dv/v relation, too.

4. A fundamental change of the load-bearing behavior happens in the range of cracking ② and is also predicted by the F - dv/v relation.

5. In agreement with the decreasing slope of the ε_{sm} - σ_s relation , the slope of the F - dv/v relation decreases in transition from the non-cracked to the cracked state.

As expected and illustrated in Figure 6.7, the curves of sensor pairs in the neutral axis fall between the compressive and tensile sets of curves. More precisely, they are first oriented towards the curves of the compressive set. However, then, with cracking, they tend to follow the tensile set, which leads to the following conclusions:

1. The closer a sensor pair is located to the tensile zone, the more the relative velocity change drops.

2. With load increase, cracks gradually grow towards the compressive zone at top. This is well-reflected by the trend of the central axis' gradient towards the tensile one. As the cracks approach the centerline transducers, the US signal is affected more like the signal in the tensile zone.

3. Not even in the non-cracked state with linear elastic material behavior, the central trend is the average of compressive and tensile trends. Thus, the relative velocity change develops non-linear with the load.

Confined to purely mechanical considerations, influences from elastic strain and, above all, from cracks are inseparably linked to the signal. The scanned volume (cf. Figure 6.1) integrates and mixes impacts from unloaded, elastically loaded and cracked regions. Their proportions are reflected in the magnitude of the relative velocity

change.
Moreover, uncertain onset of cracking, load-dependent crack growth, as well as the variable compressive and tensile zone heights, cause these proportions to vary with time and load. Different sensitivity to tensile and compressive strains in general and with respect to the material state, cracked or non-cracked, is another factor that affects the magnitude of the relative velocity change.

6.4.2 Establishing a Correlation Function

Figure 6.8 combines the average steel strain computed from the FOS results and the relative velocity changes of the US transducer pairs in the tensile zone from Figure 6.7. Both are coupled via the load level. Three nearly straight curves are obtained. Even at first glance, average steel strain and relative velocity change appear to be linearly correlated. By linear regression, the correlation function according to Equation 6.8 can be established with great confidence.

$$\varepsilon_{\mathrm{sm}} = c \cdot dv/v \qquad \text{with} \quad c = const. \left[\frac{\mu\mathrm{strain}}{\%}\right] \tag{6.8}$$

Therein, strain is to be inserted in µstrain and the relative velocity change in %. The constant c has to be determined on each individual member. In our case c equals $-280\,\mu$strain/%. This model yields a coefficient of determination of 0.99 explaining 99 % of the strain variation by variation of the relative velocity change. The error is small and quantified to 88 µstrain on average by the Root Mean Squared Error (RMSE).
The model is ready to be used to infer from US measuring data and thereof computed relative velocity changes on the average steel strain in the sensed member.
Finally, the model's range of applicability shall be discussed. In the experiment, the load is increased step-wise up to 300 kN at maximum. Up

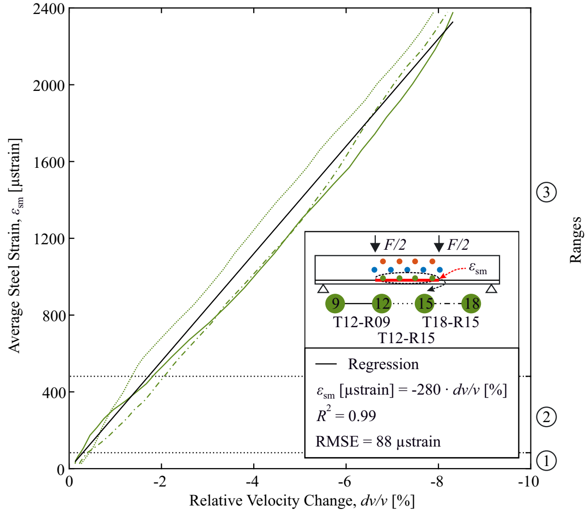

Figure 6.8: Correlation of average steel strain to relative velocity change.

to this load level, relative velocity changes and reinforcement strains are carefully tracked. From the member's design according to EC 2 [41], yielding of the reinforcement is expected at a load level of 340 kN, while the ultimate load-bearing capacity is reached at 375 kN. Thus, the model covers 80 % of the permissible load range.

Since no significant changes in the load-bearing behavior are to be expected from mechanical reasons until the reinforcement yields, the model can even be used beyond the experimentally validated range. With yielding, 90 % of the permissible load range would finally be covered by extrapolation. Both go significantly beyond any other correlations of ultrasonic and structural parameters of RC members found so far, which are all limited to the linear elastic range.

6.4.3 Impact of the Transducer Distance

The proposed model is based on US measurement data from transducer pairs of 30 cm distance throughout. This distance is not particularly long, neither with regard to usual RC members, nor (and even more so) with regard to the monitoring of entire structures. For reasons of costs and installation, the aim is to use fewer, i.e., more distant, sensors. In construction practice, the optimum is often a compromise between costs and density of the sensor network. Therefore, it has finally been investigated whether a tripled/quadrupled transducer distance has an impact on the obtained results or the found model.

The issue is addressed in Figure 6.9. At first, a mean response (dashed line) is computed from the results of the three sensor pairs per level already shown in Figure 6.7. Moreover, a shaded band of scatter is provided, that marks the minimum and maximum relative velocity changes on all load levels. Both rest on the short transducer distance of 30 cm.

From the recorded US data, the results for the longest transducer distances are then computed analogously. They are shown as solid lines and cover distances of 90 up to 120 cm. All three

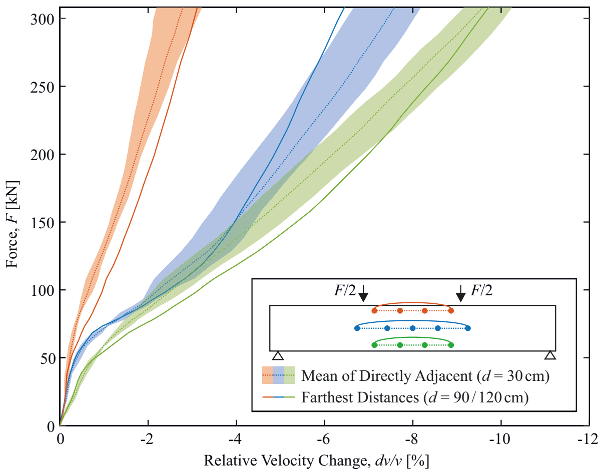

Figure 6.9: Fitting of longer transmitter-receiver combinations in the presented shorter ones.

follow the mean courses and preserve the key characteristics of the initial curves. No clearly deviating trends can be identified. Thus, it is concluded that even with greater transducer distances, a similar model would be obtained. As long as this is not available, the proposed model might be used instead. One must not expect significant deviations in the proposed steel strains.

6.5 Conclusions

In the context of an ever-increasing need for structural health monitoring of existing RC structures, the paper links essential key parameters computed from the coda of US signals to structural state variables and their evolution with time and load. Based on empirical data obtained on a simply supported RC beam subjected to four-point bending, a linear model is derived that correlates the relative velocity change of the coda dv/v to the mean strain of the reinforcement ε_{sm} from FOS. Mechanically, ε_{sm} integrates all characteristics of RC structures as known from moment-curvature relations and enables to infer the material state consistently. In detail:

- For the first time, a correlation between a key parameter of ultrasound and a structural state variable is established that covers 90 % of the complex load-bearing behavior of RC members. It integrates load-dependent stiffness and concrete cracking.
- For the beam and a sensor distance of 30 cm, a linear model is established with great confidence: $\varepsilon_{\text{sm}} = c \cdot dv/v$ with: $c = -280,\ R^2 = 0.99,\ \text{RMSE} \approx 90\,\mu\text{strain}$.
- Tripled sensor distances do not impair the proposed correlation function much.
- Whether in compression or tension, dv/v obtained from step-wise CWI is found to be negative throughout.
- The closer a sensor pair is located to the tensile zone, the more dv/v drops.
- Although dv/v always integrates elastic effects as well as micro- and macro-cracking, the latter seems to dominate. Compared to the compressive zone, dv/v is more sensitive to changes in the tensile zone.
- Conversely, changes in the compressive zone are more difficult to detect because they are easily superimposed by tension.

Of course, a general, component-independent correlation relationship for arbitrary RC members has not yet been established. Just a possible approach to achieve this goal has been shown. To get there, further experiments are certainly needed, which have to cover not only structural quantities or different concrete composition but also environmental conditions and changes of these. The wide range of influences on the US signal has to be considered for real-world application of this approach. With the consideration of environmental conditions and structural influences, the presented approach can be used to infer the loading of the RC structure by US measurements. A statement about its health becomes possible.

Chapter 7

Supplement: Fiber Optic Sensing of Strain and Temperature Fields

The following chapter is taken verbatim from:

> KONERTZ, D.; LÖSCHMANN, J.; CLAUß, F. and MARK, P. *Faseroptische Messung von Dehnungs- und Temperaturfeldern*. Bauingenieur, 2019. 94(7/8): pp. 292–300. doi: 10.37544/0005-6650-2019-07-08-70.

Text and figures have been adjusted to the format and layout of this thesis. The content remains identical. The literature used is jointly referred to at the end of the thesis.

Abstract

Fiber optic sensing allows an almost continuous recording of strains and temperatures along measuring fibers. For strain measurement, the fiber should be applied directly to the component with adhesives. For temperature measurements, the fiber should usually be sheltered and guided un-bonded in capillaries. Field-like, two-dimensional recordings are obtained either when the fibers are arranged crosswise in a grid or from interpolations between several staggered and graded fibers regarding the expected gradients. The paper presents the basic measuring principles of fiber optics, achievable accuracies, suitable applications in reinforced concrete members and the field-like recording of strains and temperatures. Practical application is demonstrated by means of strain sensing on anchor channels and temperature field recording in reinforced concrete beams.

Faseroptische Messung von Dehnungs- und Temperaturfeldern

Faseroptische Messsysteme ermöglichen eine nahezu kontinuierliche Aufnahme von Dehnungen und Temperaturen entlang einer Messfaser. Zur Dehnungsmessung sollte die Faser mit Klebern direkt auf dem Bauteil appliziert werden, bei Temperaturmessungen in der Regel geschützt und verbundlos in Kapillaren geführt sein. Feldartige, zweidimensionale Aufnahmen entstehen entweder, wenn die Fasern kreuzweise gerastert angeordnet sind oder aus Interpolationen zwischen mehreren, nach den erwarteten Gradienten gestaffelten Fasern einer Verlegerichtung. Der Beitrag stellt die grundlegenden Messprinzipien der Faseroptik, erzielbare Genauigkeiten, geeignete Applikationen in Stahlbetonbauteilen und die feldartige Messung von Dehnungen oder Temperaturen vor. Beispiele der Dehnungsmessung an Ankerschienen und der Temperaturfeldaufnahme in einem Stahlbetonbalken zeigen die praktische Anwendung.

7.1 Einleitung

Der Erfassung von Dehnungs- und Temperaturwerten kommt im Bauwerksmonitoring oder in der experimentellen Forschung wichtige Bedeutung zu. Güte und Dichte der Messergebnisse sind dabei entscheidend für die Auswertung und Interpretation des untersuchten Tragverhaltens. Faseroptische Messsysteme ermöglichen eine quasikontinuierliche Messpunktfolge entlang einer Messfaser mit einer Auflösung im Millimeterbereich. Im Gegensatz zu konventioneller Messtechnik (z. B. Dehnungsmessstreifen) sind damit auch Untersuchungen lokaler Phänomene möglich, ohne zuvor deren Ort exakt kennen zu müssen. Die Fasern lassen sich flexibel biegen, sodass sie linienartig, in Schlaufen oder in räumlichen Kurven nutzbar sind. So lassen sich Messwerte an Linien (1D), in Flächen (2D) oder auch Räumen (3D) direkt beziehungsweise durch Interpolationen bestimmen. Neben hochauflösenden Anwendungen mit Sensorlängen im Meterbereich sind auch Messungen über große Längen, zum Beispiel mehrere Kilometer, möglich. Entsprechende Systeme weisen zwar größere Messpunktabstände auf, eignen sich dafür aber beispielsweise für das Monitoring von Rohrleitungen im Kilometermaßstab [105].

Aufgrund der geringen Querschnittsabmessung lassen sich faseroptische Sensoren auf der Oberfläche, aber auch innerhalb von Bauteilen applizieren ohne makroskopische Verhaltensweisen wesentlich zu beeinflussen. Dabei sind sie vielfältig einsetzbar, da sie sowohl starken magnetischen Feldern, hohen Temperaturen als auch chemisch aggressiven Medien standhalten und daraus kaum relevante Beeinflussungen der Messungen auftreten.

Die Entwicklung faseroptischer Messsysteme ist eng verbunden mit dem Fortschritt der glasfaserbasierten Telekommunikationstechnik. Durch das Einschreiben von Faser-Bragg-Gittern in Glasfasern waren in den 1990er-Jahren erstmals verteilt messende Systeme kommerziell verfügbar [105]. Weitere Entwicklungen auf Basis der optischen Rückstreuung, die zunächst auf die Prüfung von Fasern ausgerichtet waren, führten dazu, dass heute auch Systeme mit quasikontinuierlicher Messpunktfolge zur Verfügung stehen. Zudem führte die rasche Entwicklung im Telekommunikationsbereich zu einer deutlichen Kostenreduktion, auch im vergleichsweise kleinen Segment der faseroptischen Messtechnik.

Im Beitrag werden die Grundlagen der faseroptischen Messung dargestellt und anschließend auf die quasikontinuierliche Messung eingegrenzt. Beispiele von feldweiser Temperatur- wie Dehnungsmessung zeigen die praktische Anwendung.

7.2 Grundlagen der faseroptischen Messung

7.2.1 Messprinzipien

Faseroptische Messsysteme erfassen Dehnungs- und Temperaturänderungen entlang einer Messfaser über die Auswertung von Rückstreusignalen eines emittierten Lichtstrahls. Je nach Messsystem werden unterschiedliche Rückstreusignale verwendet. Es wird zwischen Rayleigh-, Brillouin- und Raman-Rückstreuung unterschieden (Bild 7.1). Die spektralen Komponenten der Rückstreuungen resultieren aus der Interaktion des Lichtes mit der Glasfaser. Dabei ist die Rayleigh-Rückstreuung auf Schwankungen des Brechungsindexes infolge von Inhomogenitäten des Glasfaserkerns, wie Dichteschwankungen und Einschlüssen, zurückzuführen. Der Raman-Effekt entsteht durch thermisch-molekulare Schwingungen und die Brillouin-Rückstreuung durch Photonen-Phononen-Interaktionen [80, 105].

Die Komponenten des Rückstreusignals unterscheiden sich in ihrer Intensität und Frequenz. Die Intensität der Rayleigh-Rückstreuung ist nahezu unabhängig vom Temperatur- und Dehnungszustand der Faser [48]. Sie weist keine Frequenzverschiebung zum eingesendeten Lichtsignal auf und ist der stärkste Streuprozess [47]. Inelastische Streuprozesse wie die Brillouin- und Raman-Rückstreuung sind hingegen dadurch gekennzeichnet, dass die Frequenz des rückgestreuten Lichtes kleiner oder größer als die Frequenz des emittierten Lichtes ist. Der Frequenzversatz ist dabei materialabhängig. Die Intensität beider Komponenten ist abhängig von

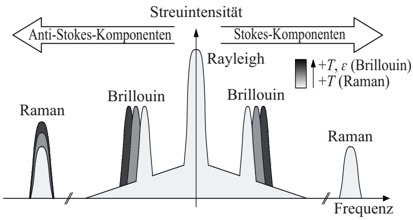

Bild 7.1: Lichtstreuung in faseroptischen Sensoren nach [148]

Figure 7.1: Light scattering in fiber optic sensors according to [148]

der Temperatur, die der Brillouin-Streuung zusätzlich von der Dehnung der Messfaser.
Den Eigenschaften der Rückstreukomponenten entsprechend, eignen sich die darauf basierenden Messverfahren für unterschiedliche Anwendungen. Ein Unterscheidungsmerkmal ist dabei die Ortsauflösung der jeweiligen Systeme, die von diskreten Punktsensoren bis zu einer quasikontinuierlichen Messpunktfolge reicht (Bild 7.2).
Verteilt messende Systeme, die auf der Raman- und Brillouin-Rückstreuung basieren, ermöglichen Temperatur- oder Dehnungsmessungen auf großen Längen von bis zu 50 km [105]. Sie eignen sich zum Beispiel für das Monitoring von Brücken, langen Rohrleitungen oder Deichen und können dort konventionelle Messtechniken ersetzen oder sinnvoll ergänzen [1, 163, 164]. Aufgrund der geringen Intensität des Rückstreusignals beträgt der minimale Messpunktabstand der Sensoren in diesen Fällen 1 m [105].
Quasikontinuierliche Messungen mittels Rayleigh-Rückstreuung eignen sich für vergleichsweise geringe Strecken bis zu 100 m [79], ermöglichen allerdings eine Messpunktfolge im Millimeterbereich. Sie bieten sich für Messungen an vergleichsweise kleinen Prüfkörpern und Detailuntersuchungen wie Spannungslokalisierungen an.

7.2.2 Sensorfasern

Übliche Glasfasern für faseroptische Messungen bestehen aus einem inneren Kern (Core) als Lichtwellenleiter, einem Mantel (Cladding) sowie einer äußeren Beschichtung (Coating). Der innere Kern sowie der Mantel bestehen zumeist aus SiO_2-Glas (Quarzglas) und unterscheiden sich in ihrem Brechungsindex [47]. Die Bruchdehnung solcher Fasern liegt bei circa 2 % bis 5 % [148]. Ohne eine äußere Beschichtung ist die Faser aufgrund der zu hohen Bruchge-

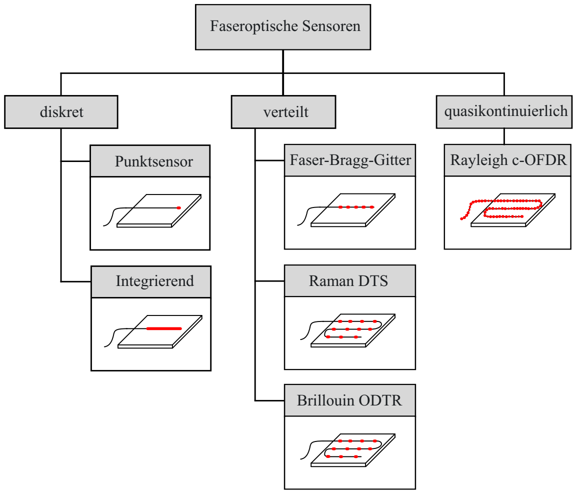

Bild 7.2: Klassifizierung faseroptischer Messsysteme nach [105]

Figure 7.2: Classification of fiber optic sensing systems according to [105]

fahr kaum nutzbar. Die zum Schutz aufgetragene Beschichtung kann der Anwendung angepasst werden und besteht üblicherweise aus Kunststoffen wie Polyimid oder Acrylat beziehungsweise Gold für den Einsatz bei hohen Temperaturen. Derart beschichtete Fasern eignen sich aber nur für den Einsatz unter Laborbedingungen. Zusätzliche Kabelmäntel, je nach Anforderung auch stahlbewehrt, ermöglichen den Einsatz in der Praxis, zum Beispiel der Geotechnik [97]. Robust ausgeführte Faserkabel können auch direkt in eine Betonmatrix eingebettet werden, um die Dehnung direkt im Betonbauteil zu erfassen [56, 80].

Es kann unterschieden werden zwischen sogenannten „Singlemode“ und „Multimodefasern“, die sich durch die Anzahl der ausbreitenden Schwingungsmoden in der Faser definieren. Diese Eigenschaft ist direkt abhängig von der Größe des Faserkerns. Besonders in der Telekommunikation werden Multimodefasern eingesetzt, da die Anzahl der Moden die getrennt voneinander übertragbaren Signale bestimmt. Bei den in diesem Beitrag im Fokus stehenden Messungen mittels Rayleigh-Rückstreuung ist hingegen lediglich die Verwendung einer Singlemode-Faser möglich [105, 148]. Die Faser dient dabei selbst als Sensor (Abschnitt 7.3.1) und ist in Bild 7.3 mit den in etwa üblichen Abmessungen für Kern, Mantel und Beschichtung dargestellt.

Die Sensoren können in gestaffelten Längen direkt vom Hersteller bezogen oder für eine bestimmte Anwendung selbst maßgeschneidert hergestellt werden. Die Verwendung möglichst passgenauer Fasern erleichtert die Handhabung und verringert das Risiko von Beschädigungen, da die freiliegenden Faserbereiche kurz gehalten werden. Bei der Herstellung wird der Sensor aus mehreren Komponenten zusammengesetzt (Bild 7.4), indem die eigentliche Messfaser jeweils mit einem Zuleitungskabel sowie

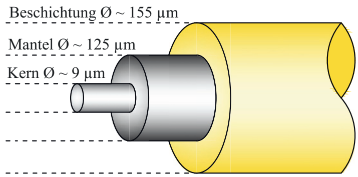

Bild 7.3: Aufbau einer Glasfaser (Singlemode), stark vergrößert

Figure 7.3: Structure of a glass fibre (single-mode), strongly enlarged

dem späteren Faserende („Terminierung“) verspleißt wird. Die gegenüber mechanischen Einwirkungen empfindliche Glasfaser ist an den Spleißstellen besonders bruchempfindlich und wird dort mit einem Spleißschutz versehen. Die Faser der Terminierung unterscheidet sich in ihren Eigenschaften (Brechungsindex) von der Messfaser. Wird sie in engen Radien um den Spleißschutz gewickelt, verlässt das Lichtsignal den Faserkern. Eine Reflexion am Faserende würde die entlang der Faser rückgestreuten Anteile überlagern und eine Messung verhindern.

7.2.3 Applikation

Allgemeines

Die Gesamtdehnung der Glasfaser setzt sich aus temperatur- und lastinduzierten Anteilen zusammen. Für eindeutige Auswertungen ist daher stets eine der beiden Größen konstant zu halten oder über Kompensationsmessungen zu bestimmen. Finden beispielsweise Dehnungsmessungen nicht in einem Labor unter konstanten Temperaturbedingungen statt, sind isolierte Temperaturmessungen erforderlich, um den mitgemessenen Anteil aus Temperaturänderungen zu quantifizieren. Bei Temperaturmessungen sind mechanisch bedingte Dehnungen der Faser auszuschließen, zum Beispiel durch entkoppelte Führung in Kapillaren. Bei der Applikation ist zu beachten, dass die

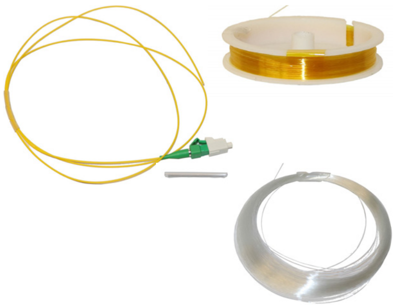

Bild 7.4: Komponenten zur Herstellung faseroptischer Sensoren

Figure 7.4: Components for the manufacturing of fiber optic sensors

Faser weder geknickt noch in zu engen Radien verlegt wird. Minimal einzuhaltende Ausrundungsradien liegen dabei im Bereich von 10 mm [123] und sind neben der mechanischen Bruchgefährdung auch von der Lichtleitfähigkeit des inneren Kerns abhängig. Es gilt sicherzustellen, dass an der Grenzschicht zwischen Kern und Coating eine Totalreflexion des emittierten Lichts stattfindet. Bei zu geringen Biegeradien verlässt das Licht den inneren Kern und verhindert dann eine Messung.

Unter Berücksichtigung dieser Randbedingungen können Fasern in beliebigen, stetigen Kurven auf und in Prüfkörpern verlegt werden. Dies ermöglicht durch die Kombination übereinander oder nebeneinander liegender Segmente die Erfassung von ebenen und dreidimensionalen Feldern bei der Verwendung von nur einer Faser. Nachfolgend werden die Grundlagen der Faserapplikation bei Dehnungs- und Temperaturmessungen getrennt voneinander beschrieben.

Dehnungsmessung

Bei der Applikation von Sensorfasern zur Dehnungsmessung ist es entscheidend, dass die Dehnung des Bauteils möglichst direkt auf die Faser übertragen wird. Für einen optimalen Verbund ist zunächst ein geeigneter Kleber in Abhängigkeit vom Material des Prüfkörpers zu wählen. Zudem muss berücksichtigt werden, welchen Umgebungsbedingungen und äußeren Einflüssen der Kleber standhalten muss. Bei der Applikation auf Stahl- und Aluminiumoberflächen bietet sich zum Beispiel Cyanacrylatkleber an [172, 182]. Dieser eignet sich nach [56] auch für die Applikation auf Betonoberflächen. Neben der Wahl des Klebers ist die Oberflächenreinigung des Prüfobjektes von besonderer Bedeutung. Die Oberfläche sollte staub- und fettfrei sein.

Einen wichtigen Einfluss besitzt die Faser selbst. Für die direkte Übertragung der Dehnung vom Prüfkörper in den eigentlichen Messkern sollte das Coating schubsteif sein. Hierfür eignen sich zum Beispiel Coatings aus Polyimid. Weichere Materialien wie Acrylat verteilen lokale Dehnungsspitzen im Messobjekt über einen Bereich der Faser [182]. Dies kann zum Schutz der Faser von Vorteil sein, wenn sonst die Bruchdehnung überschritten werden würde. Allerdings werden lokale Dehnungsmaxima dadurch verfälscht verschmiert dargestellt. Neben einem weicheren Coating können auch zusätzliche schützende Umhüllungen eingesetzt werden (z. B. Polymermatrix). Arbeiten zum Einfluss weicher Umhüllungen beschäftigen sich mit der rechnerischen Berücksichtigung der Unterschiede zwischen gemessener und tatsächlich vorhandener Dehnung [13]. Dadurch sind auch Rückschlüsse auf nicht direkt messbare Rissweiten möglich [17].

Temperaturmessung

Die Applikation zur alleinigen Bestimmung von Temperaturen unterscheidet sich grundlegend von der Verklebung bei Dehnungsmessungen. Für eine eindeutige Auswertung von Temperaturänderungen dürfen sich Bauteildehnungen – egal ob aus mechanischer oder thermischer Beanspruchung – nicht auf die Glasfaser übertragen. Dies ist mit Kapillaren (Durchmesser: $\sim$ 0,5 mm bis 1,0 mm) realisierbar, in welche die Sensorfasern verbundlos eingelegt werden (Bild 7.5). Die Fasern erfahren dann ausschließlich thermische Dehnungen. Als Kapillarmaterial bieten sich elastische Kunststoffe wie Ethylen-Tetrafluorethylen (ETFE) an. Die Messfaseranordnung ist grundsätzlich frei wählbar. Jedoch werden in regelmäßigen Abständen Punkte zum Fixieren der Kapillare benötigt, wie zum Beispiel die Bewehrung in Stahlbetonkörpern (Bild 7.5). Darüber hinaus ergeben sich unterschiedliche Einschränkungen aus dem Zeitpunkt der Integration einer Messfaser in eine Kapillare. Bei kurzen Fasern ist ein nachträgliches Einschieben in eine bereits einbetonierte Kapillare möglich. Dabei sind Grenzwerte für Kapillarinnendurchmesser und -biegeradien einzuhalten, damit die Terminierung – das steife Faserendstück – durch gekrümmte Kapillaren geschoben werden kann. Der Mindestbiegeradius sollte dazu bei einem Kapillarinnendurchmesser von 0,75 mm und einem gängigen Sensordurchmesser von 0,3 mm mindestens 5 cm betragen (Bild 7.5). Aufgrund des ansteigenden Reibwiderstands und der hohen Schubempfindlichkeit von Glasfasern ist die einführbare Faserlänge allerdings auch bei Einhaltung dieser Randbedingungen begrenzt. Der nachträgliche Einschub bietet sich daher nur bei kurzer Messlänge (wenige Meter) oder gerader Sensorführung an.

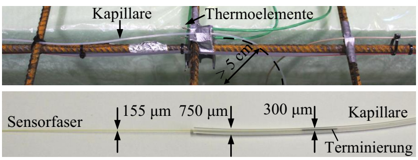

Bild 7.5: Führung von Sensorfasern in Kapillaren (unten) und eingebaute Kapillare fixiert an Bewehrung (oben)

Figure 7.5: Installation of sensor fibers in capillaries (bottom) and capillary fixed to reinforcement (top)

Größere Messlängen und kleinere Biegeradien sind möglich, sofern die Faser schon vor dem Fixieren und Betonieren in eine Kapillare integriert wird. Ein solches Messkabel ermöglicht eine nahezu freie Faseranordnung, sodass nicht nur Messungen linienartiger, sondern auch ebener und dreidimensionaler Temperaturfelder realisierbar sind. Dabei ist lediglich der Mindestbiegeradius der Glasfaser einzuhalten. Die Kapillarinnendurchmesser können kleiner als beim nachträglichen Einschub gewählt werden, so dass die Luftschicht zwischen Faser und Kapillarinnenwand minimiert wird. Bei Innendurchmessern von 0,75 mm kann die isolierende beziehungsweise verzögernde Wirkung der Luftschicht bei ambienten Bedingungen beziehungsweise üblichen Wärmeausbreitungen in Probekörpern bereits vernachlässigt werden. Referenzmessungen an Betonkörpern haben gezeigt, dass in der Kapillare nahezu die Temperaturen des umgebenden Betons vorliegen (Abschnitt 7.4.3).

Vorgefertigte Messkabel, bei denen die Faser bereits in die Kapillare eingeschoben wurde, müssen beim Betonieren und Ausschalen mit Sorgfalt behandelt werden, um Schädigungen – die dann zum Ausfall des gesamten Sensors führen – zu vermeiden. Eine Wiederverwendung von fertigen Messkabeln ist in der Regel nicht möglich.

Messung von Feldern

Feldartige Aufnahmen von Temperaturen oder Dehnungen entstehen aus der quasikontinuierlichen Linieninformation entlang einer beliebig gekrümmten Faser (Bild 7.6a) und Interpolationen zwischen den Fasern selber (Bild 7.6b). Dabei ist die Informationsdichte entlang der Faser üblicherweise größer als die nur auf Einzelpunkten gestützte Interpolation, sodass es sich empfiehlt die Fasern bei Temperaturmessungen in Richtung der erwartet hohen Messwertänderungen zu verlegen. Dehnungen können hingegen als gerichtete Größen ausschließlich in Faserrichtung gemessen werden. Treten hohe Messwertänderungen senkrecht zu der zu erfassenden Dehnung auf, kann dieser Verlauf nur durch parallel geführte Fasern erfasst werden (Bild 7.6b). Ähnlich der adaptiven Verfeinerung zur Vernetzung mit Finiten Elementen (z. B. [8]) sollte bei hohen erwarteten Gradienten der Messgröße ein kleinerer Faserabstand, bei geringen Gradienten ein größerer Abstand gewählt werden. Bild 7.6b zeigt das Prinzip. Günstig sind meist

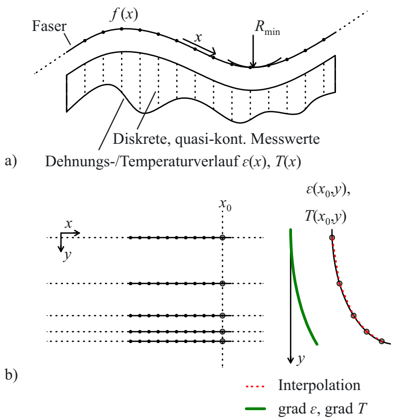

Bild 7.6: a) Quasikontinuierliche Messung entlang einer Kurve, b) Abstandsrasterung nach erwarteten Gradienten

Figure 7.6: a) Quasi-continuous measurement along a curve, b) Grid spacing according to expected gradients

Anordnungen in Schlaufen (Bild 7.7b) oder – zur Erfassung zweiachsiger Dehnungszustände – in Schlaufenrastern (Bild 7.7c).

Wesentlich für die Auswertung ist es, jedem Punkt entlang der Faser den tatsächlichen Ort im Messfeld zuordnen zu können (Bild 7.7a). Dies ist durch gezielte, lokale Erwärmung der Faser an einem beliebigen Ort möglich ($x_1, x_2 \cdots x_i$; Bild 7.7b). Die zum Beispiel mit einer erhitzten Stecknadel markierte Stelle wird bei laufender Messung sichtbar und kann von einigen Systemen automatisch erfasst werden („Touch to locate“).

7.2.4 Randbedingungen

Bei Glasfasersensoren ohne äußeren Schutzmantel, die häufig unter Laborbedingungen zum Einsatz kommen, spielt ihr Schutz zur Vermeidung von Beschädigungen eine wichtige Rolle. Die geringe Robustheit gegenüber mechanischen Einwirkungen erfordert eine durchgehend vorsichtige Handhabung von der Herstellung und Applikation der Sensoren über die Vorbereitung bis zur Durchführung der Messungen. Eine einzelne Beschädigung, egal an welcher Stelle, schließt die Verwendung des gesamten Sensors aus. Schutzmaßnahmen verbessern die Robustheit, jedoch verbleibt eine weit höhere Empfindlichkeit im Vergleich zu herkömmlicher Messtechnik, wie zum Beispiel DMS. Es empfiehlt sich freiliegende Abschnitte der Faser in einem Schutzschlauch, zum Beispiel aus Teflon oder einen gummierten Schrumpfschlauch, zu führen.

Besondere Schutzmaßnahmen sind bei Anwendungen in Betonbauteilen erforderlich, wenn Dehnungen zum Beispiel entlang eines Bewehrungsstabs oder an Verankerungsmitteln gemessen werden. In eigenen Experimenten führte der direkte Kontakt zwischen Beton und

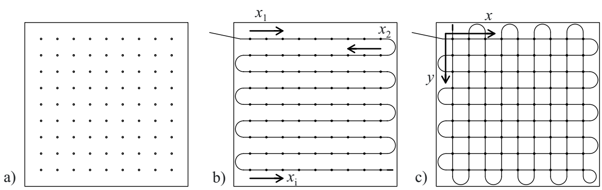

Bild 7.7: Zu erfassende Punkte in einem gleichmäßigen Raster (a) von Temperaturen (b) oder zweiachsigen Dehnungen (c)

Figure 7.7: Measurement in a uniform grid (a) of temperatures (b) or biaxial strains (c)

der mit Messtechnik versehenen Stahloberfläche häufig zum Versagen des Sensors [172]. Abhilfe kann das Trennen der Oberflächen mittels PTFE-Folie (Polytetrafluorethylen) [14] und einer Polystyrolschicht schaffen. Allerdings hebt eine solche Trennung den Verbund zwischen beiden Oberflächen auf und beeinflusst eventuell den Tragmechanismus. Alternativ kann die Faser in einer eingefrästen Nut appliziert werden [73].

7.3 Quasikontinuierliche Messsysteme mittels Rayleigh-Rückstreuung

7.3.1 Funktionsweise und Eigenschaften

Das in dieser Arbeit genutzte Messsystem ODiSI-B der Firma Luna Technologies Inc. basiert auf dem Konzept der Rayleigh-Rückstreuung. Es arbeitet mit dem Verfahren der kohärenten optischen Frequenzbereichsreflektometrie (c-OFDR, engl. coherent Optical Frequency Domain Reflectometry). Dabei leitet ein durchstimmbarer Laser Licht in den Sensor, welches entlang der Faser infolge von Inhomogenitäten der Silikatstruktur im Kern rückgestreut wird. Jede Glasfaser weist aufgrund ihrer spezifischen Silikatstruktur ein unverwechselbares Grundcharakteristikum auf („Nullmessung“ bzw. „Fingerprint“). Die Rückstreusignale werden mit der Nullmessung verglichen und erfahren bei äußerer Einwirkung Frequenzverschiebungen (Bild 7.8). Diese werden über Koeffizienten in Temperatur- oder Dehnungsänderungen umgerechnet [56, 148, 161, 182].

Für die Auswertung der durch Temperaturänderung oder mechanische Dehnung veränderten Rückstreusignale wird die Faser in Auswertefenster eingeteilt, in denen jeweils ein Messwert ermittelt wird. Die Länge dieser Fenster und der Abstand einzelner Messpunkte kann dabei prinzipiell frei gewählt werden. Bei sehr kleinen Fenstern ist so eine (makroskopisch) quasikontinuierliche Messpunktfolge möglich. Grenzen sind dabei durch die Datenverarbeitung

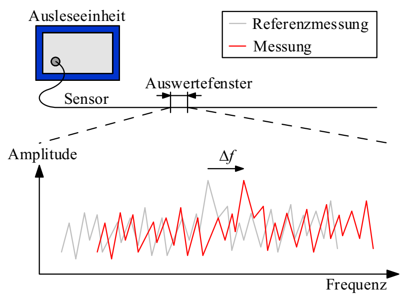

Bild 7.8: Frequenzverschiebung in einem Auswertefenster

Figure 7.8: Frequency shift in the evaluation block

gesetzt. Beim verwendeten System sind vier Messmodi vorgesehen, die Messpunktabstände bis minimal 0,65 mm ermöglichen (Tabelle 7.1). Tabelle 7.1 fasst für die vier Messmodi (erste Zeile) die wesentlichen Randbedingungen und erzielbaren Genauigkeiten nach Herstellerangaben zusammen. Sensorlängen können bei Messpunktabständen von wenigen Millimetern bis etwa 20 m betragen. Messfrequenzen bis 50 Hz und darüber reichen für quasistatische Beanspruchungen beziehungsweise übliche Temperaturänderungen aus Wärmetransporten bei Bauteilen beziehungsweise Bauwerken sicher aus. Die Genauigkeit der Dehnungsmessung liegt bei etwa 0,03 ‰, was durch eigene Experimente an Stahlproben mit konventioneller Messtechnik (DMS) und analytischen Vergleichen verifiziert wurde. Auch die Wiederholgenauigkeit, die im Versuch als Messrauschen zu erkennen ist, konnte für Dehnungs- sowie Temperaturmessungen bestätigt werden.

Eingesetzt werden kann das System für Dehnungen von ±10 ‰ und Temperaturen zwischen −50 °C und 300 °C, falls entsprechend temperaturbeständige Fasern genutzt werden.

7.3.2 Grenzen der Auflösung

Die räumliche Auflösung ist durch die minimale Größe der sogenannten Auswertefenster begrenzt. Dehnungen werden darin als Mittelwerte bestimmt. Beim genutzten System beträgt die kleinste Fensterlänge 1,3 mm. Durch Überlappung der Fenster reduziert sich der Messpunktabstand auf die Hälfte, also 0,65 mm. Bei lokalen Dehnungsspitzen wie etwa an Kerben werden die Extrema daher unterschätzt. Bild 7.9 zeigt dies an einem theoretischen Beispiel. Aus den Werten an den Messpunkten bei treppenartig konstanter Auflösung (schwarze Balken) ist durch lineare Interpolation (grüne Linien) beziehungsweise eine polynomiale Ausgleichskurve (rote Kurve) die tatsächliche Dehnungsverteilung $\varepsilon(x)$ angenähert. Erwartungsgemäß wird der Spitzenwert nicht erreicht.

Die zeitliche Auflösung ist durch die Messfrequenz und die zeitliche Variabilität der Messgröße bestimmt. Dazu sollten bei Schwingungsuntersuchungen die üblichen Grenzen der Abtastung beachtet werden (z. B. [8]), also mehrere (> 10) Messzeiten je Periode vorgesehen sein.

Tab. 7.1: Messmodi des Systems ODiSI-B mit Randbedingungen und Genauigkeiten

Table 7.1: Modes of operation ODiSI-B with limits and accuracies

Messmodus		Standard	High-Speed	High-Resolution	Extended Length
Maximale Sensorlänge	m	10	2	10	20
Messfrequenz	Hz	100	250	23,8	50
Messlänge	mm	5,2	5,2	1,3	5,2
Messpunktabstand	mm	2,6	2,6	0,65	2,6
Genauigkeit Dehnung	$\mu\varepsilon$	± 30	± 30	± 25	± 25
Wiederholgenauigkeit Dehnung	$\mu\varepsilon$	± 5	± 5	± 20	± 10
Wiederholgenauigkeit Temperatur	°C	± 0,4	± 0,4	± 1,6	± 0,8

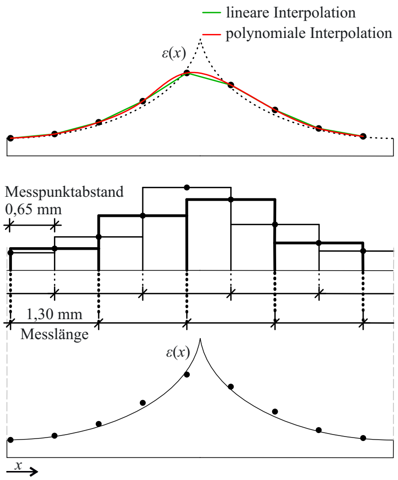

Bild 7.9: Dehnungsverlauf mit Lokalisierung und Messergebnis mit festem Messpunktabstand

Figure 7.9: Strain curve with localization and measurement result with fixed distance between measuring points

Aufgrund der hohen entstehenden Datenmengen bei faseroptischen Messungen ist stets ein Kompromiss nötig aus der Auflösung entlang der Faser (Messpunktmenge), Messfrequenz (Repetitionsrate) und Länge der Fasern (Gesamtmenge). Konkret schließen sich daher hohe Auflösung und gleichzeitig hohe Frequenzen aus, vielmehr ist der Fokus eher auf eine Zielgröße zu legen, die andere zurückzunehmen. Tabelle 7.1 zeigt diese Kopplung zwischen den Einzelgrößen.

7.4 Anwendungen

7.4.1 Allgemeines

Anhand von zwei Experimenten wird der Einsatz faseroptischer Sensoren zur Erfassung von Dehnungs- beziehungsweise Temperaturfeldern im Labor gezeigt. Dabei wurden bei den Dehnungsmessungen angefertigte Sensoren verwendet. Bei den Temperaturmessungen kamen vorgefertigte Sensoren zum Einsatz, da sich diese günstig mit einer Terminierung mit geringem Durchmesser in Kapillaren einführen lassen.

7.4.2 Dehnungsmessungen an Ankerschienen

Zur Untersuchung des Tragverhaltens einbetonierter Ankerschienen wurden Messungen an den Seitenflächen der Schienenprofile durchgeführt. Ziel der Versuche ist es, die Lastverteilung einer Längskraft F_x auf die einzelnen Anker und die Beanspruchungen innerhalb des oberen Schienenprofils zu ermitteln (Bild 7.10) [98, 101].

Faseroptische Sensoren wurden daher zu je drei Reihen an die Seitenflächen des Schienenprofils appliziert, und zwar je eine am oberen beziehungsweise am unteren Rand und eine weitere in Schwerpunktlage. Bild 7.11 zeigt die Sensorpositionen (rote Punkte) im Querschnittsschema beziehungsweise an der Schiene. Für die

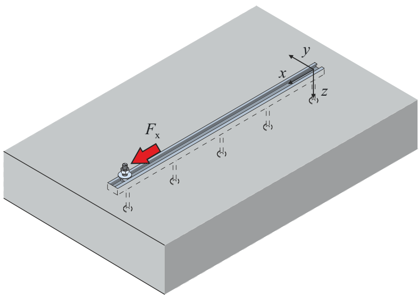

Bild 7.10: Einbetonierte Ankerschiene unter Längsbeanspruchung F_x

Figure 7.10: Embedded anchor channel under longitudinal load F_x

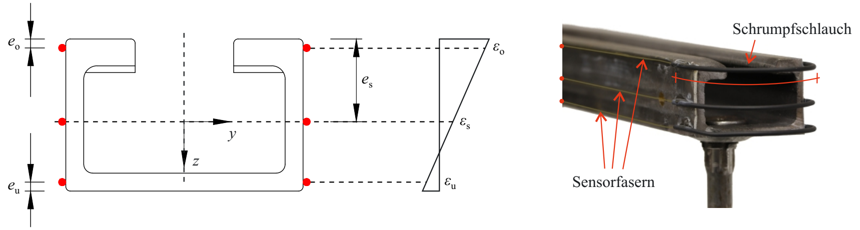

Bild 7.11: Position der Sensoren (rote Punkte) am Schienenquerschnitt (Prinzip und Applikation) und Dehnungsebene

Figure 7.11: Position of the sensors (red dots) at the channels cross-section (Concept and Application) and plane strain

Erfassung der Längsdehnungen reicht eine allein longitudinale Anordnung der Sensoren aus. Ziel dieser Feldanordnung ist es, einfach redundant Normalkräfte N und Biegemomente M_y entlang der Schiene zu ermitteln. Dabei wird eine ebene Dehnungsverteilung vorausgesetzt und durch die Überbestimmtheit durch drei statt zwei Messpunkte über den Querschnitt kontrolliert. Es gilt:

$$N = EA \cdot \varepsilon_s \tag{7.1}$$

$$\begin{aligned} M_y &= (\varepsilon_o - \varepsilon_s) \cdot \frac{EI_y}{z_o} \\ &= (\varepsilon_u - \varepsilon_s) \cdot \frac{EI_y}{z_u} \end{aligned} \tag{7.2}$$

Darin bezeichnen EA und EI_y Normal- beziehungsweise Biegesteifigkeiten des Querschnitts, z_o beziehungsweise z_u die Vertikalabstände vom Schwerpunkt zu den Messpunkten und ε_o, ε_s und ε_u die Dehnungswerte nach Bild 7.11.

Bild 7.12 zeigt exemplarisch die ermittelten Normalkraft- und Biegemomentenverläufe entlang der Schiene. Diese sind vereinfacht linienförmig dargestellt und basieren auf den Ergebnissen mit einem Messpunktabstand von 2,6 mm (Messmodus: „Extended Length"). Die Ankerkräfte können aus den Differenzen der sich stufenartig ausbildenden, horizontalen Lastniveaus im Normalkraftverlauf als „Kraftsprünge" zwischen den einzelnen Ankern ermittelt werden. Deutlich zu erkennen sind lokale Lasteinleitungseffekte im Bereich der Anker, die zur Ankerkraftabschätzung nicht herangezogen werden. Hier treten stark von der Horizontalen abweichende Hauptspannungen mit lokalen Lastspitzen auf, die die rein horizontal gerichteten Fasern nur unzureichend erfassen können. Bild 7.12a zeigt dazu ein Spannungsdetail aus einer numerischen Vergleichsberechnung, wo die Lasteinleitungseffekte deutlich hervortreten. Erst nach einem gewissen Abstand von den Ankern stellt sich der günstig identifizierbare, normalspannungsdominante Biegespannungszustand ein. Der Biegemomentenverlauf in Bild 7.12b zeigt, dass aufgrund der exzentrischen Lasteinleitung durch die Schraube ein Biegemoment in die Schiene eingeleitet wird. Das Moment baut sich bis zum dahinter liegenden Anker ab und erzeugt eine senkrecht wirkende Zugkraft an diesem Anker. Der weitere, näherungsweise linear veränderliche Momentenverlauf ergibt sich durch geringe Ankerzugkräfte und Betonpressungen an der Schienenunterseite. Im Versuch wurden die Schienen vor der Betonage seitlich und an den Enden mit Polystyrol und PTFE-Folie

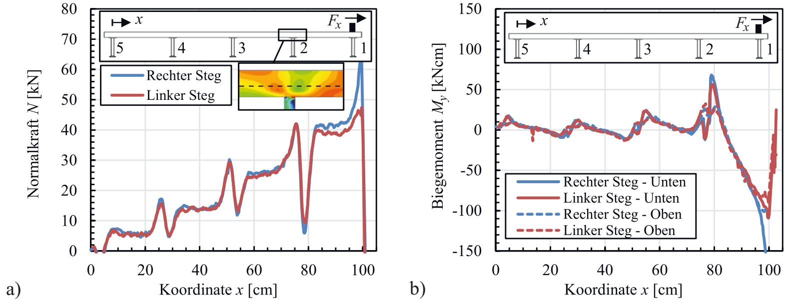

Bild 7.12: Schnittgrößenverläufe entlang einer Ankerschiene: a) Normalkraft N, b) Biegemoment M_y

Figure 7.12: Internal forces along an anchor channel: a) Normal force N, b) Bending moment M_y

umhüllt. Diese Maßnahme sorgt für den Schutz der Faser sowie eine gewünschte Entkopplung zwischen Schienenprofil und Beton. Dadurch wurde sichergestellt, dass die Lasteinleitung in den Beton ausschließlich über die Anker stattfand ohne Anteile aus Adhäsion und Reibung.

7.4.3 Temperaturmessungen in Betonbauteilen

An einem Betonbalken mit Rechteckquerschnitt ($b\,/\,h = 0{,}30\,/\,0{,}50\,[\mathrm{m}]$) wurde das Temperaturfeld aus einer einseitigen Erwärmung untersucht. Bild 7.13a zeigt dazu den Balken von 2 m Länge unter einem Wärmeeintrag durch Heizkabel an der Oberseite. Die Oberflächen sind mit Ausnahme der Unterseite durch 40 mm starke Polystyrolplatten thermisch isoliert, sodass aus der Erwärmung ein transienter, nicht-linearer Wärmefluss mit zunehmender Gesamtwärme im Balken entsteht. Bild 7.13b zeigt den Balken zur Veranschaulichung halbseitig verkleidet. Bild 7.13c stellt das erwartete Temperaturfeld für einen definierten Zeitpunkt ($t = 2{,}3\,\mathrm{h}$) bei einer Oberflächentemperatur von circa 40 °C dar. Es besitzt starke Nichtlinearität über die Höhe. In horizontaler Richtung treten größere Temperaturänderungen ausschließlich in den Randbereichen des Heizgitters auf.

Im Experiment wird das zeitlich veränderliche Temperaturfeld durch zwei separate Sensorfasern im Messmodus „Extended Length“ erfasst. Eine Faser verläuft in vertikaler Richtung in Balkenmitte und eine zweite in horizontaler Richtung entlang der Balkenachse (Bild 7.13a). Auf eine schlaufenartige Anordnung einer einzigen Faser wird dabei vereinfachend verzichtet. Durch elf separate Thermoelemente, fünf über die Höhe verteilt, sechs in Längsrichtung des Balkens orientiert, werden die Ergebnisse der Faseroptik verifiziert. Bild 7.14 (oben) zeigt dies an einem definierten Punkt des Balkens über die Zeit, und zwar am Thermoelement T_2, welches an der vertikalen Faser 15 cm unterhalb des Heizgitters liegt. Neben experimentellen Daten sind auch Ergebnisse einer numerischen Simulationsrechnung ([78, 165]) zum Vergleich dargestellt. Es stellt sich in allen drei Temperaturkurven nach circa einer Stunde ein weitgehend linearer Anstieg aus der Erwärmung ein. Nach vier Stunden flachen die Kurven ab, was mit einem abnehmenden Temperaturunterschied zwischen Wärmequelle und Betonbalken zu erklären ist. Nach sechs Stunden wird die Wärmezufuhr

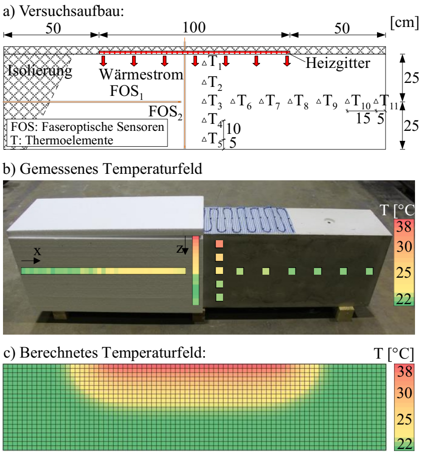

Bild 7.13: a) Prinzipskizze des Laborversuchs zur Wärmeeinleitung in einen Betonbalken, b) Foto des Versuchskörpers mit Messergebnissen, c) Temperaturfeld aus numerischer Berechnung

Figure 7.13: a) Principle sketch of the laboratory test of heat transfer into a concrete beam, b) Photo of the test beam with measurement results, c) Temperature field from numerical simulation

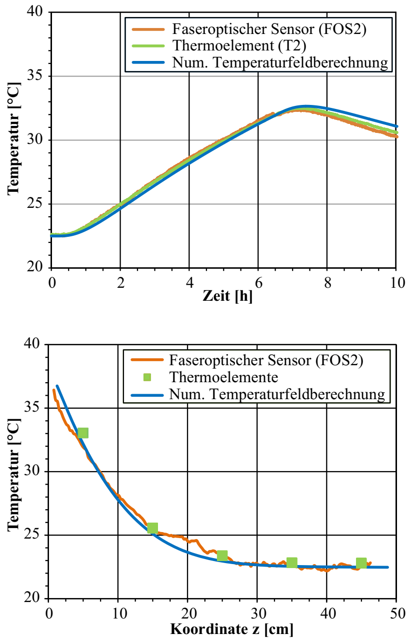

Bild 7.14: Temperaturentwicklung über die Zeit für einen definierten Ort ($z = 15$ cm) aus Messung und numerischer Simulation (oben); vertikaler Temperaturgradient für den Zeitpunkt $t = 2{,}3$ h (unten)

Figure 7.14: Temperature development over the time at a defined point ($z = 15$ cm) from measurement and numerical simulation (top); vertical temperature gradient for the time $t = 2{,}3$ h (bottom)

gestoppt. Die Temperaturkurven erreichen – aufgrund der Trägheit der Wärmeleitung – mit einer Verzögerung von circa einer Stunde ihre Maxima und fallen anschließend ab. Die über die Zeit gemittelten Abweichungen zwischen den faseroptischen und den konventionellen Messergebnissen liegen für die untersuchte Stelle bei circa 0,7 °C. Die Abweichungen resultieren einerseits aus Messungenauigkeiten, die vor allem bei der Umrechnung von Frequenzverschiebungen in Temperaturen entstehen. Andererseits treten Abweichungen aus Ungenauigkeiten bei der Sensorpositionierung auf. Zu beachten ist dabei auch eine Messunschärfe der Thermoelemente, die hier nicht in die Auswertung eingeflossen ist.

Bild 7.14(unten) zeigt einen quantitativen Vergleich der Mess- und Berechnungsergebnisse über die Querschnittshöhe für den definierten Zeitpunkt $t = 2{,}3$ h bei einer Oberflächentemperatur von circa 40 °C und 23,5 °C im Schwerpunkt. Der stark nicht-lineare, vertikale Temperaturverlauf wird durch die numerischen Simulationsrechnungen wie durch die Messwerte beider Verfahren passend erfasst. Die Temperaturwerte der beiden Messverfahren liegen nahe beieinander mit einer durchschnittlichen lokalen Abweichung von circa 0,2 °C. Während die Thermoelemente nur punktweise Informationen liefern können, entsteht aus den beiden Temperaturlinien der Fasern eine leicht interpretierbare Feldinformation (Bild 7.13b).

Die Messdaten der Sensorfasern lassen sich auch zu Temperaturprofilen über die Zeit aufarbeiten. Bild 7.15 zeigt solch ein Profil aus den Daten der horizontalen Sensorfaser (Bild 7.13b) vom Bauteilrand bis zum Faserende nahe der Balkenmitte ($x = 0{,}85$ m). Es ist die Erwärmungsphase von circa 7 h zu erkennen, auf die eine Abkühlung folgt. Hohe Temperaturen bis circa 30 °C entstehen nahe der Balkenmitte und nehmen zu den Rändern kontinuierlich ab.

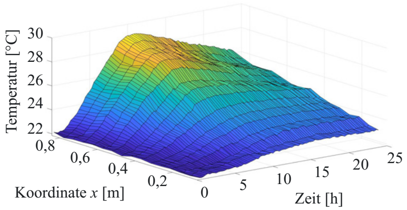

Bild 7.15: Quasikontinuierliches Temperaturprofil in horizontaler Balkenrichtung über die Versuchsdauer

Figure 7.15: Almost continuous temperature profile in horizontal beam direction during the test period

7.5 Schlussfolgerungen

Faseroptische Sensoren lassen sich günstig zur Aufnahme von Feldern von Dehnungen beziehungsweise Temperaturen nutzen. In Rastern oder Schlaufen verlegt entsteht aus der Linieninformation entlang der Faser und Interpolationen dazwischen die gesuchte Feldgröße. Das Konzept lässt sich analog auch auf räumlich verteilte Messwerte ausdehnen mit dann räumlicher Interpolation zwischen den Einzelfasern des Gitters. Wichtig ist die genaue Zuordnung von Positionen auf einer Faser zu den korrespondierenden Orten am Bauteil beziehungsweise am Probekörper. Dies gelingt durch gezielte punktweise Erwärmung, die sich in der Auswertung eindeutig abzeichnet und im Bauteil klar fixiert werden kann.

Bei der Applikation der Sensoren ist zur Dehnungsmessung darauf zu achten, dass die Dehnungen des Messobjekts verlustfrei auf die Faser übertragen werden. Hierzu sollten sowohl die Beschichtung der Faser als auch der verwendete Kleber schubsteif sein. Bei Temperaturmessungen sollte die Faser verbundlos in Kapillaren geführt sein, um für alleinige Temperaturdaten gleichzeitige mechanische Dehnungen auszuschließen.

Von großer Bedeutung ist der Schutz der empfindlichen Messfaser, da eine einzelne Beschädigung – egal an welcher Stelle – zum Ausfall des gesamten Sensors führt. Es empfiehlt sich daher freiliegende Abschnitte in Schutzschläuchen zu verlegen und den direkten Kontakt mit Beton zu vermeiden, wenn die Faser auf einem einbetonierten Messobjekt appliziert wird. Neben der Verwendung robuster Messkabel mit zusätzlichem Schutzmantel eignet sich dafür eine Trennung der Oberflächen mittels (PTFE-)Folien oder eine Einbettung der Faser in eine Nut.

Chapter 8

Supplement: Strengthening of Reinforced Concrete Structures with Temperature Induction

The following chapter is taken verbatim from:

> LÖSCHMANN, J.; CLAUß, F. and MARK, P. *Verstärken von Stahlbetontragwerken mit Temperaturinduktion*. Beton- und Stahlbetonbau, 2020. 115(10): pp. 746–757. doi: 10.1002/best.202000038.

Text and figures have been adjusted to the format and layout of this thesis. The content remains identical. The literature used is jointly referred to at the end of the thesis.

Abstract

Subsequent strengthening is not effective for dead loads. Without lifting or pre-stressing, stresses generated by dead loads remain imprinted into the existing member and are not transferred to the additional reinforcement before considerable cracks have formed. Controlled external temperature induction yields a solution to this problem as suggested here. It can be used for statically indeterminate structures and increases the bending resistance due to reinforcement subsequently glued into slots.
The fundamental idea is a systematic induction of temperature gradients. This enables to alter internal forces as required. The bending moments due to dead load are superimposed with stresses induced by temperature constraints so that regions which require strengthening are relieved. Once strengthening is applied the temperature gradient is lowered. This way, strengthening already contributes to carry the dead load. The method is exemplified on two-span girders in the lab. Its potential is demonstrated by strengthening of the reinforcement at the internal support on high and low dead load levels.

Verstärken von Stahlbetontragwerken mit Temperaturinduktion

Nachträgliche Verstärkungen wirken nicht für Eigengewichte. Ohne ein Anheben oder Vorspannen bleiben durch sie erzeugte Spannungen im Bestand eingeprägt und lagern sich erst bei erheblicher Rissbildung auf die Verstärkung um. Zur Lösung wird hier eine Temperierung von außen vorgeschlagen (Temperaturinduktion). Sie ist nutzbar für statisch unbestimmte Tragwerke und dient der Verstärkung der Biegetragfähigkeit mit nachträglich eingeschlitzter Bewehrung.
Grundprinzip ist das planmäßige Einbringen von Temperaturgradienten. Damit lassen sich Schnittgrößen beliebig verändern. Die Eigengewichtsmomente werden derart mit induzierten Zwangsspannungen aus der Temperatur überlagert, dass die zu verstärkenden Bereiche entlastet sind. Es folgen Verstärkung und Rückgang der Temperierung. Die Verstärkung ist dann bereits für die Aufnahme des Eigengewichts wirksam. Die Methode wird an einem Zweifeldträger im Labor umgesetzt und für die Verstärkung der Stützbewehrung bei hohen bzw. geringen Eigenlasten demonstriert.

8.1 Einleitung

Die Erhaltung alternder Bestandsbauwerke gewinnt zunehmend an Bedeutung. In den EU-Staaten sind Schätzungen zufolge mehr als 60 % des gesamten Bestands zu ertüchtigen oder zu erneuern [11]. Insbesondere Infrastrukturbauwerke wie Brücken weisen infolge stark angestiegener Verkehrslasten einen kritischen Zustand auf [163, 164, 204].

Eine nachhaltige Alternative zum Ersatzneubau bieten nachträgliche Verstärkungen. Sie schonen Ressourcen, reduzieren Emissionen und minimieren störende Eingriffe in die umgebende Infrastruktur. Typische Querschnittsverstärkungen erfolgen mit Beton, Stahl bzw. Carbon [30, 204]. Sie haben allerdings den Nachteil, ohne ein temporäres Anheben oder Vorspannen des Tragwerks nicht für das Konstruktionseigengewicht wirksam zu sein und ausschließlich Teile der Verkehrslasten abzutragen. Durch den hohen Anteil des Eigengewichts an der Gesamtlast – bei Brücken [116] oder Deckenplatten sind rund 70 % üblich – ist die eingeschränkte Wirksamkeit bei Betontragwerken besonders nachteilig.

Bild 8.1 zeigt das Prinzip der Biegeverstärkung durch Erweiterung (oben) oder Ergänzung (unten) eines Balkenquerschnitts mit oben liegender Zugzone. Es sind qualitativ die aus Eigengewicht g und Nutzlasten q resultierenden Dehnungsverläufe abgebildet. Der obere Querschnitt wird durch Aufbeton und eingebettete Zulagebewehrung (ΔA_s) erweitert [30]. Unter dem Biegemoment aus Eigengewicht (M_g) ist die Erweiterung ohne Entlastung oder Anheben während der Verstärkung zunächst dehnungsfrei und nicht am Lastabtrag beteiligt. Die Dehnung der Initialbewehrung A_s erhöht sich sogar durch das angestiegene Eigengewicht [204]. Erst zusätzliche Nutzlasten q werden vom Gesamtquerschnitt (Schwerpunkt S_1) abgetragen und bewirken in diesem eine lineare Dehnungsverteilung. Da M_g weiterhin im alten Schwerpunkt S_0 ausschließlich auf den Bestandsquerschnitt einwirkt, weist die Dehnungsverteilung einen Sprung zwischen Alt- und Aufbeton auf. In der Zulagebewehrung stellt sich die Dehnung $\varepsilon_{s,\Delta A}$ ausschließlich aus q ein. Auch bei einer Querschnittsergänzung durch in Nuten eingeschlitzte Bewehrungsstäbe (ΔA_s) muss das Eigengewicht nach der Verstärkung weiter allein vom Bestandsquerschnitt aufgenommen werden (Bild 8.1, unten). Die Dehnung ε_s der initialen Bewehrung bleibt nahezu unverändert. Weitere Nutzlasten belasten den Gesamtquerschnitt und es stellt sich eine Dehnung $\varepsilon_{s,\Delta A}$ in der nachträglichen Bewehrung ein. Die in Bild 8.1 gezeigten Dehnungsverläufe gelten ähnlich auch für andere Ergänzungen wie oberflächlich angeklebte Stahl- und Carbonlaschen [11, 12, 90] oder Textilbewehrung [19, 50, 92]. Kriechumlagerungen sind durch den kriechfähigen Neubeton und den bereits gealterten Bestandsbeton kaum möglich [43].

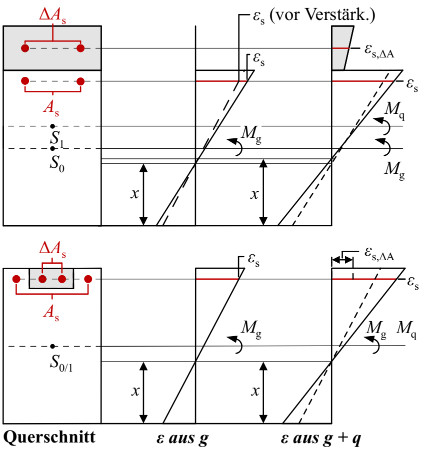

Bild 8.1: Prinzip der Querschnittsverstärkung durch in Aufbeton eingebettete (oben) und in Nuten eingeschlitzte (unten) Zulagebewehrung mit Dehnungsverläufen

Figure 8.1: Principle of cross-sectional strengthening by supplementary reinforcement embedded into concrete (top) and glued into slots (bottom) along with strain curves

Zur Aktivierung der Biegeverstärkung auch für die Eigengewichte wird hier eine neue Methode entwickelt. Dabei werden Tragwerke durch temperaturinduzierte Zwangsmomente während der Verstärkung entlastet [118]. Ein gezieltes Hervorrufen von Bauwerksreaktionen durch Temperaturinduktion ist im Bauingenieurwesen bisher nicht gebräuchlich. Jedoch sind Simulationen von Temperaturfeldern [16, 46, 165] und deren Bauwerksreaktionen [10, 44, 164] vielfach erforscht. Eine aktive Nutzung von Temperaturen erfolgt nur vereinzelt, z. B. zur Beschleunigung der Festigkeitsentwicklung von Beton [189] oder zur Verhinderung des Einfrierens von Fahrbahnen

[221]. Im Maschinenbau und der Elektrotechnik ist eine gezielte Regelung von Temperaturen hingegen üblich [74, 95, 168].
Im Beitrag wird zunächst die Methode der Temperaturinduktion vorgestellt. Es folgt die Anwendung auf die Biegeverstärkung von Balken. Abschließend wird die Methode experimentell verifiziert und für den ungerissenen und den gerissenen Zustand demonstriert. Dazu werden zwei Zweifeldträger durch vertikale Temperaturgradienten im Stützbereich entlastet und verstärkt.

8.2 Methode der Temperaturinduktion

8.2.1 Theoretische Grundlagen

Temperaturinduktion ermöglicht eine gezielte Steuerung von Schnittgrößen in statisch unbestimmten Systemen. Dafür sind die grundlegenden mechanischen Auswirkungen von Temperaturfeldern in Bauwerken zu diskutieren. Temperaturänderungen bewirken innere Verformungen. Solche aus nichtlinearen Temperaturverläufen werden direkt auf Querschnittsebene zurückgehalten und als innerer Zwang bezeichnet. Es entstehen Eigenspannungen, welche sich auf Querschnittsebene im Gleichgewicht befinden und daher keine Schnittgrößen hervorrufen.
Konstante und lineare Temperaturänderungen wirken sich auf der Systemebene aus [46]. Bei statischer Bestimmtheit stellen sich die temperaturinduzierten Verformungen frei ein. Eine konstante Temperaturänderung ΔT führt zu einer Dehnung $\varepsilon_{\Delta \mathrm{T}}$, Gl. 8.1. Ein vertikaler Temperaturunterschied ΔT_z ruft eine Krümmung $\kappa_{\Delta \mathrm{T}}$ hervor, Gl. 8.2.

$$\varepsilon_{\Delta \mathrm{T}} = \alpha_\mathrm{T} \Delta T \qquad (8.1)$$

$$\kappa_{\Delta \mathrm{T}} = \frac{\alpha_\mathrm{T} \Delta T_\mathrm{z}}{h} \qquad (8.2)$$

mit:

α_T	Wärmeausdehnungskoeffizient
ΔT	konstante Temperaturänderung
ΔT_z	linearer vertikaler Temperaturunterschied
h	Querschnittshöhe

In statisch unbestimmten Systemen werden die eingeprägten Verformungen durch Lager oder angrenzende Bauteile zurückgehalten (äußerer Zwang). Daraus entstehen Schnitt- und Auflagergrößen [102]. Diese sind – anders als bei direkten Einwirkungen – proportional von der korrespondierenden Tragwerkssteifigkeit EA bzw. EI abhängig [10, 44, 46]. Die Berechnung von Lastzuständen aus eingeprägten Verformungen erfolgt wie bei direkten Einwirkungen mittels Kraftgrößen- oder Weggrößenverfahren [102]. Beim Kraftgrößenverfahren wird ein statisch unbestimmtes System auf ein statisch bestimmtes Grundsystem reduziert. An den Stellen der gelösten Kraftgrößen X_i werden mithilfe des Prinzips der virtuellen Kräfte (PVK) Verschiebungen $\delta_{\mathrm{i}0}$ bestimmt, Gl. 8.3. Verformungslastfälle wie Temperaturänderungen $\varepsilon_{\Delta \mathrm{T}}$ und -krümmungen $\kappa_{\Delta \mathrm{T}}$ fließen direkt in die Berechnung der Verschiebung ein. Sie rufen keine Schnittgrößen im statisch bestimmten Grundsystem hervor, sodass Normalkraft N_0 und Moment M_0 ohne äußere Lasten entfallen.

$$\delta_{\mathrm{i}0} = \int_0^L N_\mathrm{i} \left[\frac{N_0}{EA} + \alpha_\mathrm{T} \Delta T \right] \mathrm{d}x + \cdots$$
$$\int_0^L M_\mathrm{i} \left[\frac{M_0}{EI} + \alpha_\mathrm{T} \frac{\Delta T_\mathrm{z}}{h} \right] \mathrm{d}x \qquad (8.3)$$

Durch die Systemreduktion werden die Verträglichkeitsbedingungen verletzt. Zur Erfüllung der Verformungsgeometrie werden die gelösten Kraftgrößen X_i in sogenannten „Einheitssystemen“ als Unbekannte aufgebracht und es werden hierfür Verschiebungsgrößen δ_{ik} mittels PVK bestimmt, Gl. 8.4.

$$\delta_{ik} = \int_0^L \frac{N_i N_k}{EA} dx + \int_0^L \frac{M_i M_k}{EI} dx \tag{8.4}$$

Aus den Verträglichkeitsbedingungen ergeben sich die gelösten Kraftgrößen X_n, Gl. 8.5, womit sich dann die temperaturinduzierten Schnitt- und Auflagergrößen ermitteln lassen [102].

$$\delta_i = \delta_{i0} + X_1\delta_{i1} + X_2\delta_{i2} + \cdots + X_n\delta_{in} = 0 \tag{8.5}$$

8.2.2 Momentensteuerung durch Temperaturinduktion

Vorgehen

Es können nach Abschn. 8.2.1 für beliebige statisch unbestimmte Systeme analytische Formeln zur Berechnung temperaturinduzierter Schnittgrößen abgeleitet werden. Mit den Formeln sind ebenso die für vorgegebene Schnittgrößen erforderlichen Temperaturfelder bestimmbar. Durch gezielte Temperaturinduktion können so Schnittgrößen eines Tragwerks beliebig gesteuert werden. Der Beitrag fokussiert sich auf die Steuerung von Biegemomenten. Analog dazu ist die Methode auch für Normal und Querkräfte anwendbar.

Die Eintragung eines linearen vertikalen Temperaturgradienten ruft Zwangsmomente hervor, mit denen Biegemomente aus Belastungen kompensiert, reduziert oder günstig umverteilt werden können. Die Steuerung von Biegemomenten wird zunächst an beidseitig eingespannten Balken entwickelt (Abschn. 8.2.2) und dann auf Mehrfeldträger übertragen, deren Felder eingespannten Balken mit reduziertem Einspanngrad entsprechen (Abschn. 8.2.2). Die Herleitung der analytischen Formeln Gl. 8.6 und Gl. 8.7 erfolgt mittels Kraftgrößenverfahren (Abschn. 8.2.1). Der absolute Temperaturunterschied ΔT_z des Gradienten wird nachfolgend vereinfacht als Gradient bezeichnet.

Beidseitig eingespannter Balken

Das induzierte Zwangsmoment M_i hängt vom Gradienten ΔT_z und den folgenden Faktoren ab [119]:

- Wärmeausdehnungskoeffizient (α_T)
- Biegesteifigkeit des Balkens (EI)
- Position a/L und Länge b/L der Temperierung

Bei symmetrischer Beanspruchung aus ΔT_z entsteht ein konstantes Moment M_i (Bild 8.2, oben), welches von der Krümmung $\kappa_{\Delta T}$ und der Biegesteifigkeit EI abhängt, Gl. 8.6 [119]. Eine symmetrisch verkürzte Temperierlänge b bewirkt eine proportionale Abnahme von M_i. Für die Erzeugung eines vorgegebenen Moments kann demnach ein großer Gradient ΔT_z über eine kleine Länge b oder ein kleiner Gradient über eine große Länge aufgebracht werden.

$$\begin{aligned} M_i(x) &= \kappa_{\Delta T} \cdot \frac{b}{L} EI \\ &= \frac{\alpha_T \Delta T_Z}{h} \cdot \frac{b}{L} EI \end{aligned} \tag{8.6}$$

$$\begin{aligned} M_i(x) = \frac{\alpha_T \Delta T_z}{h} \cdot \frac{b}{L^3} \cdot \cdots \\ (6x(2a+b-L) + \cdots \\ L(-6a-3b+4L))EI \end{aligned} \tag{8.7}$$

mit:

a	Abstand der Temperierung von linker Einspannung
b	Temperierlänge
L	Feldlänge

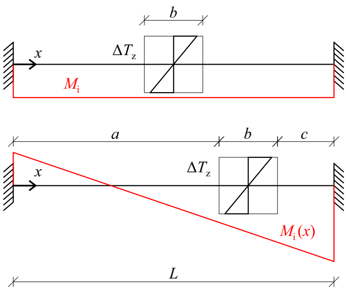

Bild 8.2: Biegemomente aus einem symmetrisch (oben) und asymmetrisch (unten) positionierten Temperaturgradienten in einem beidseitig eingespannten Balken

Figure 8.2: Bending moments due to symmetrically (top) and asymmetrically (bottom) positioned temperature gradients in a beam clamped on both ends

Bei asymmetrischer Anordnung von ΔT_z ergibt sich ein linearer Momentenverlauf (Bild 8.2, unten). Er hängt von der Temperierlänge b und den Abständen zwischen der Temperierung und den beiden Einspannungen – definiert durch die Längen a und c – ab, Gl. 8.7. Das Einspannmoment wird maximal, wenn der Gradient über die angrenzenden zwei Drittel des Feldes wirkt [119].

Mehrfeldträger

In Mehrfeldträgern können durch Temperaturinduktion beliebige lineare Momentenverläufe erzeugt werden (Bild 8.3). Ein einzelner Gradient im Stützbereich führt zu einem linearen Verlauf in den beiden angrenzenden Feldern (rote Linien). Bei Positionierung in Feldmitte und beidseitig gleicher Anschlusssteifigkeit wird im gleichen Feld ein konstantes und in den benachbarten ein linear abfallendes Moment erzeugt (blaue Linien). Die Linien setzen sich mit abnehmenden Werten in den benachbarten Feldern fort. Durch Überlagerung mehrerer Zwangsmomente infolge weiterer Gradienten können diese Effekte vollständig eliminiert oder gesteuert werden, sodass ideale dreiecks- und trapezförmige Gesamtmomente resultieren. Letztlich ist das Moment an jeder Stütze beliebig einstellbar.

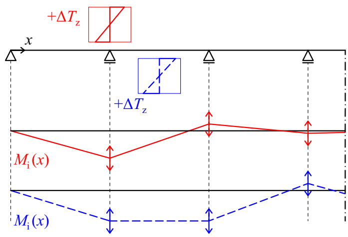

Bild 8.3: Biegemomente aus Temperaturgradienten in einem Durchlaufträger

Figure 8.3: Bending moments due to temperature gradients in a multi-span beam

Der absolute Wert eines Zwangsmoments hängt neben den in Abschn. 8.2.1 genannten Parametern vom Einspanngrad der Auflager ab. Dieser resultiert aus der Biegesteifigkeit und dem statischen System (Feldlängen, Anzahl an Feldern). Bei hohen Einspanngraden entspricht der Momentenverlauf fast dem eines beidseitig eingespannten Trägers, Gl. 8.7. Bei niedrigen Graden nähert sich das System einem Einfeldträger an, sodass das Biegemoment gegen null geht.

8.2.3 Technische Umsetzung

Zur Erzeugung eines vertikalen Gradienten empfiehlt sich ein Temperieren von der Ober- und der Unterseite des Tragwerks. Geeignet sind z. B. Heizmatten, temperierte Wasserkreisläufe oder Trockeneis. Die erzielbaren Gradienten werden durch das Temperierverfahren sowie das thermische Verhalten des Tragwerksmaterials [78] limitiert. Um Schäden zu vermeiden, sollten die natürlichen Umgebungsbedingungen (ca. −20 °C bis 80 °C) eingehalten werden.
Praktisch erfolgt an einem Balken auch eine Tem-

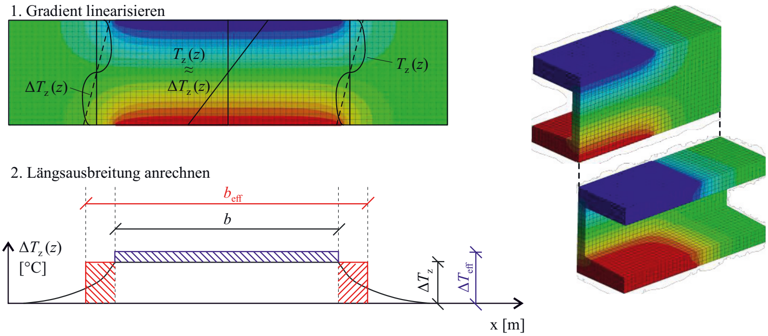

Bild 8.4: Temperaturausbreitung in Längsrichtung mit effektiver Länge und effektivem Temperaturgradienten

Figure 8.4: Temperature flow in longitudinal direction with effective length and effective temperature gradient

peraturausbreitung in Längsrichtung. Bild 8.4 zeigt das Ergebnis einer Temperaturfeldberechnung für einen Träger mit I-Querschnitt. Das Feld ist innerhalb b weitgehend konstant, sein vertikaler Verlauf linear (Bild 8.4, oben). Am Rand treten nichtlineare Verläufe $T(z)$ auf. Um die gesamte Biegewirkung zu erfassen, sind im ersten Schritt linearisierte Gradienten ΔT_z zu bestimmen. Dazu werden die Temperaturen über die Querschnittsfläche integriert und entsprechend ihrem Abstand z zum Schwerpunkt gewichtet, Gl. 8.8 [119]. [165] schlägt eine numerische Lösung mittels Tabellenkalkulation mit Unterteilung eines Querschnitts in i Elemente vor, Gl. 8.8.

$$\Delta T_z = \frac{h}{I} \int T(y,z) \cdot z \, \mathrm{d}A \cong \cdots$$

$$\frac{h}{I} \sum_{\mathrm{i}} T_{\mathrm{i}} \cdot z_{\mathrm{i}} \cdot A_{\mathrm{i}} \quad (8.8)$$

mit:

I	Flächenträgheitsmoment
z	Abstand zum Schwerpunkt

Im zweiten Schritt sind die linearisierten Gradienten in Längsrichtung zu betrachten (Bild 8.4, unten). Sie nehmen an den beiden Rändern von b nichtlinear ab. Zur Berechnung des Zwangsmoments nach Gl. 8.6 und Gl. 8.7 kann der veränderliche Gradient in einen äquivalenten konstanten Gradienten umgerechnet werden. Die zusätzliche mechanische Wirkung der Längsausbreitung wird alternativ durch eine Verlängerung der Temperierlänge (b_{eff}, rot) oder eine Erhöhung des Gradienten (ΔT_{eff}, blau) rechnerisch berücksichtigt. Dazu ist die Randfläche durch Integration oder näherungsweise durch Ausgleichsgeraden zu bestimmen und anzurechnen, Gl. 8.9.

$$b_{\mathrm{eff}} = \frac{\int_0^L \Delta T_z(x) dx}{\Delta T_z} \quad \text{bzw.}$$
$$T_{\mathrm{eff}} = \frac{\int_0^L \Delta T_z(x) dx}{b} \quad (8.9)$$

8.3 Temperaturinduktion bei Tragwerksverstärkungen

Die Anwendung der Induktion bei nachträglichen Verstärkungen dient der Aktivierung der Verstärkung für das Eigengewicht. Dazu wird das

Tragwerk kurzfristig mit induzierten Temperaturen entlastet. Zur Veranschaulichung wird ein Zweifeldträger betrachtet, der über der Mittelstütze zu verstärken ist (Bild 8.5). Die Temperaturinduktion ist so zu steuern, dass der Balken durch ΔT_z im Stützbereich entlastet wird. Induziertes Moment und Eigengewichtsmoment heben sich auf. Gradienten rufen in einem Zweifeldträger stets ein dreieckförmiges Zwangsmoment hervor (Bild 8.5). Das Maximum liegt über der Mittelstütze. Die Berechnung des erforderlichen Gradienten erfolgt mit Gl. 8.10, hergeleitet mittels Kraftgrößenverfahren (Abschn. 8.2.1).

$$\text{erf.}\,\Delta T_z = \frac{M_\mathrm{i}(x_1)}{x_1} \cdot \frac{h}{\alpha_\mathrm{T}} \cdot \cdots \frac{4L^3}{3b(2a+b)} \frac{1}{EI} \tag{8.10}$$

Die Entlastung von parabolischen Biegemomenten ist auf lokale Stellen begrenzt, da ausschließlich lineare Zwangsmomente induzierbar sind (Bild 8.5). Daher wird nur die bemessungsrelevante Stelle über der Stütze voll entlastet. Nach erfolgter Verstärkung und Rückgang des Temperaturgradienten stellt sich das initiale Moment im Gesamtquerschnitt ein. Bei Querschnittsergänzungen ergeben sich gleiche Dehnungen in der initialen und der nachträglich eingeschlitzten Bewehrung. Bei Querschnittserweiterungen unterscheiden sich die Dehnungen allein durch die unterschiedliche Höhenlage. Der verstärkte Gesamtquerschnitt ist somit bereits für die Aufnahme des Eigengewichts wirksam. Dies wirkt sich vor allem positiv auf die Gebrauchstauglichkeit (Verformungen, Rissbreiten) aus.

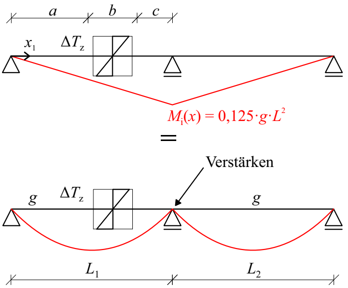

Bild 8.5: Biegemomente aus Eigengewicht (oben) und induziertem Temperaturgradienten (Mitte) und resultierendes Moment (unten)

Figure 8.5: Bending moments from dead load (top), temperature gradient (middle) and overall moment (bottom)

8.4 Experimentelle Untersuchungen

8.4.1 Versuchsziel

Die Tragwerksverstärkung mit Induktion soll für den in Bild 8.5 dargestellten Zweifeldträger experimentell gezeigt werden. Das Stützmoment infolge Eigengewicht und weiterer Auflasten ist durch einen aufgebrachten Temperaturgradienten während der Verstärkung zu neutralisieren. Nach dem Rückgang des Gradienten sollen sich gleiche Spannungszustände in der initialen und der nachträglich ergänzten Bewehrung einstellen, sodass das Last-Verformungsverhalten im abschließenden Belastungstest dem eines initial verstärkten bzw. direkt voll bewehrten Balkens entspricht. Die Verstärkung wird im ungerissenen (Balken 1) und gerissenen Zustand (Balken 2) durchgeführt.

8.4.2 Versuchsaufbau

Es werden zwei identische Balken mit einer Gesamtlänge von 5,20 m und Stützweiten von 2,50 m hergestellt (Bild 8.6). Die Auflager bestehen aus stählernen Halbzylindern, welche frei verdrehbar in Halbschalen liegen. Die beiden

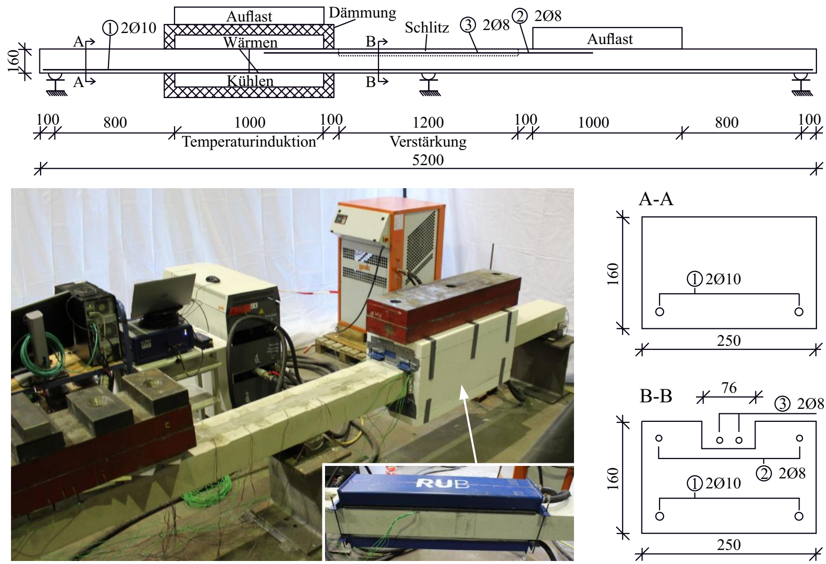

Bild 8.6: Prinzipskizze und Foto des Versuchsaufbaus mit Querschnitten, Maße [mm]

Figure 8.6: Test setup with sketches of the cross-sections, dimensions [mm]

äußeren Lager werden mittels PTFE-Gleitschicht [14] verschieblich ausgeführt.

Der Querschnitt des Balkens ist rechteckig ($b = 0{,}25$ m, $h = 0{,}16$ m) (Bild 8.6). An der Oberseite des Querschnitts ist über eine Länge von 1,20 m im Stützbereich eine Nut für die nachträgliche Bewehrung eingelassen. Die Versuchskörper wurden zeitgleich aus einer Charge Transportbeton C20/25 mit einem Größtkorn von 16 mm hergestellt. Unten im Querschnitt verläuft die Biegezugbewehrung (2 Ø 10 mm, Pos. 1). Oben liegen im Stützbereich über eine Länge von 2,00 m zwei Bewehrungsstäbe (Ø 8 mm, Pos. 2), die im Versuch durch zwei weitere Stäbe (Pos. 3) des gleichen Durchmessers ergänzt werden. Die zusätzliche Bewehrung weist unter Beachtung der Zugkraftdeckung eine Länge von 1,20 m auf.

Zwei Temperiergeräte erzeugen im Balken über eine Länge von 1,00 m einen Temperaturgradienten (Bild 8.6). Das Heizgerät *Teco 300* von der Firma *gwk* hat einen Temperaturbereich von 30 °C bis 95 °C. Das Kühlgerät *Weco 09 A* ermöglicht Temperaturen zwischen 5 °C und 30 °C. Die Geräte pumpen temperiertes Wasser über Druckschläuche in Stahlboxen, die auf und unter dem Betonbalken positioniert und über Gewindestangen gegen den Balken gepresst werden. Die geschweißten Boxen stehen nur an ihren seitlichen Stirnflächen auf dem Balken auf, um die gewünschten Temperaturkrümmungen nicht zu behindern. Der 10 mm hohe Hohlraum zwischen Box und Balken wird zur Verbesserung der thermischen Leitung mit mehreren, in Längsrichtung unterteilten Stahlplatten ausgefüllt. Die Stahlboxen werden mit Polystyrol isoliert.

Die Balken enthalten jeweils sieben Thermoelemente (Messungenauigkeit: 0,4 °C) zur Aufnahme von vertikalen Temperaturgradienten im temperierten (T_1 bis T_5, Schnitt C-C, Bild 8.7c) und im unbeeinflussten Bereich (T_6 und T_7, Schnitt E-E) sowie 17 Dehnungsmessstreifen (S_1 bis S_{17}), (Bild 8.7a). Zusätzlich zu den eingebauten Sensoren liegen zwei Thermoelemente (T_h und T_k) außerhalb des Balkens in Nuten in den Stahlplatten zwischen dem Balken und der Heiz- bzw. Kühlbox. Der Temperaturverlauf in Längsrichtung wird von einem faseroptischen Sensor (FOS) quasikontinuierlich mit einer Auflösung im Millimeterbereich [125, 172] und einer Genauigkeit von 0,3 °C erfasst. Da die Sensorfaser Dehnungs- und Temperaturänderungen gleichzeitig erfasst, wird die Faser in einer druckbeständigen Kapillare aus Kunststoff (PEEK) geführt und vom Beton entkoppelt (Bild 8.7b), sodass mechanische Dehnungen ausgeschlossen sind [100].

8.4.3 Versuchsablauf

Die Tab. 8.1 fasst die wesentlichen System-, Querschnitts- und Materialparameter zusammen, Tab. 8.2 zeigt die damit berechneten Biegemomente und Temperaturgradienten der einzelnen Lastschritte. Balken 1 weist infolge Belastung (Eigengewicht, Stahlboxen, Auflasten) ein Stützmoment von $-1{,}4\,\mathrm{kNm}$ auf, was deutlich unterhalb des Rissmoments (M_cr =

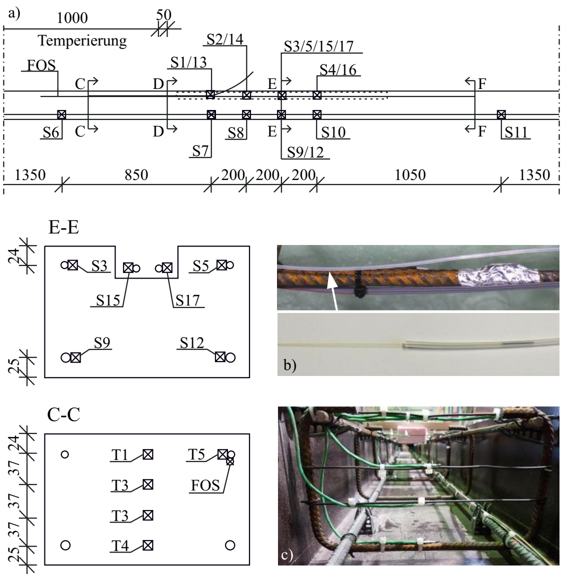

$\mathrm{S_i}$: DMS $\mathrm{T_i}$: Thermoelemente FOS: Faseroptischer Sensor

Bild 8.7: Längsschnitt und Querschnitte mit Positionen der Dehnungs (S)- und Temperatursensoren (T) (a); Fotos des faseroptischen Sensors in einer Kapillare (b) und des Messquerschnitts C-C mit Thermoelementen (c), Maße [mm]

Figure 8.7: Longitudinal section and cross-sections with positions of the strain (S) and temperature (T) sensors (a); photos of the fibre optic sensor in a capillary (b) and of the cross-section B-B equipped with thermocouples (c), dimensions [mm]

Tab. 8.1: System-, Querschnitts- und Materialparameter der Versuche

Table 8.1: System, cross-section and material parameters of the specimens

System- und Querschnittsparameter	
Feldlänge L	2,50 m
Position der Temperierung a	0,80 m
Temperierlänge b	1,00 m
Querschnittshöhe h	0,16 m
Bewehrungsmenge (Stützbereich)	
vor / nach Verstärkung	1,01 / 2,02 cm^2
Materialparameter	
Beton	C20/25
Betonstahl	B500A
Wärmeausdehnungskoeffizient α_T	$1{,}2 \cdot 10^{-5}$ 1/K
Biegesteifigkeit EI (geschlitzt / verstärkt)	2,13 / 2,51 MNm^2

−2,3 kNm) liegt. Balken 2 erreicht bei linear elastischer Schnittgrößenberechnung ein Moment von −3,9 kNm und befindet sich im Zustand II.

Anschließend folgt die Entlastung des Stützbereichs durch die Einleitung eines Temperaturgradienten. Seine erforderlichen Größen ergeben sich aus Gl. 8.10. Zur Erzeugung der entlastenden Biegemomente von 1,4 kNm und 3,9 kNm sind Temperaturgradienten von 28,1 °C (Balken 1, Gl. 8.5) und 78,2 °C (Balken 2) erforderlich (Tab. 8.2). Eine Wärmeausbreitung über den Temperierbereich hinaus ist dabei noch nicht berücksichtigt. Der zweite Gradient ergibt sich vereinfacht ohne Berücksichtigung einer Rissbildung. Die Eintragung der Gradienten erfolgt durch Anpassung der Wassertemperaturen, zunächst mithilfe der oberflächennahen Tempe-

Tab. 8.2: Lastschritte mit den zu erzielenden Temperaturgradienten und den erwarteten Biegemomenten

Table 8.2: Load steps, required temperature gradients and expected bending moments

	Balken 1 (Zustand I)		Balken 2 (Zustand II)	
Lastschritt	Gradient ΔT	Biegemoment M	Gradient ΔT	Biegemoment M
1. Belastung (Eigengewicht, Stahlboxen, Auflast)	-	−1,4 kNm	-	−3,9 kNm
2. Entlastung (Aufbringung Temperaturgradient) – Bauteilverstärkung	28,1 °C	1,4 kNm	78,2 °C	3,9 kNm
3. Belastung (Rückgang Temperaturgradient)	−28,1 °C	−1,4 kNm	−78,2 °C	−3,9 kNm
4. Belastung (bis Fließen der Bewehrung)	-	−14,1 kNm	-	−14,1 kNm

raturen T_h und T_k. Für die Feinregelung werden dann die einbetonierten Thermoelemente (T_1 bis T_5) und der faseroptischen Sensor zur Berücksichtigung der Temperaturlängsausbreitung herangezogen. Die Anpassung der Wassertemperaturen ist abgeschlossen, wenn das Temperaturfeld stationär ist und der effektive Gradient dem theoretisch erforderlichen entspricht. Eine kontinuierliche Temperaturregelung zum Ausgleich variierender Umgebungsbedingungen ist aufgrund der Laborbedingungen nicht notwendig.

Im entlasteten Zustand wird der Stützbereich des Balkens durch Einschlitzen der zwei zusätzlichen Bewehrungsstäbe (Ø 8 mm) und Verfüllen mit Vergussmörtel in der Zugzone verstärkt (Bild 8.8, links). Nach 24 Stunden Aushärtezeit werden die Temperiergeräte ausgeschaltet, sodass der Gradient zurückgeht und sich das ursprüngliche Moment einstellt.

Abschließend werden die Balken durch einen hydraulischen Prüfzylinder bis zum duktilen Versagen belastet. Über einen horizontalen Stahlträger wird die Last in den beiden Feldmitten eingeleitet (Bild 8.8, rechts). Das erwartete Verformungsverhalten entspricht dem eines initial voll bewehrten Balkens mit einem Fließmoment von $-13{,}2$ kNm (Tab. 8.2).

8.4.4 Ergebnisse

Verstärkung

Bild 8.9 zeigt den Temperatur- und Dehnungsverlauf im ersten Balken infolge Belastung sowie Aufbringung und Rückgang des Gradienten.

Temperaturen

Der Temperaturgradient stellt sich infolge der sukzessiven Anpassung der Wassertemperaturen stufenartig ein. Bei der Einleitung treten thermische Verluste auf. Aus den initialen Wassertemperaturen von $T_{h,w} = 40\,°C$ und $T_{k,w} = 5\,°C$ resultieren Temperaturen in den wärmeleitenden Metallplatten von $T_h = 30\,°C$ und $T_k = 10\,°C$. Die Differenz im Balken ist infolge weiterer Verluste noch geringer. Um den erforderlichen Gradienten zu erreichen, wird die Wassertemperatur des Heizkreislaufs ($T_{h,w}$) stufenweise auf 75 °C erhöht, wodurch T_h auf 56 °C ansteigt. Die einbetonierten Sensoren reagieren aufgrund der Trägheit der Wärmeleitung verzögert. T_1 (24 mm vom oberen Rand) erhöht sich final auf 37 °C. Die

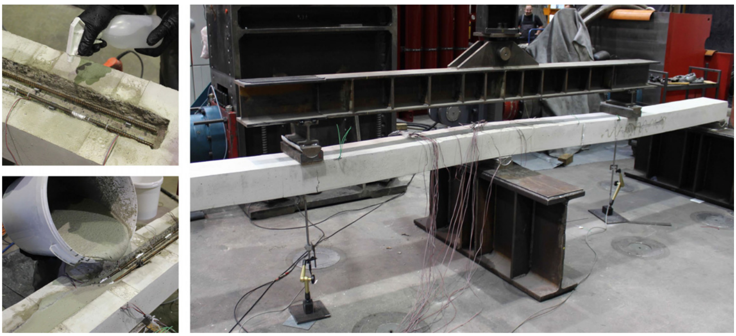

Bild 8.8: Verstärkung im Stützbereich durch Einlegen von Bewehrung in eine angefeuchtete Nut (links oben) und Verfüllen mit Vergussmörtel (links unten); verstärkter Balken im Belastungszustand (rechts)

Figure 8.8: Strengthening at the internal support: Glueing reinforcement into moistened slots (top left); filling slots with mortar (bottom left); strengthened beam subjected to load (right)

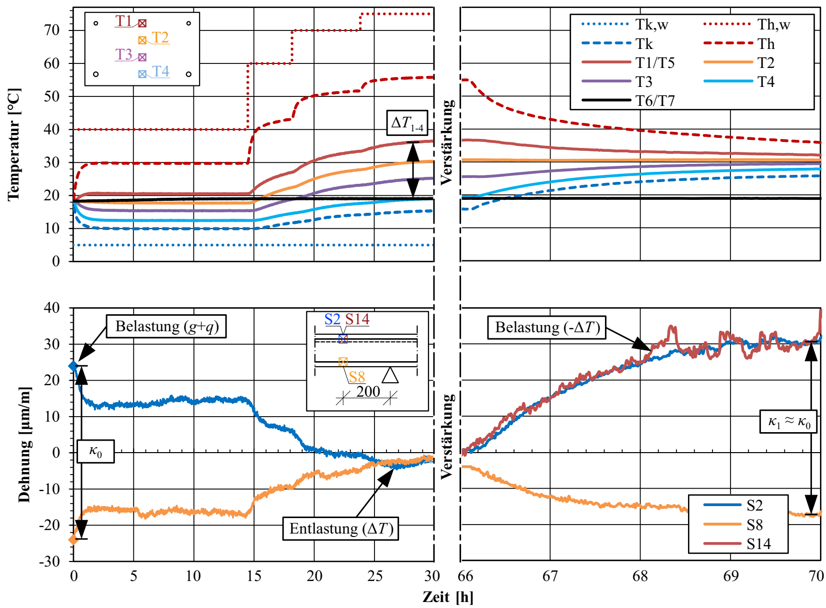

Bild 8.9: Temperatur- (oben) und Dehnungsverlauf (unten) im ungerissenen Balken während der Verstärkung

Figure 8.9: Development of temperature (top) and strain (bottom) during strengthening in the non-cracked beam

Kühltemperatur kann aus technischen Gründen nicht weiter reduziert werden. Durch die erhöhte Wärmezufuhr nimmt die Temperatur auch in der unteren, zu kühlenden Querschnittshälfte zu, wodurch der Gradient abgemindert wird. Es stellt sich $T_k = 15\,°C$ in der unteren Stahlplatte ein. T_4 (25 mm vom unteren Rand) geht wieder auf seine Ursprungstemperatur von 18,2 °C hoch. Aufgrund der Laborbedingungen und der Isolierung ist das erzeugte Temperaturfeld nun annähernd stationär. Die Temperatur im unbeeinflussten Bereich des Balkens bleibt durchgehend etwa konstant. T_6 und T_7 variieren zwischen 18,2 und 19 °C.

Der temperierte Bereich des Balkens erfährt innerhalb von 25 Stunden einen über den Querschnitt konstanten Temperaturanstieg ΔT_N von 9,5 °C (Bild 8.10, links). Die leichte Längsdehnung daraus gleicht sich durch die gleitende Lagerung an den Außenlagern zwangsfrei aus. Der vertikale Gradient zwischen den einbetonierten Thermoelementen ergibt sich linear extrapoliert zu 23,9 °C (Balken 1) und 30,1 °C (Balken 2). ΔT_z ist aufgrund der Temperaturausbreitung in Balkenlängsrichtung zu erhöhen. Für die Berechnung des effektiven Gradienten ΔT_{eff} wird der faseroptische Sensor herangezogen, welcher Temperaturänderungen (ΔT_{FOS}) zur initialen Referenzmessung misst. Die mittlere Temperatur im temperierten Bereich ($\Delta T_{\text{FOS}} = 16{,}3\,°C$) zeigt für Balken 1 eine gute Übereinstimmung mit den Werten der Thermoelemente auf

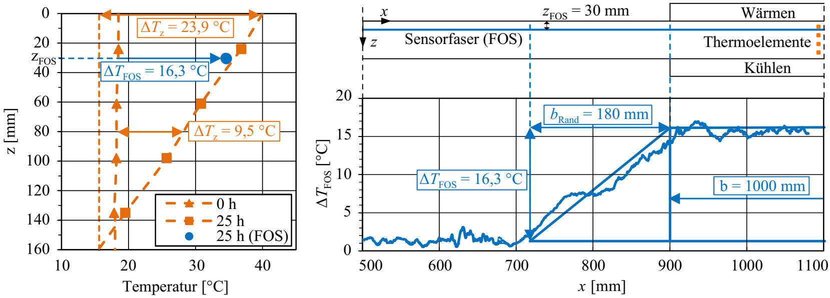

Bild 8.10: Vertikaler Temperaturgradient aus diskreten Messwerten der Thermoelemente (links) und quasikontinuierliche Messwerte des faseroptischen Sensors in Balkenlängsrichtung (rechts) am Balken 1

Figure 8.10: Vertical temperature gradient from discrete readings of thermocouples (left) along with the quasi-continuous temperature gradient in longitudinal direction recorded by a fibre-optic sensor (right) in beam 1

(Bild 8.10, links). An den Rändern fällt die Temperatur über eine Länge von ca. 180 mm (b_{Rand}) näherungsweise linear ab (Bild 8.10, rechts). Der effektive Gradient ΔT_{eff} ergibt sich nach Gl. 8.9 aus der Fläche unter der Temperaturkurve, hochgerechnet auf den Temperaturunterschied über die gesamte Höhe ($\approx$ 23,9 °C). ΔT_{eff} von 28,2 °C entspricht aufgrund der Echtzeitregelung während des Versuchs sehr genau dem theoretisch erforderlichen Wert (28,1 °C). ΔT_{eff} des zweiten Balkens (34,4 °C) beträgt dagegen wegen der beschränkten Temperierleistung nur 44 % des Zielwerts (78,2 °C).

Dehnungen

Bild 8.9 zeigt unten – beispielhaft für den Balken 1 – die geringen Dehnungen im Stützbereich anhand der 0,20 m vom Mittelauflager entfernt applizierten DMS S_2, S_8 (initiale Bewehrung) und S_{14} (Verstärkungsbewehrung). Aus der Belastung (Eigengewicht, Stahlboxen, Gewichte) resultieren Dehnungen von $+/-24$ µm/m ($t = 0$). Sie bleiben deutlich unter der Rissdehnung von ca. 0,08 ‰ [125]. Die Dehnungen folgen dann der stufenartigen Eintragung des Temperaturgradienten. Der positive Gradient (Oberseite wärmer als Unterseite) wirkt dem negativen Stützmoment entgegen. Mit Erreichen des effektiven Temperaturgradienten (28 °C) nach ca. 25 Stunden ist die Bewehrung nahezu dehnungsfrei.

Nach erfolgter Querschnittsverstärkung, einer Aushärtezeit des Vergussmörtels von rund einem Tag (Festigkeit: ca. 40 N/mm^2) und dem Rückgang des Gradienten innerhalb von ca. 4 Stunden stellen sich in der initialen und der nachträglich ergänzten Bewehrung näherungsweise gleiche Dehnungen von 31 µm/m ein. Diese weichen um 7 µm/m von der Ausgangsdehnung (24 µm/m) ab. Auch S_8 unten in der Druckzone erhöht sich um 7 µm/m auf -17 µm/m. Aufgrund des konstanten Dehnungsanstiegs im Querschnitt entspricht die Krümmung κ_1 der initialen Krümmung κ_0.

Belastungstest

Im abschließenden Belastungstest wird das Last-Verformungsverhalten der zwei verstärkten Balken ermittelt. Bild 8.11 zeigt die mittels Wegaufnehmern in Feldmitte aufgenommenen Kraft-Wegdiagramme. Im ungerissenen

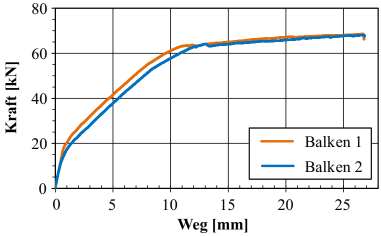

Bild 8.11: Kraft-Weglinien der zwei verstärkten Balken

Figure 8.11: Force-displacement diagrams of the two strengthened beams

Zustand liegen die beiden Linien übereinander. Mit einsetzender Rissbildung bei ca. 15 kN ($\hat{=}\ M \approx 2{,}9$ kNm, rechn. $M_{\text{cr}} = 2{,}6$ kNm) sinkt in beiden Balken die Steifigkeit. Der bei Teilbelastung verstärkte Balken weist etwas größere Verformungen auf. In beiden Balken beginnt die Bewehrung bei ca. 63 kN zu fließen, ersichtlich durch stark ansteigende Verformungen bei geringer Laststeigerung. Die Kraft entspricht unter Annahme der klassischen Balkentheorie und konstanter Biegesteifigkeit einem Feldmoment von 12,3 kNm (rechn. Fließmoment $M_{\text{y}} = 11{,}7$ kNm) und einem Stützmoment von $-14{,}8$ kNm. Im Gegensatz zum vollständig entlastet verstärkten Balken weist die Kurve von Balken 2 bereits bei 53,0 kN einen leichten Knick auf, was auf das Erreichen der Fließdehnung der initialen Bewehrung im Stützbereich zurückzuführen ist.

8.5 Diskussion der Ergebnisse

In Bild 8.11 werden Abweichungen im Verformungsverhalten zwischen dem vollständig und dem teilweise entlastet verstärkten Balken deutlich. Um zu klären, ob dies beim Balken 2 auf das materiell nichtlineare Verhalten durch Rissbildung oder die nicht vollständige Entlastung durch den lediglich anteilig (44 %) induzierten Temperaturgradienten zurückzuführen ist, werden die experimentellen Daten zu Momenten-Krümmungsbeziehungen (M-κ) aufgearbeitet und theoretisch abgeleiteten Linien gegenübergestellt. Bild 8.12 zeigt dazu experimentell (gestrichelte Linien) und theoretisch (durchgezogene Linien) ermittelte M-κ-Beziehungen für den Stützquerschnitt. Für die experimentell basierten Kurven werden die Momentenwerte aus den Zylinderkräften abgeleitet. Die Krümmungen werden aus den Dehnungswerten der DMS am Stützquerschnitt ermittelt. Die rechnerischen M-κ-Linien werden über Gleichgewichtsbedingungen am Querschnitt bestimmt. Der verwendete trilineare Ansatz berücksichtigt näherungsweise die Tragwirkung des Betons zwischen den Rissen (Zugversteifung). Die angesetzte Fließdehnung von 3,0 ‰ wurde in Begleitversuchen bestimmt.

Die experimentelle M-κ-Linie des entlastet verstärkten Balkens (orange gestrichelt) folgt weitgehend der rechnerischen Linie bei initialer Verstärkung (orange). Das Fließmoment von $-14{,}1$ kNm entspricht recht genau dem Berechnungswert. Theoretische Untersuchungen zeigen allerdings, dass sich die Entlastung während der Verstärkung im Zustand I kaum auf das Verformungsverhalten auswirkt. Da die Dehnung in der initialen Bewehrung im ungerissenen Zustand sehr gering ist, tritt auch bei einer Verstärkung unter Belastung kein signifikanter Dehnungsunterschied zwischen den Bewehrungen auf. Die M-κ-Linie entspricht auch dann annähernd der Linie der initialen Verstärkung (orange).

Bei nachträglicher Verstärkung initial bereits gerissener Balken wirkt sich die eingeschränkte Wirksamkeit der zusätzlichen Bewehrung hingegen stärker auf das Verformungsverhalten aus

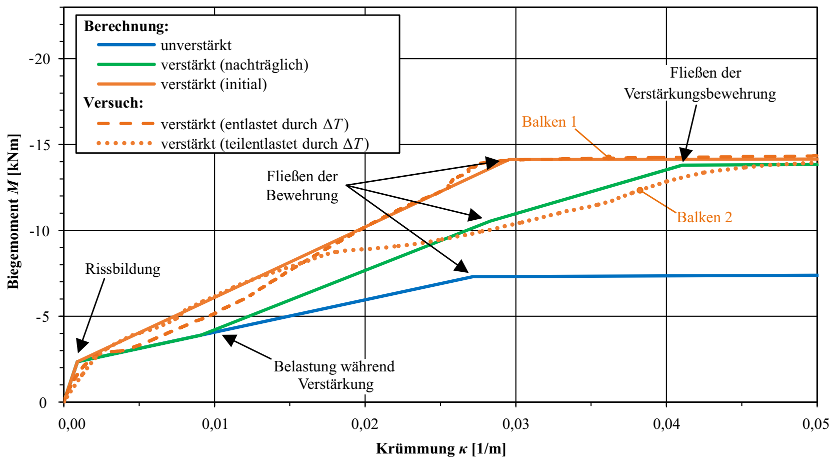

Bild 8.12: Rechnerische und experimentell bestimmte Momenten-Krümmungsbeziehungen von unverstärkten und nachträglich bzw. initial verstärkten Querschnitten

Figure 8.12: Theoretically and experimentally determined moment-curvature relations of cross-sections with and without subsequent or initial strengthening

(Bild 8.12, grün). Aufgrund des großen Dehnungsunterschieds zwischen den Bewehrungen erreicht die Initalbewehrung bereits bei $-10{,}5$ kNm ihre Fließdehnung. Die Steifigkeit des Querschnitts reduziert sich dadurch zunächst nur leicht. Eine stärkere Verformungszunahme erfolgt erst mit Fließen der nachträglich ergänzten Bewehrung bei knapp -14 kNm. Das Fließmoment entspricht dem Moment des entlastet verstärkten Balkens (orange), allerdings ist die Krümmung (0,041 1/m) um 66 % größer. Die experimentell ermittelte M-κ-Linie des teilentlastet verstärkten Balkens (orange gepunktet) liegt erwartungsgemäß zwischen den rechnerischen Linien eines nachträglich und eines initial verstärkten Querschnitts. Sie folgt zunächst der bei initialer Verstärkung erwarteten Linie, bei höheren Momenten tritt dann eine unerwünschte Annäherung an die nachträgliche Verstärkung auf. Die fehlende Entlastung aus dem unvollständigen Temperaturgradienten tritt zutage.

8.6 Schlussfolgerungen

Temperaturinduktion kann zur gezielten Steuerung von Schnittgrößen in statisch unbestimmten Tragwerken genutzt werden. Durch vertikale Temperaturgradienten an bestimmten Positionen sind beliebige lineare Momentenverläufe in Mehrfeldträgern induzierbar. Große Gradienten über kleine Längen können dabei äquivalent durch kleine Gradienten über größere Längen ersetzt werden. Bei der Induktion entsteht eine zusätzliche, günstige Wirkung infolge Temperaturlängsausbreitung, welche in Nachrechnungen über einen effektiven Gradienten berücksichtigt werden kann.

Bei Tragwerksverstärkungen ermöglicht die Anwendung der Temperaturinduktion eine Aktivierung des Gesamtquerschnitts bereits für die Aufnahme des Eigengewichts. Dazu ist das Tragwerk während der Verstärkung lokal zu entlasten. Das entwickelte Verstärkungsverfahren lässt sich auf Balkentragwerke wie Brücken oder in Hochbauten anwenden. Die reduzierten Verformungen wirken sich vor allem positiv auf den Gebrauchszustand aus.

Die Umsetzung erfolgt hier an Zweifeldträgern, welche im Stützbereich mittels Gradienten entlastet und durch eingeschlitzte Bewehrung nachträglich verstärkt werden. Der unter Eigengewicht ungerissene Balken ist planmäßig bei einem effektiven Gradienten von 28 °C (Temperaturunterschied: 24,5 °C) entlastet. Nach Rückgang des Gradienten stellen sich die Eigengewichtsspannungen gleichmäßig im neuen Gesamtquerschnitt ein. Theoretisch ergeben sich bei Verstärkung im ungerissenen Zustand aber auch ohne Entlastung nur sehr kleine, für das Verformungsverhalten kaum relevante Spannungsunterschiede in initialer und nachträglicher Bewehrung. Im bereits gerissenen Zustand hingegen reduzieren sich die Verformungen durch die Aktivierung der Verstärkungsbewehrung rechnerisch bis zu 65 %. Dazu ist zur Entlastung des zweiten Balkens ein deutlich größerer Gradient von 78 °C erforderlich. Die erreichten 34 °C entlasten den Stützbereich nur anteilig um 44 %. Die experimentell erzielte Momenten-Krümmungsbeziehung liegt daher erwartungsgemäß zwischen den rechnerischen Linien eines initial und eines nachträglich verstärkten Querschnitts.

In weiterführenden Versuchen sollen größere Gradienten mit elastischen Heizmatten realisiert werden. Zur besseren Erfassung des Bauteilverhaltens bei Rissbildung ist der Einsatz von Kraftmessdosen und quasikontinuierlich messenden faseroptischen Sensoren geplant.

Chapter 9

Supplement: Damage Detection at a Reinforced Concrete Specimen with Coda Wave Interferometry

The following chapter is taken verbatim from:

> GRABKE, S.; CLAUß, F.; BLETZINGER, K.-U.; AHRENS, M. A.; MARK, P. and WÜCHNER, R. *Damage Detection at a Reinforced Concrete Specimen with Coda Wave Interferometry*. Materials, 2021. 14(17): 5013. doi: 10.3390/ma14175013.

Text and figures have been adjusted to the format and layout of this thesis. The content remains identical. The literature used is jointly referred to at the end of the thesis.

Abstract

Reinforced concrete is a widely used construction material in the building industry. With the increasing age of structures and higher loads there is an immense demand for structural health monitoring of built infrastructure. Coda wave interferometry is a possible candidate for damage detection in concrete whose applicability is demonstrated in this study. The technology is based on a correlation evaluation of two ultrasonic signals. In this study two ways of processing the correlation data for damage detection are compared. The coda wave measurement data is obtained from a four-point bending test at a reinforced concrete specimen that is also instrumented with fiber optic strain measurements. The used ultrasonic signals have a central frequency of 60 kHz which is a significant difference to previous studies. The experiment shows that the coda wave interferometry has a high sensitivity for developing cracks and by solving an inverse problem even multiple cracks can be distinguished. A further special of this study is the use of finite elements for solving a diffusion problem which is needed to state the previously mentioned inverse problem for damage localization.

9.1 Introduction

Concrete is a material commonly used in the construction industry. Especially the combination of concrete and steel reinforcement results in many advantages. During the lifespan of a concrete structure, the appearance of cracks in the structure is very typical. Those cracks are either intentional or due to environmental influences, increased loads, aging or local failure. Regular inspections and assessments are therefore very important to ensure the functionality of concrete structures. In addition to regular visual inspections, permanent structural health monitoring techniques are increasingly used. Established techniques use, for example, strain gauges on concrete and steel.

Coda wave interferometry (CWI) is a rather novel monitoring and damage detection technique applicable to concrete. It is based on elastic waves and originates from geophysics, more precisely, seismology. [107] were one of the first to apply the technique to concrete and [150] are giving a good review on CWI in concrete. The application of CWI to concrete is possible due to the high heterogeneity of the material that creates scattering. This increases the area to which a signal is sensitive and additionally increases the sensitivity to very small changes. The CWI is based on the principle that signals with their diffuse tail created by the scattering can be reproduced. When evaluating a signal, it is compared to a reference signal. As soon as small perturbations appear in the medium, the signal undergoes small changes. An evaluation of these changes in the signal subsequently allows a localization of the cause that are often cracks in the concrete.

For concrete structures, the used signals have a central frequency in the ultrasonic spectrum. [150] differ the single scattering regime with frequencies between 20 kHz and 150 kHz and the multiple scattering regime with frequencies between 150 kHz and 1 MHz. In general, an increase of the signal scattering improves the CWI performance. This is accompanied by the use of higher frequencies, which, however, reduces the maximum possible distance between the source and receiver. [108] and [218, 219] have successfully applied CWI for damage detection in real concrete structures with frequencies in the multiple scattering regime. A more recent experiment of [93] and [213] has conducted a similar, inverse problem based, imaging and successfully detected multiple cracks whose position, however, strongly correlates with the ultrasound sensors that were attached to the surface after cracking. On a structural scale, several groups [72, 139, 199, 201, 202, 214] have conducted field experiments with CWI and demonstrated the immense potential of the technology based on an signal evaluation but without a damage localization as it is done in the present study. For the monitoring at a very large, structural scale, greater measuring distances are required. Thus this study tests the use of 60 kHz that in concrete rather belongs to the single scattering regime but based on [62] should be applicable for CWI in concrete. For this purpose, CWI is applied to a four-point bending test on a reinforced concrete specimen.

In Section 9.2 the general principle of CWI is described and two methods for the localization of damage are introduced. A special and novel feature of the first damage localization approach is a substitute model which is based on a finite element simulation. The second approach to damage localization is a very simple, novel technique based on the arithmetic mean, that in contrast to the first approach does not require the solution of an inverse problem an thus is very fast. Section 9.3 gives an overview of the experiment with the used test set-up and expected behavior of the material. Next to ultrasound measurements, strain in a reinforcement bar is measured with fiber optic sensors (FOS). In Section 9.4 the CWI data is analyzed and a damage localization is performed at different damage states. For the localization, the two used ultrasound based imaging techniques are compared to the FOS data. In the end the damage localization results with CWI at the four-point bending test are discussed.

9.2 Ultrasound Methods

Coda wave interferometry uses diffuse ultrasound to measure relative changes of a signal compared to a reference state. Those changes are typically created by a change of the concrete's temperature [210], moisture [94] and stresses [107, 114] that mostly affect the wave speed of the signal but also changes in the propagation medium due to cracks modify the signal [109]. If none of these changes occur in the medium, signals and their diffuse tails can be reproduced. This study puts a focus on damage detection that requires a CWI specific signal processing described in Section 9.2.1 which then allows to localize damage.

9.2.1 Basics

The central measurement parameter in CWI is a cross-correlation coefficient (*CC*) that quantifies the similarity of two compared signals. It is computed for a time frame of length T in the signal φ at time t as following [155, 159]:

$$CC(t) = \frac{\int_{\mathrm{t-T/2}}^{t+T/2} \varphi_{\mathrm{ref}}(t)}{\sqrt{\int_{\mathrm{t-T/2}}^{t+T/2} \varphi_{\mathrm{ref}}^2(t)\,\mathrm{d}t}} \cdots$$

$$\frac{\varphi(t)\,\mathrm{d}t}{\int_{\mathrm{t-T/2}}^{t+T/2} \varphi^2(t)\,\mathrm{d}t} \tag{9.1}$$

Very often, the *CC* is translated into a decorrelation coefficient (*DC*) that uses a magnitude from zero to one to describe how large the changes are in a signal. The relation of *CC* and *DC* is as follows:

$$DC = 1 - CC \tag{9.2}$$

The decorrelation of two signals is used for imaging the cause of the signals' changes. Depending on the used method, the signal is either evaluated in one long time frame or multiple successive shorter time frames. Multiple evaluation windows can evaluate a *DC* development that tends to increase in later parts of the signal because more random wave paths cross the new scatterer and create different interferences with other wave fronts that all add up to an increased decorrelation. This described increasing development is very characteristic for the relative position of a cause to the source-receiver pair and is modeled by the sensitivity kernel introduced in Section 9.2.3. With this substitute model, an inverse problem can then be formulated whose solution localizes the cause of the changes. When evaluating only one time frame per measurement, one *DC* can be assigned to each measurement pair. With the use of influence areas for each pair (Section 9.2.5) the decorrelations can then be mapped on the geometry.

With an ongoing monitoring, there are multiple measurements performed with each pair. For choosing a reference, there are typically two possibilities. One is a fixed reference measurement, e.g., the first one. The other one is a stepwise update of the reference signal such that the used reference is always the previous measurement. The CWI is based on small changes in the signal and a general reproducibility of the signals. This is usually fulfilled with the stepwise updated reference approach but not necessarily with a fixed reference. Thus, the stepwise approach is chosen for this study.

The measured decorrelations are typically created by two slightly different phenomenons. One is a waveform distortion and the other one is a phase-shift of the signal. The phase-shift is created by a change of the signals' wave speed that is inducted, e.g., by the acoustoelastic effect [114] that links wave velocity and stresses in the medium. Waveform distortions are typically caused by new scatterers such as cracks. With a focus on damage detection, the impact of phase-shifts on the decorrelation should be minimized by stretching the signal with a stretching factor ε. This cancels out the phase-shifts and is done with the technique introduced by [177]. After stretching, the remaining decorrelation of two compared signals is assumed to be mainly caused by new scatterers such as cracks.

In this study, signals with a length of 2000 µs after the signals' time-of-flight (tof) are evaluated. For computing one overall *DC* of a measurement, the time frame is of length $T = 2000\,\mu\text{s}$. When evaluating a *DC* development within the signal, five successive time frames with length $T = 400\,\mu\text{s}$ are used. This is exemplary shown in Figure 9.1.

9.2.2 Diffusion Approximation

When thinking of a simulation that resembles the performed experiment, the model would need to contain a heterogeneous material with a very fine refinement in order to represent the used concrete. In addition, the time steps used would have to be very short to achieve numerical stability for an acoustic wave simulation. This causes great computational costs that limit the maximum size of the modeled geometry. Thus, a central simplification is used in the description of how the wave propagates through a heterogeneous medium. As [160] have shown, the spread of a waves' energy in a random media as concrete can be approximated with a diffusive spread in a homogeneous medium. This significantly improves computational costs. The main parameter of this approximation that includes the overall scattering behavior of concrete is the diffusivity D. It can be determined with an envelope fitting of the signal as shown in Figure 9.1 where one can see the relation of the complex, diffuse signal and the simple diffusion envelope. Doing so, the mean diffusivity in this study was determined at

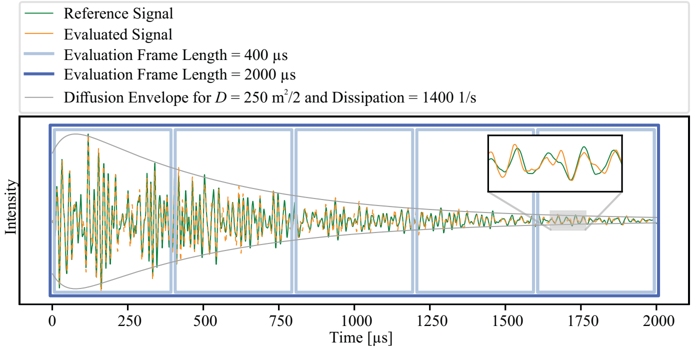

Figure 9.1: Example signal (60 kHz) with the used evaluation windows and envelope fitting with the solved diffusion equation

about 250 m^2/s.

This study uses a novel finite element (FE) based formulation that solves the given problem. The use of FE is a significant difference to previous applications that are usually based on analytical solutions and opens the door to many improvements of the technology. FE and the accompanying use of unstructured meshes allow the problem to be solved for arbitrary, complex-shaped geometries, and the generic FE approach even allows the solution to be further improved by using a different partial differential equation that better approximates the given wave phenomenon. The present study uses the open-source project KRATOS Multiphysics* for solving the FE problem.

9.2.3 Sensitivity Kernel

For simulating the actual correlation measurements of two compared signals, a substitute model introduced by [145] is used that computes sensitivities of a measurement to a local change. This so called sensitivity kernel describes the possibility that a wave has passed a location x during a travel time t from the source S to the receiver R and thus describes where a wave got its information from. It is calculated as follows:

$$K(S,R,x,t) = \frac{\int_0^t I(S,x,u)\cdots}{I(S,R,t)}$$
$$\underline{\cdots I(x,R,t-u)\,\mathrm{d}u} \qquad (9.3)$$

In Equation 9.3, $I(pos\,1, pos\,2, t)$ stands for the wave intensity which here is equated to the possibility of a wave traveling from $pos\,1$ to $pos\,2$ in time t. Instead of an actual wave intensity, the approximation of Section 9.2.2 is used and the FE solution of the simulation with KRATOS Multiphysics is inserted for I. At each position x the sensitivity kernel gives a development over time that resembles the DC development over the signals' length in case a scatter is added at the corresponding position x.

9.2.4 Imaging with an Inverse Problem

Being able to simulate the DC development for any location x allows to formulate a problem that,

*www.cimne.com/kratos/

when solved, localizes the cause for the decorrelation. [152] describes this problem as

$$Gm = d \tag{9.4}$$

where G is a matrix that contains the sensitivity kernel for one specific measurement pair at a specific time in each row. The vector d contains the measured decorrelation in the signal with pair and time matching the sensitivity kernel in the corresponding row. The vector m contains the damage at each node of the mesh and is the unknown in this equation. The size of G is $n \times m$ with n referring to the amount of nodes in the mesh and m referring to the total amount of measurements. Typically the amount of nodes in the mesh is larger than the amount of measurements and thus, the problem is underdetermined. The equation system of Equation 9.4 is inconsistent and reformulated to a least-squares optimization problem:

$$\min \|d - Gm\|_2 \tag{9.5}$$

For solving this large-scale ill-posed problem, a trust region reflective algorithm by [15] called STIR is used in this study. It is referred to as a subspace, interior and conjugate gradient method for bound-constrained minimization problems. Especially the boundary on the variables is very useful since damage effects in the coda signal can only add up (no negative values allowed) and the maximum effect of one node in the mesh should also be limited to $m_{\max}$.

9.2.5 Imaging with Influence Areas

Next to a simulation that should resemble the *DC* measurements, a second, simpler approach is used in this study. For this novel approach, an influence area is assigned to each measurement pair. In order to choose such an area, a signals sensitivities computed with the sensitivity kernel are used. The used sensitivity kernel has a source-receiver distance of 30 cm which resembles the typical distance used in the experiment that is introduced in Section 9.3. However, a different source-receiver distance of the kernel produces a similar looking sensitivity kernel and thus the approach can be used for other source-receiver distances as well. By limiting the sensitivities to a minimum threshold, a nearly elliptical area is obtained. The ellipse is transferred to a generic description that depends on the source-receiver distance r which is visualized in Figure 9.2. In this study an ellipse with the semi-major axis $a = 0.875 \cdot r$, the semi-minor axis $b = 0.6 \cdot r$ and an eccentricity $e = r/2$ is used. The obtained ellipse parameters are depending in the chosen sensitivity threshold which is a free parameter. Thus the influence areas can be varied in case the obtained imaging has too strong contrasts or if the smoothing is to be reduced. In order to obtain a smooth overlap with other regions, the influence vanishes to the ellipse border, which is indicated by blue on the right of Figure 9.2. With the influence areas, the transfer of measured decorrelation to a spatial representation on the geometry is done with the weighted arithmetic mean. The *DC* at a position x is obtained as follows:

$$DC(x) = \frac{\sum_{\mathrm{p}} DC(p) \cdot w(x,p)}{\sum_{\mathrm{p}} w(x,p)} \tag{9.6}$$

where $w(x,p)$ is the influence of a pair p at a position x and $DC(p)$ the overall decorrelation per pair evaluated with a frame length $T = 2000\,\mu\mathrm{s}$.

9.3 Experiment

In order to prove the stated imaging on both the inverse problem and the influence areas, a structural test was carried out at the Ruhr University

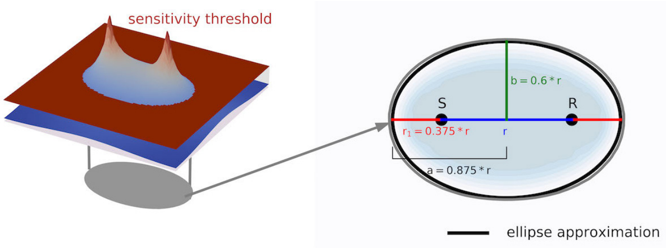

Figure 9.2: Graphical explanation of the derivation of the influence areas with the help of a sensitivity kernel

Bochum. The reinforced concrete specimen is a beam with a depth of 500 mm, width of 250 mm and length of 3900 mm. Resulting from the loading in a 4-point bending test, flexural reinforcement (3 Ø 20 mm) as well as staggered stirrup reinforcement (Ø 12 mm / 300 mm / 2) are placed. With a field length of 3500 mm (cf. Figure 9.3) and a spacing of the two concentrated loads of 1200 mm, this system represents a challenging way to demonstrate imaging. Substantiated by regularly occurring cracks between the concentrated loads. These cracks, which appear in multiplicity, unlike a single very local crack, render it difficult for the algorithm to output detailed predictions. Thus, the system provides a good means to prove the algorithm's performance.

To detect cracks, an ultrasonic signal is intentionally to be guided into the concrete. For this purpose, ultrasonic transducers (SO807 transducers from Acoustic Control Systems, Ltd., Saarbrücken, Germany) embedded in the concrete are arranged in a net-like manner throughout the specimen (cf. Figure 9.3). The aim was to cover the whole specimen with the sensor-net to be able to see differences of cracked and intact regions. With expected cracking in the middle third the density of the sensor-net was increased in this part to be able to closer investigate the effects of

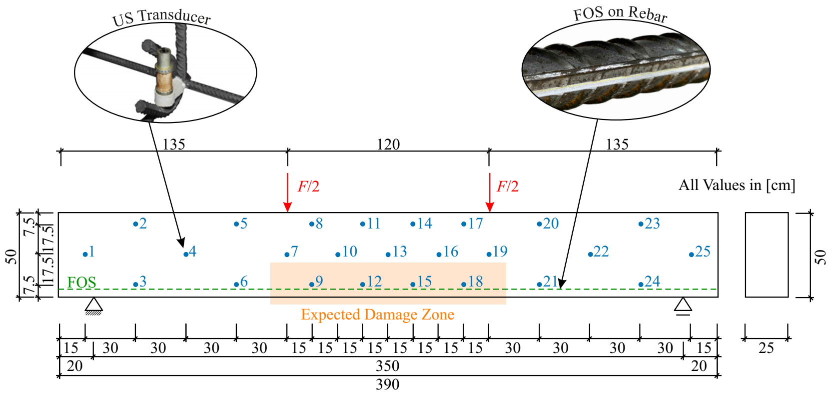

Figure 9.3: Dimensions of the test specimen with FOS in green and US transducers in blue. Results of the US transducer 16 proved to be erroneous and were not taken into account for the evaluation.

cracks on different measurement pairs. The transducers, consisting of a piezoceramic cylinder, exhibit a central frequency of approx. 60 kHz. The radiation takes place almost uniformly, perpendicular to the longitudinal axis of the transducer. Cement fasteners are used to attach the transducers to the reinforcement. Due to the similarity of the cement fasteners to the surrounding concrete, the fastener's influence on the load-bearing behavior can be prevented. During the evaluation process it became evident that transducer 16 is erroneous and thus related measurements were not taken into account.

In addition to ultrasonic measurement technology, FOS were used in particular. The FOS technology provides the possibility to measure strains and temperatures [26, 100] with high resolution (point distance about 0.65 mm). For this experiment, the Luna ODiSI 6108 fiber optic instrument (Roanoke, TX, USA) was used. A FOS was glued to a rebar (Ø 20 mm). The application of the fiber onto the rebar was realized by the adhesive Polytec PT AC2411 (Karlsbad, Germany). This adhesive proved to be suitable in detailed investigations [25] into the adhesive and fiber to be used.

From the very continuity of the fiber optic strain measurement (both temporal and spatial), it becomes evident that a lot of strain data is acquired. The measured strains along the rebar for a load from 0 to 100 kN is shown in Figure 9.4. The increasing force is reflected in the (color) profile of the strains.

Due to the low tensile strength of concrete, it cracks even when subjected to a low tensile stress. The tensile strength f_{ctm} given in Table 9.1 corresponds to the mean value from three individual samples. Variations around this mean value are a matter of course and, like many other natural processes, can be regarded as a log-normal distribution. Consequently, it is probable that cracking (an excess of the scattering tensile strength) begins earlier than ($< f_{\text{ctm}}$) the given mean value. If concrete cracks, the force, which was previously carried by the entire intact cross-section, is transferred to the reinforcing steel. The strain or stress of the reinforcing steel thus rises in the crack. As the distance to the crack increases, force is transferred back into the concrete via the bonding effect of the reinforcement and the con-

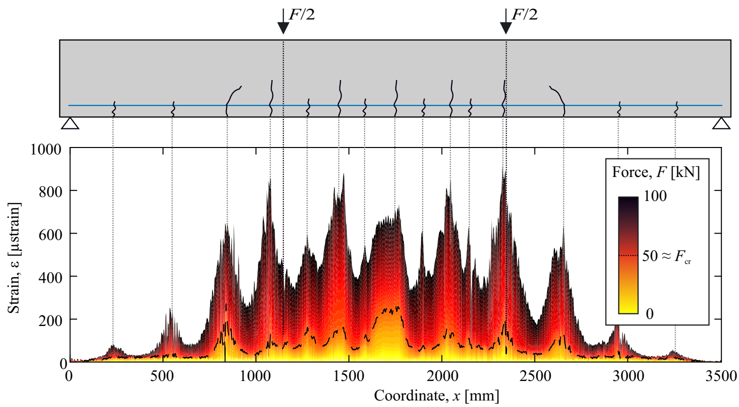

Figure 9.4: Strain results from 0 to 100 kN of the FOS. Due to the continuous measurement, the colors are referring to the load of the corresponding strain measurement.

crete. When sufficient force is again transferred into the concrete and the tensile strength is again exceeded, the next crack forms. With complete formation of the crack pattern ($> 1.3\,F_{cr}$), the peaks and valleys in the strain profile shown in Figure 9.4 appear. This defining characteristic of the load-bearing behavior of reinforced concrete can be used to capture the development of cracks and serves as a reference for the used ultrasonic measurement technology.

Table 9.1: Material properties of the concrete.

$f_{cm,cube}$ [N/mm^2]	f_{ctm} [N/mm^2]	E_{cm} [N/mm^2]
38.2	2.8	28,800

9.4 Results

The evaluation of the CWI data is performed in two different ways. Section 9.4.1 analyses the overall *DC* development of selected signals during the whole load increase process and Section 9.4.2 performs a damage localization at three different load states.

9.4.1 Decorrelation Investigations on Selected Measurement Pairs

Figure 9.5 shows the *DC* development of seven selected measurement pairs. The aim of this selection is to cover areas in the structure with different stresses. The following paragraphs group comparable pairs with the numbering relating to Figure 9.5.

Pair 1 & 6

Pair 1 and 6 are in a zone with comparable small stresses that is also the furthest away from developing cracks. The *DC* development with values around 0 up to load step 22 confirms this. Further load increases generate a slight increase of the *DC* that is relatively small compared to other measurement pairs. The reason are probably massive cracks in the middle third and a crack development further to the sides. This shows that measurement pairs have a limited extended sensitivity and the influence of ballistic waves passing through the specimen several times is very small.

Pair 3 & 4

Pair 3 and 4 are in the zone with the highest tension stresses and an area where multiple cracks are expected to develop. The *DC* development shows a first significant increase in the *DC* around load step 8 and continues to increase until approximately load step 16. This indicates strong crack formation. The constant increase of the *DC* can be explained by the fact that the cracks open up more and more and thus, the transmission of the ultrasonic waves becomes increasingly worse. The time of crack formation coincides approximately with the average tensile strength of the concrete and is closer investigated in Section 9.4.2.

Pair 5 & 7

Pair 5 and 7 are closer investigated due to an observation that led to problems in the damage localization. Figure 9.6 shows the FOS data at load step 9 next to the transducer positions.
The FOS indicates cracks close to transducers 6, 9 and 21 at load step 9. For transducer 21 at $x = 2.85\,\mathrm{m}$ the formed crack seems to have a large impact on the general reproducibility of the signals related to that transducer. It is possible that a crack into the mounting position of transducer 21 massively impacts the transmission of ultrasound into the concrete. This generates unusually large decorrelation. The fact that the decorrelation is unusually large also be-

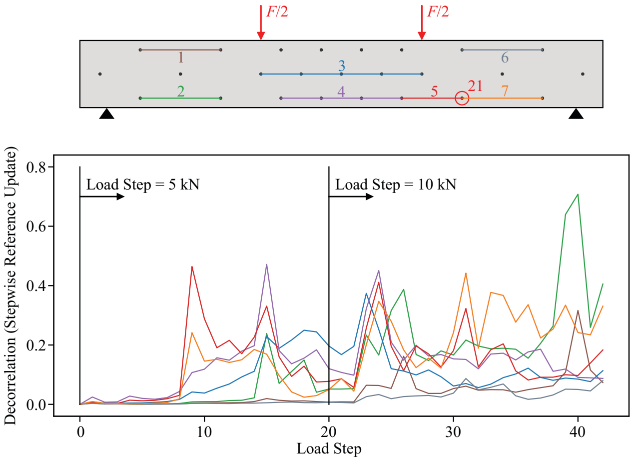

Figure 9.5: Decorrelation development on selected measurements

comes apparent when comparing pair 2 and 7. Also, the *DC* of pair 5 and 7 would be expected to be smaller than for pair 4. The unusual large decorrelation becomes a problem for the damage localization since the modeled approximation of measurements is not valid anymore. Affected measurements are therefore filtered from the used measurement set.

9.4.2 CWI Damage Localization

For the damage localization, three states are distinguished. One is before cracks are detected by the FOS (Section 9.4.2), one is during the formation of first cracks (Section 9.4.2) and the last one is after the average tensile strength is reached (Section 9.4.2). For all three states, the FOS data is compared to a damage localization by solving an inverse problem (Section 9.2.4) and the spatial representation of the correlations with the help of influence areas (Section 9.2.5).

State 1: Uncracked

In the early load stages, it is expected that the different monitoring systems detect no damage. An evaluation of load step 3 at 15 kN shown in Figure 9.7 generally confirms this assumption but indicates first tendencies. Those tendencies are the formation of first little peaks in the FOS (marked with red color in Figure 9.7) and an imaging of

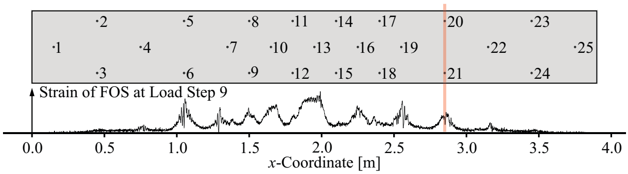

Figure 9.6: Comparison of FOS data to transducer positions at load step 9

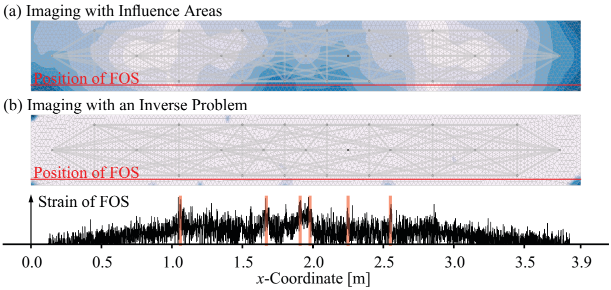

Figure 9.7: Evaluation at load step 3 with 15 kN load applied

the overall decorrelation with the influence areas that among others tends to the tension zone in the middle. Those first tendencies of the coda correlations underline the high sensitivity of the technique to very little changes in the medium such as micro cracks. The high values in the lateral edge areas of Figure 9.7a are presumably related to the low density of measurement pairs. An evaluation at the next load step with 20 kN applied confirms the first trends from the previous load step. Especially the first tendencies of the FOS data in Figure 9.7 that are marked in red have now become clearly visible peaks. For comparison, the six positions marked in red in Figure 9.7 are also shown in Figure 9.8. One can see that the high values in the lateral edge regions of the influence areas imaging have nearly vanished presumably because decorrelation in the tension zone is clearly greater. Additionally, one can notice that the tension zone shows the largest decorrelation but also the top middle part indicates large *DC* values. Besides the expansion of the influence areas, this is presumably related to the larger changes of the stress state compared to the other areas. At this load step, where the first cracks are clearly detected by the FOS, the solution of the inverse problem shows first tendencies as well. However, the localization does not match the FOS data and rather determines the center of several small cracks. This load state with a manageable crack pattern is used to determine the magnitude of the solution and the

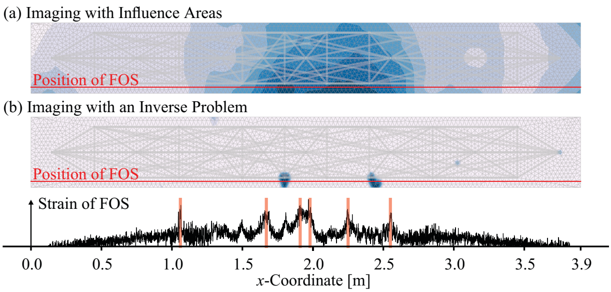

Figure 9.8: Evaluation at load step 4 with 20 kN load applied

maximum boundary $m_{\max}$ for the inverse problem. A value of $m_{\max} = 2$ shows a reasonable crack extension and is thus used for an evaluation at all other load steps.

State 2: Crack Formation

Load step 4 shows that the first micro cracks already occur at stresses significantly below the average tensile strength of the concrete used f_{ctm}, which is reached at load step 10. This shows that a clear determination of the first real damage is difficult. For an evaluation of the crack formation, the load steps 9 to 12, which are around the calculated crack formation, are closer investigated. A comparison of these consecutive load steps 9–12 shows similarities in the detection but also clear differences at certain located crack positions can be noticed. A possible reason could be a non-uniform crack development. In order to reduce such influences, the imaging shown in Figure 9.9 superimposes the four individual damage images of load steps 9 to 12 which are the load steps where the first cracks are most likely to develop. Adding up the damage is justified insofar as the stepwise reference update as described in Section 9.2.1 is used and the superposition then represents the change from load step 8 to 12. In Figure 9.9a one can see that in general, the positions of several transducers are detected as most likely damage locations. By exploiting the symmetry of the experiment, unusually large decorrelation developments for certain measurement pairs as they are also described in Section 9.4.1 can be noticed. These unusually large decorrelation measurements are filtered from the total set. The remaining measurement net of 61 pairs with the corresponding superposed imaging of load steps 9 to 12 is shown in Figure 9.9b.
The image from Figure 9.9b looks insofar good that transducer positions are generally no longer detected as most likely damage location. Figure 9.10 compares the results to the influence areas imaging and FOS data. The influence areas imaging indicates significantly larger decorrelation for the middle third as it is expected. The extension of this middle area is also in relative good accordance to the extension of the crack pattern determined with the FOS. Large changes over the height can only be detected to a limited extent, which is probably related to the relatively large sensitivities of the upper measurement pairs for the bottom area and the use of vertical and diagonal measurement pairs.
The crack pattern obtained with the inverse problem shows a good correlation with the more reliable FOS data. Remarkable is the distinction of multiple cracks which is strongly influenced by three factors. One is the superposed imaging.

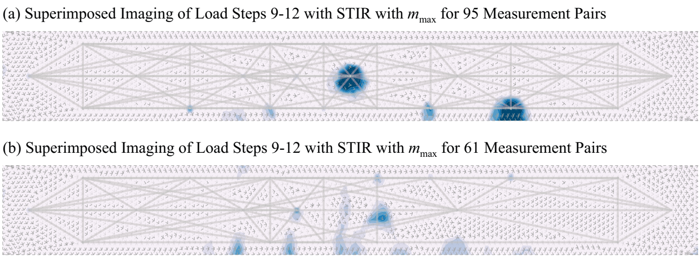

Figure 9.9: Comparison of the damage localization with an inverse problem for 95 pairs (a) and *DC*-based selected 61 pairs (b) using the STIR method with $m_{\max} = 2.0$

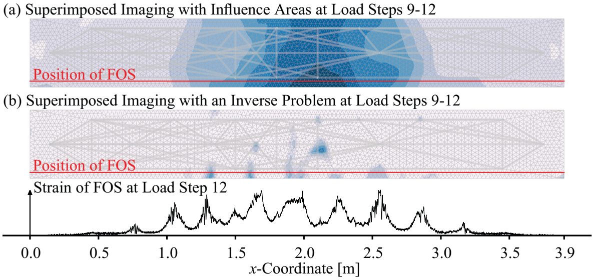

Figure 9.10: Evaluation of the change between load step 8 and 12

Each of the four individual damage images has a tendency to certain cracks or areas. Superimposing multiple states smoothes out this observation that possibly is related to a non-uniform crack development between each load step. The second factor is the use of an upper boundary on the variables of $m_{\max} = 2$ for the given set-up. This prevents a localization at the center of multiple cracks. The last factor is the pre-selection of used measurements pairs based on unusually large decorrelation development whose impact can be seen in Figure 9.9.

State 3: Cracked

The third evaluation state is chosen relativity late in the loading progress. The aim is to investigate the extent to which a crack pattern still changes and what effect this has on the coda measurement technique. As in Section 9.4.2 several measurement pairs are taken from the set of used pairs because with those measurements mainly installation positions of transducers are localized as damage location. Figure 9.11 shows the detected changes between load step 27 and 30.

The FOS data and also the inverse problem imaging show that the crack development in the middle third is completed and changes in the specimen now appear in the previously unaffected areas further to the sides. This underlines the fact that existing cracks can only be detected to a limited extent with CWI. Once a crack development is completed, the CWI with a stepwise updated reference will not detect that crack since no more changes appear in the medium. The FOS

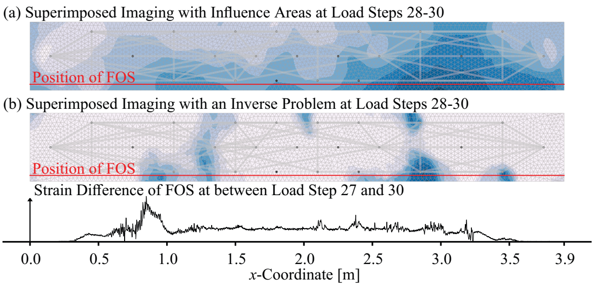

Figure 9.11: Evaluation of the change between load step 27 and 30

data shows one clearly visible peak on the left and also the inverse problem localizes that area. Additionally, there are a few other areas detected that can not be seen in the FOS data. This can have two possible causes. First one is that the crack development at the height of the FOS is completed and a crack only develops above the FOS mounting height. The second one is that the filtering of unusually large decorrelated measurement pairs by engineering instinct was not sufficient. A further filtering would, however, affect an equally balanced measurement net. Thus, the conclusion is that in such a highly cracked condition, the application of CWI in concrete is very difficult.

9.5 Discussion

9.5.1 Overall Discussion with an Outlook to General Improvements

The material behavior in the four-point bending test is as expected. The FOS data appears very reliable and detects multiple cracks at already a very early load state. Its crack detection however is limited to one reinforcement bar only and the installation on a large structural scale shows problems since the careful application of the fiber on the reinforcement is labor intensive and thus expensive. Here are advantages of the CWI that shows the potential to detect multiple cracks and covers a larger area with a simpler installation. Despite a longer wavelength compared to previous experiments by [108] and [218, 219], the sensitivity of the CWI is remarkably high. The damage localization by solving an inverse problem for the time of crack formation as shown in Figure 9.10 is of good accuracy compared to the FOS data and especially the distinguishing of multiple close cracks is remarkable. The comparable experiment of [93] and [213] achieved similar results but with the very close positions of cracks and transducers the problem of the present study with a detection at transducer positions (cf. Figure 9.9) can not be excluded. The used frequency of 60 kHz is a novelty in damage localization with CWI in concrete and opens the door for an application on a large structural scale with longer distances between source and receiver. The present experiment used a rather dense measurement net as the aim was to localize multiple cracks as exact as possible in a controlled environment. When applying CWI on large structures, e.g., bridges, and the aim is to trigger an alarm when cracks in concrete appear but need no precise localization, the transducer network can be chosen less dense and with larger source-receiver distances to cover the whole structure. However, estimating transducer density and localization accuracy is quite difficult and part of ongoing research. Experiments by [200, 202] and [60, 61] demonstrated the applicability of CWI with source-receiver distances of at least 1 m. In the present experiment transducers are embedded into the concrete which ensures good transmission of the ultrasonic signal into the concrete and general robustness. As several experiments [211, 213, 218, 219] have shown, the use of external transducers attached to the surface is also possible and allows monitoring of existing structures.

9.5.2 Crack Detection and Related Challenges

The exact definition of one load step at which cracking happens is rather difficult. Thus, several load steps around the load level at which the concretes tensile strength is reached are evaluated and superimposed. With comparably large changes in the structure, the CWI is susceptible to bad measurements in the dataset. Those bad measurements can be caused by cracks into the mounting position of transducers. For the given specimen, this is not unusual because the ultrasound transducers weaken the cross section and thus attract cracks. Related measurements need to be filtered from the used dataset since the *DC* are unusually large and do not match used assumptions, e.g., a general good reproducibility of the signals. So far, this is done with engineering instinct, but will be parameterized and automated in future studies. A statement about the size of the cracks is not yet possible. The goal of future research will be to find structure-related damage limits for the coda technology. The analysis in the cracked state revealed a weakness of the CWI that existing damage is difficult to detect with a stepwise updated reference.

9.5.3 Comparison of Imaging Approaches

Comparing the two CWI imaging approaches, the solution for an inverse problem can locate damage locations better than what is possible with influence areas. The computational effort however is significantly larger since an ill-posed problem needs to be solved whereas with influence areas only a matrix vector product is computed. Nevertheless, the influence areas have proven to be a useful tool for transferring the measured decorrelation to a spatial representation on the geometry. Especially with a lot of overlapping of measurement pairs, the technique is advantageous to simpler interpolations as, e.g., used by [139]. The extension of highly "decorrelated" regions was also in accordance to computed stresses and crack regions. For future research, it would be conceivable to use the fast mapping with influence areas as an initial guess for the inverse problem.

The FE formulation for the given problem is a major difference compared to previous studies [93, 213, 218, 219] that use an analytic solution of the diffusion problem or the radiative transfer equation. The generic FE approach is based on unstructured meshes and allows for several improvements such as an application to arbitrary, complex geometries as it is needed when transferring the technology to real structures such as bridges.

9.6 Conclusion

Overall the present study shows the high potential of CWI as a monitoring and damage detection technique for large structures. The used set-up with a central frequency of 60 kHz that belongs to the single scattering regime is a novelty in for inverse problem based damage detection with CWI in concrete. The high sensitivity to small changes in the concrete as well as a good localization and distinguishing of multiple appearing cracks underline the immense potential of CWI in concrete. The addressed problem of unusually large decorrelations that do not fit the model of the inverse problem (sensitivity kernel) in a suitable way and thus hinder a good localization is a challenging problem that was solved in a rather simple way by removing related measurements from the problem to be solved. The finite element based methodology is a significant difference and improvement over established approaches that use analytical solutions. The use of a new solving technique that contains boundary constraints for the inverse problem is another presented novelty that significantly improves the imaging results. The presented imaging using influence areas marks a new, simpler but less accurate way of imaging CWI results that is more independent of a good match between the model and measurement data and thus a more robust way of imaging. In summary, the frequency range used in combination with finite element based localization has proven to be suitable for damage localization in concrete with CWI and the experiment and used methods provide a reliable basis for upscaling the technology to large existing structures.

Chapter 10

Conclusions

This thesis is devoted to ameliorating health monitoring of RC structures by US coda waves. Said objective is pursued bilaterally. On the one hand, the presented research investigates the metrological recording of strain, individually and coupled with temperature. It focuses on the assembly, application and accuracy of different measurement techniques as well as the metrological cross-influences. On the other hand, it focalizes on coda measurements and its response to changes in strain. More precisely, it deduces a correlation from the comparison between strain and the relative velocity change. Based on this correlation, the thesis derives an empirical model to evaluate the load-bearing capacity of RC structures subjected to bending using coda waves.

The model is developed for *large-scale* structures and enables predicting *internal* strain states. The focus lies on the tensile zone, which is central to structures subjected to bending. In general, as in this model, cracks in RC structures are not treated a priori as damage. Rather, RC's complex material behavior is accounted for holistically. This comprises the linear-elastic range and covers initial as well as completed cracking ranges. This work constitutes a step towards achieving the greater vision of monitoring the condition of RC structures well *before* deficiencies become critical.
The model's centerpiece is the correlation between relative velocity change and strain. Based on the integrative recording of the influences by coda waves, averaged reinforcement strains are determined from fiber optic's continuous measured data. This average steel strain is correlated to the relative velocity change of the coda. A linear relationship is found. It exhibits a high level of quality and a low error: $R^2 = 0.99$, RMSE ≈ 0.09 ‰.

The accuracy and depth of information of suited reference measurement techniques must be high due to the characteristics of coda waves, which are sensitive to small changes and the integral collection of influences in the traversed region. FOS (1D readings) and DIC (2D readings) yield this necessary depth of information. The accuracies of these strain measurement techniques have here been demonstrated to be comparable. By contrast, significant differences concerning repeatability are found. For DIC, the repeatability differs to an extent of approximately a power of ten, depending on the facet size (19^2 pixel^2: 0.3 ‰ to 100^2 pixel^2: 0.03 ‰). For fiber optics, the repeatability is much higher, at 0.007 ‰.

The fiber optic strain and temperature measurements are characterized by a high degree of mutual influence. Thus, temperature changes impair strain measurements and vice versa. It has been shown that a variation of 1 °C leads to strain deviations of 0.01 ‰. Vice versa, a 0.001 ‰ strain variation induces temperature deviations of 0.1 °C. In perspective of practical applications in construction, strain conventionally ranges between 0.1 ‰ to several ‰, whereas temperature changes only account for few °C. The experiments indicate that already a tensile force in the fiber of 0.05 N (5 g weight force) causes a temperature error of 6 °C. This illustrates the high sensitivity of fiber optic temperature measurements concerning corrupting mechanical impacts. As described, strain measurements are significantly less affected by temperature and well suited for application in practice.

To comprehensively extend the model, additional experiments are required to examine different geometries, concrete compositions and strengths as well as reinforcement amounts and layouts. It can be postulated that all these factors have influence, since they do bear an impact on moment-curvature relationships.
In its current form, the model can evaluate 90 % of the load-bearing capacity (except the yielding of the reinforcement) of RC structures subjected to bending loads. Further research must verify the validity beyond this.

The model is proven for sensor distances of 30 cm. Its validity up to 120 cm is experimentally demonstrated. These findings give evidence for the monitoring of entire structures with only a *few sensors* (i.e., distance in meter range). Nevertheless, said distance has to be discussed with respect to practical feasibility and application as well as a monetary point of view. Larger distance means fewer sensors. Concurrently, larger sensor distances imply the scanning of larger volumes and thus coarser resolution.

To apply the model to real structures, the influence of temperature and humidity has to be considered due to changing environmental conditions (day ⇔ night, summer ⇔ winter). First, the coda wave's sensitivity to these two factors should be scrutinized. If they are significant, the model needs to be updated. This work already proves a firm basis for updating regarding temperature through the thermo-mechanical experiment. In general, temperature-related humidity changes can hardly be ruled out in experiments on large structures. Small-scale investigations in climate chambers are deemed more suitable. In long-term investigations, temperature can be varied when humidity is kept constant. A correlation between the temperature change and the relative velocity change can be established through temperature and US measurements. This correlation can be considered employing the model presented in this thesis. It follows that the load-bearing capacity is assessable even under changing temperature conditions. From a metrological point of view, in practical application on real structures, this implies that temperature has to be measured with additional sensors.
The procedure described for temperature changes can be transferred analogously to humidity change contexts.

To a large extent, concrete bridges are built using prestress. In theory, prestressed concrete bridges are completely in compression. According to plan, no tensile stress occurs. Nevertheless, bending still arises as a result of dead-load or traffic on the structure. For this reason, it is conceivable to apply the presented model for prestressed concrete bridges. However, the model's compatibility with prestressed concrete structures should be carefully investigated beforehand.

Appendix A

Work Share in Publications

CLAUß, F.; AHRENS, M. A. and MARK, P. *A Comparative Evaluation of Strain Measurement Techniques in Reinforced Concrete Structures—A Discussion of Assembly, Application, and Accuracy*. Structural Concrete, 2021. 22(5): pp. 2992–3007. doi: 10.1002/suco.202000706.

- Conceptualization: Clauß
- Visualization: Clauß
- Experiments: Clauß
- Investigations: Clauß
- Writing—original draft preparation: Clauß
- Writing—review and editing: Clauß, Ahrens
- Supervision: Ahrens, Mark

CLAUß, F.; LÖSCHMANN, J.; AHRENS, M. A. and MARK, P. *Temperaturinduktion in Betontragwerke – Experimentelle Untersuchungen zur Methode*. Beton- und Stahlbetonbau, 2021. 116(7): pp. 539–550. doi: 10.1002/best.202100010.

- Conceptualization: Clauß
- Visualization: Clauß
- Experiments: Clauß, Löschmann
- Investigations: Clauß, Löschmann
- Writing—original draft preparation: Clauß, Löschmann
- Writing—review and editing: Clauß, Löschmann
- Supervision: Ahrens, Mark

CLAUß, F.; AHRENS, M. A. and MARK, P. *Thermo-Mechanical Experiments on Reinforced Concrete Beams—Assessing Thermal, Mechanical and Mixed Impacts on Fiber Optic Measurements*. Submitted to Structural Concrete in December, 2021.

- Conceptualization: Clauß
- Visualization: Clauß
- Experiments: Clauß

- Investigations: Clauß
- Writing—original draft preparation: Clauß
- Writing—review and editing: Clauß, Ahrens
- Supervision: Ahrens, Mark

CLAUß, F.; EPPLE, N.; AHRENS, M. A.; NIEDERLEITHINGER, E. and MARK, P. *Comparison of Experimentally Determined Two-Dimensional Strain Fields and Mapped Ultrasonic Data Processed by Coda Wave Interferometry*. Sensors, 2020. 20(14): 4023. doi: 10.3390/s20144023.

- Conceptualization: Clauß
- Visualization: Clauß
- Experiments: Clauß
- Investigations: Clauß
- Writing—original draft preparation: Clauß, Epple
- Writing—review and editing: Clauß, Epple, Ahrens
- Supervision: Ahrens, Niederleithinger, Mark

CLAUß, F.; EPPLE, N.; AHRENS, M. A.; NIEDERLEITHINGER, E. and MARK, P. *Correlation of Load-Bearing Behavior of Reinforced Concrete Members and Velocity Change of Coda Waves*. Materials, 2022. 15(3): 738. doi: 10.3390/ma15030738.

- Conceptualization: Clauß
- Visualization: Clauß
- Experiments: Clauß
- Investigations: Clauß
- Writing—original draft preparation: Clauß, Epple
- Writing—review and editing: Clauß, Epple, Ahrens
- Supervision: Ahrens, Niederleithinger, Mark

KONERTZ, D.; LÖSCHMANN, J.; CLAUß, F. and MARK, P. *Faseroptische Messung von Dehnungs- und Temperaturfeldern*. Bauingenieur, 2019. 94(7/8): pp. 292–300. doi: 10.37544/0005-6650-2019-07-08-70.

- Conceptualization: Konertz, Löschmann
- Visualization: Konertz, Löschmann, Clauß
- Experiments: Konertz, Löschmann, Clauß
- Investigations: Konertz, Löschmann
- Writing—original draft preparation: Konertz, Löschmann
- Writing—review and editing: Konertz, Löschmann, Clauß
- Supervision: Mark

LÖSCHMANN, J.; CLAUß, F. and MARK, P. *Verstärken von Stahlbetontragwerken mit Temperaturinduktion*. Beton- und Stahlbetonbau, 2020. 115(10): pp. 746–757. doi: 10.1002/best.202000038.

- Conceptualization: Löschmann
- Visualization: Löschmann
- Experiments: Löschmann, Clauß

- Investigations: Löschmann
- Writing—original draft preparation: Löschmann
- Writing—review and editing: Löschmann, Clauß
- Supervision: Mark

GRABKE, S.; CLAUß, F.; BLETZINGER, K.-U.; AHRENS, M. A.; MARK, P. and WÜCHNER, R. *Damage Detection at a Reinforced Concrete Specimen with Coda Wave Interferometry*. Materials, 2021. 14(17): 5013. doi: 10.3390/ma14175013.

- Conceptualization: Grabke
- Visualization: Grabke, Clauß
- Experiments: Clauß
- Investigations: Grabke, Clauß
- Writing—original draft preparation: Grabke, Clauß
- Writing—review and editing: Grabke, Clauß
- Supervision: Bletzinger, Ahrens, Mark, Wüchner

Appendix B

Complementary Test Data

B.1 Initial Remarks

As part of the research for this thesis, three series of experiments were conducted, each with different objectives. These experiments have been significantly incorporated into the chapters (or publications). The type of investigation as well as the chapters related to the specimen are listed in Table B.1.

Table B.1: Assignment of specimens to type of investigation and related chapters

Specimen	Type of investigation	Related chapter
1	Mechanical	2, 5
2	Mechanical & thermal	6, 9
3 & 4	Mechanical & thermal & thermo-mechanical	4

B.2 Specimen 1

Table B.2: Dimensions

w [mm]	d [mm]	L [mm]	L_{eff} [mm]	d_1 [mm]	d_2 [mm]	c_{v} [mm]
150	400	2400	2000	38	34	22

Table B.3: Reinforcement amounts

A_{s1}	A_{s2}	a_{sw}
2 Ø 16 mm	2 Ø 8 mm	Ø 10 mm / 20 cm / 2

Table B.4: Material parameters of the concrete

$f_{cm,cube}$ $[N/mm^2]$	f_{ctm} $[N/mm^2]$	E_{cm} $[N/mm^2]$
35.0	2.5	28,618

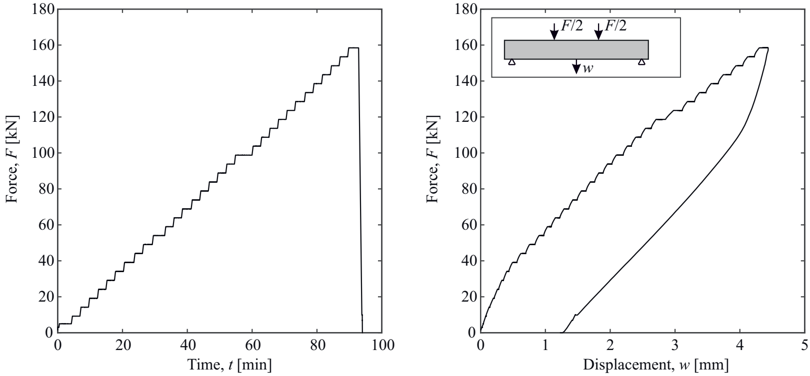

Figure B.1: a) Force-time and b) force-displacement curves

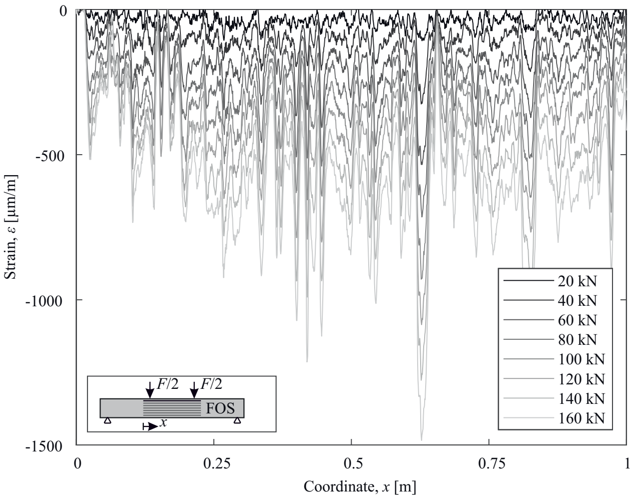

Figure B.2: Strain results of FOS 1 (concrete)

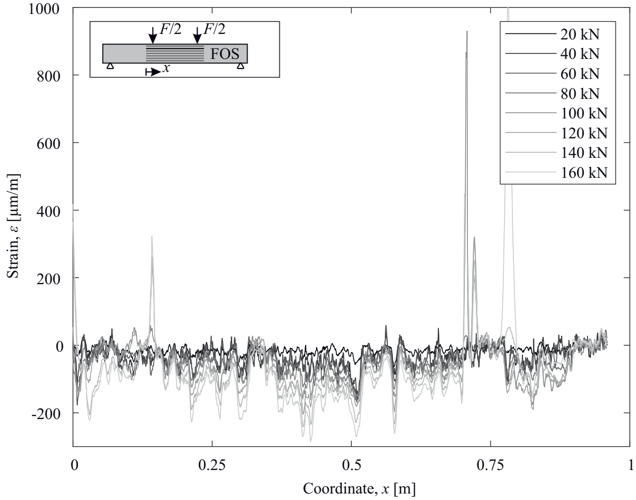

Figure B.3: Strain results of FOS 2 (concrete)

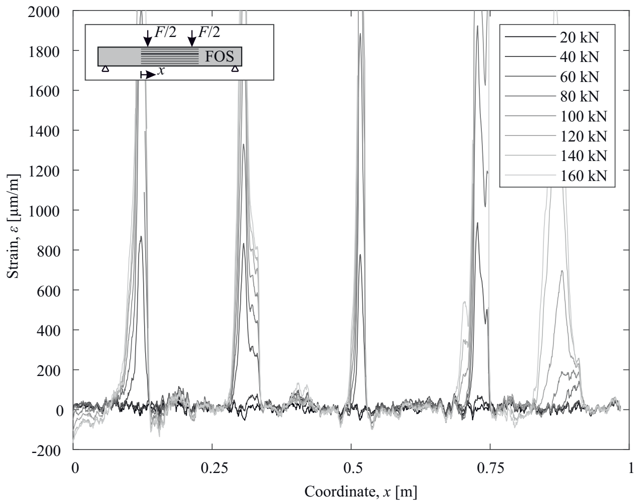

Figure B.4: Strain results of FOS 3 (concrete)

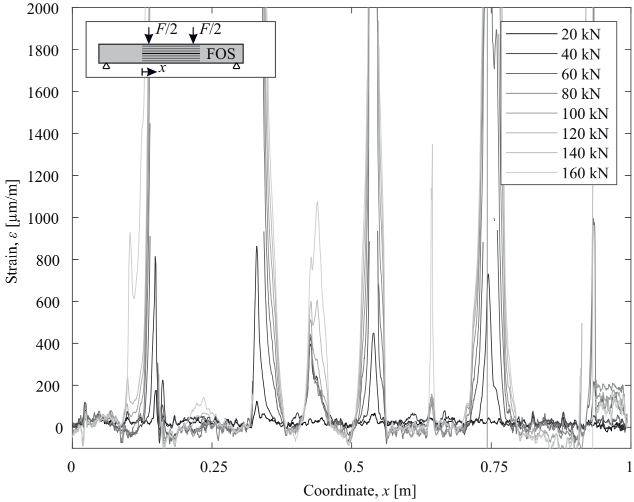

Figure B.5: Strain results of FOS 4 (concrete)

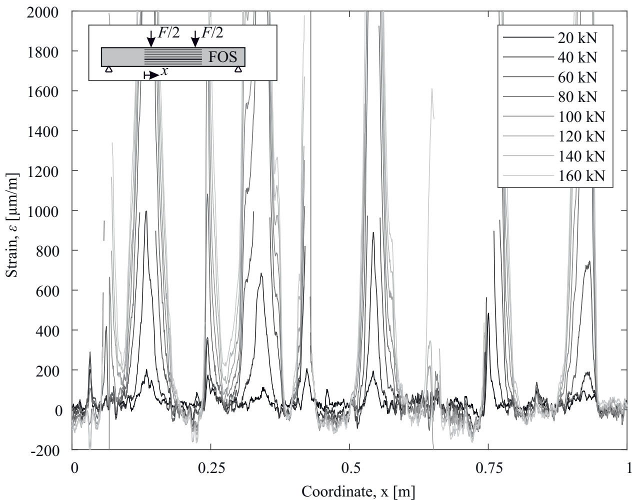

Figure B.6: Strain results of FOS 5 (concrete)

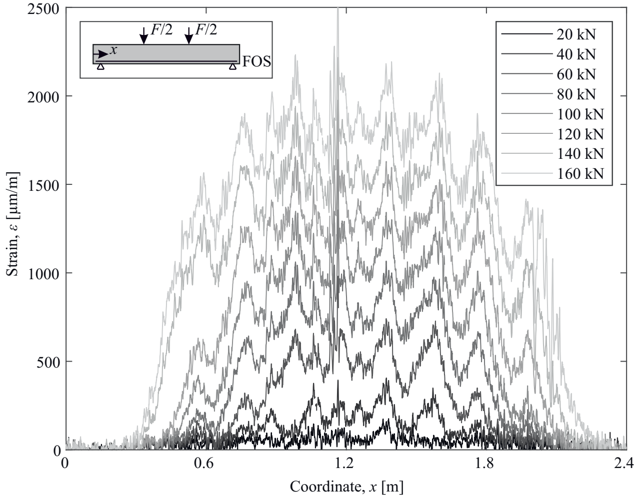

Figure B.7: Strain results of FOS 6 (reinforcement)

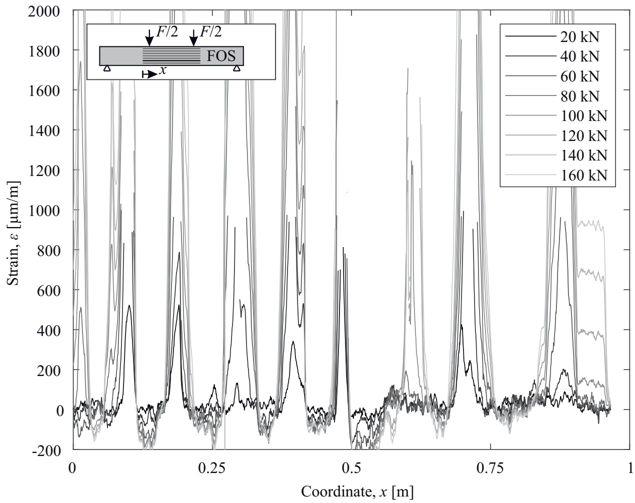

Figure B.8: Strain results of FOS 7 (concrete)

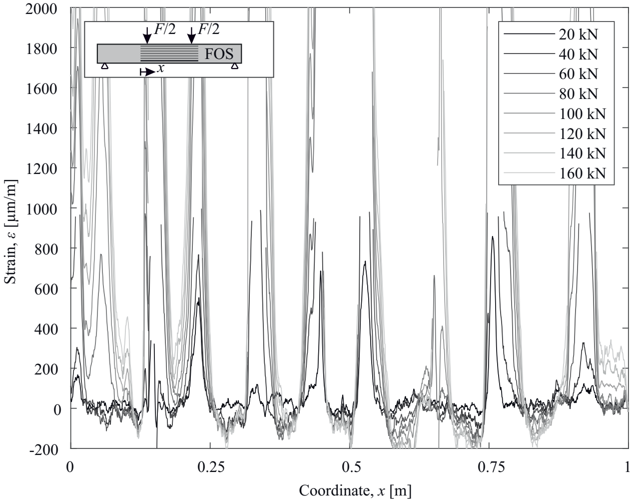

Figure B.9: Strain results of FOS 8 (concrete)

B.3 Specimen 2

Table B.5: Dimensions

w [mm]	d [mm]	L [mm]	L_{eff} [mm]	d_1 [mm]	d_2 [mm]	c_v [mm]
250	500	3900	3500	44	38	22

Table B.6: Reinforcement amounts

A_{s1}	A_{s2}	a_{sw}
3 Ø 20 mm	2 Ø 8 mm	Ø 12 mm / 30 cm / 2

Table B.7: Material parameters of the concrete

$f_{cm,cube}$ [N/mm^2]	f_{ctm} [N/mm^2]	E_{cm} [N/mm^2]
38.2	2.8	28,800

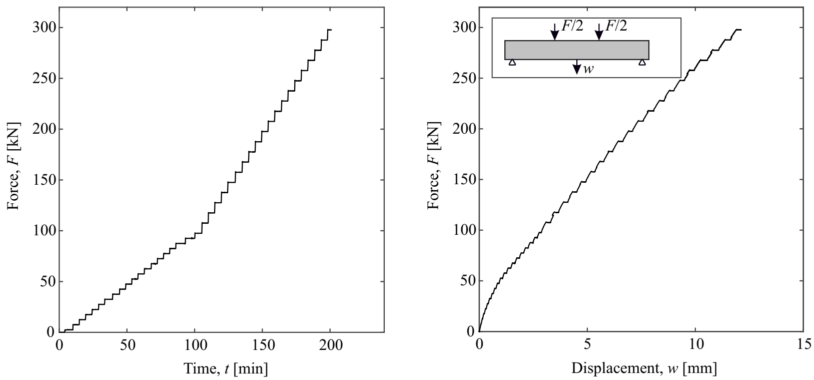

Figure B.10: a) Force-time and b) force-displacement curves

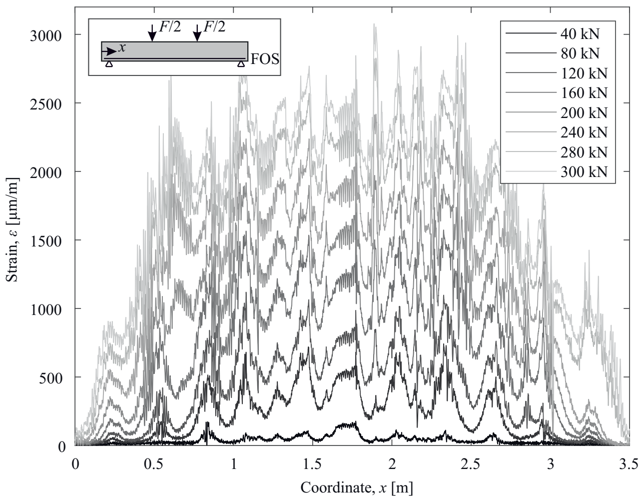

Figure B.11: Strain results of FOS 3 (reinforcement)

B.4 Specimens 3 & 4

Table B.8: Dimensions

w [mm]	d [mm]	L [mm]	L_{eff} [mm]	d_1 [mm]	d_2 [mm]	c_v [mm]
250	500	3900	3500	44	38	22

Table B.9: Reinforcement amounts

A_{s1}	A_{s2}	a_{sw}
3 Ø 20 mm	2 Ø 8 mm	Ø 12 mm / 30 cm / 2

Table B.10: Material parameters of the concrete

$f_{cm,cube}$ [N/mm²]	f_{ctm} [N/mm²]	E_{cm} [N/mm²]
23.3	2.2	22,570

B.4.1 Mechanical Test

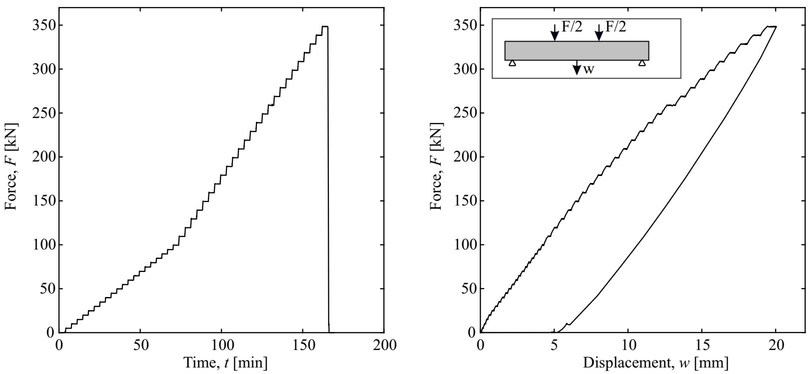

Figure B.12: a) Force-time and b) force-displacement curves

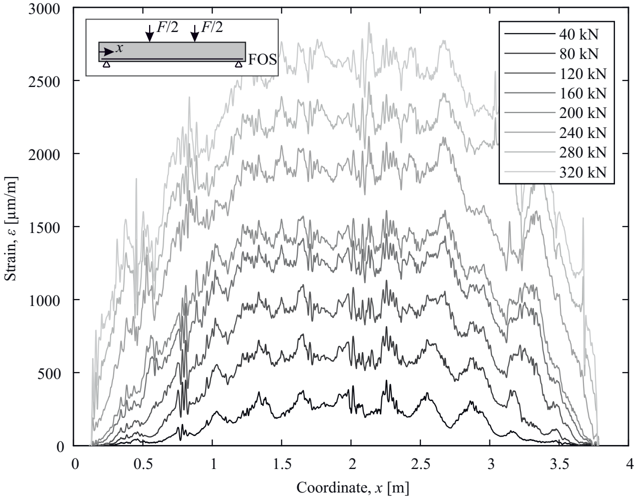

Figure B.13: Strain results of FOS 3 (reinforcement)

B.4.2 Thermal Test

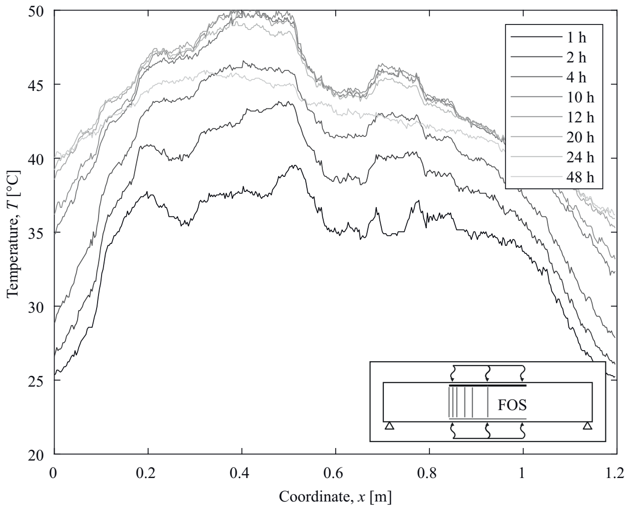

Figure B.14: Temperature results of FOS 7

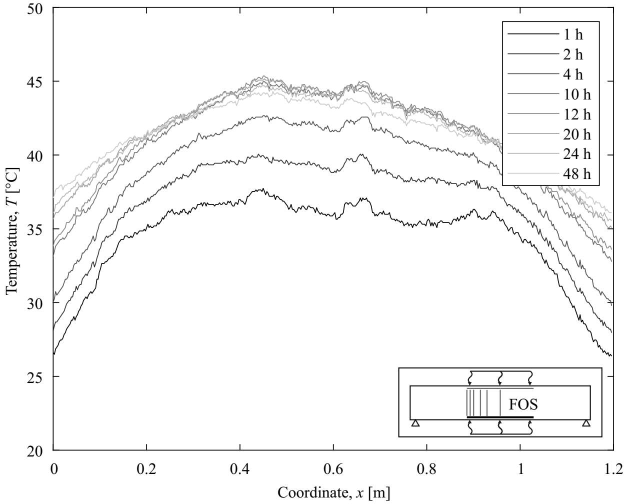

Figure B.15: Temperature results of FOS 8

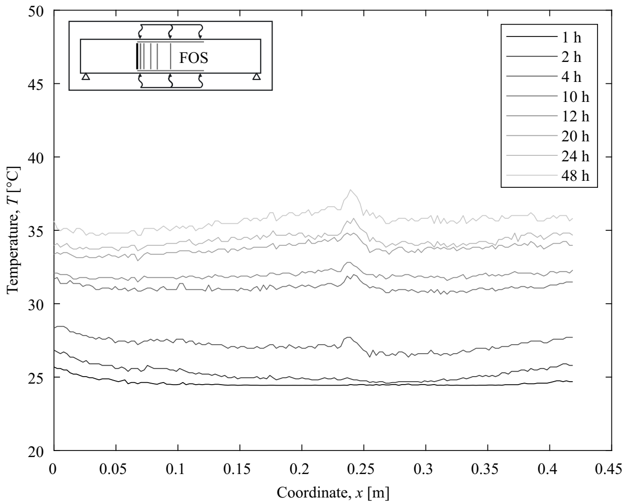

Figure B.16: Temperature results of FOS 9

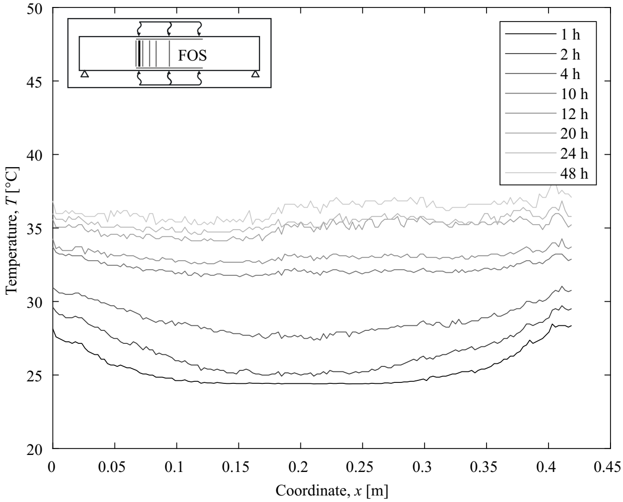

Figure B.17: Temperature results of FOS 10

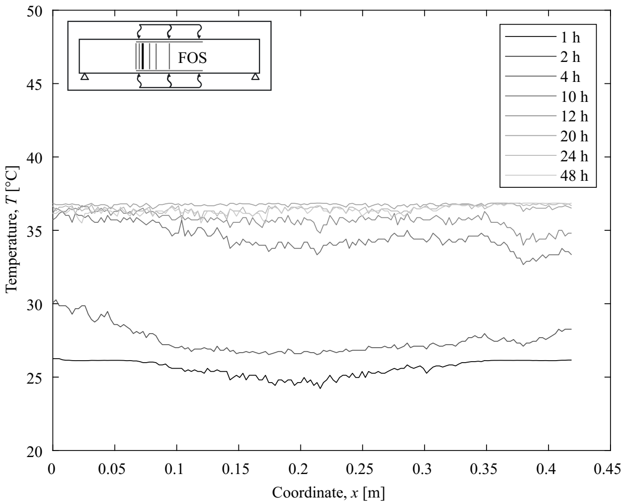

Figure B.18: Temperature results of FOS 11

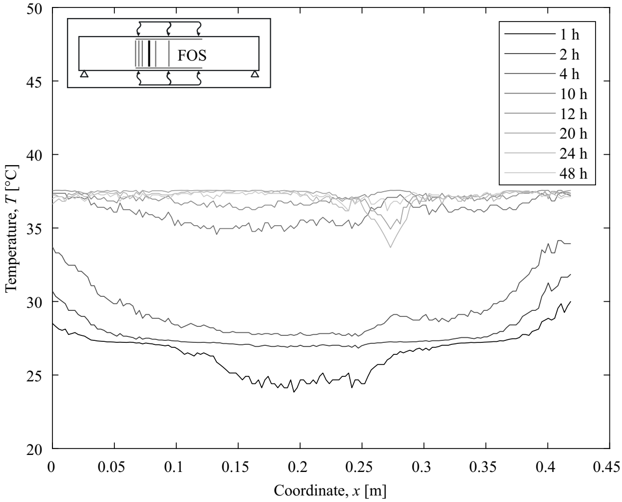

Figure B.19: Temperature results of FOS 12

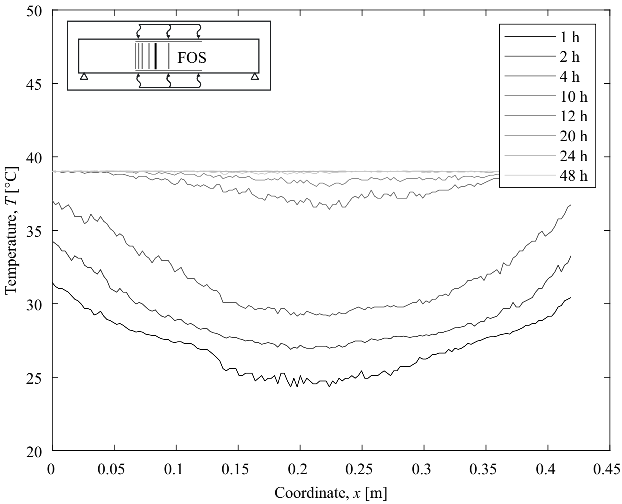

Figure B.20: Temperature results of FOS 13

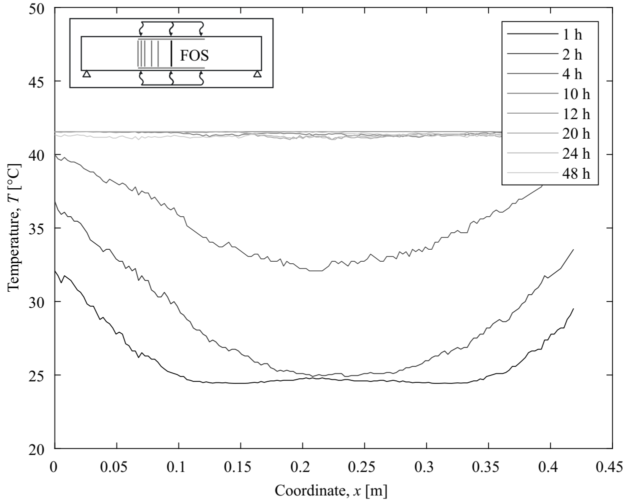

Figure B.21: Temperature results of FOS 14

B.4.3 Thermo-Mechanical Test

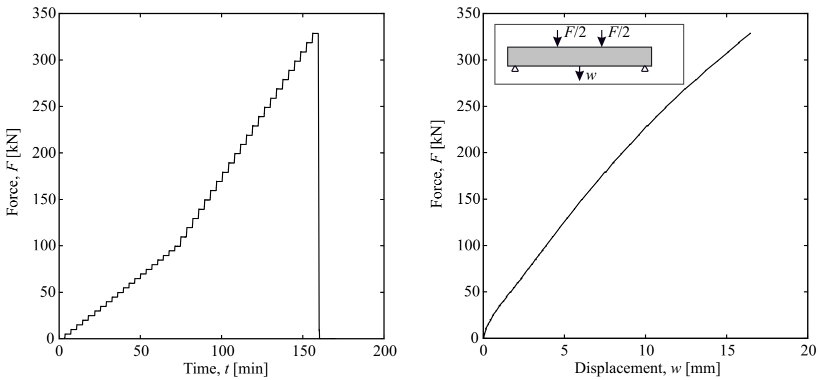

Figure B.22: a) Force-time and b) force-displacement curves

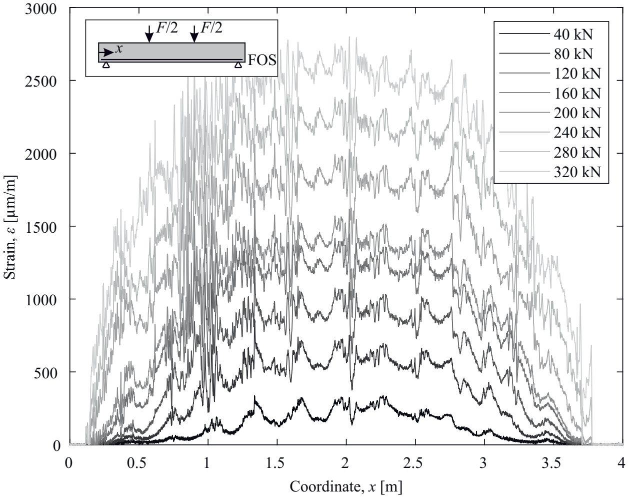

Figure B.23: Strain results of FOS 3 (reinforcement)

Bibliography

[1] AHRENS, M. A. and MARK, P. *Lebensdauersimulation von Betontragwerken*. Beton- und Stahlbetonbau, 2011. 106(4): pp. 220–230. doi:10.1002/best.201000092.

[2] AKI, K. *Correlogram Analyses of Seismograms by Means of a Simple Automatic Computer*. Journal of Physics of the Earth, 1956. 4(2): pp. 71–79. doi:10.4294/jpe1952.4.71.

[3] AMERICAN CONCRETE INSTITUTE. *Report on Nondestructive Test Methods for Evaluation of Concrete in Structures*, 2013.

[4] ANSARI, F. *Practical Implementation of Optical Fiber Sensors in Civil Structural Health Monitoring*. Journal of Intelligent Material Systems and Structures, 2007. 18(8): pp. 879–889. doi:10.1177/1045389X06075760.

[5] BADO, M. F. and CASAS, J. R. *A Review of Recent Distributed Optical Fiber Sensors Applications for Civil Engineering Structural Health Monitoring*. Sensors, 2021. 21(5): pp. 1–83. doi:10.3390/s21051818.

[6] BARRIAS, A.; RODRIGUEZ, G.; CASAS, J. R. and VILLALBA, S. *Application of distributed optical fiber sensors for the health monitoring of two real structures in Barcelona*. Structure and Infrastructure Engineering, 2018. 14(7): pp. 967–985. doi:10.1080/15732479.2018.1438479.

[7] BASSIL, A. *Distributed Fiber Optics Sensing for Crack Monitoring of Concrete Structures*. Ph.D. Thesis, University of Nantes, Nantes, France, 2019.

[8] BATHE, K.-J. *Finite Element Procedures*. Prentice Hall, New Jersey, USA, 1996.

[9] BAYOUMI, A.; MINTEN, T. and MUELLER, I. *Determination of Detection Probability and Localization Accuracy for a Guided Wave-Based Structural Health Monitoring System on a Composite Structure*. Applied Mechanics, 2021. 2(4): pp. 996–1008. doi:10.3390/applmech2040058.

[10] BERGER, J. and FEIX, J. *Constraint forces from imposed deformations*. Structural Concrete, 2019. 20(2): pp. 650–659. doi:10.1002/suco.201800123.

[11] BERGMEISTER, K. *Ertüchtigung im Bestand - Verstärkungen mit Kohlenstofffasern*. In: BERGMEISTER, K.; FINGERLOOS, F. and WÖRNER, J.-D. (eds.), *Beton-Kalender 2009*, pp. 185–230. Wiley-VCH Verlag GmbH & Co. KGaA, Weinheim, Germany, 2008. doi: 10.1002/9783433600344.ch9.

[12] BERGMEISTER, K. *Verstärkung mit Kohlenstofffasern*. Beton- und Stahlbetonbau, 2008. 103(S2): pp. 26–32. doi:10.1002/best.200810205.

[13] BILLON, A.; HENAULT, J.-M.; QUIERTANT, M.; TAILLADE, F.; KHADOUR, A.; MARTIN, R.-P. and BENZARTI, K. *Qualification of a distributed optical fiber sensor bonded to the surface of a concrete structure: a methodology to obtain quantitative strain measurements*. Smart Materials and Structures, 2015. 24(11): pp. 1–13. doi:10.1088/0964-1726/24/11/115001.

[14] BOCKLENBERG, L.; WINKLER, K.; MARK, P. and RYBARZ, S. *Low Friction Sliding Planes of Greased PTFE for High Contact Pressures*. Open Journal of Civil Engineering, 2016. 06(02): pp. 105–116. doi:10.4236/ojce.2016.62010.

[15] BRANCH, M. A.; COLEMAN, T. F. and LI, Y. *A Subspace, Interior, and Conjugate Gradient Method for Large-Scale Bound-Constrained Minimization Problems*. SIAM Journal on Scientific Computing, 1999. 21(1): pp. 1–23. doi:10.1137/S1064827595289108.

[16] BRANCO, F. A. and MENDES, P. A. *Thermal Actions for Concrete Bridge Design*. Journal of Structural Engineering, 1993. 119(8): pp. 2313–2331. doi:10.1061/(ASCE)0733-9445(1993)119:8(2313).

[17] BRAULT, A. and HOULT, N. *Monitoring Reinforced Concrete Serviceability Performance Using Fiber Optic Sensors*. ACI Structural Journal, 2019. 116(1): pp. 57–70. doi:10.14359/51710870.

[18] BRUCK, H. A.; MCNEILL, S. R.; SUTTON, M. A. and PETERS, W. H. *Digital image correlation using Newton-Raphson method of partial differential correction*. Experimental Mechanics, 1989. 29(3): pp. 261–267. doi:10.1007/BF02321405.

[19] BRÜCKNER, A.; ORTLEPP, R. and CURBACH, M. *Textile reinforced concrete for strengthening in bending and shear*. Materials and Structures, 2006. 39(8): pp. 741–748. doi: 10.1617/s11527-005-9027-2.

[20] BUNDESMINISTERIUM FÜR VERKEHR. *Zusätzliche Bestimmungen zu DIN 4227 für Brücken aus Spannbeton*, 1966.

[21] BUNDESMINISTERIUM FÜR VERKEHR UND DIGITALE INFRASTRUKTUR. *Bericht „Stand der Modernisierung von Brücken der Bundesfernstraßen“: Bericht an den Ausschuss für Verkehr und digitale Infrastruktur des Deutschen Bundestages*, 2020.

[22] CARINO, N. J. *The Impact-Echo Method: An Overview*. In: CHANG, P. C. (ed.), *Structures 2001*. American Society of Civil Engineers, Reston, VA, USA, 2001 pp. 1–18. doi:10.1061/40558(2001)15.

[23] CHEN, J.; YU, Q.; CUI, X.; DONG, M.; ZHANG, J.; WANG, C.; FAN, J.; ZHU, Y. and GUO, Z. *An overview of stretchable strain sensors from conductive polymer nanocomposites*. Journal of Materials Chemistry C, 2019. 7(38): pp. 11710–11730. doi:10.1039/C9TC03655E.

[24] CHU, T. C.; RANSON, W. F. and SUTTON, M. A. *Applications of digital-image-correlation techniques to experimental mechanics*. Experimental Mechanics, 1985. 25(3): pp. 232–244. doi:10.1007/BF02325092.

[25] CLAUSS, F.; AHRENS, M. A. and MARK, P. *A Comparative Evaluation of Strain Measurement Techniques in Reinforced Concrete Structures – A Discussion of Assembly, Application, and Accuracy*. Structural Concrete, 2021. 22(5): pp. 2992–3007. doi:10.1002/suco.202000706.

[26] CLAUSS, F.; EPPLE, N.; AHRENS, M. A.; NIEDERLEITHINGER, E. and MARK, P. *Comparison of Experimentally Determined Two-Dimensional Strain Fields and Mapped Ultrasonic Data Processed by Coda Wave Interferometry*. Sensors, 2020. 20(14): pp. 1–16. doi:10.3390/s20144023.

[27] CLAUSS, F.; LÖSCHMANN, J.; AHRENS, M. A. and MARK, P. *Temperaturinduktion in Betontragwerke: Experimentelle Untersuchungen zur Methode*. Beton- und Stahlbetonbau, 2021. 116(7): pp. 539–550. doi:10.1002/best.202100010.

[28] D'ALESSANDRO, A.; MEONI, A.; UBERTINI, F. and LUIGI MATERAZZI, A. *Strain Measurement in a Reinforced Concrete Beam Using Embedded Smart Concrete Sensors*. In: DI PRISCO, M. and MENEGOTTO, M. (eds.), *Proceedings of Italian Concrete Days 2018*, vol. 42, pp. 289–300. Springer-Verlag, Cham, Switzerland, 2020. doi:10.1007/978-3-030-23748-6.

[29] DEUTSCHER AUSSCHUSS FÜR STAHLBETON. *DAfStb-Heft 466: Grundlagen und Bemessungshilfen für die Rißbreitenbeschränkung im Stahlbeton und Spannbeton sowie Kommentare, Hintergrundinformationen und Anwendungsbeispiele zu den Regelungen nach DIN 1045, EC2 und Model Code 90*. Beuth Verlag, Berlin, Germany, 1996. doi:10.2366/3721089.

[30] DEUTSCHER AUSSCHUSS FÜR STAHLBETON. *DAfStb-Heft 467: Verstärken von Betonbauteilen - Sachstandsbericht*. Beuth Verlag, Berlin, Germany, 1996. doi:10.2366/3721164.

[31] DEUTSCHER AUSSCHUSS FÜR STAHLBETON. *DAfStb-Heft 630: Bemessung nach DIN EN 1992 in den Grenzzuständen der Tragfähigkeit und der Gebrauchstauglichkeit*. Beuth Verlag, Berlin, Germany, 2018.

[32] DEUTSCHES INSTITUT FÜR BAUTECHNIK. *Mitteilungen des Deutschen Instituts für Bautechnik: Geänderte Fassung der Zulassungsbescheide vom 8.2.1977 für Spannverfahren (Soforterlass)*, 1977.

[33] DIN Deutsches Institut für Normung e.V. *DIN 1072:1952-06: Straßen- und Wegbrücken - Lastenanahmen*, 1952.

[34] DIN Deutsches Institut für Normung e.V. *DIN 4227-1:1979-12: Spannbeton; Bauteile aus Normalbeton, mit beschränkter oder voller Vorspannung*, 1979.

[35] DIN Deutsches Institut für Normung e.V. *DIN 5030-2: Spektrale Strahlungsmessung – Strahler für spektrale Strahlungsmessungen*, 1982.

[36] DIN Deutsches Institut für Normung e.V. *DIN 1072:1985-12: Straßen- und Wegbrücken; Lastannahmen*, 1985.

[37] DIN Deutsches Institut für Normung e.V. *DIN 4227-1/A1:1995-12: Spannbeton - Teil 1: Bauteile aus Normalbeton mit beschränkter oder voller Vorspannung; Änderung A1*, 1995.

[38] DIN Deutsches Institut für Normung e.V. *DIN 1076:1999-11: Ingenieurbauwerke im Zuge von Straßen und Wegen - Überwachung und Prüfung*, 1999. doi:10.31030/8499929.

[39] DIN Deutsches Institut für Normung e.V. *DIN 1076:1999-11: Ingenieurbauwerke im Zuge von Straßen und Wegen - Überwachung und Prüfung*, 1999.

[40] DIN Deutsches Institut für Normung e.V. *DIN-Fachbericht 101:2003: Einwirkungen auf Brücken*, 2003.

[41] DIN Deutsches Institut für Normung e.V. *DIN EN 1992-1-1:2011-01: Eurocode 2: Bemessung und Konstruktion von Stahlbeton- und Spannbetontragwerken - Teil 1-1: Allgemeine Bemessungsregeln und Regeln für den Hochbau; Deutsche Fassung EN 1992-1-1:2004 + AC:2010*, 2011.

[42] DIN Deutsches Institut für Normung e.V. *DIN EN 1991-2/NA:2012-08: Nationaler Anhang - National festgelegte Parameter - Eurocode 1: Einwirkungen auf Tragwerke - Teil 2: Verkehrslasten auf Brücken*, 2012.

[43] Docevska, M.; Markovski, G. and Mark, P. *Experimental investigation on the reversibility of concrete creep under repeating loads*. Materials and Structures, 2019. 52(4): pp. 1–16. doi:10.1617/s11527-019-1384-3.

[44] Dridiger, A.; Albert, A. and Schnell, J. *Zur Ermittlung von Zwangschnittgrößen in einachsig gespannten Hochbaudecken*. Beton- und Stahlbetonbau, 2019. 114(9): pp. 610–619. doi:10.1002/best.201900029.

[45] Eilers, M.; Friedrich, H.; Quaas, B. and Rogalski, E. (eds.). *Kanalbrücke Berkenthin mit temperierter Fahrbahn: Pilotprojekt*. Fachverlag NW in Carl Ed. Schünemann KG, Bremen, 2020.

[46] ELBADRY, M. M. and GHALI, A. *Temperature Variations in Concrete Bridges*. Journal of Structural Engineering, 1983. 109(10): pp. 2355–2374. doi:10.1061/(ASCE)0733-9445(1983)109:10(2355).

[47] ENGELBRECHT, R. *Nichtlineare Faseroptik: Grundlagen und Anwendungsbeispiele*. Springer-Verlag, Berlin, Germany, 2014.

[48] ENGELBRECHT, R. *B6.1 - Fiber Optic Strain and Temperature Sensing: Overview of Principles*. In: *Proceedings Sensor 2017*. AMA Service GmbH, Wunstorf, Germany, 2017 pp. 255–260. doi:10.5162/sensor2017/B6.1.

[49] EPPLE, N.; BARROSO, D. F. and NIEDERLEITHINGER, E. *Towards Monitoring of Concrete Structures with Embedded Ultrasound Sensors and Coda Waves – First Results of DFG for CoDA*. In: *Rizzo P., Milazzo A. (eds) European Workshop on Structural Health Monitoring, EWSHM 2020*, vol. 127, pp. 266–275. Springer-Verlag, 2021.

[50] ERHARD, E.; WEILAND, S.; LORENZ, E.; SCHLADITZ, F.; BECKMANN, B. and CURBACH, M. *Anwendungsbeispiele für Textilbetonverstärkung*. Beton- und Stahlbetonbau, 2015. 110(S1): pp. 74–82. doi:10.1002/best.201400124.

[51] FARRAR, C. R. and WORDEN, K. *An introduction to structural health monitoring*. Philosophical Transactions of the Royal Society A: Mathematical, Physical and Engineering Sciences, 2007. 365(1851): pp. 303–315. doi:10.1098/rsta.2006.1928.

[52] FEIX, J.; LECHNER, J.; SPIEGL, M. and WALKNER, R. *Nachhaltige Bauwerksverstärkung mit Betonschrauben*. In: *Beton Kalender 2021*, pp. 953–1005. Wiley, 2021. doi:10.1002/9783433610206.ch11.

[53] FINGERLOOS, F. *Normen und Regelwerke*. In: BERGMEISTER, K.; FINGERLOOS, F. and WÖRNER, J.-D. (eds.), *Beton-Kalender 2010*, pp. 193–668. Wiley-VCH Verlag GmbH & Co. KGaA, Weinheim, Germany, 2009. doi:10.1002/9783433600443.ch11.

[54] FISCHER, O.; LECHNER, T.; WILD, M.; MÜLLER, A. and KESSNER, K. (eds.). *Nachrechnung von Betonbrücken - systematische Datenauswertung nachgerechneter Bauwerke*. Fachverlag NW in Carl Ed. Schünemann KG, Bremen, Germany, 2016.

[55] FISCHER, O.; MÜLLER, A.; LECHNER, T.; WILD, M. and KESSNER, K. *Ergebnisse und Erkenntnisse zu durchgeführten Nachrechnungen von Betonbrücken in Deutschland*. Beton- und Stahlbetonbau, 2014. 109(2): pp. 107–127. doi:10.1002/best.201300084.

[56] FISCHER, O.; THOMA, S. and CREPAZ, S. *Distributed fiber optic sensing for crack detection in concrete structures*. Civil Engineering Design, 2019. 1(3-4): pp. 97–105. doi:10.1002/cend.201900008.

[57] FISCHER, O.; THOMA, S. and CREPAZ, S. *Quasikontinuierliche faseroptische Dehnungsmessung zur Rissdetektion in Betonkonstruktionen*. Beton- und Stahlbetonbau, 2019. 114(3): pp. 150–159. doi:10.1002/best.201800089.

[58] FROGGATT, M. and MOORE, J. *High-spatial-resolution distributed strain measurement in optical fiber with rayleigh scatter*. Applied Optics, 1998. 37(10): pp. 1735–1740. doi:10.1364/AO.37.001735.

[59] FROGGATT, M. E.; GIFFORD, D. K.; KREGER, S. T.; WOLFE, M. S. and SOLLER, B. J. *Distributed Strain and Temperature Discrimination in Unaltered Polarization Maintaining Fiber*. In: *Optical Fiber Sensors*. OSA, Washington, D.C., USA, 2006 doi:10.1364/OFS.2006.ThC5.

[60] FRÖJD, P. and ULRIKSEN, P. *Continuous wave measurements in a network of transducers for structural health monitoring of a large concrete floor slab*. Structural Health Monitoring, 2016. 15(4): pp. 403–412. doi:10.1177/1475921716642139.

[61] FRÖJD, P. and ULRIKSEN, P. *Detecting damage events in concrete using diffuse ultrasound structural health monitoring during strong environmental variations*. Structural Health Monitoring, 2017. 17(2): pp. 410–419. doi:10.1177/1475921717699878.

[62] FRÖJD, P. and ULRIKSEN, P. *Frequency selection for coda wave interferometry in concrete structures*. Ultrasonics, 2017. 80: pp. 1–8. doi:10.1016/j.ultras.2017.04.012.

[63] GE, Y.; ELSHAFIE, M. Z.; DIRAR, S. and MIDDLETON, C. R. *The response of embedded strain sensors in concrete beams subjected to thermal loading*. Construction and Building Materials, 2014. 70(4): pp. 279–290. doi:10.1016/j.conbuildmat.2014.07.102.

[64] GIFFORD, D. K.; SOLLER, B. J.; WOLFE, M. S. and FROGGATT, M. E. *Distributed fiber-optic temperature sensing using Rayleigh backscatter*. In: *31st European Conference on Optical Communications (ECOC 2005)*. IET, 2005 doi:10.1049/cp:20050584.

[65] GOM GMBH. *GOM Testing Technische Dokumentation ab V8 SR1: Grundlagen der digitalen Bildkorrelation und Dehnungsberechnung*, 2016.

[66] GRABKE, S.; CLAUSS, F.; BLETZINGER, K.-U.; AHRENS, M. A.; MARK, P. and WÜCHNER, R. *Damage Detection at a Reinforced Concrete Specimen with Coda Wave Interferometry*. Materials (Basel, Switzerland), 2021. 14(17). doi:10.3390/ma14175013.

[67] GRÊT, A.; SNIEDER, R. and SCALES, J. *Time–lapse monitoring of rock properties with coda wave interferometry*. Journal of Geophysical Research, 2006. 111: pp. 1–11. doi:10.1029/2004JB003354.

[68] GRIESINGER, A. *Wärmemanagement in der Elektronik – Theorie und Praxis*. Springer Vieweg, Berlin, Germany, 2019.

[69] GROSSE, C. U.; OHTSU, M.; AGGELIS, D. G. and SHIOTANI, T. *Acoustic Emission Testing*. Springer International Publishing, Berlin, Germany, 2022. doi:10.1007/978-3-030-67936-1.

[70] GWK GESELLSCHAFT WÄRME KÄLTETECHNIK MBH. *Gebrauchsanleitung, teko*.

[71] GWK GESELLSCHAFT WÄRME KÄLTETECHNIK MBH. *Gebrauchsanleitung, weko*.

[72] HAFIZ, A. and SCHUMACHER, T. *Monitoring of Stresses in Concrete Using Ultrasonic Coda Wave Comparison Technique*. Journal of Nondestructive Evaluation, 2018. 37(4): pp. 1–13. doi:10.1007/s10921-018-0527-8.

[73] HÄFLIGER, S.; MATA FALCON, J. and KAUFMANN, W. *Application of distributed optical measurements to structural concrete experiments*. In: *SMAR 2017 Proceedings*, pp. 159–167. ETH Zurich, Zürich, Switzerland, 2017. doi:10.3929/ETHZ-B-000186477.

[74] HAINES, R. W. and HITTLE, D. C. *Control Systems for Heating, Ventilating, and Air Conditioning*. Springer US, Boston, MA, USA, 1993. doi:10.1007/978-1-4615-3108-1.

[75] HANNOSCHÖCK, N. *Wärmeleitung und -transport: Grundlagen der Wärme- und Stoffübertragung*. Springer-Verlag, Berlin, Germany, 2018.

[76] HEEK, P. *Modellbildung und numerische Analysen zur Ermüdung von Stahlfaserbeton*. Ph.D. Thesis, Ruhr-Universität Bochum, Bochum, Germany, 2017.

[77] HEEK, P.; AHRENS, M. A. and MARK, P. *Incremental-iterative model for time-variant analysis of SFRC subjected to flexural fatigue*. Materials and Structures, 2017. 50(1): pp. 1–15. doi:10.1617/s11527-016-0928-z.

[78] HEEK, P.; TKOCZ, J. and MARK, P. *A thermo-mechanical model for SFRC beams or slabs at elevated temperatures*. Materials and Structures, 2018. 51(4): pp. 1–16. doi: 10.1617/s11527-018-1218-8.

[79] HENAULT, J.-M.; QUIERTANT, M.; DELEPINE-LESOILLE, S.; SALIN, J.; MOREAU, G.; TAILLADE, F. and BENZARTI, K. *Quantitative strain measurement and crack detection in RC structures using a truly distributed fiber optic sensing system*. Construction and Building Materials, 2012. 37: pp. 916–923. doi:10.1016/j.conbuildmat.2012.05.029.

[80] HENAULT, J. M.; SALIN, J.; MOREAU, G.; DELEPINE-LESOILLE, S.; BERTAND, J.; TAILLADE, F.; QUIERTANT, M. and BENZARTI, K. *Qualification of a truly distributed fiber optic technique for strain and temperature measurements in concrete structures*. EPJ Web of Conferences, 2011. 12: pp. 1–8. doi:10.1051/epjconf/20111203004.

[81] HENKE, V. and EMPELMANN, M. *Rissbreitenberechnung bei "Kombibewehrung"*. Beton- und Stahlbetonbau, 2007. 102(2): pp. 66–79. doi:10.1002/best.200600532.

[82] HERBRAND, M.; ADAM, V.; CLASSEN, M.; KUERES, D. and HEGGER, J. *Strengthening of Existing Bridge Structures for Shear and Bending with Carbon Textile-Reinforced Mortar*. Materials (Basel, Switzerland), 2017. 10(9): pp. 1–15. doi:10.3390/ma10091099.

[83] HERING, E.; MARTIN, R. and STOHRER, M. *Physik für Ingenieure*. Springer-Verlag, Berlin, Germany, 2016. doi:10.1007/978-3-662-49355-7.

[84] HILL, K. O. and MELTZ, G. *Fiber Bragg grating technology fundamentals and overview*. Journal of Lightwave Technology, 1997. 15(8): pp. 1263–1276. doi:10.1109/50.618320.

[85] HOFFMANN, K. *An introduction to stress analysis using strain gauges: The definitive work on strain gauge measurement*. HBM, 2012.

[86] HUGENSCHMIDT, M. *Lasermesstechnik: Diagnostik der Kurzzeitphysik*. Springer-Verlag, Berlin, Germany, 2007. doi:10.1007/978-3-540-29921-9.

[87] IBT.INFRABIOTECH GMBH. *Einbauerklärung SIR-Strahler DRS 1000x80/4.0, Version 1.0*.

[88] INTERNATIONAL ATOMIC ENERGY AGENCY. *Guidebook on non-destructive testing of concrete structures*, 2002.

[89] ISOHEAT GMBH. *Gebrauchsanleitung ISOHEAT MIL-SM mit Temperaturregler MIL-EC 550-PT*.

[90] IVANYI, G. and BUSCHMEYER, W. *Verstärkung von Spannbetonbrücken durch Stahllaschen - Anwendungskriterien*. Beton- und Stahlbetonbau, 1992. 87(11): pp. 265–271. doi:10.1002/best.199200460.

[91] JCSS JOINT COMMITTEE ON STRUCTURAL SAFETY. *JCSS Probabilistic Model Code Part 3: Resistance Models*, 2000.

[92] JESSE, F. and CURBACH, M. *Verstärken mit Textilbeton*. In: BERGMEISTER, K.; FINGERLOOS, F. and WÖRNER, J.-D. (eds.), *Beton-Kalender 2010*, pp. 457–565. Wiley-VCH Verlag GmbH & Co. KGaA, Weinheim, Germany, 2009. doi:10.1002/9783433600443.ch7.

[93] JIANG, H.; ZHAN, H.; MA, Z. and JIANG, R. *Comparative Study of Three-Dimensional Stress and Crack Imaging in Concrete by Application of Inverse Algorithms to Coda Wave Measurements*. Sensors, 2020. 20(17): p. 4899. doi:10.3390/s20174899.

[94] JU, T.; LI, S.; ACHENBACH, J. and QU, J. *Effects of moisture on ultrasound propagation in cement mortar*. AIP Conference Proceedings, 2015. 1650(1): pp. 1409–1414. doi:10.1063/1.4914756.

[95] JUNKER, P. and HACKL, K. *A thermo-mechanically coupled field model for shape memory alloys*. Continuum Mechanics and Thermodynamics, 2014. 26(6): pp. 859–877. doi:10.1007/s00161-014-0345-x.

[96] KERSEY, A. D.; DAVIS, M. A.; PATRICK, H. J.; LEBLANC, M.; KOO, K. P.; ASKINS, C. G.; PUTNAM, M. A. and FRIEBELE, E. J. *Fiber grating sensors*. Journal of Lightwave Technology, 1997. 15(8): pp. 1442–1463. doi:10.1109/50.618377.

[97] KINDLER, A. and GROSSWIG, S. *Distributed Strain Sensing in der Geotechnik: Empfehlungen für ortsverteilte faseroptische Dehnungsmessungen in der Geotechnik*. Bautechnik, 2018. 95(5): pp. 385–393. doi:10.1002/bate.201800005.

[98] KONERTZ, D.; KOCUR, G. K.; CLAUSS, F.; HÄUSLER, F. and MARK, P. *Anchor Channels under 3D-Load Interaction - New Approaches to Load Distribution and Design*. In: DERKOWSKI, M.; GWOZDZIEWICZ, P.; HOJDYS, L.; KRAJEWSKI, P. and PANTAK, M. (eds.), *CONCRETE Innovations in Materials, Design and Structures, Proceedings of the fib Symposium 2019 in Krakow, Poland*. FIB – International Federation for Structural Concrete, Lausanne, Switzerland, 2019.

[99] KONERTZ, D.; KOCUR, G. K.; HÄUSLER, F. and MARK, P. *Longitudinal shear transmission of anchor channels into concrete—An experimental approach*. Structural Concrete, 2021. 22(2): pp. 1072–1084. doi:10.1002/suco.202000133.

[100] KONERTZ, D.; LÖSCHMANN, J.; CLAUSS, F. and MARK, P. *Faseroptische Messung von Dehnungs- und Temperaturfeldern*. Bauingenieur, 2019. 94(7/8): pp. 292–300. doi:10.37544/0005-6650-2019-07-08-70.

[101] KONERTZ, D.; MAHRENHOLZ, C. and MARK, P. *Ankerschienen unter räumlicher Belastung - Experimente zur Horizontallastinteraktion*. In: *Doktorandensymposium 2017 5. DAfStb-Jahrestagung mit 58. Forschungskolloqium*. DAfStb, Kaiserslautern, Germany, 2017.

[102] KRÄTZIG, W. B.; HARTE, R.; KÖNKE, C. and PETRYNA, Y. S. *Tragwerke 2*. Springer-Verlag, Berlin, Germany, 1990. doi:10.1007/978-3-642-41723-8.

[103] KRAUSE, M.; MIELENTZ, F.; MILMANN, B.; MÜLLER, W.; SCHMITZ, V. and WIGGENHAUSER, H. *Ultrasonic imaging of concrete members using an array system*. NDT & E International, 2001. 34(6): pp. 403–408. doi:10.1016/S0963-8695(01)00007-X.

[104] KREGER, S. T.; GIFFORD, D. K.; FROGGATT, M. E.; SOLLER, B. J. and WOLFE, M. S. *High Resolution Distributed Strain or Temperature Measurements in Single- and Multi-Mode Fiber Using Swept-Wavelength Interferometry*. In: *Optical Fiber Sensors*. OSA, Washington, D.C., 2006 doi:10.1364/OFS.2006.ThE42.

[105] KÜNZEL, A. *Parameteridentifikation auf Basis faseroptisch gemessener quasi-kontinuierlicher Dehnungssignale*. Ph.D. Thesis, Technische Universität Berlin, Berlin, Germany, 2016. doi:10.14279/depositonce-5558.

[106] LAROSE, E.; DE ROSNY, J.; MARGERIN, L.; ANACHE, D.; GOUEDARD, P.; CAMPILLO, M. and VAN TIGGELEN, B. *Observation of multiple scattering of kHz vibrations in a concrete structure and application to monitoring weak changes*. Physical Review E, 2006. 73(1): pp. 1–7. doi:10.1103/PhysRevE.73.016609.

[107] LAROSE, E. and HALL, S. *Monitoring stress related velocity variation in concrete with a $2{\cdot}10^{-5}$ relative resolution using diffuse ultrasound*. The Journal of the Acoustical Society of America, 2009. 125(4): pp. 1853–1856. doi:10.1121/1.3079771.

[108] LAROSE, E.; OBERMANN, A.; DIGULESCU, A.; PLANÈS, T.; CHAIX, J.-F.; MAZEROLLE, F. and MOREAU, G. *Locating and characterizing a crack in concrete with diffuse ultrasound*

A four-point bending test. The Journal of the Acoustical Society of America, 2015. 138(1): pp. 232–241. doi:10.1121/1.4922330.

[109] LAROSE, E.; PLANÈS, T.; ROSSETTO, V. and MARGERIN, L. *Locating a small change in a multiple scattering environment*. Applied Physics Letters, 2010. 96(20): pp. 1–9. doi:10.1063/1.3431269.

[110] LEGLAND, J.-B.; THÉRY, R.; ABRAHAM, O.; VILLAIN, G.; DURNAD, O.; LAROSE, E. and TOURNAT, V. *Influence of moisture on the estimation of nonlinear parameters in concrete with Nonlinear ultrasonic Coda Wave Interferometry*. In: *Proceedings of 12th European Conference on Non-Destructive Testing (ECNDT 2018)*, Gothenburg, Sweden. 2018 .

[111] LEZGY-NAZARGAH, M.; SAEIDI-AMINABADI, S. and YOUSEFZADEH, M. A. *Design and fabrication of a new fiber-cement-piezoelectric composite sensor for measurement of inner stress in concrete structures*. Archives of Civil and Mechanical Engineering, 2019. 19(2): pp. 405–416. doi:10.1016/j.acme.2018.12.007.

[112] LIEHR, S. *Fibre optic sensing techniques based on incoherent optical frequency domain reflectometry*. Ph.D. Thesis, Technische Universität Berlin, Berlin, Germany, 2014.

[113] LIENIG, J. and BRUEMMER, H. *Elektronische Gerätetechnik – Grundlagen für das Entwickeln elektronischer Baugruppen und Geräte*. Springer-Verlag, Heidelberg, Germany, 2014. doi:10.1007/978-3-642-40962-2.

[114] LILLAMAND, I.; CHAIX, J.-F.; PLOIX, M.-A. and GARNIER, V. *Acoustoelastic effect in concrete material under uni-axial compressive loading*. NDT & E International, 2010. 43(8): pp. 655–660. doi:10.1016/j.ndteint.2010.07.001.

[115] LOBKIS, O. I. and WEAVER, R. L. *Coda-Wave Interferometry in Finite Solids: Recovery of p-to-s Conversion Rates in an Elastodynamic Billiard*. Physical Review Letters, 2003. 90(25): pp. 1–4. doi:10.1103/PhysRevLett.90.254302.

[116] LÖSCHMANN, J.; AHRENS, M. A.; DANKMEYER, U.; ZIEM, E. and MARK, P. *Methoden zur Reduktion des Teilsicherheitsbeiwerts für Eigenlasten bei Bestandsbrücken*. Beton- und Stahlbetonbau, 2017. 112(8): pp. 506–516. doi:10.1002/best.201700027.

[117] LÖSCHMANN, J.; CLAUSS, F. and MARK, P. *Verstärken von Stahlbetontragwerken mit Temperaturinduktion*. Beton- und Stahlbetonbau, 2020. 115(10): pp. 746–757. doi:10.1002/best.202000038.

[118] LÖSCHMANN, J. and MARK, P. *Betonbauteile mit eingeschlitzter Bewehrung - Verstärkung mittels Temperaturinduktion*. BFT International, 2020. 86(2): p. 130.

[119] LÖSCHMANN, J.; STOLZUOLI, N.; AHRENS, M. A. and MARK, P. *Steering of continuity stresses in beam structures by temperature induction*. Engineering Structures, 2021. 229(6). doi:10.1016/j.engstruct.2020.111621.

[120] LÖSCHMANN, J.; STÖTZEL, A.; DANKMEYER, U. and MARK, P. *Gekoppelte Vermessungsstrategien für intelligente, digitale 3D-Stadtmodelle*. Messtechnik im Bauwesen, 2018. pp. 6–11.

[121] LUNA INNOVATIONS INC. *Distributed Fiber Optic Sensing: Temperature Coefficient for Polyimide Coated Low Bend Loss Fiber, in the 10 °C - 80 °C Range*.

[122] LUNA INNOVATIONS INC. *Distributed Fiber Optic Sensing: Temperature Coefficient for the Polymide Coated Low Bend Loss Fiber, in the -40 °C to 200 °C Range*.

[123] LUNA INNOVATIONS INC. *High-Definition Fiber Optic Strain Sensors*, 2016.

[124] LUNA INNOVATIONS INC. *Optical distributed sensor interrogator model ODiSI-B: User's guide: version 5.2.1; ODiSI-B software 5.2.0*, 2017.

[125] MARK, P. and SCHNÜTGEN, B. *Grenzen elastischen Materialverhaltens von Beton*. Beton- und Stahlbetonbau, 2001. 96(5): pp. 373–378. doi:10.1002/best.200100400.

[126] MASERA, D.; BOCCA, P. and GRAZZINI, A. *Coda Wave Interferometry Method Applied in Structural Monitoring to Assess Damage Evolution in Masonry and Concrete Structures*. Journal of Physics Conference Series, 2011. 305: pp. 1–9. doi:10.1088/1742-6596/305/1/012108.

[127] MAURER, R.; HEEKE, G.; KIZILITAN, H.; KOLODZIEJCZYK, A.; ZILCH, K.; DUNKELBERG, D. and FITIK, B. *Nachrechnung von Betonbrücken zur Bewertung der Tragfähigkeit bestehender Bauwerke: Bericht zum Forschungsprojekt FE 15.0490/2010/FRB*. Wirtschaftsverl. NW Verl. für neue Wiss, Bremerhaven, 2012.

[128] MEASURES, R. M. *Structural Monitoring with Fiber Optic Technology*. Elsevier Professional, San Diego, USA, 2001.

[129] MESCHEDE, D. *Gerthsen Physik*. Springer-Verlag, Heidelberg, Germany, 2015. doi:10.1007/978-3-662-45977-5.

[130] MONSBERGER, C. M. and LIENHART, W. *Distributed fiber optic shape sensing along shotcrete tunnel linings: Methodology, field applications, and monitoring results*. Journal of Civil Structural Health Monitoring, 2021. 11(2): pp. 337–350. doi:10.1007/s13349-020-00455-8.

[131] MÜLLER, A.; SODEIKAT, C.; SCHÄNZLIN, J.; KNAB, F.; ALBRECHT, L.; GROSCHUP, R. and OBERMEIER, P. *Die Gänstorbrücke in Ulm – Untersuchung, Probebelastung und Brückenmonitoring*. Beton- und Stahlbetonbau, 2020. 115(3): pp. 164–178. doi:10.1002/best.201900071.

[132] MÜLLER, E.; SCHMIDT, A.; SCHUMANN, A.; MAY, S. and CURBACH, M. *Biegeverstärkung mit Carbonbeton*. Beton- und Stahlbetonbau, 2020. 115(10): pp. 758–767. doi:10.1002/best.202000012.

[133] MURNAGHAN, F. D. *Finite Deformations of an Elastic Solid*. American Journal of Mathematics, 1937. 59(2): pp. 235–260. doi:10.2307/2371405.

[134] MYERS, R. H. and MONTGOMERY, D. C. *Response surface methodology: Process and product optimization using designed experiments*. Wiley, New York, USA, 1995.

[135] NARANIECKI, H.; HARTUNG, R.; MARX, S. and KLEMT-ALBERT, K. *Zustandsprognose von Ingenieurbauwerken auf Basis von digitalen Zwillingen und Bestandsdaten*. Bautechnik, 2022. doi:10.1002/bate.202100100.

[136] NAUMANN, J. *Brücken und Schwerverkehr – eine Bestandsaufnahme*. Bauingenieur, 2010. 85: pp. 1–9.

[137] NIEDERLEITHINGER, E.; HERBRAND, M. and MÜLLER, M. *Monitoring von Querkraftversuchen an Spannbetondurchlaufträgern mit Ultraschall und Codawelleninterferometrie*. Bauingenieur, 2017. 92(11): pp. 474–481. doi:10.37544/0005-6650-2017-11-60.

[138] NIEDERLEITHINGER, E.; SENS-SCHÖNFELDER, C.; GROTHE, S. and WIGGENHAUSER, H. *Coda Wave Interferometry Used to Localize Compressional Load Effects in a Concrete Specimen*. In: LE CAM; VINCENT; MEVEL; LAURENT; SCHOEFS and FRANCK (eds.), *EWSHM - 7th European Workshop on Structural Health Monitoring*. Nantes, France, 2014 .

[139] NIEDERLEITHINGER, E.; WANG, X.; HERBRAND, M. and MÜLLER, M. *Processing Ultrasonic Data by Coda Wave Interferometry to Monitor Load Tests of Concrete Beams*. Sensors, 2018. 18(6). doi:10.3390/s18061971.

[140] NIEDERLEITHINGER, E.; WOLF, J.; MIELENTZ, F.; WIGGENHAUSER, H. and PIRSKAWETZ, S. *Embedded Ultrasonic Transducers for Active and Passive Concrete Monitoring*. Sensors, 2015. 15(5): pp. 9756–9772. doi:10.3390/s150509756.

[141] NIEDERLEITHINGER, E. and WUNDERLICH, C. *Influence of small temperature variations on the ultrasonic velocity in concrete*. AIP Conference Proceedings. AIP, 2013 pp. 390–397.

[142] NOVÁK, B.; STEIN, F.; REINHARD, J. and DUDONU, A. *Einsatz kontinuierlicher faseroptischer Sensoren zum Monitoring von Bestandsbrücken*. Beton- und Stahlbetonbau, 2021. 116(10): pp. 718–726. doi:10.1002/best.202100070.

[143] OBEL, M.; MARWAN, A.; ALSAHLY, A.; FREITAG, S.; MARK, P. and MESCHKE, G. *Schadensbewertungskonzepte für innerstädtische Bauwerke bei maschinellen Tunnelvortrieben*. Bauingenieur, 2018. 93(12): pp. 482–491. doi:10.37544/0005-6650-2018-12-44.

[144] OUYANG, J.; CHEN, X.; HUANGFU, Z.; LU, C.; HUANG, D. and LI, Y. *Application of distributed temperature sensing for cracking control of mass concrete*. Construction and Building Materials, 2019. 197(5): pp. 778–791. doi:10.1016/j.conbuildmat.2018.11.221.

[145] PACHECO, C. and SNIEDER, R. *Time-lapse travel time change of multiply scattered acoustic waves*. The Journal of the Acoustical Society of America, 2005. 118(3): pp. 1300–1310. doi:10.1121/1.2000827.

[146] PAN, B.; QIAN, K.; XIE, H. and ASUNDI, A. *Two-dimensional digital image correlation for in-plane displacement and strain measurement: a review*. Measurement Science and Technology, 2009. 20(6): pp. 1–17. doi:10.1088/0957-0233/20/6/062001.

[147] PAN, B. and TIAN, L. *Advanced video extensometer for non-contact, real-time, high-accuracy strain measurement*. Optics Express, 2016. 24(17): pp. 1–12. doi:10.1364/OE.24.019082.

[148] PETERS, K. J. and INAUDI, D. *Fiber optic sensors for assessing and monitoring civil infrastructures*. In: *Sensor Technologies for Civil Infrastructures*, vol. 15, pp. 121–158. Elsevier, 2014. doi:10.1533/9780857099136.121.

[149] PFEIFFER, U. *Die nichtlineare Berechnung ebener Rahmen aus Stahl- oder Spannbeton mit Berücksichtigung der durch das Aufreißen bedingten Achsendehnung*. Ph.D. Thesis, Technische Universität Hamburg-Harburg, Hamburg, Germany, 2004.

[150] PLANÈS, T. and LAROSE, E. *A review of ultrasonic Coda Wave Interferometry in concrete*. Cement and Concrete Research, 2013. 53: pp. 248–255. doi:10.1016/j.cemconres.2013.07.009.

[151] PLANÈS, T.; LAROSE, E.; ROSSETTO, V. and MARGERIN, L. *LOCADIFF: Locating a weak change with diffuse ultrasound*. In: THOMPSON, D. O. and CHIMENTI, D. E. (eds.), *AIP Conference Proceedings 2013: Review of progress in quantitative nondestructive evaluation, volume 32*, pp. 405–411. American Institute of Phyics, Melville, NY, USA, 2013. doi:10.1063/1.4789076.

[152] PLANÈS, T.; LAROSE, E.; ROSSETTO, V. and MARGERIN, L. *Imaging multiple local changes in heterogeneous media with diffuse waves*. The Journal of the Acoustical Society of America, 2015. 137(2): pp. 660–667. doi:10.1121/1.4906824.

[153] POLYTEC GMBH. *Luna ODiSI 6000: Optical Distributed Sensor Interrogators (Data Sheet)*.

[154] POUPINET, G.; ELLSWORTH, W. L. and FRECHET, J. *Monitoring velocity variations in the crust using earthquake doublets: An application to the Calaveras Fault, California*. Journal of Geophysical Research: Solid Earth, 1984. 89(B7): pp. 5719–5731. doi:10.1029/JB089iB07p05719.

[155] PRIESTLEY, M. B. *Spectral analysis and time series*. Academic Press, New York, USA, 1981.

[156] QUAST, U. *Zur Mitwirkung des Betons in der Zugzone*. Beton- und Stahlbetonbau, 1981. 76(10): pp. 247–250. doi:10.1002/best.198100440.

[157] REGIER, R. and HOULT, N. A. *Distributed Strain Behavior of a Reinforced Concrete Bridge: Case Study*. Journal of Bridge Engineering, 2014. 19(12). doi:10.1061/(ASCE)BE.1943-5592.0000637.

[158] ROBERTS, P. M. *Development of the active doublet method for monitoring small changes in crustal properties*. Seismological Research Letters, 1991. 62(1): pp. 36–37.

[159] ROBERTS, P. M.; PHILLIPS, W. S. and FEHLER, M. C. *Development of the active doublet method for measuring small velocity and attenuation changes in solids*. The Journal of the Acoustical Society of America, 1992. 91(6): pp. 3291–3302.

[160] RYZHIK, L.; PAPANICOLAOU, G. and KELLER, J. B. *Transport equations for elastic and other waves in random media*. Wave Motion, 1996. 24(4): pp. 327–370. doi:10.1016/S0165-2125(96)00021-2.

[161] SAMIEC, D. *Verteilte faseroptische Temperatur- und Dehnungsmessung mit sehr hoher Ortsauflösung*. Photonik, 2011. (6): pp. 34–37.

[162] SANIO, D.; AHRENS, M. A. and MARK, P. *Tackling uncertainty in structural lifetime evaluations*. Beton- und Stahlbetonbau, 2018. 113(S2): pp. 48–54. doi:10.1002/best.201800036.

[163] SANIO, D.; AHRENS, M. A.; MARK, P. and RODE, S. *Untersuchung einer 50 Jahre alten Spannbetonbrücke zur Genauigkeitssteigerung von Lebensdauerprognosen*. Beton- und Stahlbetonbau, 2014. 109(2): pp. 128–137. doi:10.1002/best.201300079.

[164] SANIO, D.; LÖSCHMANN, J.; MARK, P. and AHRENS, M. A. *Bauwerksmessungen versus Rechenkonzepte zur Beurteilung von Spannstahlermüdung in Betonbrücken*. Bautechnik, 2018. 95(2): pp. 99–110. doi:10.1002/bate.201700092.

[165] SANIO, D.; MARK, P. and AHRENS, M. A. *Temperaturfeldberechnung für Brücken*. Beton- und Stahlbetonbau, 2017. 112(2): pp. 85–95. doi:10.1002/best.201600068.

[166] SCHABOWICZ, K. *Non-Destructive Testing of Materials in Civil Engineering*. Materials (Basel, Switzerland), 2019. 12(19): pp. 1–13. doi:10.3390/ma12193237.

[167] SCHACHT, G.; KÄDING, M.; BOLLE, G. and MARX, S. *Konzepte für die Bewertung von Brücken mit Spannungsrisskorrosionsgefahr*. Beton– und Stahlbetonbau, 2018. 114(2): pp. 85–94. doi:10.1002/best.201800087.

[168] SCHAUM, A. and MEURER, T. *Dissipativity-based output-feedback control for a class of semilinear unstable heat equations*. IFAC-PapersOnLine, 2019. 52(16): pp. 316–321. doi:10.1016/j.ifacol.2019.11.798.

[169] SCHENATO, L. *A Review of Distributed Fibre Optic Sensors for Geo-Hydrological Applications*. Applied Sciences, 2017. 7(9): pp. 1–42. doi:10.3390/app7090896.

[170] SCHERR, J. F. and GROSSE, C. U. *Delamination detection on a concrete bridge deck using impact echo scanning*. Structural Concrete, 2021. 22(2): pp. 806–812. doi:10.1002/suco.202000415.

[171] SCHICKERT, M. and KRAUSE, M. *Ultrasonic techniques for evaluation of reinforced concrete structures*. In: *Non-Destructive Evaluation of Reinforced Concrete Structures*, pp. 490–530. Elsevier, 2010. doi:10.1533/9781845699604.2.490.

[172] SCHMIDT-THRÖ, G.; SCHEUFLER, W. and FISCHER, O. *Kontinuierliche faseroptische Dehnungsmessung im Stahlbetonbau*. Beton- und Stahlbetonbau, 2016. 111(8): pp. 496–504. doi:10.1002/best.201600026.

[173] SCHNELLENBACH-HELD, M.; PEETERS, M. and SCHEERBAUM, F. *Sachstand Verstärkungsverfahren - Verstärken von Betonbrücken im Bestand: Bericht zum Forschungsprojekt 89.217/2008/AP*. Wirtschaftsverl. NW Verl. für neue Wiss, Bremerhaven, Germany, 2010.

[174] SCHURR, D. P.; KIM, J.-Y.; SABRA, K. G. and JACOBS, L. J. *Damage detection in concrete using coda wave interferometry*. NDT & E International, 2011. 44(8): pp. 728–735. doi:10.1016/j.ndteint.2011.07.009.

[175] SELLECK, S. F.; LANDIS, E.; PETERSON, M.; SHAH, S. and ACHENBACH, J. D. *Ultrasonic Investigation of Concrete with Distributed Damage*. ACI Materials Journal, 1998. 95: pp. 27–36.

[176] SELLENG, C.; MENG, B.; GRÖGER, K. and FONTANA, P. *Einflussgrößen auf die Wirksamkeit einer Wärmebehandlung von Ultrahochfestem Beton (UHFB)*. Beton- und Stahlbetonbau, 2017. 112(1): pp. 12–21. doi:10.1002/best.201600059.

[177] SENS-SCHÖNFELDER, C. and WEGLER, U. *Passive image interferometry and seasonal variations of seismic velocities at Merapi Volcano, Indonesia*. Geophysical Research Letters, 2006. 33(21): pp. 1–5. doi:10.1029/2006GL027797.

[178] SNIEDER, R. *Coda wave interferometry and the equilibration of energy in elastic media*. Physical Review E, 2002. 66(4): pp. 1–8. doi:10.1103/PhysRevE.66.046615.

[179] SNIEDER, R. *The Theory of Coda Wave Interferometry*. Pure and Applied Geophysics, 2006. 163(2-3): pp. 455–473. doi:10.1007/s00024-005-0026-6.

[180] SNIEDER, R.; GRÊT, A.; DOUMA, H. and SCALES, J. *Coda wave interferometry for estimating nonlinear behavior in seismic velocity*. Science, 2002. 295(5563): pp. 2253–2255. doi:10.1126/science.1070015.

[181] SOLLER, B. J.; GIFFORD, D.; WOLFE, M. S. and FROGGATT, M. *High resolution optical frequency domain reflectometry for characterization of components and assemblies*. Optics Express, 2005. 13(2): pp. 666–674. doi:10.1364/OPEX.13.000666.

[182] SPECK, K.; VOGDT, F.; CURBACH, M. and PETRYNA, Y. *Faseroptische Sensoren zur kontinuierlichen Dehnungsmessung im Beton*. Beton- und Stahlbetonbau, 2019. 114(3): pp. 160–167. doi:10.1002/best.201800105.

[183] STÄHLER, S. C.; SENS-SCHÖNFELDER, C. and NIEDERLEITHINGER, E. *Monitoring stress changes in a concrete bridge with coda wave interferometry*. The Journal of the Acoustical Society of America, 2011. 129(4): pp. 1945–1952. doi:10.1121/1.3553226.

[184] STEGEHAKE, C.; GRÜNEWALD, M.; ZANTHOFF, H.-W. and HECHT, C. *Faseroptische Temperaturprofilmessungen in Festbettreaktoren zur modellgestützten Evaluierung der effektiven radialen Wärmeleitung*. Chemie Ingenieur Technik, 2018. 90(5): pp. 602–614. doi:10.1002/cite.201700158.

[185] STOJIĆ, D.; NESTOROVIĆ, T.; MARKOVIĆ, N. and MARJANOVIĆ, M. *Experimental and numerical research on damage localization in plate-like concrete structures using hybrid approach*. Structural Control and Health Monitoring, 2018. 25(9). doi:10.1002/stc.2214.

[186] SÜDDEUTSCHE ZEITUNG DIGITALE MEDIEN GMBH / SÜDDEUTSCHE ZEITUNG GMBH. *Autobahnbrücke eingestürzt*, 08-14-2018.

[187] SÜDWESTRUNDFUNK. *Salzbachtalbrücke auf der A66 - ein Fall für die Abrissbirne: KEINE 60 JAHRE ALT*, 06-21-2021.

[188] SUTTON, M. A.; ORTEU, J. J. and SCHREIER, H. *Image Correlation for Shape, Motion and Deformation Measurements - Basic Concepts, Theory and Applications*. Springer US, Boston, MA, USA, 2009.

[189] TKOCZ, J. and MARK, P. *Heat treatment and shrinkage steering of precast thin walled concrete tubes in Concrete – innovations in materials, design and structures*. In: DERKOWSKI, M.; GWOZDZIEWICZ, P.; HOJDYS, L.; KRAJEWSKI, P. and PANTAK, M. (eds.), *CONCRETE Innovations in Materials, Design and Structures, Proceedings of the fib Symposium 2019 in Krakow, Poland*. FIB – International Federation for Structural Concrete, Lausanne, Switzerland, 2019.

[190] TONDOLO, F.; MATTA, E.; QUATTRONE, A. and SABIA, D. *Experimental test on an RC beam equipped with embedded barometric pressure sensors for strains measurement*. Smart Materials and Structures, 2019. 28(5): pp. 1–18. doi:10.1088/1361-665X/ab1172.

[191] TOUPIN, R. A. and BERNSTEIN, B. *Sound waves in deformed perfectly elastic materials. Acoustoelastic effect*. The Journal of the Acoustical Society of America, 1961. 33(2): pp. 216–225. doi:10.1121/1.1908623.

[192] UWE ELECTRONIC GMBH. *Datenblatt & Leistungsdiagramme Peltier Modul uwe electronic GmbH UEPT-140-127-086E120S*.

[193] UWE ELECTRONIC GMBH. *Peltier-Elemente - Hintergrundwissen*, 2021.

[194] VILLALBA, S. and CASAS, J. R. *Application of optical fiber distributed sensing to health monitoring of concrete structures*. Mechanical Systems and Signal Processing, 2013. 39(1-2): pp. 441–451. doi:10.1016/j.ymssp.2012.01.027.

[195] VOGDT, F.; SPECK, K.; PETRYNA, Y.; CURBACH, M. and LOUTFI, J. *Experimentell gewonnene Erkenntnisse zur Plastizität von Beton unter multiaxialem Druck*. Beton- und Stahlbetonbau, 2022. 117(1): pp. 3–11. doi:10.1002/best.202100074.

[196] VOGEL, M.; KOTAN, E. and MÜLLER, H. S. *Zerstörungsfreie Untersuchung von Beton mittels Impuls-Echo-Methode - Möglichkeiten und Grenzen*. Bautechnik, 2018. 95(2): pp. 148–156. doi:10.1002/bate.201700075.

[197] VU, G.; DIEWALD, F.; TIMOTHY, J. J.; GEHLEN, C. and MESCHKE, G. *Reduced Order Multiscale Simulation of Diffuse Damage in Concrete*. Materials (Basel, Switzerland), 2021. 14(14). doi:10.3390/ma14143830.

[198] WALZ, K. *Der Einfluß einer Wärmebehandlung auf die Festigkeit von Beton aus verschiedenen Zementen*. Springer VS, Wiesbaden, Germany, 1960. doi:10.1007/978-3-663-04570-0.

[199] WANG, X.; CHAKRABORTY, J.; BASSIL, A. and NIEDERLEITHINGER, E. *Detection of Multiple Cracks in Four-Point Bending Tests Using the Coda Wave Interferometry Method*. Sensors, 2020. 20(7): pp. 1–17. doi:10.3390/s20071986.

[200] WANG, X.; CHAKRABORTY, J. and NIEDERLEITHINGER, E. *Noise Reduction for Improvement of Ultrasonic Monitoring Using Coda Wave Interferometry on a Real Bridge*. Journal of Nondestructive Evaluation, 2021. 40(1): pp. 1–15. doi:10.1007/s10921-020-00743-9.

[201] WANG, X. and NIEDERLEITHINGER, E. *Coda Wave Interferometry Used To Detect Loads And Cracks In A Concrete Structure Under Field Conditions*. In: *9th European Workshop on Structural Health Monitoring (EWSHM 2018)*. 2018.

[202] WANG, X.; NIEDERLEITHINGER, E.; CHAKRABORTY, J. and KLIKOWICZ, P. *Monitoring a concrete bridge girder with the coda wave interferometry method*. In: *Fifth International Conference on Smart Monitoring, Assessment and Rehabilitation of Civil Structures (SMAR 2019)*. doi:10.5281/zenodo.3520603.

[203] WANG, X.; NIEDERLEITHINGER, E. and HINDERSMANN, I. *The installation of embedded ultrasonic transducers inside a bridge to monitor temperature and load influence using coda wave interferometry technique*. Structural Health Monitoring, 2021. 12(9): pp. 1–15. doi:10.1177/14759217211014430.

[204] WELSCH, T.; REISSEN, K.; SCHNELLENBACH-HELD, M.; HEGGER, J.; VON WESCHPFENNIG, D. and HAARDT, P. *Praxiserfahrungen zum Verstärken von Betonbrücken*. Beton- und Stahlbetonbau, 2016. 111(4): pp. 241–252. doi:10.1002/best.201600005.

[205] WENZEL H. *Health monitoring of bridges*. John Wiley & Sons, New Jersey, USA, 2008.

[206] WIGGENHAUSER, H.; NIEDERLEITHINGER, E. and MILMANN, B. *Zerstörungsfreie Ultraschallprüfung dicker und hochbewehrter Betonbauteile*. Bautechnik, 2017. 94(10): pp. 682–688. doi:10.1002/bate.201700040.

[207] WINKLER, K.; MARK, P.; HEEK, P.; ROHLÄNDER, S. and SOMMER, S. *Punching shear tests on symmetrically reduced slab quarters*. Structural Concrete, 2014. 15(4): pp. 484–496. doi:10.1002/suco.201400022.

[208] WINTER, D. *Optische Verschiebungsmessung nach dem Objektrasterprinzip mit Hilfe eines flächenorientierten Ansatzes*. Ph.D. Thesis, Technische Universität Carola-Wilhelmina zu Braunschweig, Braunschweig, Germany, 1993.

[209] WOLF, J.; NIEDERLEITHINGER, E.; MIELENTZ, F.; GROTHE, S. and WIGGENHAUSER, H. *Überwachung von Betonkonstruktionen mit eingebetteten Ultraschallsensoren*. Bautechnik, 2014. 91: pp. 783–796. doi:10.1002/bate.201400073.

[210] WUNDERLICH, C. and NIEDERLEITHINGER, E. *Evaluation of Temperature Influence on Ultrasound Velocity in Concrete by Coda Wave Interferometry*. In: *Nondestructive Testing of Materials and Structures*, pp. 227–232. Springer Netherlands, 2011. doi:10.1007/978-94-007-0723-8_33.

[211] XUE, Q.; LAROSE, E.; MOREAU, L.; THERY, R.; ABRAHAM, O. and HENAULT, J.-M. *Ultrasonic monitoring of stress and cracks of the 1/3 scale mock-up of nuclear reactor concrete containment structure*. Structural Health Monitoring, 2021. pp. 1–9. doi:10.1177/14759217211034729.

[212] ZEMAN, O.; SCHWENN, M.; GRANIG, M. and BERGMEISTER, K. *Assessment of the Deterioration State of Post-Installed Bonded Anchors Using Ultrasonic*. Materials (Basel, Switzerland), 2021. 14(8): pp. 1–13. doi:10.3390/ma14082077.

[213] ZHAN, H.; JIANG, H. and JIANG, R. *Three-dimensional images generated from diffuse ultrasound wave detections of multiple cracks in concrete structures*. Structural Health Monitoring, 2019. 19(1): pp. 12–25. doi:10.1177/1475921719834045.

[214] ZHAN, H.; JIANG, H.; ZHANG, J. and JIANG, R. *Condition Evaluation of an Existing T-Beam Bridge Based on Neutral Axis Variation Monitored with Ultrasonic Coda Waves in a Network of Sensors*. Sensors, 2020. 20(14): pp. 1–13. doi:10.3390/s20143895.

[215] ZHAN, H.; JIANG, H.; ZHUANG, C.; ZHANG, J. and JIANG, R. *Estimation of Stresses in Concrete by Using Coda Wave Interferometry to Establish an Acoustoelastic Modulus Database*. Sensors, 2020. 20(14). doi:10.3390/s20144031.

[216] ZHANG, Y.; ABRAHAM, O.; GRONDIN, F.; LOUKILI, A.; TOURNAT, V.; LE DUFF, A.; LASCOUP, B. and DURAND, O. *Study of stress-induced velocity variation in concrete under direct tensile force and monitoring of the damage level by using thermally-compensated Coda*

Wave Interferometry. Ultrasonics, 2012. 52(8): pp. 1038–1045. doi:10.1016/j.ultras.2012.08.011.

[217] ZHANG, Y.; ABRAHAM, O.; TOURNAT, V.; LE DUFF, A.; LASCOUP, B.; LOUKILI, A.; GRONDIN, F. and DURAND, O. *Validation of a thermal bias control technique for Coda Wave Interferometry (CWI)*. Ultrasonics, 2013. 53(3): pp. 658–664. doi:10.1016/j.ultras.2012.08.003.

[218] ZHANG, Y.; LAROSE, E.; MOREAU, L. and D'OZOUVILLE, G. *Three-dimensional in-situ imaging of cracks in concrete using diffuse ultrasound*. Structural Health Monitoring, 2017. 17(2): pp. 279–284. doi:10.1177/1475921717690938.

[219] ZHANG, Y.; PLANÈS, T.; LAROSE, E.; OBERMANN, A.; ROSPARS, C. and MOREAU, G. *Diffuse ultrasound monitoring of stress and damage development on a 15-ton concrete beam*. The Journal of the Acoustical Society of America, 2016. 139(4): pp. 1691–1701. doi:10.1121/1.4945097.

[220] ZHONG, B.; ZHU, J. and MORCOUS, G. *Measuring acoustoelastic coefficients for stress evaluation in concrete*. Construction and Building Materials, 2021. 309. doi:10.1016/j.conbuildmat.2021.125127.

[221] ZICHNER, T. *Temperaturunterschied infolge Witterungseinfluß und Beheizung von massiven Brücken*, 1976.

[222] ZILCH, K. and ZEHETMAIER, G. *Bemessung im konstruktiven Betonbau: Nach DIN 1045-1 (Fassung 2008) und EN 1992-1-1 (Eurocode 2)*. Springer-Verlag, Berlin, Germany, 2010. doi:10.1007/978-3-540-70638-0.

CURRICULUM VITAE

Personal Information

Name:	Felix Clauß
Date of Birth:	May 16, 1994
Place of Birth:	Hattingen, Germany

Professional Experience

2019 – today	Institute of Concrete Structures, Ruhr University Bochum, Bochum, Germany, Research Assistant
2016 – 2018	Institute of Concrete Structures, Ruhr University Bochum, Bochum, Germany, Student Assistant

Education

2016 – 2018	Faculty of Civil and Environmental Engineering, Ruhr University Bochum, Bochum, Germany, Master of Science (M. Sc.)
2013 – 2016	Faculty of Civil and Environmental Engineering, Ruhr University Bochum, Bochum, Germany, Bachelor of Science (B. Sc.)
2010 – 2013	Städtische Gesamtschule Hattingen, Hattingen, Germany Abitur
2009 – 2010	Marie-Curie Realschule, Hattingen, Germany
2004 – 2009	Gymansium Holthausen, Hattingen, Germany